

© 2008

Memduh Volkan Demirbař

ALL RIGHTS RESERVED

MICROSTRUCTURE-PROPERTY RELATIONSHIP IN SILICON CARBIDE
ARMOR CERAMICS

by

MEMDUH VOLKAN DEMİRBAŞ

A dissertation submitted to the
Graduate School-New Brunswick
Rutgers, The State University of New Jersey

In partial fulfillment of the requirements

For the degree of

Doctor of Philosophy

Graduate Program in Materials Science and Engineering

Written under the direction of

Professor Richard A. Haber

And approved by

New Brunswick, New Jersey

May, 2008

ABSTRACT OF THE DISSERTATION

MICROSTRUCTURE-PROPERTY RELATIONSHIP IN SILICON CARBIDE

ARMOR CERAMICS

by

MEMDUH VOLKAN DEMİRBAŞ

Dissertation Director:
Professor Richard A. Haber

Defects are one of the factors that show a negative effect on the ballistic performance. Uniform microstructures with a low percentage of well distributed porosity could possibly demonstrate high ballistic strength; therefore, it is of interest to estimate the parameters that define the spatial arrangement of defects. This aspect of microstructures was investigated in a variety of silicon carbide ceramics ranging from off-density sintered samples to high density hot-pressed armor grade samples.

The spatial distribution of defects was examined by various techniques including nearest neighbor distance distributions, tessellation analysis, and pair correlation functions. Random distributions were observed for most of the samples with some degree of clustering. Hardness was selected as a mechanical property to correlate with microstructural findings. Hardness contour maps were constructed by indenting samples with a statistically significant number of indents per load to see the variation in terms of location. The large number of indents allowed for Weibull analysis to be used to examine the spread in the data and to test spatial variability. A high degree of correlation was

obtained between microstructural parameters and hardness/Weibull modulus values. Smaller defect sizes and homogenous distribution of defects were shown to provide higher hardness values.

A sintered SiC tile was examined using ultrasound to determine high and low amplitude regions in C-scan image maps. Serial sectioning was performed on diced samples from these two regions. Although no significant difference was observed in terms of density and average defect size, statistical tests showed that the difference in the largest defect size detected in low amplitude and high amplitude regions was significant. Clusters of defects were also identified in the samples from the low amplitude regions. The signal loss that was observed in C-scans maps could partially be attributed to these results.

A particularly high degree of correlation was shown between average defect size, spatial distribution parameters and hardness data. These findings exhibit the strong effect of microstructure on the quasi-static properties and may affect ballistic performance.

ACKNOWLEDGEMENTS

First and foremost, I would like to start by thanking my thesis advisor Dr. Richard A. Haber for his continued support and invaluable suggestions during this work. He was always there for help and guidance when needed. I am extremely grateful to him for giving me an opportunity and having faith in me.

Secondly, I would like to thank my committee members Dr. Dale E. Niesz, Dr. W. Roger Cannon and Dr. Vimal K. Pujari for helping this work head in the right direction with their valuable comments and ideas.

I would like to acknowledge the Ceramic and Composite Materials Center and Materials Center of Excellence for funding this research.

I wish to thank Dr. Lisa Klein for all her help as a graduate director. I would like to thank Dr. Victor Greenhut not only for his assistance on electron microscopy but also for his enlightening speeches on anything in life, including the origin of my name, which I had not known before. I wish to acknowledge Dr. George Siegel and Dr. Manish Chhowalla for their support all throughout my studies at Rutgers.

I am thankful to the all departmental staff, specifically, Laura Chirichillo, Phyllis Cassell, Claudia Kuchinow, Michelle Sole. I also would like to thank John Yaniero, who has been a crucial part of this department as the lab manager.

I would like to acknowledge the past and current members of Haber Group, including Ray Brennan, Navin Venugopal, Dan Mairoano, Steve Mercurio, Steve Bottiglieri, Andrew Portune, Cari August, Vlad Domnich, Mihaela Jitianu, Chris Ziccardi, Anil Kaza, Laura Reynolds, Shawn Nycz. They were the members of such a pleasant working environment that made come to work enthusiastically every day. I

would like thank the undergrad technicians, Han Lin, Joe Pantina and Rich Delgado for spending many hours in the lab to help doing repetitive duties.

Finally, I would like to thank my family starting with my mother, Nagehan Demirbaş, and my father, Bülent Demirbaş for their constant and irreplaceable love and support. I wish to thank my aunt, Neslihan Karakaya, who has been like a second mother to me. I would like to acknowledge my fiancé and soon-to-be wife Başak Alptürk for helping me get through the fun but stressful final year of this degree. Lastly, I apologise to the people I overlooked in these few paragraphs but I am thankful for anyone who has touched my life.

TABLE OF CONTENTS

ABSTRACT OF THE DISSERTATION	ii
ACKNOWLEDGEMENTS	iv
TABLE OF CONTENTS	vi
LIST OF TABLES	xii
LIST OF ILLUSTRATIONS	xiii
1. INTRODUCTION	1
2. LITERATURE REVIEW	4
2.1. Response of Ceramics to Dynamic Loading.....	4
2.2. Defects in Ceramics	10
2.2.1. Types and Sources of Defects	10
2.2.2. Defect Populations	13
2.2.3. Defects in SiC	14
2.2.4. Identification of Porosity by Image Analysis	19
2.3. Spatial Data Analysis.....	31
2.3.1. Randomness, Regularity and Clustering.....	32
2.3.2. Planar Point Processes	33
2.3.3. K-function	34
2.3.4. Pair Correlation Function.....	35
2.3.5. Nearest Neighbor Distance Distributions	36
2.3.6. Tessellation Analysis	38
2.4. Hardness of Ceramics and Its Relation with Armor Performance.....	43
2.4.1. Hardness of Ceramics	43

2.4.2. Dependence of hardness on porosity	46
2.4.3. The Relationship between Hardness and Ballistic Performance	47
2.5. Statistical Examination of Property Data in Ceramics	53
2.5.1. Normal Distribution	53
2.5.2. Log-normal Distribution	53
2.5.3. Weibull distribution	54
2.5.4. Weibull Statistics and Its Correlation with Defect Distributions.....	58
2.5.3. Weibull Distribution of Hardness data	61
2.6. Nondestructive Evaluation by Ultrasound.....	64
3. METHOD OF ATTACK.....	66
3.1. First objective: To develop a method for determining microstructural uniformity of second phases.....	67
3.2. Second objective: To assess microstructural uniformity of second phases on a series of commercially available armor ceramics.....	67
3.3. Third objective: To determine microstructural uniformity using quasi-static properties	69
3.4. Fourth objective: To correlate microstructural parameters with the quasi-static properties	69
4. EXPERIMENTAL PROCEDURE	71
4.1. Sample Preparation for Microscopy	72
4.1.1 Grinding and Polishing	72
4.1.2. Serial Sectioning	72
4.1.3. Etching	73

4.2. FE-SEM	73
4.3. Optical Microscopy.....	74
4.4. Spatial Data Analysis.....	74
4.4.1. Nearest Neighbor Distance Distributions	74
4.4.2. Tessellation of Microstructures.....	76
4.4.3. Pair Correlation Functions	77
4.5. Image Analysis	78
4.5.1. Porosity Measurements	78
4.5.2. Defect Size Distributions	78
4.6. Mechanical Testing.....	78
4.6.1. Microindentation.....	78
4.6.2. Grain size analysis	79
4.6.3. Fracture Mode.....	80
4.7. Nondestructive Evaluation by Ultrasound.....	81
5. RESULTS AND DISCUSSION.....	86
5.1. Off-Density Sintered Hexoloy-like Samples	86
5.1.1. Density	86
5.1.2. Micrographs	86
5.1.3. Average Pore Size and Pore Size Distribution	87
5.1.4. Nearest Neighbor Distance Distributions	87
5.1.5. Tessellation Analysis	88
5.1.6. Pair Correlation Functions	90
5.1.7. Assessment of Spatial Data Analysis Techniques	90

5.1.8. Serial Sectioning	91
5.1.8.1. Average Pore Size and Pore Size Distribution	91
5.1.8.2. Nearest Neighbor Distance Distributions	92
5.2. Cercom Hot-Pressed SiC Samples.....	93
5.2.1. First Set of Hot-Pressed SiC Samples.....	93
5.2.1.1. Density	93
5.2.1.2. Microstructural Evaluation	93
5.2.1.3. Average Pore Size and Pore Size Distribution	94
5.2.1.4. Nearest Neighbor Distance Distributions	94
5.2.2. Lundberg Samples	95
5.2.2.1. Microstructural Evaluation	95
5.2.2.2. Density	96
5.2.2.3. Average Pore Size and Size Distribution.....	96
5.2.2.4. Nearest Neighbor Distance Distributions	97
5.3. SiC Hexoloy SA Tile	98
5.3.1. Ultrasound Image.....	98
5.3.2. High Magnification Images	99
5.3.2.1. Average Defect Size and Size Distribution	99
5.3.2.2. Nearest Neighbor Distance Distributions	100
5.3.3. Low Magnification Results.....	101
5.3.3.1. Nearest Neighbor Distance Distributions	102
5.3.3.2. Locating Defect Clusters.....	103
5.3.4. Serial Sectioning of Hexoloy SA Tile.....	104

5.3.4.1. Nearest Neighbor Distance Distributions	106
5.4. Property Measurements	140
5.4.1. Off-density Hexoloy SiC	140
5.4.1.1. Average Hardness	140
5.4.1.2. Comparison of Hardness Results with Rice's model.....	142
5.4.1.3. Hardness Contour Maps.....	143
5.4.1.4. Weibull Analysis.....	145
5.4.1.5. Interpretation of Weibull plots.....	147
5.4.1.6. Crack Paths	148
5.4.2. Cercom Hot-Pressed SiC Samples.....	150
5.4.2.1. Average Hardness	150
5.4.2.2. Weibull Analysis.....	151
5.4.2.3. Grain Size Distribution around High and Low Density Regions	153
5.4.3. SiC Hexoloy SA Tile	154
5.4.3.1. Average Hardness	154
5.4.3.2. Hardness Contour Maps.....	154
5.4.3.3. Weibull Analysis.....	155
5.4.4. Lundberg Samples	155
5.4.4.1. Average Hardness	156
5.4.4.2. Weibull Analysis.....	156
5.5. Correlation between Microstructural Findings and Property Data	176
5.5.1. Off-Density Hexoloy Samples.....	176
5.5.2. SiC Hexoloy SA Tile	177

5.5.3. Cercom Hot-Pressed Samples	178
5.5.4. Lundberg Samples	180
5.5.5. Comparison between hot-pressed and sintered	182
5.6. Practical Implications of This Thesis.....	197
6. CONCLUSION.....	199
6.1. Off-Density Hexoloy Samples.....	199
6.2. Cercom Hot-pressed SiC samples.....	201
6.3. Lundberg Samples	202
6.4. Hexoloy SA Tile	204
6.5. Overall Conclusions.....	206
7. FUTURE WORK.....	208
8. REFERENCES	210
9. CURRICULUM VITA	220

LIST OF TABLES

Table 4.1. Grinding/Polishing Procedure at 5-8 lbs/sample of force at 150 rpm	81
Table 4.2. Data generated in Image Processing Toolkit 5.0	83
Table 5.2. P_1 and P_2 values of off-density sintered SiC samples	113
Table 5.3. Q and V results from each layer	115
Table 5.5. T-test results of density between Region 1 and Region 2.....	135
Table 5.6. T-test results of density between Region 3 and Region 2.....	135
Table 5.7. T-test results of average defect size between Region 1 and Region 2.....	136
Table 5.8. T-test results of average defect size between Region 3 and Region 2.....	136
Table 5.9. T-test results of largest defect size observed between Region 1 and Region 2	137
Table 5.10. T-test results of largest defect size observed between Region 3 and Region 2	137
Table 5.11. Weibull modulus values for different loads.....	165
Table 5.12. Percentage of fracture modes.....	166
Table 5.13. Percentage of hardness values in each hardness range	172
Table 5.14. Quasi-static and dynamic properties of Lundberg samples [14,183]	174
Table 5.15. Number of defects and average defect size for sintered and hot-pressed SiC	194

LIST OF ILLUSTRATIONS

Figure 1.1. An example of random variation in microstructures from location to location	3
Figure. 2.1. An illustration of the projectile penetrating the ceramic armor [1].....	8
Figure 2.2. Representative shock compression profile in ceramics and schematic of brittle shear fracture process within shock-wave front [5].....	9
Figure 2.3. Pore distributions in a sintered body and variations present due to (a) variation in grain sizes (b) die friction (c) local packing and agglomeration differences and (d) more rapid pore elimination near surfaces.....	18
Figure 2.4. The hypothetical situation of a pore connected to three grains in an infinite solid.....	24
Figure 2.5. SEM micrographs of four different coatings showing pullouts [84].....	25
Figure 2.6. SEM images of a PSZ coating showing differences between a pore and a pullout [86].....	26
(a)	27
(b).....	27
Figure 2.7. The images of (a) a pore, and (b) a pullout, after segmentation.....	27
Figure 2.8. (a) SEM image of a sintered SiC (b) Blown up feature in the center of the image (c) Form factor values shown after segmentation	28
Figure 2.9. (a) Another SEM image of a sintered SiC (b) Blown up area from the center (c) Form factor values shown after segmentation.....	29
Figure 2.10. (a) Another SEM image of a sintered SiC (b) Blown up image of an oval shaped feature (c) Form factor values shown after segmentation.....	30
Figure 2.11. Four different types of spatial point pattern	41
Figure 2.12. Map of Q and V indices.....	42

Figure 2.13. Variation of the Minimum Solid Area with porosity for idealized pores cubic stacking (1) cylindrical pore axis perpendicular to the stress axis (2) cylindrical pore axis parallel to the stress axis [131].....	51
Figure 2.14. Ballistic mass efficiency as a function of Knoop hardness for the materials tested using depth of penetration [138].....	52
Fig. 2.15. Relative density of flaw sizes versus flaw size. The dashed line shows a typical distribution, the full line the behavior necessary for a Weibull distribution. The dashed area gives the density of destructive flaws [164].....	63
Figure 4.1. The shape of indent after each polishing step during serial sectioning.....	82
Figure 4.3. (a) Part of an original FESEM image (b) Processed image (c) After application of “invert” filter (d) “Skeletonize” filter applied (e) Second application of “invert” (f) Combined image of defects and cells around defects	84
Figure 4.4. Conversion of a rectangle shape into a circle for obtaining $d_{\text{equivalent}}$ where the areas of the figures are equal	85
Figure 5.1. Micrographs of (a) SA-1 (b) SA-2 (c) EXT (d) SP	108
Figure 5.2. Average defect size for all samples	108
Figure 5.3. Pore size distribution (a) SA-1 (b) SA-2 (c) EXT (d) SP	109
Figure 5.4. NND distribution of (a) SA-1 (b) SA-2 (c) EXT (d) SP	110
Figure 5.5. Tessellated microstructures of (a) SA-1 (b) SA-2 (c) EXT (d) SP.....	111
Figure 5.6. Cell area distributions of (a) SA-1 (b) SA-2 (c) EXT (d) SP	112
Figure 5.7. P_1 and P_2 for all four samples	112
Figure 5.8. Pair correlation function plots of (a) SA-1 (b) SA-2 (c) EXT (d) SP.....	113

Figure 5.9. Pore size distributions from (a) 1 st layer (b) 2 nd layer (c) 3 rd layer (d) 4 th layer	114
Figure 5.10. Nearest neighbor distance distribution from for (a) 1 st layer (b) 2 nd layer (c) 3 rd layer (d) 4 th layer.....	115
Figure 5.11. Micrographs of (a) LD (b) DEF (c) AG	116
Figure 5.12. Average defect size for all three hot-pressed samples.....	116
Figure 5.13. Defect size distribution of all three hot-pressed samples	117
Figure 5.14. Nearest neighbor distance distributions of all three hot-pressed samples..	117
Figure 5.15. Q-V plot of all three hot-pressed samples	118
Figure 5.16. Micrographs of (a)SiC-HPN (b)SiC-SC-1RN (c)SiC-N (d)SiC-B	118
Figure 5.17. Average defect size of Lundberg samples.....	119
Figure 5.18. Pore size distribution of Lundberg samples	119
Figure 5.19. Nearest neighbor distance distribution of (a)SiC-HPN (b)SiC-SC-1RN (c)SiC-N (d)SiC-B	120
Figure 5.20. Q-V map showing (a) each individual point (b) all points combined	120
Figure 5.21. C-scan image by ultrasound of Hexoloy SA3	121
Figure 5.22. Representative micrographs of (a) N1 (b) N4 (c) N5 (d) N8 (e) N9 (f) N12	122
Figure 5.23. Average defect size of each sample.....	122
Figure 5.24. Defect size distribution of (a) N1 (b) N4 (c) N5 (d) N8 (e) N9 (f) N12	123
Figure 5.25. Defect size distribution of (a) Region 1 (b) Region 2 (c) Region 3	124
Figure 5.26. Nearest neighbor distance distributions of (a) N1 (b) N4 (c) N5 (d) N8 (e) N9 (f) N12.....	125

Figure 5.27. Nearest neighbor distance distributions of each region.....	126
Figure 5.28. Q-V plots based on (a) region (b) sample	126
Figure 5.29. Low magnification images of (a) N1 (b) N4 (c) N5 (d) N8 (e) N9 (f) N12	127
Figure 5.30. Average defect size of all examined samples.....	128
Figure 5.31. Defect size distributions of (a) N1 (b) N4 (c) N5 (d) N8 (e) N9 (f) N12...	129
Figure 5.32. Nearest neighbor distance distributions of (a) N1 (b) N4 (c) N5 (d) N8 (e) N9 (f) N12.....	130
Figure 5.33. Q-V plot according to the low magnification images	131
Figure 5.34. An illustration of the interevent distance.....	131
Figure 5.35. One of the ten images from N9	132
Figure 5.36. Binary image of N9	132
Figure 5.37. Optimum limiting interevent distance determination.....	133
Figure 5.38. Demonstration of clusters when $R=20\text{ }\mu\text{m}$	133
Figure 5.39. Demonstration of clusters and random background when $R=20\text{ }\mu\text{m}$	134
Figure 5.40. Demonstration of clusters in the original image.....	134
Figure 5.41. Density values from 5 layers obtained by serial sectioning	135
Figure 5.42. Average defect size values from 5 layers obtained by serial sectioning	136
Figure 5.43. Largest defect observed at 5 layers obtained by serial sectioning.....	137
Figure 5.44. Q-V maps showing (a) The identified regions (b) 1 st layer (c) 2 nd layer (d) 3 rd layer (e) 4 th layer (f) 5 th layer	138
Figure 5.45. Q-V maps of all five layers from (a) N1 (b) N4 (c) N5 (d) N8 (e) N9 (f) N12	139
Figure 5.46. Average hardness vs. load for off-density SiC samples.....	158

Figure 5.47. Average hardness values of off-density SiC samples (a) 2 Kg (b) 1 Kg (c) 0.5 Kg (d) 0.3 Kg (e) 0.1 Kg.....	159
Figure 5.48. Contour maps at 2 Kg for (a) SA-1 (b) SA-2 (c) EXT (d) SP.....	160
Figure 5.49. Contour maps at 1 Kg for (a) SA-1 (b) SA-2 (c) EXT (d) SP.....	161
Figure 5.50. Contour maps at 0.5 Kg for (a) SA-1 (b) SA-2 (c) EXT (d) SP.....	162
Figure 5.51. Contour maps at 0.3 Kg for (a) SA-1 (b) SA-2 (c) EXT (d) SP.....	163
Figure 5.52. Contour maps at 0.1 Kg for (a) SA-1 (b) SA-2 (c) EXT (d) SP.....	164
Figure 5.53. Weibull plot at (a) 2 Kg (b) 1 Kg (c) 0.5 Kg (d) 0.3 Kg (e) 0.1 Kg where A = SA-1, B = SA-2, C = EXT, D = SP	165
Figure 5.54. Average hardness at (a) 2 Kg (b) 1 Kg (c) 0.5 Kg (d) 0.3 Kg (e) 0.1 Kg...	166
Figure 5.55. Weibull plot at 2 Kg for Cercom SiC samples	167
Figure 5.56. Weibull plots of (a) AG (b) LD (c) DEF at all loads.....	167
Figure 5.57. (a) Selected areas in the contour map of Cercom SiC samples (b) a micrograph from high hardness region (c) a micrograph from low hardness region	168
Figure 5.58. Grain size distribution around (a) high hardness region (b) low hardness region	169
Figure 5.59. Grain size clustering around high and low hardness regions	170
Figure 5.60. Indents from Hexoloy samples of (a) N2 (Region 1) (b) N6 (Region 2) (c) N10 (Region 3).....	171
Figure 5.61. Average hardness of Hexoloy samples (N2, N6 and N10)	171
Figure 5.62. Contour maps of Hexoloy samples N2, N6 and N10	172
Figure 5.63. % Hardness vs. hardness range	173
Figure 5.64. Weibull modulus of each Hexoloy sample at 2 Kg.....	173

Figure 5.65. Average hardness of Lundberg samples at 2 Kg	174
Figure 5.66. Weibull plots for each sample	175
Figure 5.67. Average hardness vs. $d(1,1)$ for off-density SiC density samples.....	185
Figure 5.68. Average hardness vs. average defect size for off-density SiC samples	185
Figure 5.69. Average hardness vs. average defect size for SiC Hexoloy tile	186
Figure 5.70. Weibull modulus vs. average defect size for SiC Hexoloy tile.....	186
Figure 5.71. Average hardness vs. $d(1,1)$ for SiC Hexoloy tile.....	187
Figure 5.72. Weibull modulus vs. $d(1,1)$ for SiC Hexoloy tile.....	187
Figure 5.73. % Hardness vs. average defect size for SiC Hexoloy tile	188
Figure 5.74. % Hardness vs. $d(1,1)$ for SiC Hexoloy tile	188
Figure 5.75. Average hardness at 2 Kg vs. $d(1,1)$ for hot-pressed SiC samples from Cercom.....	189
Figure 5.76. Average hardness at 0.3 Kg vs. $d(1,1)$ for hot-pressed SiC samples from Cercom.....	189
Figure 5.77. Average hardness vs. average defect size for hot-pressed SiC samples from Cercom.....	190
Figure 5.78. Weibull modulus at 0.1 Kg vs. average defect size for hot-pressed SiC samples from Cercom	190
Figure 5.79. Weibull modulus at 0.1 Kg vs. $d(1,1)$ for hot-pressed SiC samples from Cercom.....	191
Figure 5.80. (a) Average hardness vs. average defect size (b) Average hardness vs. $d(1,1)$ for Lundberg samples	191

Figure 5.81. (a) Elastic modulus vs. average defect size (b) Elastic modulus vs. $d(1,1)$ for Lundberg samples	192
Figure 5.82. (a) Fracture toughness vs. average defect size (b) Fracture toughness vs. $d(1,1)$ for Lundberg samples.....	192
Figure 5.83. (a) Transition velocity vs. average defect size (b) Transition velocity vs. $d(1,1)$ for Lundberg samples.....	193
Figure 5.84. (a) Penetration velocity vs. average defect size (b) Penetration velocity vs. $d(1,1)$ for Lundberg samples.....	193
Figure 5.85. (a) Average normalized projectile erosion rate vs. average defect size (b) Average normalized projectile erosion rate vs. $d(1,1)$ for Lundberg samples.....	194
Figure 5.86. Defect size distribution of (a) sintered (b) hot-pressed SiC	195
Figure 5.87. Nearest neighbor distance distributions of sintered and hot-pressed SiC ..	195
Figure 5.88. Q-V plot for sintered and hot-pressed SiC	196
Figure 5.89. Average hardness for sintered and hot-pressed SiC	196

1. INTRODUCTION

Armor ceramics are important components of advanced armor systems designed to defeat a variety of threats. Therefore, the material properties of armor ceramics are vital in order to be capable of handling the kinetic energy and momentum of the projectile.

Ceramics offer many promising properties for armor applications, such as high specific stiffness, high specific strength, high hardness, and chemical inertness. The unique combination of the low density, superior hardness, and high compressive strength has made wide varieties of ceramics primary candidates for armor systems that are subject to ballistic threats. If properly designed, ceramic armors can erode or fragment armor piecing projectiles and spatially spread the impact energy.

However, ceramics must be free of any unwanted inclusions and possess high formed density with small amounts of porosity so that their potential superior properties could be realized. Carbonaceous defects are commonly present in ceramic armor samples and porosity in small percentages is also unavoidable, therefore, more thorough characterization on these flaws is required. The spatial arrangement of pores or second phases, such as inclusions, is a microstructural characteristic expected to affect the ballistic performance of ceramic armor materials. For example, at a given volume fraction and average size of pores, clustered porosity or agglomerated second phases are expected to be more detrimental to the ballistic performance of an armor plate than it is when porosity or second phase is uniformly distributed. Therefore, it is of interest to estimate the statistical descriptors of the spatial arrangement of porosity and inclusions.

High percent theoretical density has generally been desired for maintaining structural integrity and is believed to be one of the acceptance criteria for product selection. Hot pressing is a more powerful technique to produce dense SiC than sintering is; however, inclusions and especially porosity are inevitable in both techniques. Pores may be present in different shapes and volumes, which will have a certain effect on the ballistic performance of the final product. The microstructure of armor materials must be examined thoroughly to set selection standards.

The scale of microstructural examination is a key issue in determining the microstructural integrity of materials. Micro-scale observations lead to morphology characterization such as shapes, sizes, spatial distributions, networks, volume fractions. Therefore, some techniques are required to quantitatively describe microstructures.

In this thesis, the relationship between flaw density/distribution and quasi-static properties will be correlated. When loading leads to localized stresses, local flaw distributions dominate. Weak spots at the micro-scale might lead to macro-scale failures. In view of this information, microstructural characterization concentrated on the spatial arrangement of features must be performed due to its importance in the performance of final product.

Different types of defects or flaws, such as carbon inclusions, metallic inclusions, pores could be found in sintered or hot-pressed materials. The emphasis in this thesis is given to density reducing and porosity attributed to carbon inclusions. Location of a feature is an important concept as well as its size and size distribution. Microstructure usually varies randomly from location to location as demonstrated in Fig. 1.1 and still, spatial distribution is often times overlooked. However, these microstructural

inhomogeneities cause the variations in density, which might be detrimental to the properties such as elastic modulus, hardness and strength of a material. Microstructural investigation is a good way to assess these variations in density, which is a result of pores, inclusions, their location and possible clustering.

Small scale variations

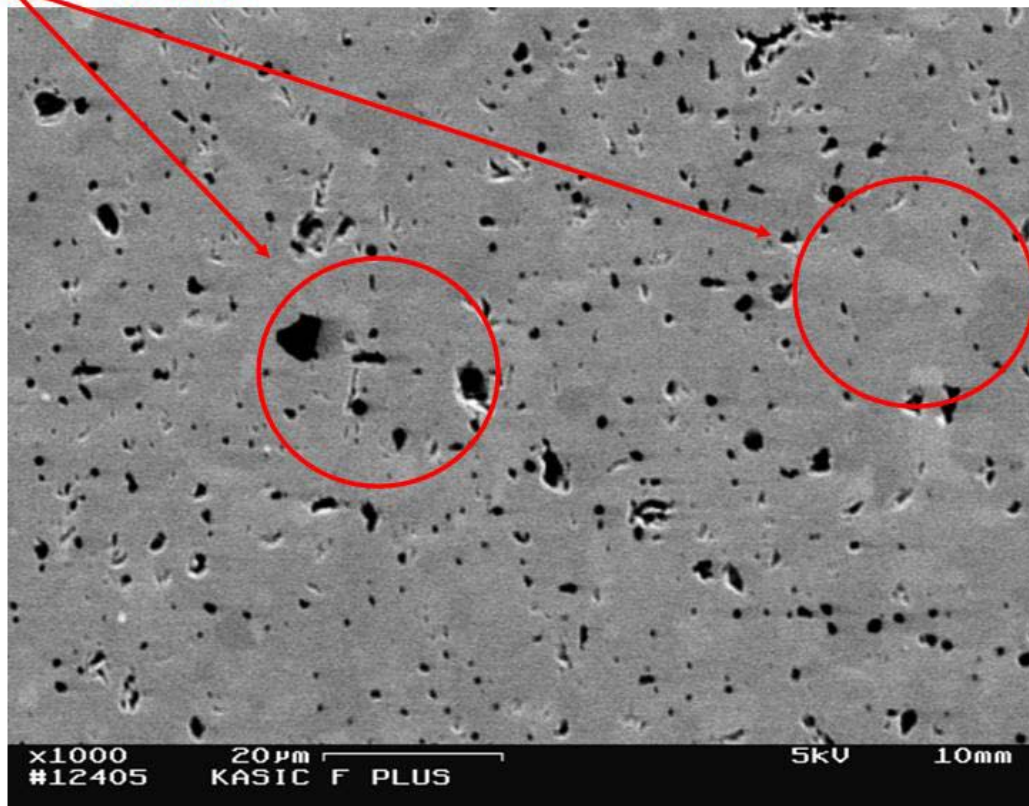


Figure 1.1. An example of random variation in microstructures from location to location

2. LITERATURE REVIEW

2.1. Response of Ceramics to Dynamic Loading

The reaction of a ceramic material to a ballistic event is complex. Several parameters come into play in the ballistic performance of a material. The sequence of events during penetration of a projectile can simply be explained using Figure 2.1 [1]. According to Luo et al. [1], as the projectile hits the target ceramic material, it is either stopped or dwells. This dwell allows the shock wave to propagate through the ceramic. It is through the interaction of the shockwave and the microstructure where cracks are introduced. These cracks will rapidly propagate and form a crack network, which will create a comminuted zone around the tip of the penetrator. Small ceramic fragments ahead of the penetrator flow radially around the tip of penetrator as it proceeds into the damaged zone. Then, those fragments are pushed back as erosion of the penetrator occurs. In the later stages of penetration, the fragments continue to wear down the penetrator up to the point where either the projectile erodes or the target material is penetrated. Ballistic performance of a material is highly influenced by the resistance of material to comminution [2, 3].

Time plays a key role in ballistic events, where the duration of loading drastically affects the response of a material [4-8]. The loading rate has a direct correlation with the amount of energy lost to the mechanisms other than crack propagation [9,10]. The energy absorbed by a specimen in dynamic fragmentation has several components, such as the surface energy consumed in the formation of fragments and the kinetic energy of fragments. In addition, branching cracks near the fracture surface and micro-cracks within the fragments produced under dynamic loading were also detected [11,12]. Both the branching cracks near the fracture surfaces and the micro-

cracks within the fragments must consume input energy to a certain degree. Therefore, the energy absorbed by the target consists of three main parts: the surface energy, the kinetic energy, and the energy spent during producing inner cracking damage of the fragments.

Shock waves created during a ballistic event show different loading paths depending on the target material. The loading starts elastically in metals. A sharp “knee” is observed at the beginning of inelastic deformation. This “knee” stands for the Hugoniot Elastic Limit (HEL), which in metals is defined as the point where plastic deformation starts. In ceramics, a different structure of the compressive loading path is monitored. The intensity of the incoming shock dictates the shape of the curve. If the stress is in the range of 1.0–1.5 times the HEL, the curve rises until the stress is relieved by a release wave. When the stress range approaches twice the HEL value or more, the curve starts ramping and continues with a steeper slope [5].

Compression wave profiles were studied by Grady, where he observed three distinct regions before failure, shown in Fig. 2.2. Initially, a sudden elastic rise to the failure limit (HEL) is observed. The failure ramp is a representation of rapidly changing compressibility. This stage is followed by deformation shock, where shear fracture grows within the shock front. [5].

Armor system designs have been focused on the capability of defeating high velocity projectiles on the surface of the ceramic, which is called interface defeat. This concept shows that the projectile material is forced to flow radially outwards on the surface of the ceramic without any considerable penetration. When the surface load produced by the penetrator goes above a critical value, a transition between interface

defeat and normal penetration behavior occurs at a critical impact velocity of the projectile [13,14]. Ceramic behaves as exceptionally strong below this transition velocity while it behaves considerably worse at a value above [13]. The amount of time spent by a projectile before it starts penetrating is called dwell time. This notion is important in the sense that a longer dwell time dissipates more energy and increasing dwell time will help interface defeat [15].

Three regimes of penetration can be observed in a range of impact velocities, which varies from the subsonic velocity to hyper velocities. In the first regime of lower velocity range (less than 10^3 m/s), non-deformable projectile penetration is valid where physical property values dictate the degree of penetration. Studies by Chen and Li [16,17] introduced two parameters, which were the impact function I and the geometry function of projectile N , in order to predict depth of penetration. The results showed good agreement with penetration on various types of materials.

The second regime is based on the Alekseevskii–Tate model, concerning long-rod penetration into a thick target where erosion and penetration occurs simultaneously [18]. 1.0 km/s to 3.0 km/s is the typical impact velocity range for this regime, which also depends very much on the material properties of the projectile and the target material. This part is also called the semi-hydrodynamic regime, followed by the hydrodynamic regime of penetration, where the impact velocity is greater than 3.0 km/s. Unlike the lower velocity range, material properties of neither the projectile nor the target material is important since fluid-fluid interaction occurs [19,20].

The effect of microstructure and the presence of defects play an important role in a ballistic event. When microstructure is considered, defects should also be taken into

account as they are inevitable components of a system. The effect of stress rate plays an important role as very low stress rates instigate the breaking of the dominant defect of a whole population [20]. A model was developed by Paliwal and Ramesh, for brittle failure under compressive loading by accounting of micro-crack interactions. It was shown that the influence of flaw distribution at different strain rates is significant. The spread of the distribution is the determining factor at low rates whereas total defect density starts to dominate as strain rate increases [21].

Molinari et al. modeled the ballistic event in a solid having a microstructure [22-26]. He looked at the influence of defect distributions on the fragmentation process, which showed rate-hardening of the material. An increase in the failure strength of the test bar was observed with strain rate increases. In the extreme condition of very high strain rate, the material demonstrated average material strength rather than the weakest-link strength in the quasi-static region. The spatial distribution of defects was taken into account in that study as well. The relationship between the average fragment size and the strain rate was examined using spatial distribution of defects, where, random distribution and regular distribution were contrasted. A smooth hardening effect was observed as well as a continuous strain rate and average fragment size relationship, where the defects were randomly distributed in a material. It was also found that the spread in fragment size distributions were narrower when the spatial distribution of defects were regular [26].

As a part of the microstructural investigation, Warner and Molinari proposed a model to study the intergranular fracture in alumina by taking the constitutive properties of the grain boundaries into account. An insight on the relationship between the grain boundary strength and macroscopic response was developed. According to the model, the

length of the longest microcrack cluster or the variance of microcrack length might offer a standard to predict possible catastrophic failure [24].

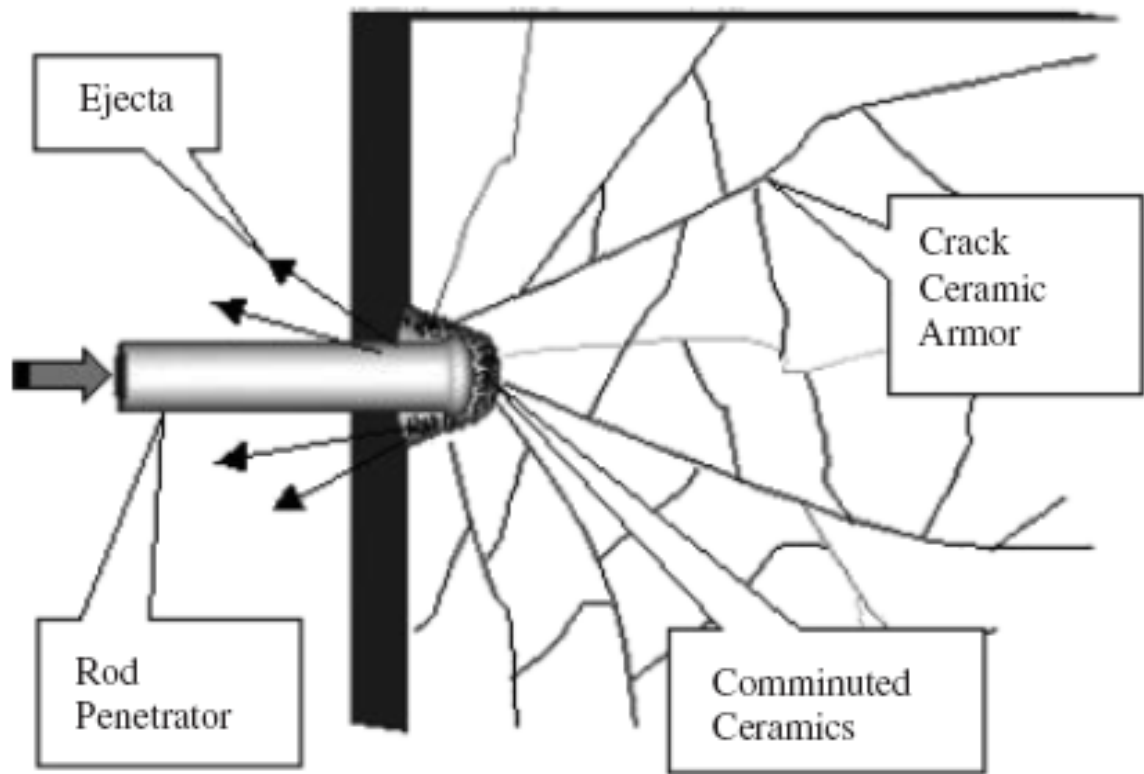


Figure. 2.1. An illustration of the projectile penetrating the ceramic armor [1]

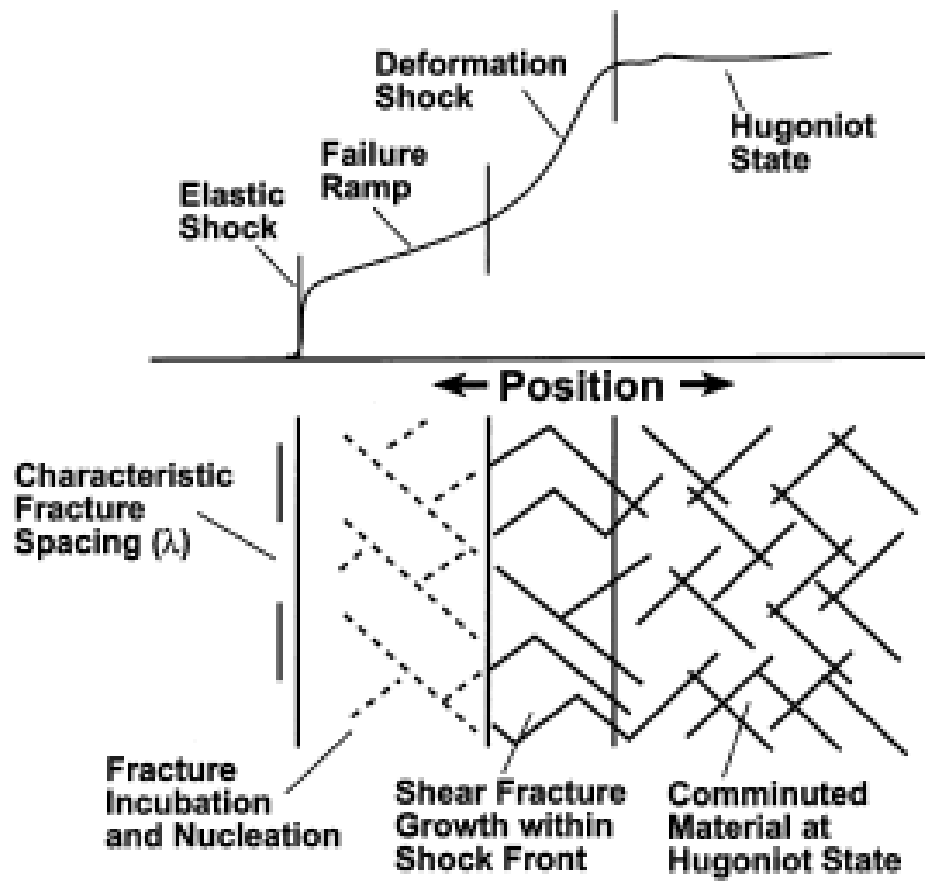


Figure 2.2. Representative shock compression profile in ceramics and schematic of brittle shear fracture process within shock-wave front [5]

2.2. Defects in Ceramics

2.2.1. Types and Sources of Defects

Defects are critical for ceramics since they are the root causes of mechanical failure. Porosity, inclusions, density gradients, insufficient or excessive additive use, non-uniform additive distributions, large grains could be listed as the main categories in the subject of defects [27]. Most defects are introduced into the system during processing. Some are initiated during post-processing, such as surface cracks created during machining or surface finishing [28].

Process-derived defects could arise from the starting powder. Particle size variations in the starting material might produce pore concentration differences throughout the material. A significant amount of defects were caused by the presence of agglomerates of the fine particles. These fine particles sinter rapidly, which leads to inter-agglomerate pores. Bridging of agglomerates might also lead to larger voids during sintering. These variations in the initial green body might give rise to a wide pore size distribution and the lack of elimination of larger pores might contribute to this in the final product [27].

Careful and proper application of dry-pressing step in ceramic manufacturing is important as it has a significant effect on sintering shrinkage, final density, microstructure and mechanical properties [29-31]. The inhomogeneities in the green body unavoidably cause development of defects. The importance of particle size distributions on sinterability were studied by Yeh and Sacks [29]. The conclusion of this study was that less shrinkage was observed in the materials with broad particle size distributions. Zhao and Harmer [30] studied the densification rate as a function of increasing green densities.

They observed an increase in densification rate in addition to a rise in grain growth rate with increasing pre-sintering densities.

The effect of green density on the final properties was examined by Occhionero and Halloran [31]. Samples with equal sintered densities but different green densities were analyzed in terms of the pore size distribution and significant differences were observed in the size range of voids. The sample with the highest green density showed a narrow pore size distribution, while the sample with the lowest density displayed a much broader distribution. This study could provide explanation to density variations inside green bodies. While high density regions possess narrow pore size distribution, broader size distributions could be present in lower density regions. Therefore, local porosity differences inside samples could be linked to particle packing [32-34]. An important factor to fluctuations of density inside a sample is the die-wall friction during pressing. More rapid pore elimination near surfaces has been observed in ceramic pieces during sintering which promotes inhomogeneous distribution of pores [27].

Binder removal is another issue that plays a key role in the defect and porosity formation. This process might cause structural change; therefore, the distribution of binders in a green body is critical [35,36]. Molten binder at high temperatures is redistributed inside the material by capillary forces, which is variable with physical properties of the binder and volatile product removal rate. Due to the common problem of non-uniform sample density, binder redistribution and differential shrinkage are frequently observed. This leads to inhomogeneous dimensional changes and distortion of the end product [36].

Low levels of binder (<10 vol%) are employed in pressing operations and sintering, which might produce green bodies that have enough open porosity for removal of volatile materials from the core to the surface. Green bodies of this type are called open-pore compacts. The connected porosity acts as a route for volatile material elimination. This aspect of green compacts makes it fairly easy to debind [37]. Although it is advantageous to use these chemical stabilizers as explained above, the presence of sintering aids and binders causes a certain amount of porosity in the final product. [38-41]. Flaws could also be introduced into ceramics by post-processing steps such as machining damage resulting in cracks and cracks triggered by thermal expansion anisotropy [38,39,42]. Pore distributions in a sintered body are given in Fig. 2.3.

Inclusions are another type of flaws common in ceramics. It is the result of a foreign material trapped within the host material, and can occur from impurities, contamination, or excess sintering additives. They are one of the major sources of failure since they act as stress concentrators. Thermal expansion coefficient mismatch between the inclusion and the matrix is a possible source of generating interfacial stresses. [28]

Contraction of grains during cooling in the densification stage is another possible source of producing interfacial stresses due to the resistance from neighboring grains. As contraction and resistance occur simultaneously, residual stresses build up inside the material at grain boundaries and triple junctions. Microcracking might occur as a result of this interaction [43].

2.2.2. Defect Populations

Defect populations were studied extensively due to their close relationship with the failure of ceramics. Size distributions and orientation of flaws were investigated by Jayatilaka and Trustrum. The conclusion to their study was that the distribution of the strength data is caused by the distribution of sizes and orientations of the flaws for a brittle and homogeneous material. Weibull distribution of strength was observed for flaw populations with a monotonically decreasing density of flaw sizes [44].

Uematsu et al. did noteworthy research on defect size distributions, where they looked at thin sections of alumina using transmission optical microscopy [45-47]. Pore size distributions were plotted and it was related to the experimental strength tests. The size distribution of defects was found to follow power law function [45,46,48] shown below:

$$y = ax^{-b} \quad 2.1$$

The fit to power law has been observed in other studies where distribution changed monotonously in the region of defect size larger than a few micrometers for sintered Si_3N_4 [49] and HIP- Al_2O_3 [47]. Takahashi et al. [49] reported the relationship between the defect distribution in sintered silicon nitride and the dispersion of the slurry. The defect size distribution follows the power law, and the constants, a and b, for the materials made from the flocculated slurry were bigger than those from well-dispersed slurry.

Gee studied the dependence of the predictions on the assumed form the defect-size distribution for two different distributions: a power law and an exponential law for 6

wt.% Co-WC. The two derived failure stress distributions were compared with three point bend test results and both fit the experimental data well. However, when predictions were later made for larger components, a discrepancy was found between the predictions made with the two distributions. As the component volume was increased and the required failure probability was decreased, the power law gave the most conservative best failure probability predictions [50].

In his PhD thesis, Bakas examined rubbles of ballistically tested hot pressed SiC tiles and he focused on inclusions, mainly C and Al/Fe/O. He examined ballistically impacted tiles that performed well and tiles that performed poorly and tried to identify differences in terms of inclusion populations. He observed that the distribution of inclusions on the rubble made a good fit to a modified inverse power law function derived by Jayatilaka and Trustrum [51].

Defect size distributions have been a key part in several studies involving different materials and they appeared to obey the power law. This will be put to the test in this thesis as pore size distributions will be obtained from sintered and hot-pressed silicon carbide samples.

2.2.3. Defects in SiC

As any other ceramic, silicon carbide armor materials are known to contain microstructural defects, including inclusions, isolated pores and porous areas, large grains, non-uniform distribution of additives at grain boundaries. These defects play an important role mechanical property variations and possibly, in ballistic efficiency. As some of the defects are common such as porosity, some of them are anomalous in the

sense they are not as frequent. Examples to the anomalous defects are pores that are much greater than the grain size, foreign inclusions or a very low percentage of porous areas within a dense matrix. Although not as common, these could be equally significant in the ballistic performance of a silicon carbide armor plate as they might activate macroscopic cracking near the beginning of a ballistic event [52,53].

SiC is a covalently bonded material, possessing only 9% to 12% ionic character. The shortness, directionality and strength of the bonds make it very difficult to achieve to high density [54]. A partial solution to this problem is using additives such as boron, carbon and aluminum during sintering [54-64] or hot pressing [65-70]. Although they considerably enhance densification, they might also act as defects in the cases where non-uniform distribution and their excessive or insufficient use come into play.

Carbon is the most common additive among the ones mentioned above. Hamming [54] studied the inclusions of excess free carbon, which was found in the form of graphite, using Auger electron spectroscopy and TEM. The size range of these carbon inclusions showed a large variation, mainly due to the starting concentration and the uniformity distribution. He stressed the importance of their spatial distribution as inhomogeneities of these defects could lead to agglomerate-type flaw dimensions.

More et al. studied boron-containing phases in sintered SiC. This phase, which was B_4C containing minor levels of Si, was a result of the densification aids used in the sintering. It was stated that they could also evolve as 20 nm precipitates during annealing well below the sintering temperature. According to the observations, grain boundaries were free of any boron-containing phase [71].

Extensive TEM analysis of SiC grain boundaries was performed by Carpenter et al. They examined liquid phase sintered SiC with additions of Al_2O_3 and Al_4C_3 using high resolution TEM. It was found out that grain triple junctions and some grain boundaries have considerable amounts of Al, C, O and Si. These zones were mostly free of glassy phases, indicating that high degree of crystallization was obtained during cooling stage [72].

Prior to the study by Zhang et al. [73], secondary-phase inclusions in ABC–SiC phases [74], such as $\text{Al}_8\text{B}_4\text{C}_7$ [75,76] and $\text{Al}_4\text{C}_4\text{O}$ [77] were identified, which were mostly isolated or located at triple junctions [78]. Zhang et al extended these studied by looking at triple junctions, inside grains and at grain boundaries using TEM. Boron-free phases of $\text{Al}(\text{Si})\text{-O-C}$ and $\text{Al}(\text{Si})\text{-O}$ were observed at triple junctions. Sulfur contamination was also detected in $\text{Al}(\text{Si})\text{-O-C}$ phase. $\text{Al}_2\text{O}_{2.2}(\text{B}_{0.9}\text{C}_{2.1})$ was the composition of the phase found as intra-grain and inter-grain inclusions, although fluctuations of B and C content were observed other than the specified composition. Shape differences between these inclusions were also seen as intra-grain inclusions were spherical while slabs of the same phase were squeezed in between grains [73].

Sherman studied defects in sintered and hot-pressed silicon carbide and tried to separate intergranular and transgranular chemistries using Auger electron spectroscopy. He found out that the hot pressed material he used in the study showed mixed intergranular and transgranular fracture. Si, C, Al, Ca, Zr, O, and N were the elements detected at the grain facets while transgranular facets showed only Si and C. On the other hand, sintered SiC showed mostly transgranular fracture. Both transgranular and

intergranular sites showed similar elemental data, with a small amount of boron on both [79].

As mentioned previously, Bakas examined the surface of ballistic rubble from two different hot-pressed SiC V50 targets in order to investigate any relationship between defects and ballistic performance. Two types of defects were observed; those having carbonaceous inclusions and those inclusions with Al/Fe/O peaks. Carbon inclusions could be accepted as voids in their mechanical behavior due to the elastic constant mismatch with SiC. The second type of inclusions with Al/Fe/O peaks was observed to be larger than carbon. Bakas predicted that these elements belong to alumina or aluminosilicate spinel with different levels of iron contamination. The distributions obtained from carbonaceous defects were considerably different for the “good” and “bad” target while that was not the case for Al/Fe/O inclusions [51].

Consequently, during the tailoring of SiC microstructure, a significant amount of additives are used which increase the likelihood of introducing defects to the system as pores and certain types of inclusions are common in armor silicon carbide. Since, their presence is unavoidable to a certain extent, size and spatial distribution information must be determined as these parameters possibly affect ballistic efficiency.

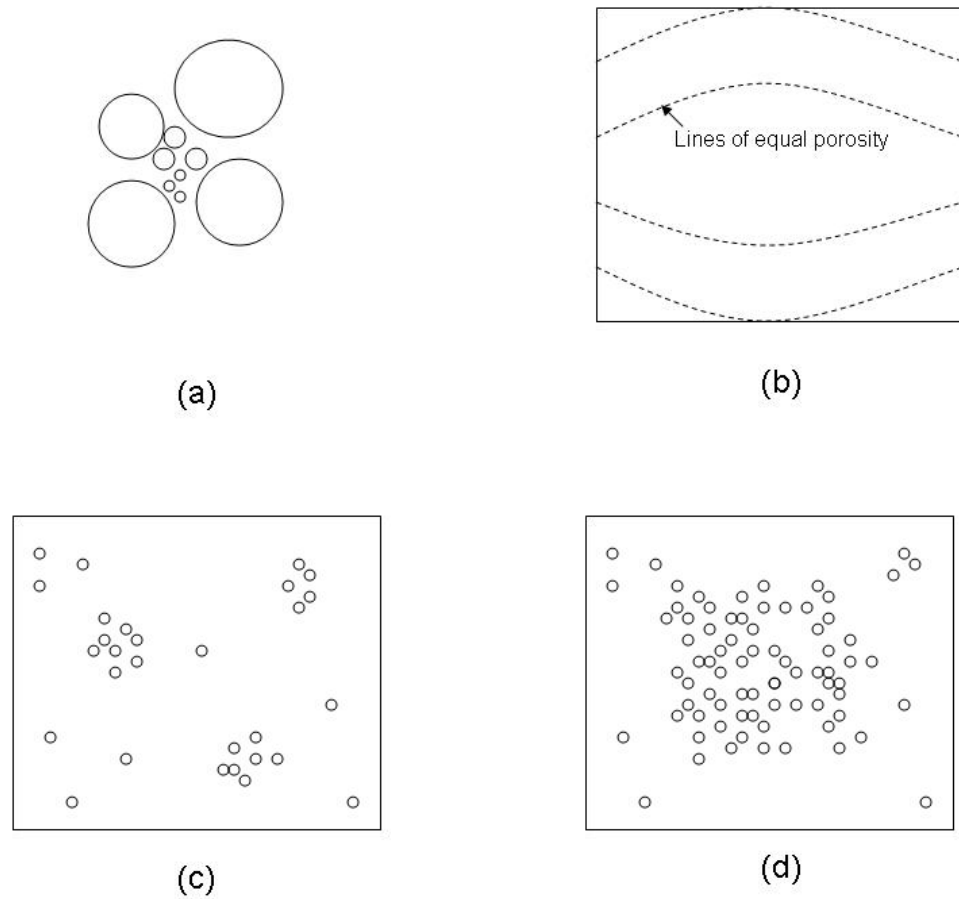


Figure 2.3. Pore distributions in a sintered body and variations present due to (a) variation in grain sizes (b) die friction (c) local packing and agglomeration differences and (d) more rapid pore elimination near surfaces

2.2.4. Identification of Porosity by Image Analysis

Pore identification is a critical step in microstructural analysis. The basics of pore evolution and curvatures in pores should be emphasized in order to make an assessment on pore morphology.

During sintering, the hypothetical situation of a pore connected to three grains in an infinite solid, given in Fig. 2.4, can be considered. Equilibrium will impose two important requirements on the geometry. First, the chemical potential of the atoms under the pore surface must be same everywhere. Therefore, the curvature of pore surface must be the same everywhere, consisting of circular arcs in two-dimensional models. Second, no net force must be present at the junction of the pore surface and the grain boundary. This leads to a specific angle of intersection between the surface and the grain boundary at the junction. Representing the interfacial tensions as vectors, with magnitudes equal to the surface and grain boundary tensions and with directions tangential to the pore surface or in the direction of the grain boundary, then force balance gives:

$$2\gamma_{sv} \cos \frac{\psi}{2} = \gamma_{gb} \quad 2.2$$

where γ_{sv} is the surface energy, γ_{sb} is the grain boundary energy, and ψ is the dihedral angle. Surface and grain boundary energies are susceptible to changes due to impurities and crystal orientation, so the dihedral angle may not be the same everywhere [80]. Careful measurements of thermal grooves in MgO and Al₂O₃ show a wide variety of dihedral angles in each material [81]. The distribution for undoped Al₂O₃ is particularly broad but becomes considerably narrower upon doping with MgO. The

average dihedral angle is $\sim 120^\circ$, but many of the angles are less than 120° , corresponding to $\gamma_{sv} < \gamma_{gb}$. Values of dihedral angle range from 105° to 113° for ceramics, implying that $\gamma_{gb} / \gamma_{sv}$ is 1.1 to 1.2 [80]. The geometrical considerations can be extended to three dimensions, in which case, the pore is a polyhedron. This analysis was carried out by Kingery and Francois [82].

During microstructural analysis, pores might not be identified as easily due to the deviation of shapes from the theoretical cases explained above. In addition to that, during grinding and polishing ceramics, specific problems are encountered that are related to the high hardness and brittle behavior of this class of materials. Pullouts are frequently observed during the grinding of ceramic samples. These pullouts can result in an incorrect microstructural analysis, since it is more difficult to identify pores. Besides, measurement of grain size, determination of particle distribution and other related problems arise due to the presence of pullouts. Although the pullout effect can be reduced by modifying the grinding parameters of the sample preparation machine, such as longer polishing times and lower applied forces that could lead to a small improvement in the quality of the polished samples, total elimination might still be difficult and the pullout problem might not be solved completely [83].

Studies were carried out to examine the polishing-induced pullouts in a microstructure [84,85]. Li and Ding characterized microstructures of plasma sprayed $\text{Cr}_3\text{C}_2\text{-NiCr}$ coatings by scanning electron microscopy and image analysis techniques. The fractal character of the circumferences of polishing-induced pull outs of plasma sprayed $\text{Cr}_3\text{C}_2\text{-NiCr}$ coatings was observed by means of the perimeter-area relationship. The purpose of this study was to report the fractal dimensions of circumferences of

polishing-induced pull outs of the coatings sprayed using different starting powders and correlate that with fracture toughness.

SEM micrographs of four different coatings from that study are given in Fig. 2.5. It was reported that although some of the pits on polished surfaces of the coatings were pores formed during spraying, most of the pits were pullouts produced during the polishing process. The circumferences of the pullouts were irregular and their lengths were obviously longer than the corresponding smooth circumferences. These pullouts were formed due to crack propagation and fracturing of lamellar splats caused by indentation stress fields of the hard abrasive particles. Li and Ding mentioned that it seemed promising to use shape parameters to characterize circumferences of polishing-induced pullouts of some thermal sprayed coatings with which fracture toughness of the coatings can be correlated [84].

In a study by Deshpande *et al.*, image analysis methods were applied to a variety of thermally sprayed coatings; materials of interest in this study being produced from partially stabilized zirconia (PSZ, $\text{ZrO}_2 + 8\% \text{Y}_2\text{O}_3$) and alumina ceramics. The results have been complemented with the microstructural information obtained using advanced characterization techniques, such as small-angle neutron scattering (SANS) and computer micro-tomography (CMT) carried out on similar coatings.

Fig. 2.6 shows an SEM image of a typical PSZ coating microstructure with various features highlighted. It can be seen how the higher depth-of-field of the SEM, to a large degree, enables to distinguish between pores and pullouts. Pores are more or less circular features with a planar inner surface whereas pullouts are irregular in shape and indicate material removal with their rough internal surface. Then, for conducting image

analysis, similar sized regions were chosen from the micrographs by discarding areas with pullouts [86].

According to the statements above, attributes to a feature, mainly shape, could be used as a determining factor for distinguishing between a pullout and a pore. The fact that “irregularity” of the shape of feature is critical; a shape parameter could be used to assign a number to each feature.

Form factor is a widely used parameter in image analysis and it can be calculated by the following formula:

$$\text{Form factor} = \frac{4\pi \cdot \text{Area}}{\text{Perimeter}^2} \quad 2.3$$

The form factor is 1.0 for a perfect circle. Any other shape will have more perimeter for the same area and the form factor describes this increase. As the irregularity of the shape increases, it becomes much smaller. A many-petalled flower may have form factors of 0.05 or even less [87]. Use of form factor serves the same purpose the fractal dimensions does, taking perimeter and area relationship into account.

Fig. 2.7 shows the images from Fig. 2.6 after segmentation was performed and the form factor values are given on the images. The form factor value for the pore was calculated as 0.867 while the value for the pullout was 0.258. This example roughly shows the distinction between a pore and a pullout in terms of a shape parameter. A certain value in between the two can be set as a baseline for removing pullouts from the images. Defining a certain threshold value for this might be difficult but density could be used to verify whether a correct threshold value is used or not.

Three images of defects from a Hexoloy SiC tile used in thesis are given in Fig. 2.8, Fig. 2.9 and Fig. 2.10. Fig. 2.8 shows a large feature at the centre and a smaller one close to the left corner. The large feature possesses an obvious irregularity and the inner part shows material removal therefore, this could easily be defined as a pullout. Although, not as distinct, same statements are valid for the other feature. Image analysis was performed on this image and the form factor values are obtained for each one, 0.358 and 0.532, for the large feature and the smaller one, respectively.

Fig. 2.9 shows a group of pores, and possibly, pullouts. The largest one in the image has the attributes to that of pullout. There is another possible pullout close to the lower right corner that looks like a “teardrop” with a very sharp corner that is a result of meeting two straight lines, which is uncharacteristics of pores according to the explanations stated earlier. A few pullouts other than these two can also be identified in the image. Form factors values were calculated again and they are written on each feature in Fig. 2.9. The values are 0.284 and 0.614 for the largest feature and “the teardrop”, respectively. The ones that look like pores have values around 0.800.

Fig. 2.10 shows an oval shaped feature. The irregularity of the perimeter is still valid and the inner part of the feature indicate material removal so this is accepted as a pullout according to the previous descriptions. There are four other features in the field of view, all of which look like pores but the one right above the central large feature. Form factor values were obtained again, with the values of 0.642 and 0.623 for the two possible pullouts.

According to the observations and the literature shown above, it is reasonable to say that form factor values of pullouts go up to approximately 0.650. The features in

images that resemble pores possesses form factor values of approximately 0.800 and above. Therefore, these observations might imply that a threshold value between these two numbers likely eliminates pullouts from micrographs and enables microstructural analysis to be more accurate. Previous tries using 0.700 as a threshold value was successful as the density obtained from micrographs matched up well with the actual density values.

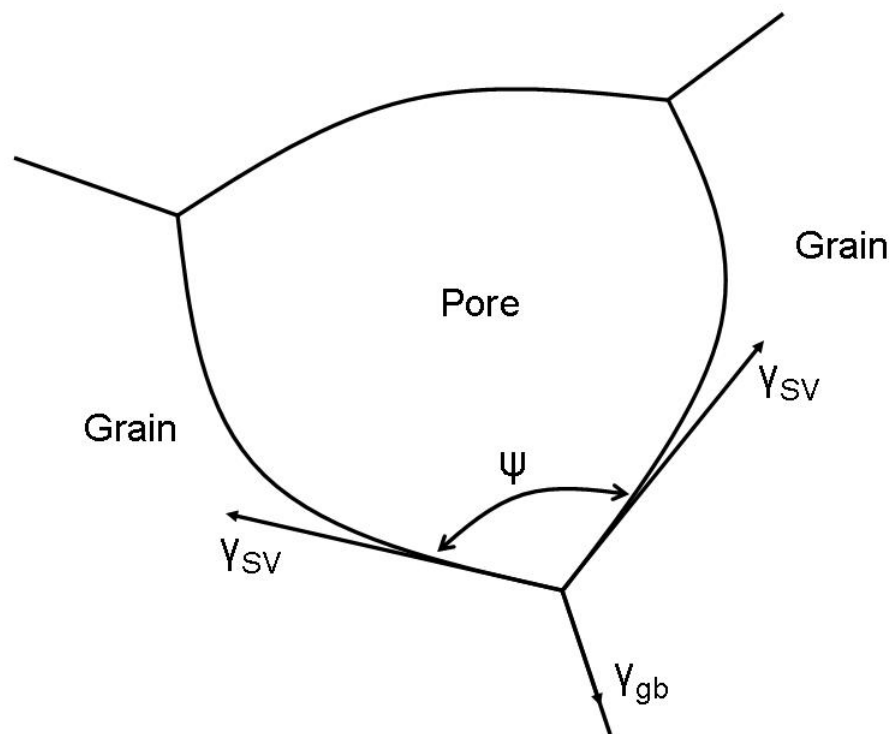


Figure 2.4. The hypothetical situation of a pore connected to three grains in an infinite solid

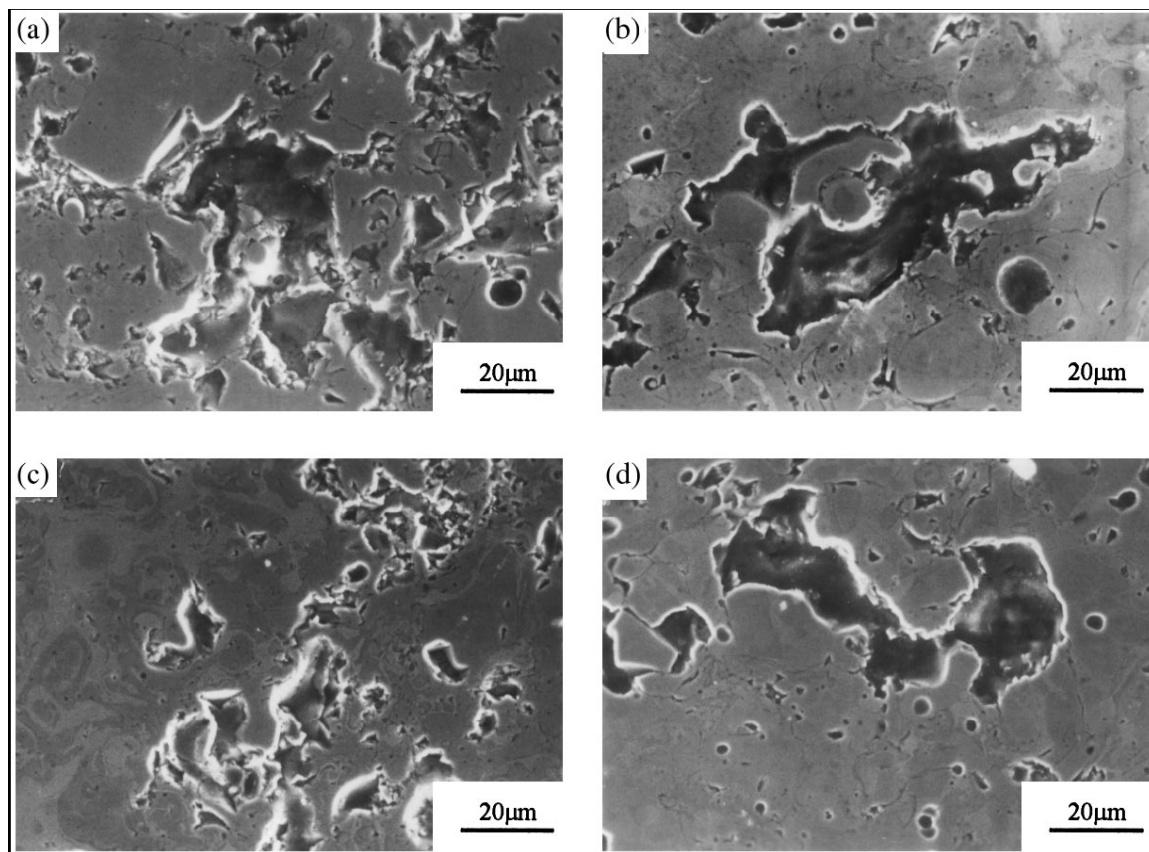


Figure 2.5. SEM micrographs of four different coatings showing pullouts [84]

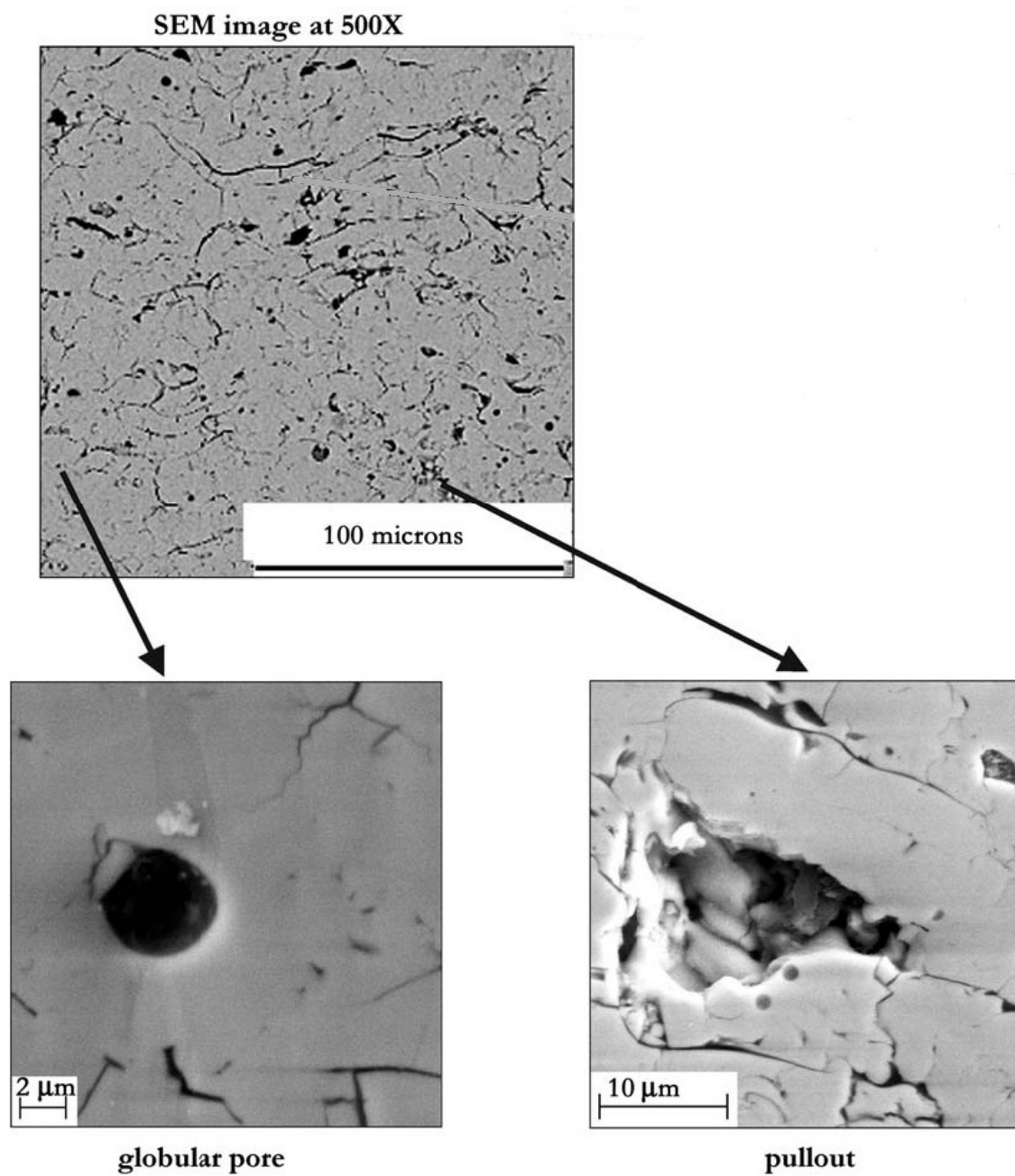
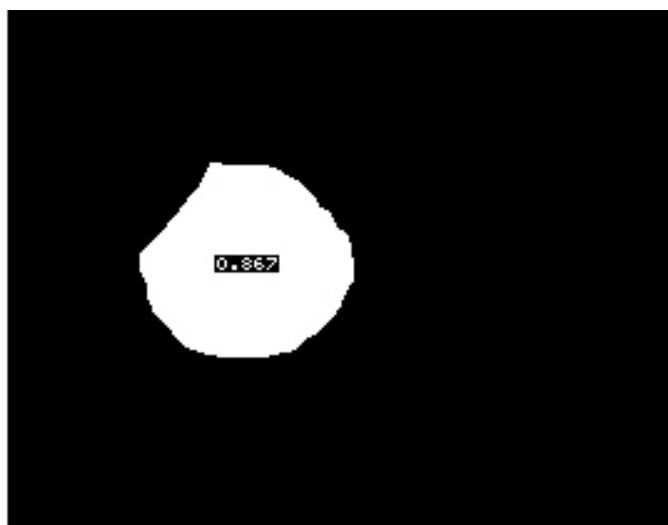
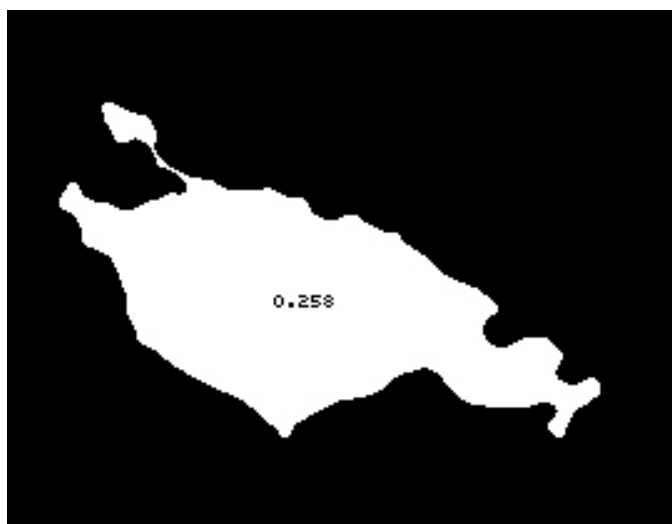


Figure 2.6. SEM images of a PSZ coating showing differences between a pore and a pullout [86]



(a)



(b)

Figure 2.7. The images of (a) a pore, and (b) a pullout, after segmentation

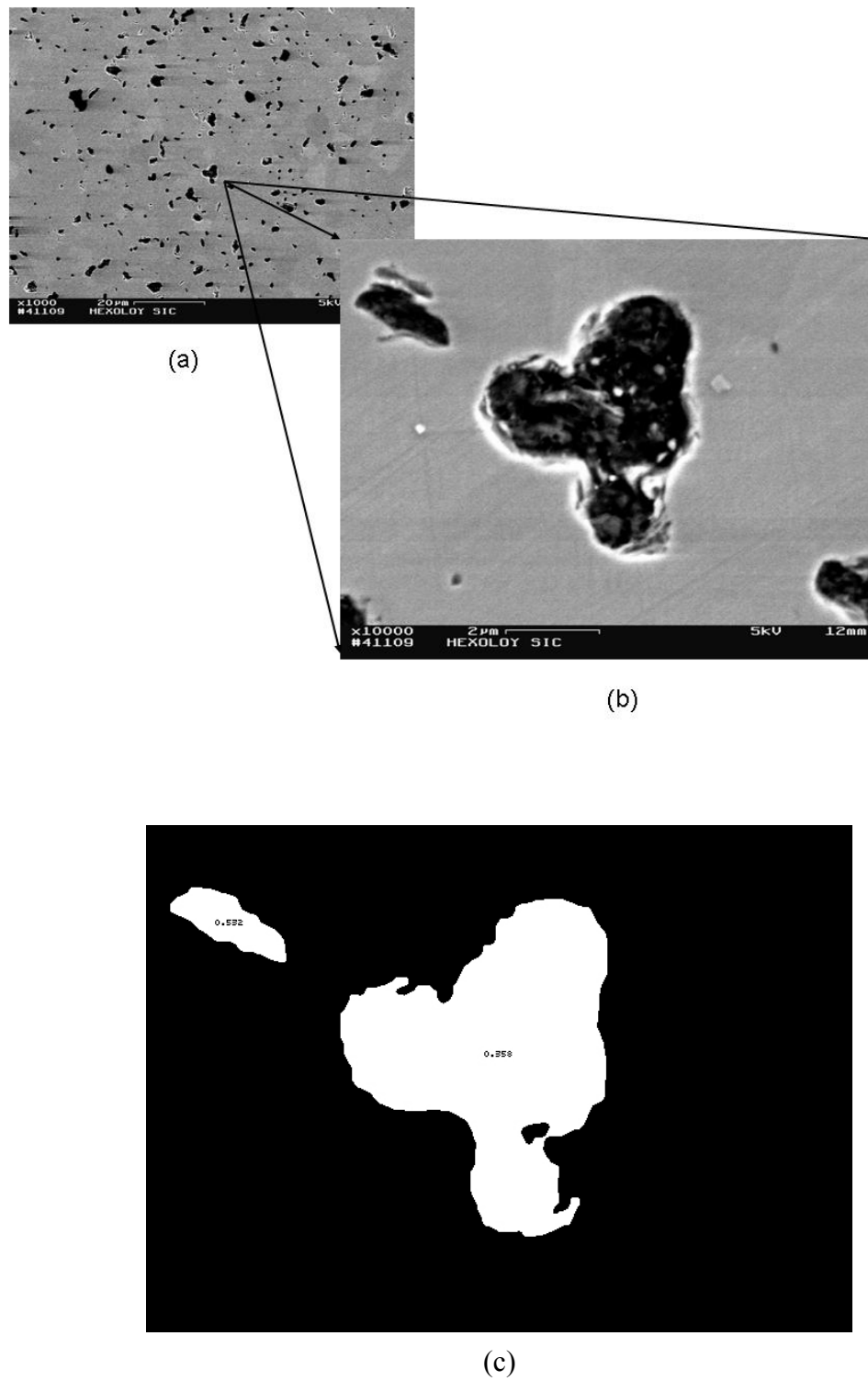


Figure 2.8. (a) SEM image of a sintered SiC (b) Blown up feature in the center of the image (c) Form factor values shown after segmentation

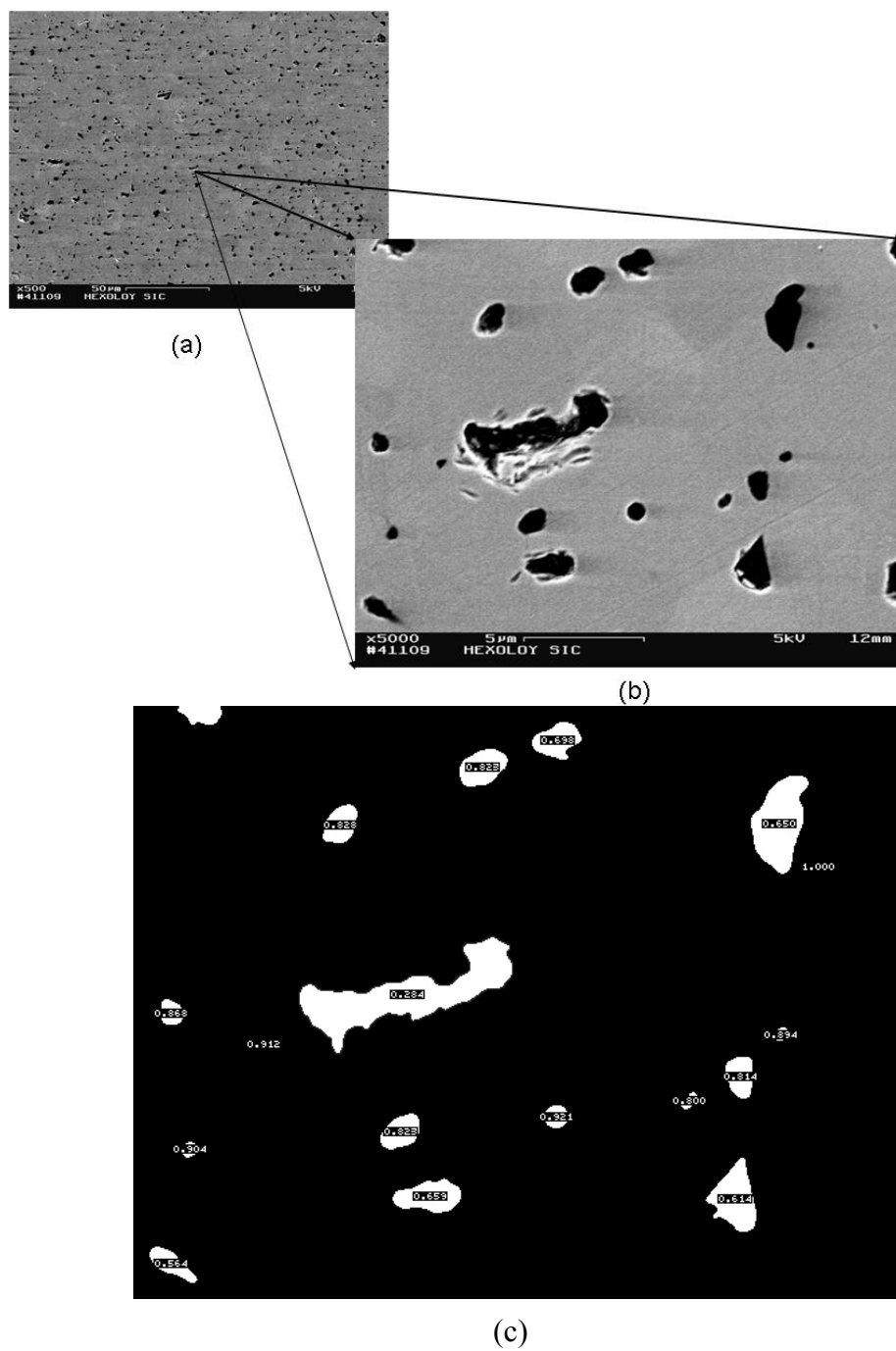


Figure 2.9. (a) Another SEM image of a sintered SiC (b) Blown up area from the center (c) Form factor values shown after segmentation

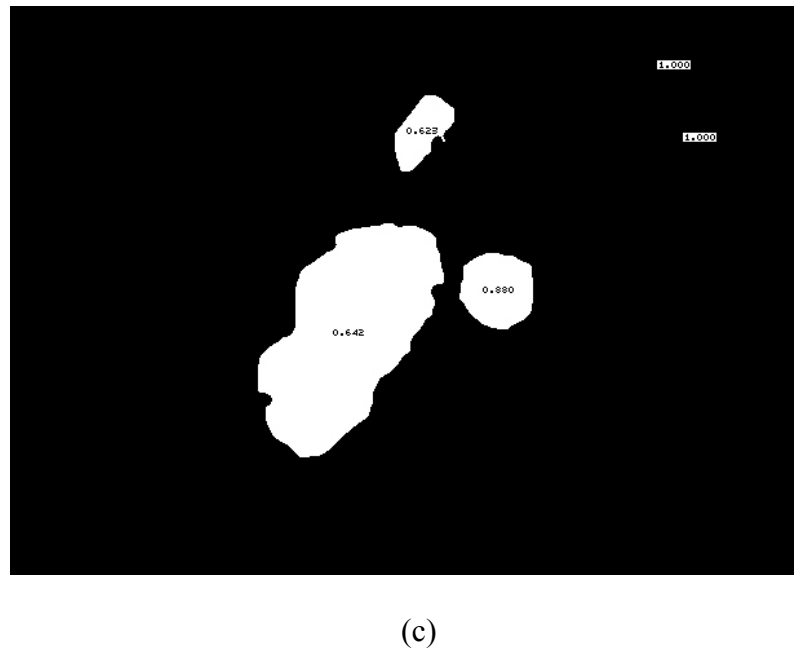
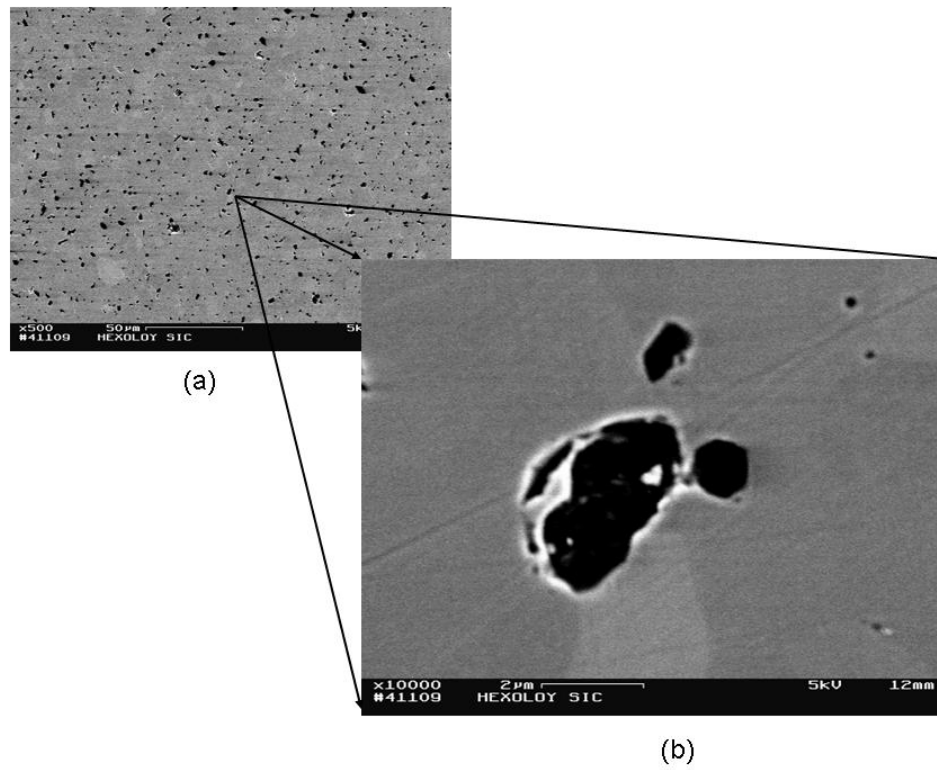


Figure 2.10. (a) Another SEM image of a sintered SiC (b) Blown up image of an oval shaped feature (c) Form factor values shown after segmentation

2.3. Spatial Data Analysis

It was shown in Section 2.2 that inhomogeneities in ceramics are common. The degree of homogeneity or how well features are distributed inside a material is one of the key aspects of materials characterization. It is believed that more uniform microstructures with small amounts inclusions demonstrate better ballistic strength. The issue, in this case, is to “quantify” the uniformity and give a rank to a specific sample while characterizing certain number of samples. For example, the difference between the performance of 3.18 gr/cm^3 and 3.19 gr/cm^3 SiC samples in a production batch cannot be predicted easily and the performance of these two materials could be dependant on the spatial distribution of defects rather than the overall percentage of defects, which is very close to each other in this case. As a result, an answer to how “uniform” the microstructure is will be determined and relate this to the ballistic data and ultrasound results, which could be ultimately used for assessing ceramic armor tiles.

The defects found in SiC will be evaluated in terms of “location” and spatial data analysis will be carried out in order to assess spatial distributions of features in a ceramic armor body. In the following sections, a review of some of the relevant aspects of spatial data analysis will be presented. The methodology that will be explained here is an approach to the particular problem of distinguishing samples with homogenous defect distributions from the ones where grouping, clustering or inhomogeneities in defects locations occur. Alternate approaches to the analysis exist [88-90], and they will be covered in the next few sections.

The distribution of the features on a metallographic section can be represented by the distribution of points on a plane. This type of a distribution is called a spatial point pattern. In general, the study of spatial point patterns is called spatial data analysis, or

cluster analysis. Spatial data analysis has been employed in a variety of areas and subjects, such as the study of the distribution of trees in the field of ecology, or the study of the distribution of cell nuclei in the area of microbiology, due to the inherent clustering nature of certain biological processes. Spatial data analysis was also utilized in the field of materials science as most studies concentrated on the study of second phase particles [88,90-94] and the characteristics of grains [95]. Yang et al. studied finite-size particles distributions in metal matrix composites to investigate the effects of particle size, shape, orientation and area fraction on the quantification of homogeneity [96]. A similar study was performed on TiB₂-Fe composites, concentrating on the analysis of the homogeneity of phase repartition [97].

Apart from the spatial analysis on second phases, pores were studied in several different materials [98-100]. Geometrical structure of the system of artificial pores in autoclaved concrete was studied by means of stereological methods [100]. Zhang et al. [98] used spatial data analysis to study the distribution of microporosity, and observed inhomogeneous distribution of porosity throughout the sample. Tewari et al. monitored clustering of pores in aluminum alloy plate casting, and concluded that the clustering tendency was relatively constant throughout the casting [99].

2.3.1. Randomness, Regularity and Clustering

It is very important to define the terms commonly used in spatial data analysis; therefore, an example drawing is given in Fig. 2.11, where four spatial point patterns are shown. Each point represents an event (e.g., a defect). Qualitative observation does not show any clear structure in Fig. 2.11(a) and this pattern is considered as completely

“random.” The second pattern in Fig. 2.11(b) could be categorized as a “regular” distribution since points are approximately homogenous over the entire area. This kind of pattern is common in systems where there is repulsion between events which promote an even spatial distribution. A good example of from forestry is the regular distribution of trees in a forest, which is a natural result of competition for light. Due to the competition for light, the trees are all kept at a minimum distance from their neighbors, producing a regular distribution. Fig. 2.11(c) shows groups, or clusters of points. However, Schwarz and Exner state that, this type of pattern is not common in material science applications [101]. Usually, clustered events are superimposed on a random background, which is shown Fig. 2.11(d). It must also be noted that that in the “random” point pattern, there seems to be a small amount of clustering, since some degree of grouping could be observed even in a random distribution, due to probability [101].

The spatial point patterns described above comes in at this point and it could be used as a tool to distinguish between samples with small differences in porosity levels from a single production batch. The separation between “good” and “bad” can be drawn by using this concept as the significance of this thesis comes from the standpoint of uniformity.

2.3.2. Planar Point Processes

In order to analyze planar point fields, which are acquired from planar images of material structures, determination of the point coordinates is sufficient in most cases. Statistical methods are employed frequently in order to describe the components of a materials system by means of functions using planar point fields.

First step in this process is the estimation of the *intensity* λ , which is the mean number of points in unit area. Usually, it is adequate to estimate the intensity by determining the number of points in the field of view. Second order characteristics such as pair correlation functions use this information in order to find out the spread of the points in a plane and their relative location to one another. The inter-point distance r is introduced in the second order functions, as the statistical data is represented as a function of this value. The statistical summary displays the type of interaction that exists in between points at any given distance. As mentioned in the previous section, the type of interaction could vary, as attraction (clustering), repulsion, or no interaction between the points might exist [102,103].

2.3.3. K-function

K -function, $K(r)$, is one of most frequently used functions in spatial data analysis. If $K^i(r)$ is the total number of points contained in a circle where (x_i, y_i) is the center of the circle, $K(r)$ can be obtained by averaging $K^i(r)$ over all the point centroid locations (x_i, y_i) in the microstructural plane. The reference point, (x_i, y_i) , is selected randomly in point processes. The other points are spread unsystematically, a state which is called complete spatial randomness of points (CSR) [104-106]. Under this condition, the product of the area of the circle and the intensity gives $\lambda\pi r^2$ points on average. When this is divided by the value of λ , the K -function is obtained for the totally random planar point process:

$$K(r) = \pi r^2 \quad 2.4$$

A value higher than this is a sign of clustering while a lower one shows repulsion. The initial part of the curve with $K(r) = 0$ shows that the inter-point distance does not go below a certain minimum value. In the case of a composite material with particulates, overlapping becomes impossible due to the physical size of the particles [107,108].

2.3.4. Pair Correlation Function

A complement to the K -function is *the pair correlation function* $g(r)$, which could be derived after differentiation of K -function:

$$g(r) = \frac{1}{2\pi r} \frac{dK(r)}{dr} \quad 2.5$$

In the case of a totally random planar point process, the following equation is obtained:

$$g(r) = 1 \quad 2.6$$

for all r by insertion of $K(r) = \pi r^2$ into $g(r)$. The concept mentioned in the previous section comes into consideration as values below this point to repulsion while values above one indicate clustering. At this point, “hard-core point field” concept must be taken into account. It is a random point field, in which the components, or points, of this field are not allowed to lie closer together than a certain minimum distance [104]. This hard-core effect once again leads to zero values of initial part of $g(r)$.

In order to simulate a planar Poisson point process or other planar point processes and to obtain illustrations of $K(r)$ and $g(r)$ functions, specific software, such as STG 4.1 (Stochastic Geometry for Windows) could be employed.

2.3.5. Nearest Neighbor Distance Distributions

Nearest neighbor distance distributions are important quantitative descriptors of short range using first nearest neighbors as well as intermediate and long-range spatial arrangements of objects in space using higher order nearest neighbors. As a result, this technique will serve as a key tool to model nearest neighbor distributions and the corresponding mean nearest neighbor distances between objects in spatial patterns [109,110].

One method to assess spatial distribution of features is to define nearest neighbor distance distribution and compare the observed and mean and variance for a random Poisson distribution.

If $P(R)$ is defined as density function, then the nearest neighbor distribution function of pores in a plane is described so that $P(R) \cdot dR$ is equal to the probability that there is no other pore centroid in R distance and there is at least one pore centroid in $(R+dR)$ distance. Then the average nearest neighbor distance is calculated by;

$$\langle R \rangle = \int_0^{\infty} R P(R) dR \quad 2.7$$

If the points are randomly distributed in a plane, then $\langle R \rangle$ is equal to $\{0.5/\sqrt{N_A}\}$, where N_A is the number of points per unit area. Second, third, n-th nearest-neighbor distributions can also be calculated by using a similar approach.

To be more quantitative, in terms of centroid distributions, two parameters, Q and V, were developed in order to describe the nature of distribution, where;

$$Q = \frac{\mu_o}{\mu_e} = \frac{\text{observed mean nearest - neighbor distances}}{\text{expected mean nearest - neighbor distances}} \quad 2.8$$

$$V = \frac{\text{var}_o}{\text{var}_e} = \frac{\text{observed variance of nearest-neighbor distances}}{\text{expected variance of nearest-neighbor distances}} \quad 2.9$$

The expected mean and variance are for a random distribution of events. Different types of distributions can be determined by these two parameters and the conditions for these distributions are as follows: (a) random distributions, $Q \approx 1$ and $V \approx 1$; (b) regular distributions, $Q > 1$ and $V < 1$; (c) clustered distribution, $Q < 1$ and $V < 1$; and (d) random distribution with clusters, $Q < 1$ and $V > 1$ [96,111,112]. Expected values are calculated by the Image Processing Toolkit 5.0. Q-V map is given as example in Fig. 2.12. The rule for calculating the expected mean and the variance of the nearest neighbor distances are given in the following formulas;

$$\text{Expected mean } (\mu_e) = 0.5 \sqrt{\frac{A}{n}} + \left(0.0514 + \frac{0.041}{\sqrt{n}} \right) \cdot \frac{L}{n} \quad 2.10$$

$$\text{Expected variance } (\text{var}_e) = 0.0703 \cdot \left(\frac{A}{n} \right) + 0.037 \cdot \left(\frac{\sqrt{A}}{\sqrt[3]{n^2}} \right) \cdot L \quad 2.11$$

where, L is the length of the boundary of the area, A , that contains n , number of events [111].

2.3.6. Tessellation Analysis

Another way to define near neighbors, detect clustering and the anisotropy of spacing is provided by *Tessellation Analysis*. This method involves a geometric construction of two dimensional cells or polygons around each particle on the plane-of-polish.

Tessellations have been used in the literature for assessing microstructures of various materials, especially composites. Metal matrix composites were studied on micrographs of 2-D images and 3-D microstructures by construction of 2-D images obtained using serial sectioning. Spatial distribution of features, orientation distributions and size distributions were examined and minor differences were observed between 2-D and 3-D [113,114].

Tessellations can be grouped into two, first of which, is called *Voronoi tessellation*. It is a basic separation method of d-dimensional space into d-dimensional polyhedral cells. It is also called *Dirichlet tessellation* [88,89,115]. If N represents a set of points, with positions r_1, r_2, \dots, r_N in volume V in d spatial dimensions, i th point at r_i is associated with a *Voronoi cell* or *tile*. This cell or tile consists of the area closer to the point at r_i than to any other point in the set. These cells in 2-D are convex polygons, while they are convex polyhedrons in 3-D [92]. All points within each polygon are closer to the center of the particle than to any particle outside the polygon. To construct the polygons, lines are drawn from a particle to neighboring particles. Subsequently,

perpendicular lines bisecting these lines are drawn. These lines will intersect and form polygons. The lines that intersect to form the polygons are from only the nearest neighbors. Thus, a unique area can be associated with each feature [88,115,116].

The second type of tessellation is called *Johnson-Mehl tessellation*. This one separates from the first by subtle differences. The main distinction between Voronoi and Johnson-Mehl tessellations is the origin of the features, according to which polygons are constructed. In Voronoi tessellations, regardless of the features size, the centroids of features are accepted as origins. However, in Johnson-Mehl tessellations, polygons are constructed according to the surface of features. Consequently, in the former technique, tile boundaries can partially or completely lie within the boundaries of the seed particles. The latter makes this impossible since starting points are on the surface of features. Due to this attribute, Johnson-Mehl tessellation is sensitive to size of the features [91].

The cell area distributions that are obtained from either type of tessellation tell a lot about the spatial distribution of any group of features. Further quantification has been implemented in different studies, one of which was performed by Murphy *et al.* Two parameters, P_1 and P_2 , were identified, which help to quantify the microstructure in terms of clustering. P_1 is based on the variance of the cell area distribution. It is a parameter that the extent of spread in a distribution can be found since the variance from a real microstructure is compared to that of a random microstructure. P_2 is a measure of skewness, which shows the asymmetry in a distribution. If there is a tail in the distribution, that would increase the skewness of that distribution. The extraction of parameters P_1 and P_2 is given in following equations: [116]

$$P_1 = \frac{V}{V_{random}} \quad 2.12$$

where;

$$\text{variance of the measured areas } (\mu\text{m}^4), \quad V = \frac{1}{n} \sum_{i=1}^n (A_i - \bar{A})^2 \quad 2.13$$

$$\text{variance of random distribution } (\mu\text{m}^4), \quad V_{random} \quad 2.14$$

$$\text{average measured cell area } (\mu\text{m}^2), \quad \bar{A} \quad 2.15$$

$$\text{average area of random distribution } (\mu\text{m}^2), \quad \bar{A}_{random} \quad 2.16$$

$$P_2 = \frac{S}{S_{random}} \quad 2.17$$

where;

$$\text{skewness of measured areas, } S = \frac{\frac{1}{n} \sum_{i=1}^n (A_i - \bar{A})^3}{V^{3/2}} \quad 2.18$$

skewness of random distribution, S_{random}

2.19

This technique is capable of providing a way to quantify local microstructural features and fluctuations [91]; therefore, it will be used as one of the methods to assess microstructures.

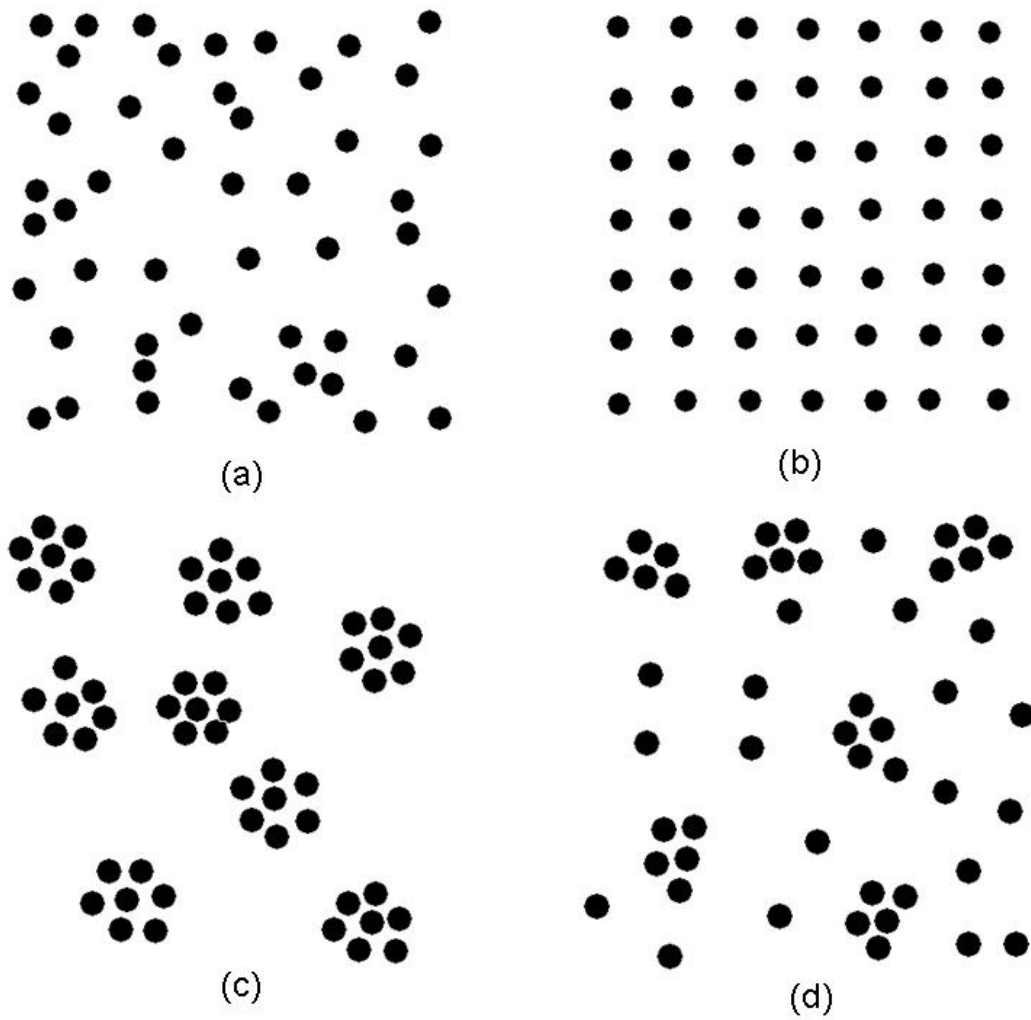


Figure 2.11. Four different types of spatial point pattern

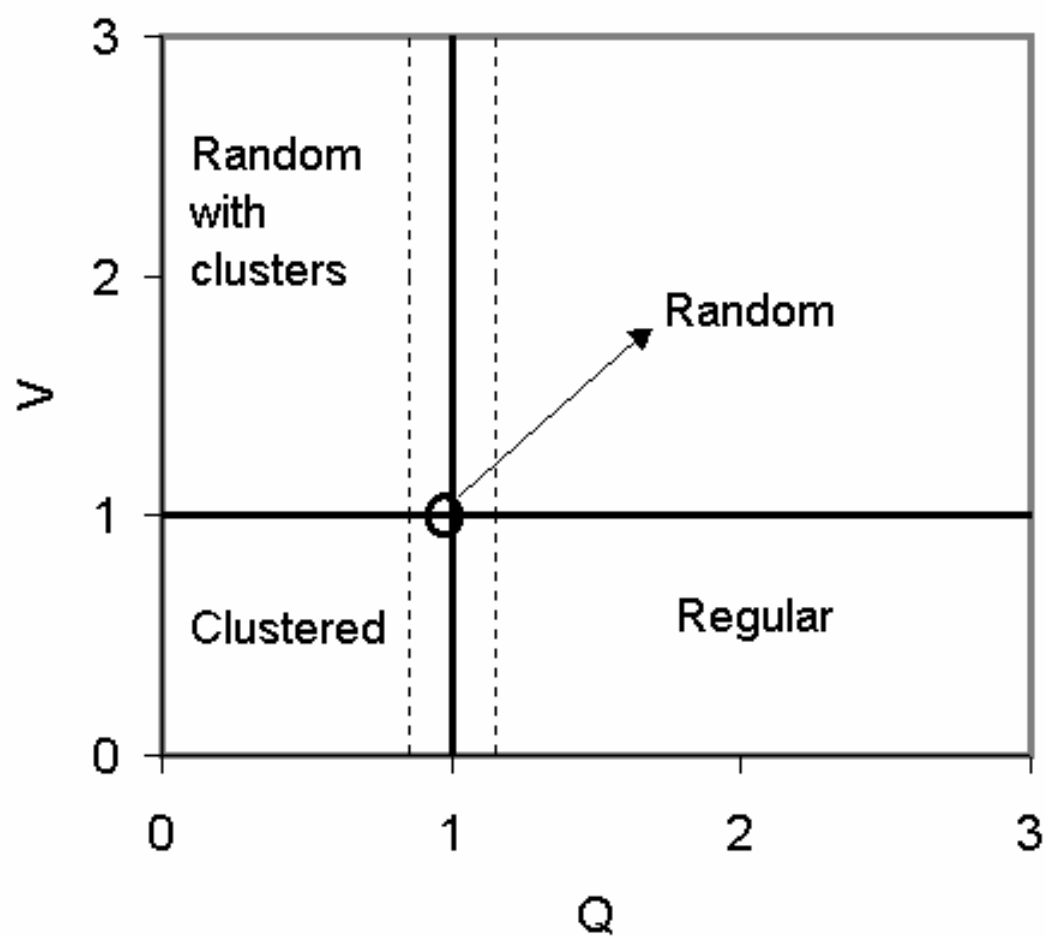


Figure 2.12. Map of Q and V indices

2.4. Hardness of Ceramics and Its Relation with Armor Performance

2.4.1. Hardness of Ceramics

Hardness can simply be described as the resistance of a material to plastic deformation by an indenter [117]. Several different models were used in order to interpret hardness in terms of tensile strength and ease of plastic flow, surface energy and chemical bond strength [118].

The hardness "number" has meaning only with reference to a specific test and the test conditions. It is a measure of a reaction of a material to the type of disturbing force imposed (different hardness test results for different techniques) and relates to the ease of dislocation movement e.g. to shear modulus G and yield stress, the type of atomic bonding, the presence of impurities in solid solution or at grain boundaries and/or as precipitates, or inclusions, the microstructure (grain size and texture, porosity), phase composition and residual stresses.

Hardness increases in an order similar to the increase in stiffness as metals rank lowest and carbides/borides rank highest in a spectrum of different materials. Oxides rank somewhere in between the two.

Attempts to calculate the hardness of defect-free monocrystals by modeling dislocation movement under an indenter give underestimated values. Theoretical hardness calculations give: $H \approx 0.001 G$, whereas hardness measurements give: $H \approx 0.1 G$, where G is Shear Modulus. The strong anisotropy of hardness values for single crystals reflects the directional characteristics of dislocation movement [119].

Usually the measured value of hardness is load-dependent. At low loads, the measured values of microhardness tend to increase. The microhardness also depends on the relationship of surface properties vs. bulk properties and on environmental

interactions. At high loads, such as several kg, the measured hardness of ceramics decrease due to the fracture of the material under the indenter [117,118].

One of the other factors that affect the hardness of a ceramic are grain-size, where Hall-Petch equation is valid as the hardness of a ceramic is inversely proportional to the square root of grain size:

$$H \sim \sqrt{\frac{1}{D}} \quad 2.20$$

where D is the grain size [120,121].

The temperature dependence of hardness reflects the mechanism of dislocation movement: athermal at low temperatures; glide, climb and diffusion at high temperatures, such that

$$H = H_0 \exp(-cT) \quad 2.21$$

where H_0 = hardness at $T=0$ K, c = thermal softening factor, a characteristic of the material. For instance, in ceramics ' c ' is sensitive to grain boundary glassy phases at intermediate temperatures and to structural obstacles to dislocation movement at high temperatures [122].

Proper selection of indenter geometry is crucial in determining hardness of ceramics. Usually, the preferred geometry is the pyramid type. Spherical or blunt indenters are not recommended in hardness measurements of ceramics due to the brittle

nature of this type of materials. With a spherical indenter, the surface stresses during loading are tensile, which might lead to extensive cracking. However, pyramid indenters such as Vickers or Knoop introduce tensile stresses only on unloading stage, which can help keep the sample away from ring cracking and surface spalling. Even, at very low loads, these damages are hard to avoid with a spherical indenter [118]

Although spherical indenters are not very common for hardness determination of ceramics, they are frequently employed in armor ceramics for the particular reason of the similarity between the damage in a ballistic event and the damage in a spherical indentation [123].

An indent made by a sharp indenter on a ceramic material is surrounded by a plastic zone, which is a result of exceeding elastic compressive strength of the ceramic material. Two crack systems of radial cracks or lateral cracks can be observed outside the plastic zone. The radial cracks observed on the surface originate from the corners of the indent. Significant amount of microcracking could be introduced by the indenter in the plastic zone [124].

In the case of a ballistic event, hardness is an important physical property both for the penetrator and the target material. The penetrating ability of a projectile is improved by increasing strength and hardness values. In order to defeat a projectile, the armor must have a higher hardness value than that of the penetrator. One of the reasons that ceramics are commonly used as armor is the incapability of steel armor to defeat high hardness projectiles, such as tungsten rods [125].

2.4.2. Dependence of hardness on porosity

Rice has set up a categorization of the different porosity dependences [126]. The first category involves properties such as lattice parameter, coefficient of thermal expansion, which do not have any dependence on porosity. The second category consists of the properties which depend only on the volume fraction of porosity, such as density and heat capacity. The third category is composed of properties which depend on both volume fraction and porosity characters. Most of the mechanical properties categorized under this group. Out of this group, the effect of porosity on Young's modulus and flexure strength were investigated extensively studies while properties such as fracture energy and toughness were not studied. In addition, most of the models were only concerned with the porosity level without considering other porosity characteristics. Therefore, Rice put forward a model based on the Minimum Solid Area concept (MSA) in order to explain the porosity dependences of the third category properties. The porosity dependence of hardness has also been in agreement with the Minimum Solid Area (MSA) model [126-128]. MSA model was utilized in numerous different studies for explaining porosity dependence on properties including ultrasonic velocity [126,129], fracture strength [130], and elastic modulus [126,131,132], dielectric constant [133] of various ceramic materials.

This model makes the assumption that different properties have similar type of dependence with porosity. MSA variation with porosity has been modeled for different pore characteristics and this is shown in Fig. 2.13. A semi-logarithmic plot of the log MSA against the volume fraction of porosity (P) demonstrates a linear decrease of MSA with P at low levels of porosity. The slope ($-b$) is a characteristic parameter of the pore stacking. Subsequently, an increase of porosity causes a higher decrease of the MSA. In

the last part, the MSA drops considerably when the volume fraction of porosity reaches the critical value of porosity P_c . This value could be accepted as the percolation limit of the solid phase. It should be mentioned that for the porosity range 0 to $1/3 - 1/2 P_c$, the variation of the MSA or property with porosity can be defined by the following equation:

$$A = A_0 \exp(-bP) \quad 2.22$$

For hardness, the MSA model can be represented by H_V

$$H_V = H_0 \exp(-bP) \quad 2.23$$

where H_V is the measured Vickers hardness, H_0 is the Vickers hardness value corresponding to a specimen with zero porosity, b is a material dependence constant and P is the volume fraction porosity of the specimen [134,135].

2.4.3. The Relationship between Hardness and Ballistic Performance

Several studies [136-143] were performed previously in order to correlate quasi-static properties to ballistic performance of armor plates. A thorough analysis of parameters that affect ballistic performance was carried out by Viechnicki et al. A group of four different materials consisting of alumina, silicon carbide, titanium boride and boron carbide, were used in this study. One of the conclusions from this study was that monolithic ceramics with minimal amounts of second phases and porosity have better ballistic performance than multiphase ceramics and composites. Regarding the quasi-

static parameters, a group of static properties, not a single one, affect ballistic performance. The group of properties consists of hardness, sonic velocities, elastic modulus, Poisson's ratio, density and porosity. Interestingly, a negative correlation was shown between fracture toughness and ballistic performance. It was also claimed that hardness was the only static property that alone helps predict the ballistic performance [136].

Medvedovski explained the factors, consisting of density and porosity, hardness, fracture toughness, Young's modulus, sonic velocity and mechanical strength, which play an important role in the ballistic performance of ceramics. He claimed that any single property is not enough to predict ballistic performance, due to the complicated nature of fracture after impact and very rapid loading. The microstructural features have a strong influence on physical properties, which drastically affects crack propagation mechanisms and ballistic performance. Therefore, ballistic performance of a material must be assessed considering all relevant properties, as well as ceramic microstructural features. As one the results of his conclusions, he stated that the hardness of a ceramic armor should be higher than the projectile hardness for desired performance [137].

Experience shows that materials with high fracture toughness values do not exhibit significant ballistic performance [138]. Ideally, some balance between levels of hardness and fracture toughness must be maintained [137,139,140]

Rozenberg and Yeshurun revealed that the performance of ceramic type armor materials is a function of material strength/hardness (typical static compression strengths of 3-7 GPa and hardness values of 2000 - 3000 kg/mm² for various ceramics). They agreed on the notion that when "interface defeat" *or* "dwell" type mechanisms are

responsible for penetrator destruction, the strength and/or hardness of the ceramic material is especially important [141].

Another study was carried out by Flinders et al., who prepared SiC by hot-pressing using Al–B–C (ABC) or Al–Y₂O₃ (YAG) as additives. After ballistic testing, it was revealed that Depth-of-penetration was controlled by hardness of the SiC-based materials, while V₅₀ values for 14.5 mm WC–Co cored projectiles were in the range of 720–750 m/s for all materials tested. The data is shown in Fig. 2.14, where increasing hardness results in lower depth of penetration and therefore a higher mass efficiency [138].

Sternberg studied the parameters that could be important in determining the resistance of ceramics to projectile penetration. This was performed by analyzing the target strength term that is included in the analytical representations of high velocity penetration

$$p = \frac{1}{2} \rho_t U^2 + R_t = \frac{1}{2} \rho_p (V - U)^2 + Y_p \quad 2.24$$

where U is the rate at which the interface is penetrating into the target and V is the rod velocity relative to the target. The strength terms for the target and the penetrator are represented by R_t and Y_p , respectively. Sternberg stated that the dependence of the strength term on the elastic moduli and yield strength of the target for ductile targets could be directly related to the pressure required for quasi-static expansion of a cavity in the material. Theoretical results should be pertinent to high velocity impact as, where the pressure required for cavity expansion could be represented by the target strength term when dynamic values of the yield stress were taken into account. Consequently, it was

claimed that hardness measurements could be used instead of the expansion theory as a basis for determining the magnitude of strength terms in ceramics. Hardness measurements were carried out to determine roughly the highest possible value for the strength term for each ceramic with ballistic data. He stated that the hardness is more or less equal to the target strength term over a broad range, on the condition that the dynamic yield stress is substituted for the static yield stress [142].

Lundberg et al. [143] used indentation as the same route to determine yield strength in a study where he investigated the critical impact velocity for the transition between interface defeat and normal penetration, both theoretically and experimentally. The transition impact velocity was assessed for different combinations of metallic projectile and ceramic target. Then, comparison between this transition impact velocity and velocities determined experimentally was performed for various combination of projectile materials such as, tungsten (WHA) and molybdenum, and five target materials, consisting of two types of silicon carbide, boron carbide, titanium diboride and Syndie (a diamond composite). The indentation method used for yield strength calculation of ceramic materials appeared to provide reasonable values. As a result, the yield strength of 10.4 GPa obtained for silicon carbide was comparable to the value of 12.5 GPa obtained from plate impact tests. When the strain rates do not reach extreme values in ceramic targets under conditions of interface defeat, static yield strengths could be utilized in the estimation of transition impact velocities [143].

To be brief, there is an agreement in armor community that hardness is one of the key parameters on prediction of ballistic performance. Therefore, it will be used as a gauge in this study in order to verify microstructural examinations. Although effect of

porosity on hardness was studied extensively, minor levels of porosity will be the main concern, therefore, providing the opportunity to study a different issue.

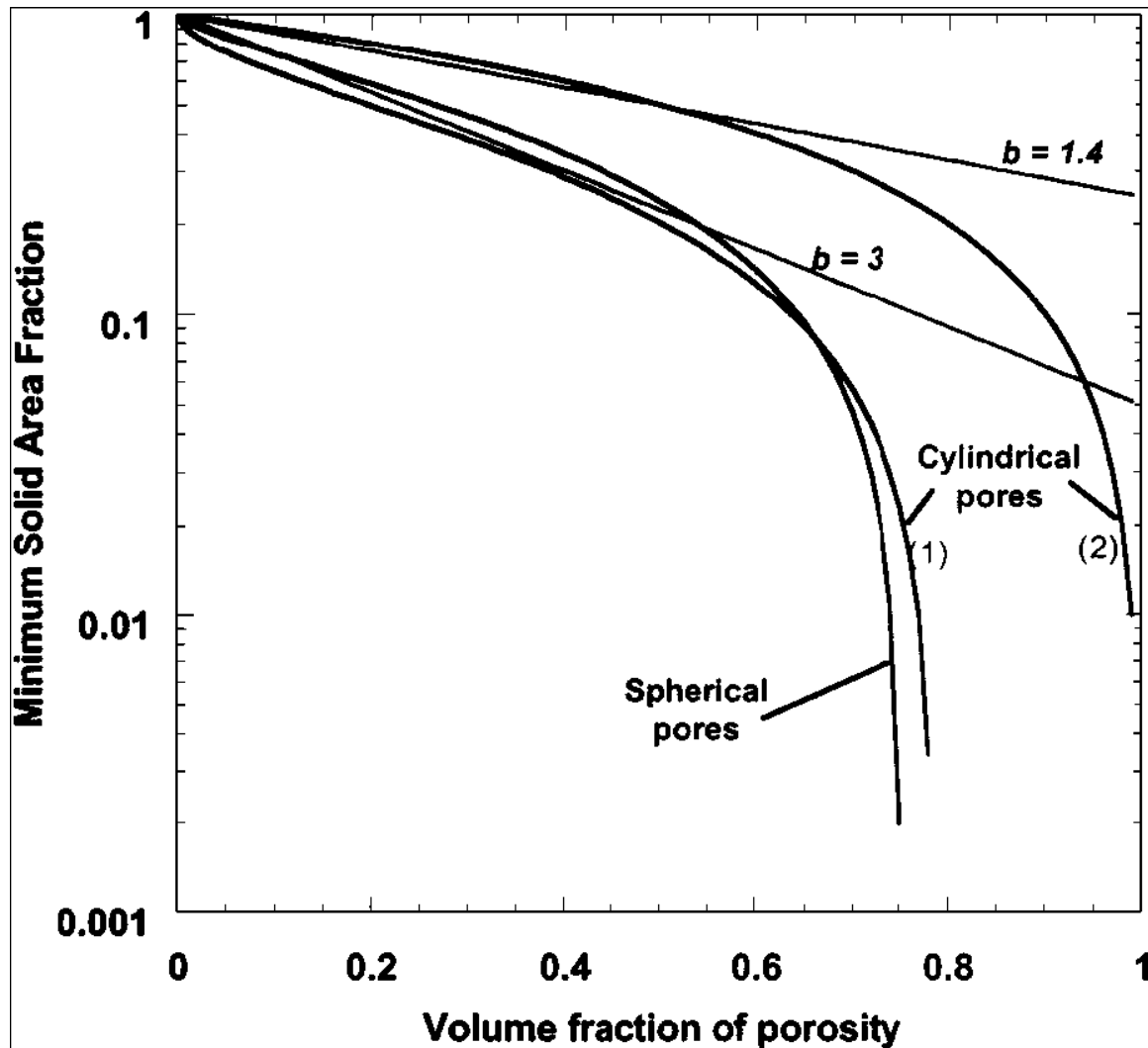


Figure 2.13. Variation of the Minimum Solid Area with porosity for idealized pores cubic stacking (1) cylindrical pore axis perpendicular to the stress axis (2) cylindrical pore axis parallel to the stress axis [131]

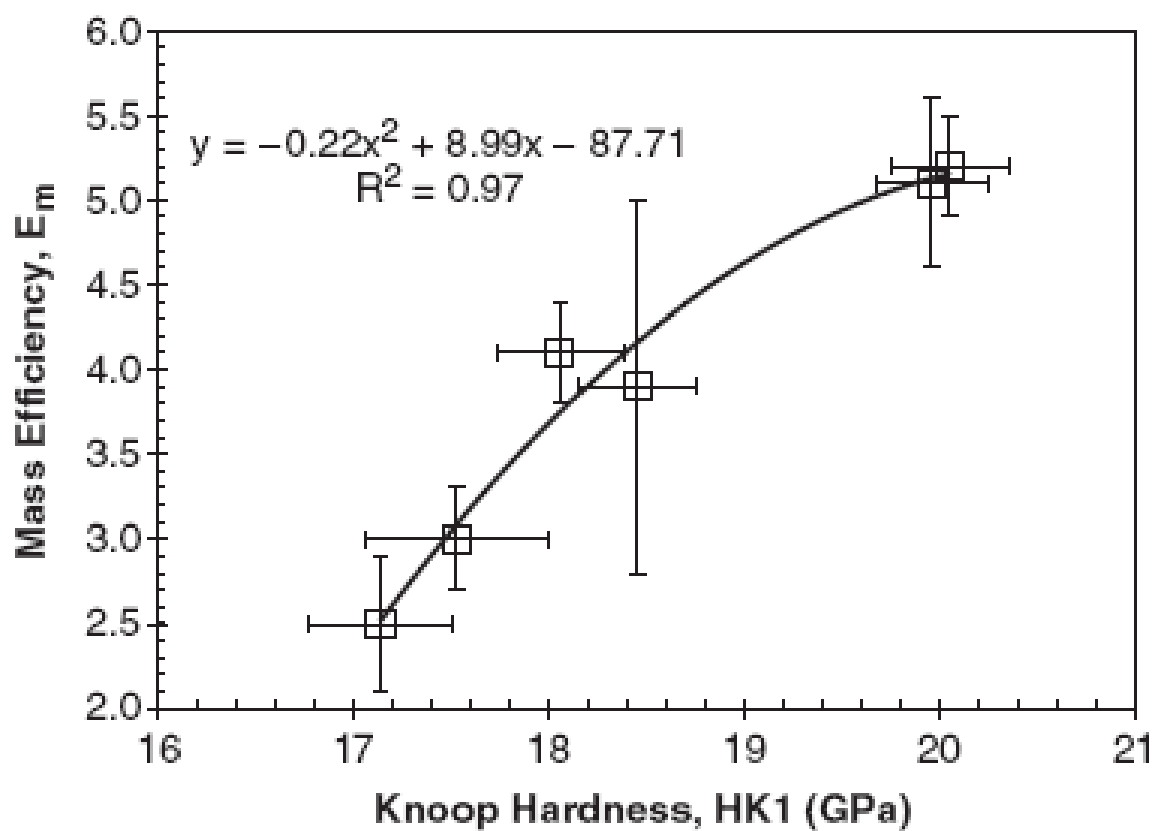


Figure 2.14. Ballistic mass efficiency as a function of Knoop hardness for the materials tested using depth of penetration [138]

2.5. Statistical Examination of Property Data in Ceramics

Flaws, which are distributed either randomly or in a certain pattern in the material, are usually the origins that lead to fracture [28]. Therefore, mechanical properties of materials are affected by the presence of flaws. This fact makes it common to determine any property of brittle materials by using statistics and probability functions [144,145]. The Normal, Lognormal and Weibull distributions are extensively used for statistical examination of experimental data, especially for ceramics [146,147].

2.5.1. Normal Distribution

Various physical measurements demonstrate the symmetrical, bell-shaped curve, which is called the normal distribution, or Gaussian distribution. The normal probability density is given below

$$f(x) = \frac{1}{\sigma\sqrt{2\pi}} \exp\left[-\frac{1}{2}\left(\frac{x-\mu}{\sigma}\right)^2\right] \quad 2.25$$

where μ is the population mean, σ is the standard deviation and $f(x)$ is the value of the curve at a specified x value [148]. This type of distribution is occasionally used in reliability field of materials regarding yield strength, tensile strength and reduction of area from the tension test [149].

2.5.2. Log-normal Distribution

This is a skewed distribution and it is especially useful to model the cases where the tail of the plot has significant amount of data points. The lognormal probability density is given by the following equation

$$f(x) = \frac{1}{x\sigma\sqrt{2\pi}} \exp\left(-\frac{[\ln(x)-\mu]^2}{2\sigma^2}\right), \quad x > 0 \quad 2.26$$

where μ is the *log* mean and σ is *log* standard deviation and $f(x)$ is the value of the curve at a specified x value [148]. This type of distribution is employed when “life” of a component is concerned, such as in the fatigue life of ceramics [150].

2.5.3. Weibull distribution

Apart from these two types of distributions, Weibull distribution has been preferred for describing properties of materials, where property distributions can be highly skewed or broadly distributed [146,147].

Weibull distribution is based on the weakest link approach, in which the property of material is dictated by the products of the survival likelihood for the individual volume elements. “Strength” is the most common mechanical property that this type of distribution has been employed [151-154]. This method usually tries to determine the probability of failure at a given stress, rather than establishing a stress at which a ceramic component fails catastrophically [155].

According to Weibull statistics, the cumulative failure probability $F(\sigma)$ of a material subjected to a stress σ is given by

$$F(\sigma) = 1 - \exp\left[-\left(\frac{\sigma - \sigma_{th}}{\sigma_0}\right)^m\right] \quad 2.27$$

where σ_0 is a normalized factor known as the characteristic strength, σ_{th} is the threshold stress below which no failure occurs, and m is the Weibull modulus. Here, the Weibull modulus is a measure of strength diversity and is also called *the shape factor*. In most cases, for the sake of simplicity, σ_{th} is usually assumed to be zero. Then, the Weibull distribution can be reduced to two-parameter form, such as

$$F(\sigma) = 1 - \exp \left[- \left(\frac{\sigma}{\sigma_0} \right)^m \right] \quad 2.28$$

Although Weibull distributions are frequently used for “strength”, any property can be substituted as x instead of σ . In that case, x_0 would be the characteristic value (or scale factor) below which 63.2 % of data lie, and m is the Weibull modulus (or shape factor), which reflects the data scatter [156-158].

There are multiple techniques to determine the Weibull parameters including the Weibull plot, maximum likelihood estimation (MLE), linear estimator, and direct non-linear curve fitting.

Weibull plots are frequently based on MOR data obtained on a representative group of samples prepared and tested in a way similar to that which the products will be subjected to during service [151-154]. In order to proceed in Weibull plot method, equation presented above can be rearranged by taking the natural logarithms twice, and it gets the following form [146,147]:

$$\ln \left\{ \ln \left[\frac{1}{1 - F(x)} \right] \right\} = m [\ln(x) - \ln(x_0)] \quad 2.29$$

The technique of determining $F(x)$, which is the cumulative density function of probability, in the above equation can be performed according the nature of the distribution [159,160]. The mean value of $F(x)$ can be obtained by sorting the data in ascending order and letting

$$F(x) = \frac{i}{n+1} \quad 2.30$$

where n is the total number of data points, and i is the i th order in ascending data set. The mean value is generally used since it signifies the expected value of the probability density function within the distribution. However, in highly skewed distributions the median value, where

$$F(x) = \frac{(i - 0.3)}{(n + 0.4)} \quad 2.31$$

might be more suitable. Other estimators such as

$$F(x) = \frac{(i - 0.5)}{n} \quad 2.32$$

$$F(x) = \frac{(i - 0.375)}{(n + 0.25)} \quad 2.33$$

have also been utilized [160].

The second approach to perform Weibull analysis is the maximum likelihood (ML) method. The likelihood function, L , is a mathematical expression, which represents the probability of acquiring the experimental data. The log-likelihood function can be obtained by taking the natural logarithm of this function:

$$\ln(L) = n \ln(m) - nm \ln(x_0) + \sum_{i=1}^n (m-1) \ln(x_i) - \sum_{i=1}^n \left(\frac{x_i}{x_0} \right)^m \quad 2.34$$

The values of m and x_0 , which maximize the Weibull likelihood function, can be found in three steps. Initially, the log-likelihood function is differentiated with respect to m and x_0 . Then, the resulting expressions were equated to zero, and finally, they were solved for m and x_0 . On reorganization, the two following equations are obtained:

$$x_0 = \left[\frac{\sum_{i=1}^n (x_i)^m}{n} \right]^{\frac{1}{m}} \quad 2.35$$

$$\frac{n}{m} + \sum_{i=1}^n \ln(x_i) - \sum_{i=1}^n \left[\ln(x_i) \left(\frac{x_i}{x_0} \right)^m \right] = 0 \quad 2.36$$

After the parameters are obtained by the Weibull plot method, they can be used as starting points for an iterative process, in which enables Weibull values to converge. Based on this method, an estimate for the confidence limits employs the χ^2 distribution. In the log-likelihood equation, the Weibull parameters are put through the following conditions:

$$-2 \ln \left[L(x_0, \tilde{m}) \right] + 2 \ln \left[L(\tilde{x}_0, \tilde{m}) \right] = \chi_{1,\alpha}^2 \quad 2.37$$

$$-2 \ln \left[L \left(\tilde{x}_0, m \right) \right] + 2 \ln \left[L \left(\tilde{x}_0, \tilde{m} \right) \right] = \chi_{1,\alpha}^2 \quad 2.38$$

where \tilde{m} and \tilde{x}_0 are Weibull parameters, acquired from any method.

An estimated α confidence interval is obtained by finding the set of x_0 , represent lower and higher bounds, and the set of m values by applying the previous two equations above [146].

The method for estimating the expected performance of a ceramic by applying the Weibull distribution to property tests is valid, as long as a sufficient number of samples are taken. The higher the Weibull modulus of a ceramic, the greater the number of test specimens is required to achieve true sampling of the defect population [44].

2.5.4. Weibull Statistics and Its Correlation with Defect Distributions

While the Weibull modulus is related to the defect population that causes failure, real ceramic materials have a number of concurrent defect populations. Different testing configurations distribute stresses within the sample differently and may manipulate failure from a specific type of defect [161,162]. During testing, samples must fail from the same types of defects that will cause failure in the final application of the material in order for the testing to be relevant. The most commonly used test is the bend bar test, loaded in either a three or four point configuration. These bars are used because of the relative ease of creating samples. Bend bars are vulnerable to failure from surface scratches and machining damage because of their size and loading configuration. A higher proportion of failures in bend bar testing occur from surface scratches than tension bars [163]. Tests with higher effective volume are more likely to fail from internal

defects, such as pores and inclusions. The performance of small volume test specimens can be used to estimate the performance of larger specimens only if failure results from the same defect population. If a different population of defects controls failure as the effective volume of the test increases, then predicting performance for a ceramic product with a large volume by using tests of small effective volume will not be accurate. Tests with small effective volume tests (bend bars) may predict high strength and performance, but at a higher effective volume, rarer and more severe defects may be encountered which lower the strength of the material [162].

The dependence of the number of destructive flaws and the applied load has to be known for design purposes. The relative frequency of flaws sizes (flaw size a) can be described by a function $g(a,r)$ [defects/m⁴], which may also depend on the position vector r [164].

Jayatilaka and Trustrum [44] demonstrated in their study that, for a brittle and homogeneous material, the distribution of the strength data is caused by the distribution of sizes and orientations of the flaws, and that a Weibull distribution of strength will be observed for flaw populations with a monotonically declining density of flaw sizes.

The decisive factor for failure ties the size of the flaw with a critical load. The Griffith/Irwin criterion forecasts that crack-like flaws get critical, if their stress intensity factor $K=\sigma Y\sqrt{\pi a}$ goes above the value of fracture toughness K_{Ic} [145,165]

$$K \geq K_{Ic} \quad 2.39$$

where Y is a geometric factor, which is of the order of one for flaws which are small compared to the specimen size. The critical crack size is then

$$a_c = \frac{1}{\pi} \cdot \left(\frac{K_{Ic}}{Y \cdot \sigma} \right)^2 \quad 2.40$$

The relative flaw size density function versus the flaw size is given in Fig. 2.15. All flaws larger in size than the critical value of $a_c(\sigma)$ leads to failure. The density of flaws could be calculated by the following formula:

$$n_c(\sigma, r) = \int_{a_c(r)}^{\infty} g(a, r) \cdot da \quad 2.41$$

The lower integration limit may shift to the left depending on the increasing stress level. This is an indication of giving a higher density of destructive flaws at higher stresses. The average number of destructive flaws can be obtained after integration over the volume

$$N_{c, S(\sigma)} = \int n_c(\sigma, r) \cdot dV \quad 2.42$$

Generally, the relative occurrence of flaw sizes $g(a, r)$ is not known. Assumptions were made such that the tensile stress field (stress amplitude r) is uniform and the flaws can be described by a single parameter which characterizes their size, (e.g. the crack

radius) and that the crack-like flaws are perpendicularly oriented to the stress direction. The flaw density is strictly related to the production process in most cases [164].

Evans gave examples of typical flaws, examples of which are large grains, pores resulting from organic inclusions, pressing defects or agglomerates [28]. Surface flaws might also be introduced by the machining of the component (surface flaws) and are then severely related to the direction of the movement of the machining tool. Poor handling in service may initiate contact damage such as Hertzian cracks [166]. In addition to previous assumptions, another one is that a material only contains homogeneously distributed volume flaws with a relative flaw size density similar to continuous line in Fig. 2.15 [164].

The strength values obey a Weibull distribution, if the number of the pores decreases with increasing pore length according to a power law [167]. Thus, the statistical distribution of the flaw dimensions is closely connected to the fracture stresses obtained by mechanical tests [168,169].

2.5.3. Weibull Distribution of Hardness data

Although advanced processing techniques are employed and high theoretical densities are achieved in armor ceramics, defects such as pores and cracks are inevitable as in any other ceramic. Since these areas have the highest probability of failure according to the weakest link theory, Weibull distribution can also be applied to this group of materials [44,159,160].

However, Weibull distribution on hardness data was often utilized in coating research rather than the armor ceramics [146,147,158,170-173]. Lin and Berndt studied a

thermal barrier coating system consisting of a NiCoCrAlY bond coat and cerium-stabilized zirconia sprayed onto a metallic substrate and Weibull statistics were utilized to assess the reliability of the coating system [146]. Lima et al. examined the mechanical behavior of nanostructured partially stabilized zirconia (PSZ) using Knoop indentation. Bimodal distribution in Weibull plots justified the presence of two separate phases, molten and non-molten [170]. Bimodal or multimodal Weibull modulus values can be observed not only due to different phases but also due to the existence of one or a combination of inhomogeneities, pores, inclusions, second phases, cracks [174].

Li and Ding measured the microhardness of plasma-sprayed $\text{Cr}_3\text{C}_2\text{-NiCr}$ coatings. Weibull distributions were also employed in this study to assess the variability of the data within the coatings [147]. In a study by Valente, Vickers microhardness tests were used to assess the heterogeneity of a wide range of thermally sprayed coatings. Three different loads were used to evaluate the influence of the test volume on load-hardness dependence. Statistical elaboration of obtained results was performed by using variance analysis using Gaussian and Weibull distributions, in order to separate variation due to scatter of data and due to different materials properties. Load-hardness dependence was evidenced specially for ceramic coatings, due to their brittle nature, whereas for the two metallic coatings tested (Ti-6Al-4V and CoNiCrAlY) a bimodal distribution seems to exist at small loads [158].

Apart from coating studies, powder metallurgy was another area where Weibull distributions were utilized to analyze the spread in hardness data. Data sets of pressed and sintered FC0208, FN0208 and Ancorloy 4 alloys prepared in a single lot were analyzed

and it was reported that Weibull statistics generated a better fit than the fits using normal distributions [157].

The effect of creep deformation of hot-pressed β -sialon on Vickers hardness and fracture toughness was investigated in a study by Lin et al. Vickers hardness values were used in Weibull distribution, and Weibull modulus values from crept samples and as-received samples were compared [175].

As examples of Weibull statistics applied on hardness data rather than conventionally on strength data have shown, this method is effective on studying hardness results.

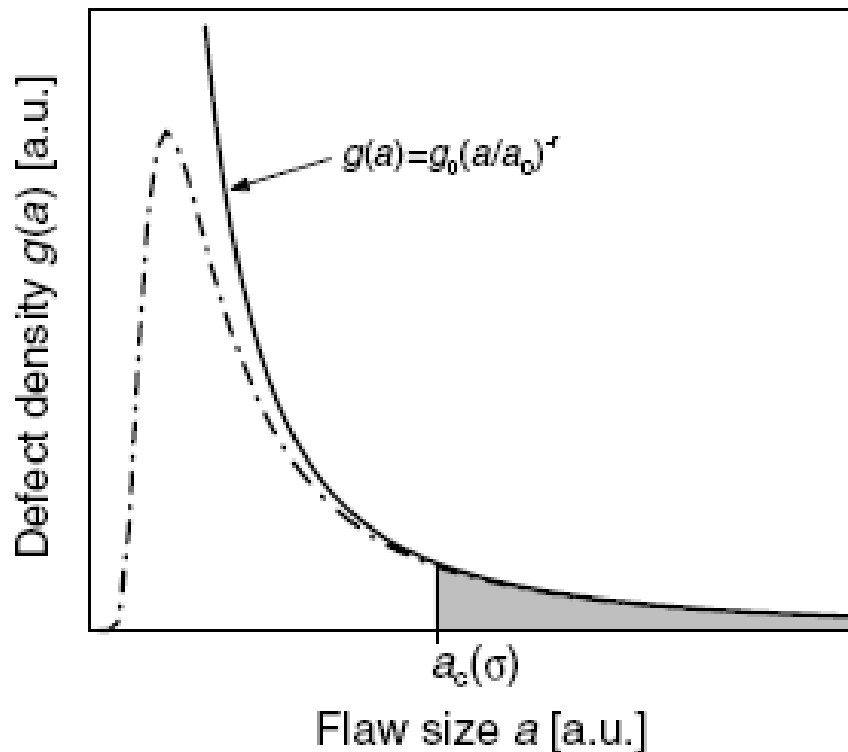


Fig. 2.15. Relative density of flaw sizes versus flaw size. The dashed line shows a typical distribution, the full line the behavior necessary for a Weibull distribution. The dashed area gives the density of destructive flaws [164]

2.6. Nondestructive Evaluation by Ultrasound

Nondestructive evaluation is a method of material characterization, performed without actually damaging the object. It is a technique for finding defects and examining internal changes in materials. This characterization method relies on propagation of sound waves in a material. The interaction between the wave and microstructural features in an object is recorded and a signal profile is obtained at the end. The signal sent through the material provides C-scan image maps, which show the variations either in the intensity of reflected signal or the transit time of signal through the sample, known as time-of-flight (TOF). TOF scans are used to examine acoustic wave velocity and impedance whereas reflected signal amplitude scans detect the loss in the ultrasound signal. Both techniques are functional in detecting and locating defects and anomalies inside an object.

Amplitude and TOF histogram curves can be used for quantitative analysis as area-under-the-curve values, full-width at half-maximum values, tail regions of plots can assist in characterizing materials and identifying differences between samples [176].

Ultrasound technique is frequently used due to the several advantages; including the opportunity for rapid evaluation, ease of adaptation to on-line manufacturing settings, non-hazardous nature, sensitivity to defects, and accuracy in determining size, position and depth of defects. In addition, elastic properties of materials can be obtained using longitudinal, shear and surface wave velocities [176,177]. Ceramic armor examination is well suited for this technique due to the qualities explained above. Size, shape and roughness of the material are key parameters in obtaining good quality scans. They could be the limitations on whether a material can be tested or not. Due to nature of large,

polished specimens with parallel surfaces, ceramic armor tiles could be easily tested using ultrasound [176].

Although, this technique is not performed by the author in this study, C-scan images of samples, further examined by the author, will be used frequently throughout the text. Therefore, this small section is provided for a brief explanation of the ultrasound technique. Much more detail could be obtained from Raymond Brennan's Ph.D. thesis, titled "Ultrasonic Nondestructive Evaluation of Armor Ceramics".

3. METHOD OF ATTACK

In armor materials, density is an important qualitative criterion that can be used as a threshold to accept or reject parts. The size and amount of secondary phases, i.e. pores or residual carbon, present in SiC armor is directly correlated with density. For equal density materials, small differences in the mixedness of a second phase can alter ballistic performance. For example, it is not reasonable to expect similar behavior between a material with a singular large pore in a theoretically dense matrix and a material consisting of micro pores dispersed throughout. Homogeneity in a microstructure is another key parameter that is often times overlooked. At a given volume fraction and average size of pores, clustered or agglomerated second phases might be more detrimental to the ballistic performance than a uniformly distributed second phase. A second phase that diminishes properties can be considered a defect. Specific defects must be examined in terms their spatial distribution as well as their size distribution.

The goal of this thesis is to determine methodology for differentiating small percentages of porosity or residual carbon in armor grade SiC and to determine the effect on physical properties. In meeting this goal, four objectives will be met. First one is to develop a method for determining microstructural uniformity of second phases. The second one is to assess microstructural uniformity of second phases on a series of commercially available armor ceramics. The third one is to determine microstructural uniformity using quasi-static properties. The fourth one is to correlate microstructural parameters with the quasi-static properties.

3.1. First objective: To develop a method for determining microstructural uniformity of second phases

The objective of the first part of this thesis is to identify second phases and assess the degree of their uniformity using multiple techniques. It is important to note that a few terms will be used interchangeably in this thesis. Second phase could be defined as density reducing defect. This description omits grain boundaries and small impurities. In SiC, the primary second phases are pores and residual carbon. This thesis will examine common second phase classes, namely porosity and carbon inclusions, that are artifacts of their process history. Later, quasi-static property measurements will be used to determine how these second phases contribute to local microstructural/property variations.

Microstructure homogeneity will be spatially quantified using tessellation, nearest-neighbor distance distribution and pair correlation functions. These techniques will enable numerical quantification of spatial defect patterns on stereological sections. The images will be obtained by FE-SEM or optical microscopy. Additionally, size and size distributions of defects will be determined, which will provide another parameter for differentiating samples. Lastly, through sample ultrasound imaging will be used as a volumetric analysis to be contrasted to the areal analysis obtained stereologically.

3.2. Second objective: To assess microstructural uniformity of second phases on a series of commercially available armor ceramics

After establishing the method for evaluating microstructures, four distinctly different set of samples will be used examined. Each set represents commercially relevant SiC material types. Initially, four sintered off-density Hexoloy-like SiC samples (Saint-Gobain Advanced Ceramics, Northboro, MA) will be evaluated. These samples will be used for establishing defect mixedness protocols. Two of these four samples (SA-1 and

SA-2) are Hexoloy SA sintered samples, although they are not the typical Hexoloy SA due their lower-than-standard density. Qualitatively, they have small, evenly distributed pores. Hexoloy Extruded (EXT) is extruded SiC which has elongated pores due to the nature of extrusion process. Hexoloy SP contains large, non-interconnected spherical pores that are dispersed throughout. The distinctive characteristics of defects in this sample set provide the opportunity to see the differences between samples clearly when microstructural parameters are obtained at the end of spatial analyses.

Two sets of hot-pressed samples will be presented. One set consists of three commercial hot-pressed SiC samples (Cercom Inc., Vista, CA) from a single production lot. Two of the samples were under a minimum density and considered “rejects” and the third one was representative of a saleable, “good” armor grade commercial material (AG). Rejected tile 1 had a low density region (LD) and rejected tile 2 had a white spot on the surface (DEF). Prior to stereological analyses, they were tested nondestructively by using ultrasound.

The second set of hot-pressed samples consists of four armor grade samples (Cercom Inc., Vista, CA) studied by Lundberg et al [1], which will referred to as “Lundberg Samples” to distinguish between the previous hot-pressed SiC set. They will be called SiC-HPN, SiC-N, SiC-SC-1RN and SiC-B throughout this thesis. These are the pieces from the actual samples that Lundberg et al. used in his ballistic study. These specific samples have known ballistic data consisting of transition velocity, penetration velocity and erosion velocity. They will be particularly valuable for the last objective of this thesis, where correlations with microstructural parameters and physical properties will be made.

The final sample class is a single, sintered SiC Hexoloy tile. A lot of eight tiles were scanned using ultrasound and low amplitude regions were determined. One tile from that lot was selected for further microstructural evaluation and the questionable regions were examined by sectioning distinct regions from identified areas. This sample will enable a correlation between an ultrasound C-scan map and microstructural characteristics stereologically derived.

3.3. Third objective: To determine microstructural uniformity using quasi-static properties

The objective of the third part of the thesis was to use hardness as a relevant and convenient method to obtain volumetric information regarding the homogeneity of microstructures. The output being volumetric comes from the fact that five different loads will be used and the area of interaction between an indent and the defects under the indent will change with each load. Hardness maps will be constructed by placing a statistically significant number of one hundred indents per load, to see the variation in terms of location since “location” is the main focus in this thesis. The large number of indents enables performing Weibull analysis to examine the spread in the data and to test spatial variability. Hardness values will provide a means of linking microstructural data and physical property variability.

3.4. Fourth objective: To correlate microstructural parameters with the quasi-static properties

The objective of the final part of this thesis is to combine microstructural parameters and physical properties. They will be graphed against each other and any

trends or correlations will be searched for in these plots. This analysis will be applied to all four sample sets that are discussed in this thesis. Additionally, Lundberg samples have the ballistic data which provides the opportunity to test any correlation between microstructure, physical property and ballistic performance.

4. EXPERIMENTAL PROCEDURE

Examination procedures were developed during the course of this thesis and used throughout for sample preparation, microstructural investigation, quasi-static tests and nondestructive testing by ultrasound.

Parameters regarding the size and shape of features might not provide sufficient information at times, as spatial distribution of features could be equally important in microstructural characterization. In order to assess features in microstructures based on location, spatial data analysis including nearest neighbor distance distributions, tessellation analysis and pair correlations were performed on several sets of SiC samples. Image analysis was applied to images from FE-SEM and optical microscope and quantitative information was obtained on microstructures.

The results from microstructural analysis were complemented by hardness tests, performed on areas which were examined previously in terms microstructural homogeneity. Cracks resulting from indentations were examined, which helped determine the fracture mode of the samples, therefore providing another parameter to evaluate materials on microstructural properties and tying other parameters with the fracture mode.

Nondestructive evaluation by ultrasound tests were carried out using 75 and 125 MHz frequency transducers to determine defect distributions from an entire tile instead of local examination using microscopy. This was incorporated into this study in order to compare results from microscopy, which provided to opportunity to look at only multiple sections at most.

4.1. Sample Preparation for Microscopy

4.1.1 Grinding and Polishing

Initially, samples were cut using a diamond saw. They were then mounted in epoxy from a mixture of EpoxiCure hardener and resin (Buehler, Lake Bluff, IL). Samples were ground and polished using two different grinder/polishers, which are VP-50 Vari/Pol grinder/polisher (Leco Corp., St. Joseph, MI) and ECOMET 3000 (Buehler, Lake Bluff, IL, USA). Grinding was performed using 125 and 45 μm diamond wheels and polished with 15, 9, 3 and 1 μm diamond suspensions. Colloidal silica was used in the final step of polishing. The exact sample preparation sequence is given in Table 4.1. Time was kept at 10 minutes at all times for each step. The force applied was maintained at 5 to 8 lbs per sample and the speed of wheels was maintained at 150 rpm.

Extreme care was taken during sample cleaning for FE-SEM examination. First, epoxy mounts were put in an organic solution named Epoxy Dissolver (Allied High Tech, Rancho Dominguez, CA) after grinding and polishing steps. The solution was brought to a boil, and epoxy mounts were kept in the solution until epoxy cracks and samples were liberated. The samples were then put into a small amount of ethanol in ultrasonic bath. Ultrasonication was performed for 10 minutes to remove any organic residue. Ultrasonication was repeated in de-ionized water.

The samples were placed on aluminum studs using carbon tape to provide conductivity and avoid effects of charging. The samples were then placed into a desiccator for removal of moisture one day prior to examination.

4.1.2. Serial Sectioning

Key component of serial sectioning was to mark the sample so that areas from the same rectangular prism were analyzed. This was achieved by using indents. Several

indents were placed on the corners of the samples after the first polishing step. They were used as points of reference during image collection and further polishing steps. The indentation sizes were measured at the beginning and the samples were polished until the indents disappeared. As a result, a certain distance between each plane was roughly kept. The shape of indent after each polishing step is given in Fig. 4.1.

4.1.3. Etching

Chemical etching was used for SiC samples using Murakami's solution, which was a mixture of H_2O - KOH - $\text{FeK}_3(\text{CN})_6$. 1 part of H_2O and 1 part of KOH was mixed with 8 parts of $\text{FeK}_3(\text{CN})_6$. The solution was brought to a boil and the samples were put into the solution. Different etching times were used starting from 10 minutes up to 30 minutes at 5 minute intervals. Mostly, grains and boundaries were revealed best at 20 minutes, but the effect of etching agents varied depending on the sintering aids so it was changed accordingly after trial and error for each sample.

4.2. FE-SEM

Leo-Zeiss 982 field emission scanning electron microscope (Leo Electron Microscopy, Inc., Thornwood, NY) with energy dispersive capability was used to examine polished surfaces, etched surfaces and indent marks after hardness tests. Imaging was performed at 5.0 keV using secondary electrons collected with a standard Everhart-Thornley detector. The working distance was kept between 10-12 mm for most of the work. Samples were uncoated due to the conductive nature of silicon carbide, which showed minimal amount of charging during examination. Pictures that were

analyzed afterwards were mostly taken at $\times 1000$. Random areas were selected for imaging defects. Consecutive pictures were taken for some samples from neighboring area in order to combine images in image analysis step. Totally random selections were made in each picture for the rest of the samples.

4.3. Optical Microscopy

An optical microscope from Olympus CKX series (Olympus, Center Valley, PA) was used for examining polished surface at low magnifications. An Olympus digital camera was attached to the microscope, which was also connected to a PC for a quick way of image collection. When the area of interest was larger, particularly for the comparison of ultrasound and microscopy, low magnification images of sintered SiC tile pieces at $\times 100$ and $\times 200$ were taken using this equipment. It was also utilized for imaging indents from hardness tests.

4.4. Spatial Data Analysis

4.4.1. Nearest Neighbor Distance Distributions

Image analysis has been used to obtain quantitative information on the microstructures. Image Processing Toolkit 5.0 (Reindeer Games, Inc., Asheville, NC) which adds many functions as a plug-in to Adobe Photoshop (Photoshop 7.0, Adobe Systems Inc, San Jose, CA) has been used for image analysis.

First step of the image analysis was “thresholding”, that is whenever a pixel’s value is greater than a certain number, its value is replaced by 1 and if its value is less

than or equal to that number, it is replaced by zero. A binary image was obtained after thresholding step.

This step was followed by “close” filter, which is defined as a “dilation” operation with a given structuring element followed by “erosion” with the same structuring element. Both “dilation” and “erosion” filters examine each binary pixel and change the value accordingly. In erosion, it is changed from ON to OFF if it has any neighbors that are OFF. Dilation is the reverse of erosion, so any OFF pixel is changed to ON if it has ON neighbors. The purpose of “close” operation is to smooth features and to remove isolated pixel noise from the image. It also helps to keep small features in the image, while small voids are filled, and gaps in features are connected.

The next filter applied after closing was “fill holes”. This filter is based on the definition that a hole within a feature is a region of background that is isolated and does not connect to the background that reaches the edge of the image. This operation eliminates the holes inside pores, which might be excluded due to thresholding. The final step was cutting off edge-touching features in order to include only the features in the field of view [87,178]. This procedure is given in Fig. 4.2. Finally, a report on the features is obtained, which provides information such as area, equivalent diameter, form factor, x- and y- coordinates of each feature in the image for further analysis. The parameters included in this report are given in Table 4.2.

For estimation of the nearest-neighbor distribution, (x,y) centroid coordinates of the pores observed in the ceramographic plane were measured. Then, if m is the total number of pores on which the measurements are performed, and $(x_1,y_1), (x_2,y_2), \dots, (x_i,y_i), \dots, (x_m,y_m)$ are the centroid coordinates of the pores, the distances between the

pore at location (x_i, y_i) and all other $(m-1)$ particles were calculated using corresponding centroid coordinates. The procedure was then repeated for all the pores. From this information, the nearest neighbor distance for each pore was calculated and a distribution of nearest neighbor distances was obtained from the features in the image.

4.4.2. Tessellation of Microstructures

This method involves a geometric construction of two dimensional cells or polygons around each particle on the plane-of-polish. It is a promising approach to characterizing especially clustering, since the cell area is a dependent on the whole surrounding environment of the particle concerned. All points within each polygon are closer to the center of the particle than to any particle outside the polygon. To construct the polygons, lines are drawn from a particle to neighboring particles. Next, perpendicular lines bisecting these lines are drawn. These lines will intersect and form polygons. The lines that intersect to form the polygons are from only the nearest neighbors. Thus, a unique area can be associated with each feature [110,116].

A certain procedure in .image analysis was performed for creating tessellated microstructures. Again, The Image Processing Toolkit 5.0 was utilized to form tessellations. Procedurally, the first step was thresholding. A binary image was created after thresholding. Then, an “invert” filter was used on the image, which reversed the pixel values assigned in thresholding step. The next step was to use Skeletonization filter. It is a specialized form of “erosion” and is also named Medial Axis Transform (MAT). This filter basically forms a line of pixels that mark the midline of a feature. If there is branching in a feature, the skeleton has also the same branches, only in reduced form and line shape [179]. Since tessellations must be made up of continuous lines, removal of

unconnected lines must be performed. This was achieved using “prune” filter, which eliminates lines with end points.

“Thicken” filter was applied to enable the software to detect each cell or tile during quantification. During application of previous filters, gray levels might appear on tile boundaries. Thresholding was used to eliminate this problem.

The image was then inverted again in order to get the quantitative information of each tile or cell created. The sequence of image analysis steps is given in Fig. 4.3.

Generation of tile boundaries was followed by generating cells or tiles using random Poisson distribution. This was accomplished by using STG Software 4.1 (Institute of Statistics, Freiberg, Germany), which is used for generation, presentation and statistical analysis of models with stochastic geometry. The average number of cells was determined per image for each sample, and the same number of points was entered under “Generate” column. This image was carried over to Adobe Photoshop and same procedure for tessellating images was performed. This part of the work provided the ground for comparison of real tessellated microstructures with that of total random microstructures.

4.4.3. Pair Correlation Functions

Generating pair correlation functions followed the previously explained image analysis procedures, where same filters were applied to images as in nearest neighbor distance distributions. The x- and y- coordinates were copied to a Notepad file and the total number of points was written on the top of the file in order to match up with format the software required. This file was carried over to STG software. Coordinates of features

formed a two dimensional point map, which was an exact representation of defects from the original image. Pair correlation functions were obtained by using the function button under statistics column.

4.5. Image Analysis

4.5.1. Porosity Measurements

One of the steps in image analysis was to measure porosity levels for each sample. After each image was converted to binary form, the image analysis software provided the percentage of defects, which were represented by black features, to the overall image. “Global” filter was performed for obtaining this type of information. Although porosity values obtained by this method gave results based on two dimensional images, this was acceptable due to the principles of stereology.

4.5.2. Defect Size Distributions

Collected images went through same image analysis procedure as in the images for calculating nearest neighbor distance distributions. The second column of the report file presented “equivalent diameter” parameter. This term is the distance of a feature which corresponds to the radius of a circle with same area [180]. This is shown in Fig. 4.4. After data bins were created, the equivalent diameters of defects were then graphed, showing the amount of defects, either in absolute values or in percentages, in each bin or data range.

4.6. Mechanical Testing

4.6.1. Microindentation

Microstructural investigation was followed by hardness tests. Microhardness was measured by Knoop indentation using Leco M-400-G3 Hardness Tester (Leco Corp., St.

Joseph, MI). The length of longer diagonal was measured in microns and it was substituted into the following equation for obtaining Knoop hardness: [117]

$$KHN = \frac{14229 \times F}{L^2} \quad 4.1$$

where KHN = Knoop Hardness Number

F = Load (g)

L = Long Diagonal Length (μm)

A series of indentations at five different loads were performed on polished samples. The loads were chosen as 2 Kg, 1 Kg, 0.5 Kg, 0.3 Kg and 0.1 Kg. Knoop indentation was used on all of the measurements and a square array of indents were performed on polished sections. Hardness maps were obtained by indentation of samples 100 times, forming a square of 10×10 indents and they are presented here as contour maps. The distance between each indent was kept constant at 0.5 mm at larger loads, and the distance was reduced down to 0.15 mm at lower loads. The dwell time was selected arbitrarily at 10 seconds. The starting position for indentation arrays was chosen arbitrarily and the place to be indented was not changed according to positions of defects.

4.6.2. Grain size analysis

Images of etched surfaces were collected using FE-SEM. This analysis was performed on microstructures from indented samples and around regions that show low and high hardness to see if grain size has any effect on the hardness results. Grain size analysis was performed after several image processing steps. Before converting image to

binary, “Kuwahara” filter, which is an edge-preserving filter that reduces noise, was applied. This filter compares the variance of subregions within the neighborhood and keeps the mean value of whichever subregion has the smallest variance [87]. It also helps lessen the appearance of polishing scratches and to reveal the grain boundaries. Then, the image was converted into binary form by using “threshold” filter. Following the conversion step, “invert” filter was applied and grains were observed as black. “Fill holes” filter was used to close any gaps inside grains and a closing operation was applied afterwards. The edge-touching features were removed from analysis by using “cut-off” filter. Finally, “watershed” filter, which uses distance maps for segmentation of features, was applied [87]. This filter helps separate touching features, however it can also draw false boundaries. Therefore, the processed image was examined closely and those types of boundaries were removed manually.

4.6.3. Fracture Mode

The indentations in hardness tests occasionally caused cracking, especially at the higher loads. The indents were made and they were observed either by the optical microscope or by FE-SEM. Electron microscope showed better assessment on transgranular/intergranular cracking due to the fact that, FESEM provides higher magnification which was required for SiC samples with small grain size. After an assessment was made on each indent, the results were presented in percentages by the amount of fracture type each sample showed.

4.7. Nondestructive Evaluation by Ultrasound

For the ultrasound study, tiles were scanned using 75 and 125 MHz transducers to provide a high degree of detail and resolution for detection of defects. Higher frequency transducers produce ultrasound waves with shorter wavelengths that enable the detection of smaller features in the test sample [176]. C-scans images were produced by 125 MHz frequency transducers. The scans shown in this thesis were mainly utilized for providing insight to determine the areas for further destructive evaluation.

Table 4.1. Grinding/Polishing Procedure at 5-8 lbs/sample of force at 150 rpm

Abrasive (μm)	Time (minutes)	Wheel/Holder Spin
125	10	Complementary
45	10	Contra
15	10	Complementary
9	10	Complementary
3	10	Contra
1	10	Complementary

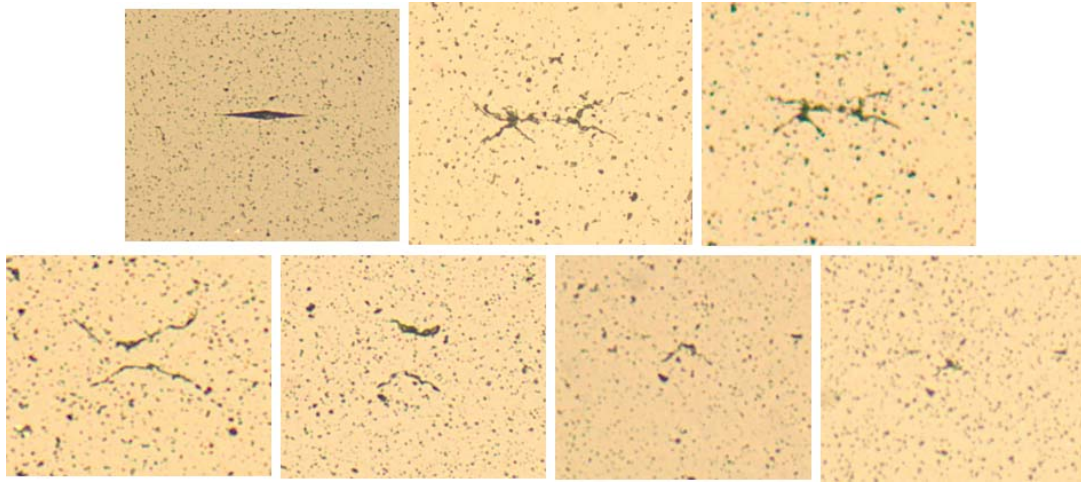


Figure 4.1. The shape of indent after each polishing step during serial sectioning

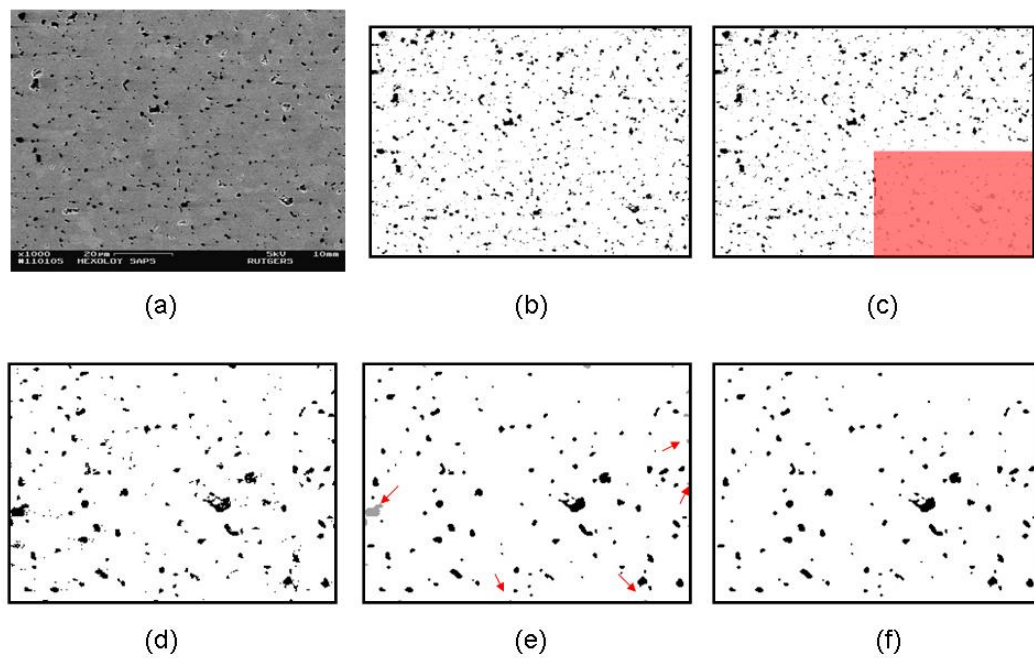


Figure 4.2. (a) Original FESEM image from a polished section (b) After thresholding (c) Previous picture with a highlighted corner for a closer look for further steps (d) After application of “close” and “fill holes” filters (e) After application of “cut-off” filter. Gray feature due to the filter were shown with red arrows (f) Final processed image

Table 4.2. Data generated in Image Processing Toolkit 5.0

Feature Number	Number of Holes	Mean Ext. Branch Length (μm)	Density
Area (μm^2)	Formfactor	Mean Int. Branch Length (μm)	Integrated Optical Density
Filled Area (μm^2)	Roundness	Mean Fiber Width (μm)	X- and Y- Centroid (μm)
Convex Area (μm^2)	Aspect Ratio	Width Standard Dev. (μm)	Moment Angle
Length (μm)	Solidity	Mean Red	Weighted X- and Y- Center (μm)
Breadth (μm)	Convexity	Mean Green	X- and Y- Geometric Center (μm)
Equivalent Diameter (μm)	Symmetry	Mean Blue	Nearest Nbor Distance (μm)
Inscribed Radius (μm)	Hole Fraction	Mean Hue	Nearest Nbor Dir.
Circum. Radius (μm)	Radius Ratio	Mean Saturated	Nearest Nbor ID
Perimeter (μm)	Elongation	Mean Luminance	Min. Seperation Distance (μm)
External Perimeter (μm)	Skeleton Length (μm)	Max. Intensity	Min. Seperation ID
Convex Peri. (μm)	Skel. End Points	Min. Intensity	Adjacent Feature Count
X- and Y- Feret	Skel. Branch Points	Intensity Std. Dev.	Adjusted Count

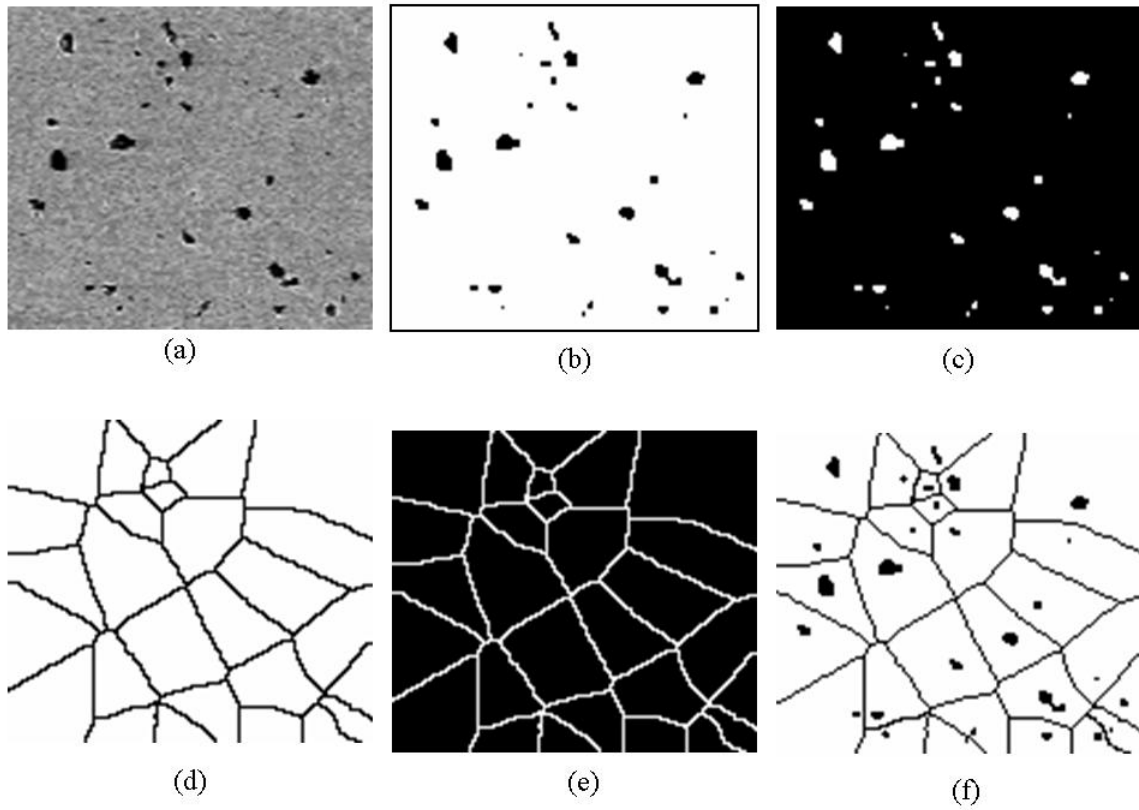


Figure 4.3. (a) Part of an original FESEM image (b) Processed image (c) After application of "invert" filter (d) "Skeletonize" filter applied (e) Second application of "invert" (f) Combined image of defects and cells around defects

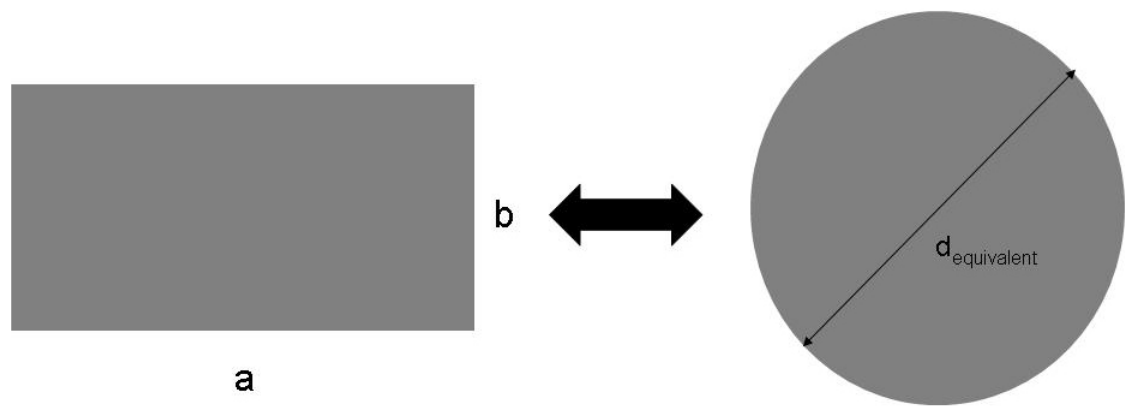


Figure 4.4. Conversion of a rectangle shape into a circle for obtaining $d_{\text{equivalent}}$ where the areas of the figures are equal

5. RESULTS AND DISCUSSION

After presenting the literature background, the method of attack and the experimental procedure, the results will be presented in this chapter with subsequent discussions. The chapter is divided into three parts, first of which involves microstructural examinations and the results from those examinations. In the second part, hardness is employed as a validation method for the microstructural results. The third part combines microstructural findings and hardness data and tries to draw conclusions from these two parts

5.1. Off-Density Sintered Hexoloy-like Samples

5.1.1. Density

Density measurements were performed using Archimedes' principle. The density values of SA-1, SA-2, EXT and SP are 3.16, 3.18, 3.11, 3.10 gr/cm³, respectively. Density of the samples was also calculated using image analysis from a total of ten micrographs for each sample at 1000× magnification. The values from image analysis are 3.11, 3.12, 3.07, 3.09 gr/cm³, respectively.

5.1.2. Micrographs

Representative micrographs for each sample are given in Fig. 5.1. SA-1 and SA-2 have qualitatively very similar microstructures with evenly distributed pores in the field of view. EXT has elongated features that are evidently the result of extrusion process. SP has large circular pores in a matrix of homogeneously distributed smaller pores. EXT and SP have visibly distinctive features which provide the opportunity to see the differences between samples clearly when microstructural parameters are obtained at the end of spatial analyses.

5.1.3. Average Pore Size and Pore Size Distribution

Average pore size and pore size distribution of four samples were calculated using the image analysis procedure that was explained in Experimental chapter. Equivalent diameter of features is used for calculation of average pore diameter. Average pore size for each sample is given in Fig. 5.2. Among all samples, SA-2 has the smallest pore size with an average value of $1.01\ \mu\text{m}$. Samples EXT and SP have an average pore size of $1.05\ \mu\text{m}$ and SA-1 has the largest average pore size with $1.28\ \mu\text{m}$. However, SA-1 has a much lower standard deviation, $\pm 0.89\ \mu\text{m}$, when compared to EXT and SP, ± 1.43 and ± 1.57 , respectively. These values verify the visual observations that samples EXT and SP have a broader pore size distribution than the other samples.

Pore size distributions are given in Fig. 5.3. The graphs were plotted based on the percentage of number of occurrences (% Frequency) on the y-axis. Among the largest peaks of each graph, SA-2 has the largest bar with the y-axis value above 45 percent. The right side of the plots for SA-1 and SA-2 do not extend beyond $6\ \mu\text{m}$, however that is not the case for the other two samples due to the presence of elongated pores for EXT and large round pores for SP. These results are in agreement with the qualitative observations obtained from the micrographs. SA-2 seems to have smaller pores when compared to EXT and SP and that is verified by the defect size distribution plots.

5.1.4. Nearest Neighbor Distance Distributions

Apart from the average pore size and pore size distribution, the focus in this study is on the location of pores and their spatial distribution, therefore more information will be extracted from the micrographs

The nearest neighbor distance (nnd) distributions for the samples are given in Fig. 5.4. Sample SA-1 and SA-2 show relatively narrow nearest neighbor distance distributions with small values for variance of the distributions, 2.32 and 2.09 μm^2 , respectively. This narrow distribution of nnd can be observed by looking at the right corner of the histogram where the % Frequency of distances longer than arbitrary 14 μm is given and it is zero for both samples. The nnd distributions for samples EXT and SP show a different behavior on the contrary. Broader nnd distributions can be seen easily for both samples, with variance values 10.83 and 6.97 μm^2 , respectively. The other important observation for these two histograms is that there is considerable amount of nnd values on the right side of the histogram. This is a clear indication of inhomogeneous microstructures that these two samples possess.

Q and V parameters were introduced in the Literature Review chapter. Observed mean and variance nearest neighbor distance (nnd) values were calculated from the distributions given in Fig. 5.4. These two parameters are given in Table 5.1. The Q values for all four samples are approximately equal to 1; however the V values differ strongly from the random case. SA-2 is the only one whose V value is roughly 1. Other three samples, especially EXT and SP, have V values way off the random value, ~ 1 . Overall, all samples can be accepted in “Random” category due to the fact that points fall in between two straight lines parallel to the y-axis.

5.1.5. Tessellation Analysis

Microstructures were tessellated and divided into smaller areas, “cells” or “tiles”, as previously explained in the Experimental chapter. This is a good way to assess

microstructures since the cell area is dependent on the whole surrounding environment of the pore concerned. After going through the image analysis steps, representative tessellated microstructures are given in Fig. 5.5. The images look like the microstructure of an etched material, where the tile boundaries resemble grain boundaries. SA-1 and SA-2 seem to have an even cell area distribution. EXT and SP possess large cells due the presence large features in the original images.

Cell area distributions are shown in Fig. 5.6. 'More' in Fig. 5.6 refers to cell areas larger than $100 \mu\text{m}^2$. The distribution for SA-1 is very broad in between the limits 0-100 μm^2 but the cell area percentage above 100 μm^2 is low when compared to EXT and SP. SA-2 has the narrowest distribution among all and the cell area percentage larger than 100 μm^2 is minimal compared to the other three samples.

P_1 and P_2 parameters were introduced in the Literature Review section, and in principle, they represent the same concepts as Q and V does that are relevant to nearest neighbor distance distributions. P_1 is based on the variance of the cell area distribution and it is a parameter that can be used to find the extent of spread in a distribution since the variance from a real microstructure is compared to that of a random microstructure. P_2 is a measure of skewness, which shows the asymmetry in a distribution.

These two parameters were calculated for all samples, which are given in Fig. 5.7. SP has the largest values, 3.28 and 15.78, respectively, as opposed to 1, which is the expected value for random distribution of particles. The complete P_1 and P_2 results are given in Table 5.2.

5.1.6. Pair Correlation Functions

Pair correlation functions (pcf) from these samples are given in Fig. 5.8. The different curves in each graph represent estimation from different micrographs. Most of the curves in each graph are dominated by plots which rise monotonically to its asymptotic value and is distinguished by relative lack of structure. Some of the curves for EXT and SP have sharp peaks very close to the y-axis. Strong first peak at a distance well below the mean interparticle distance (r_0) followed by a weak minimum at about this distance is an indication of clustering. The curves for SA-1 and SA-2 are typical random distribution curves.

An order parameter for pair correlation functions has been introduced by Hubalkova and Stoyan [102];

$$O = \frac{g(r_1)}{r_1 - r_0} \quad 5.1$$

where;

r_1 is the position, $g(r_1)$ is the value of the first maximum of the pcf and r_0 is the hard core distance. This O parameter characterizes the average growth rate of the pcf between r_0 and r_1 and a larger value indicates a lower degree of homogeneity in the structure. The values for each sample were calculated. No significant difference was observed between the O values for four samples.

5.1.7. Assessment of Spatial Data Analysis Techniques

Three different techniques, nearest neighbor distance distributions, tessellation analysis, and pair correlation functions, were used to examine spatial distribution of pores

in SiC. The trends that were observed in one technique were validated by another and consequently, no significant difference was observed among the three. Therefore, from this point on, nearest neighbor distance distributions will be used due to the ease of application compared to the other two techniques, which require more tedious effort to get the same type of information.

5.1.8. Serial Sectioning

The results shown above were from a single layer. Grinding and polishing was applied on the samples multiple times, obtaining micrographs at each layer so that the microstructural information was obtained not only from a single section but also from the volume underneath. This was performed for statistical purposes and a possible way of combining the micrographs to form a three-dimensional visualization of a volume instead of looking at the layers individually. Eventually, three dimensional images could not be obtained due to the difficulty in aligning all images from all layers but valuable information was obtained from each section.

5.1.8.1. Average Pore Size and Pore Size Distribution

Initially, pore size distributions were calculated and they are given in Fig. 5.9. Graphs were plotted based on the number of pores observed in the field of view. As it can be seen from the graphs, SA-1 has smaller number of pores; however, the average pore size is larger. The overall number of pores is the highest for SA-2 in all the layers and it has the smallest pores. EXT have similar graphs except the third layer, where the number of pores observed is significantly less than the other three layers. In the first layer for SP,

a significant number of finer pores was observed, which is not valid for the second layer. The number of pores is fairly higher for the third and fourth layer and their distribution close to each other.

5.1.8.2. Nearest Neighbor Distance Distributions

The nearest neighbor distance (nnd) distributions for the four layers are given in Fig. 5.10. In the graph for the first layer, EXT has the narrowest distribution among the four. The major peaks are around 2 μm and the graph does not extend beyond 5 μm . The second one is SA-2, where some peaks are observable beyond 5 μm mark. SA-1 and SP show relatively broader distribution, where the right part of the graphs extends further. Also, major peaks are not as strong as they are for SA-2 and EXT.

In the second layer, SA-2 has the narrowest distribution this time, with the longest major peaks and the shortest range from the smallest nnd to the longest nnd. EXT has a slightly broader range and SP is similar to EXT except that the major peaks are shorter. SA-1 behaves differently again, with the widest spread. Small peaks are observable even around 10 μm which is not the case for the other three samples.

The third layer shows different results from what is observed in the first and second layers. SA-2 and SP have very similar graphs in the sense that both have the same range and the same height of major peaks. SA-1 shows a large spread with the major peaks reaching around 400 in the number of pores axis. The graph for EXT has a similar shape except that major peaks reach about 300.

In the fourth layer, SA-2 has again the narrowest distribution among all. EXT and SP have similar ranges, only the heights of peaks change slightly. SA-1 has again an observable difference from the other three samples.

Q-V values from all layers are given in Table 5.3. The data points for SA-2 are the closest to the (1,1) point, which represents the random point. As the points move away from this spot, the deviation from randomness starts. It can be concluded that SA-2 has the closest microstructure to random.

5.2. Cercom Hot-Pressed SiC Samples

As mentioned in the introduction part of this chapter, hot-pressed samples were studied in addition to the sintered samples. First, the results from three commercial hot-pressed SiC tiles, referred to as LD, DEF and AG, from a single production lot will be presented. Then, the findings from the second set, which is “Lundberg Samples”, will be shown.

5.2.1. First Set of Hot-Pressed SiC Samples

5.2.1.1. Density

Density measurements were performed using Archimedes’ principle. The density values are 3.19, 3.18 and 3.20 gr/cm³ for DEF, LD and AG respectively.

5.2.1.2. Microstructural Evaluation

The micrographs from the three samples can be seen in Fig. 5.11. On the appearance, they have similar average pore size and spatial distribution. However, careful

analysis of the images will expose possible differences in the defect size distribution and the level of clustering of pores. Visually, DEF seems to have more of elongated shaped features while AG and LD seem to have very similar micrographs qualitatively.

5.2.1.3. Average Pore Size and Pore Size Distribution

Average pore size values are given in Fig. 5.12 and were calculated to be $0.78 \pm 0.49 \mu\text{m}$, $0.94 \pm 0.47 \mu\text{m}$, and $1.08 \pm 0.54 \mu\text{m}$ for DEF, AG and LD, respectively. Among the three samples, DEF has the smallest pore size. LD has the largest pore size and also the highest standard deviation.

Pore size distributions are given in Fig. 5.13. LD has the broadest distribution among the three, which is consistent with the previously mentioned ultrasound results. AG and DEF have tighter distributions than LD has as the peaks in each range beyond $1.5 \mu\text{m}$ have very close values for both samples. The ones lower than $1.5 \mu\text{m}$ are different as DEF has significant amount of data points in the lowest $0.5\text{-}1 \mu\text{m}$ range and AG has a very small peak in that range. In addition to that, AG has the largest peak in the $1\text{-}1.5 \mu\text{m}$, that reaches up to 70% of the of the data points. As a result, AG and DEF have narrower distributions when compared to that of LD.

5.2.1.4. Nearest Neighbor Distance Distributions

Nearest neighbor distance distributions were performed on these samples using image analysis and the results can be seen in Fig. 5.14. The 'More' column in the plot refers to values larger than $15 \mu\text{m}$ for the nnd distributions. AG and DEF show relatively narrow nearest neighbor distance distributions with the variance values of 3.47 and 2.94

μm^2 , respectively. This narrow distribution of nearest neighbor distances can be observed qualitatively on the right side of the graph, as LD has clearly higher peaks above $10\ \mu\text{m}$. LD shows a higher variance value with $5.51\ \mu\text{m}^2$ and broader distribution compared to the other two samples. This is an indication of inhomogeneous distribution of defects that LD possesses.

Q-V plots for these samples are given in Fig. 5.15. All points fall in between the two lines that could be labeled as “random”. However, there is a minor difference between LD and the other two samples where LD is in the region of random distribution with clusters while AG and DEF do not show any clustering according to the plot.

Although, this topic was extensively covered in Literature Review chapter, it would be useful to remind the reader again briefly what “random” stands for. When a qualitative observation does not show any apparent structure in a pattern, it could be regarded as “random.” When the events are about evenly spread over the entire area, the pattern could be labeled as “regular”. “Clustering” is the type of pattern where events are noticeably grouped rather than being regularly or randomly spaced. A mixture of clustering with random or regular case could also be observed in a pattern. The Q-V plots show briefly where the spatial distribution falls, (1,1) point representing the ultimate random point. More information on this matter could be found in Literature Review chapter.

5.2.2. Lundberg Samples

5.2.2.1. Microstructural Evaluation

The micrographs of four Lundberg samples are given in Fig. 5.16. Initial observations show that SiC-HPN seems to have the lowest amount of features among all

four. SiC-SC-1RN looks like it has smaller features than the other three while SiC-B possesses features with larger sizes than the rest.

One crucial step was added during image processing of micrographs, which was setting a shape factor threshold for differentiating between pullouts and pores. The details on this subject are covered extensively on the Literature Review chapter.

5.2.2.2. Density

Densities of the samples were initially calculated by Archimedes' method and they were all found to be 3.20 gr/cm^3 . Image analysis was also employed in density determination. The results from SiC-N and SiC-SC-1RN agreed with Archimedes' method as they came out to be 3.20 while SiC-B and SiC-HPN showed slight decrease in density with values of 3.19 gr/cm^3 .

5.2.2.3. Average Pore Size and Size Distribution

Some of the qualitative observations were verified using image analysis. Bar chart for average pore size is given in Fig. 5.17. SiC-N and SiC-SC-1RN have smaller average pore size than the other two samples. SiC-B and SiC-HPN have also larger standard deviation values.

Pore size distributions are given in Figure 5.18. The longest bar in SiC-HPN chart is from $0.4\text{-}0.6 \text{ }\mu\text{m}$ range and the maximum number of defects observed in that range is 300. The graph extends up to $2.8 \text{ }\mu\text{m}$. For SiC-SC-1RN, the maximum number of defects observed in a bin, which is close to 800, is from the same $0.4\text{-}0.6 \text{ }\mu\text{m}$ range. The largest bin in the graph goes up to $1.4\text{-}1.6 \text{ }\mu\text{m}$ range. SiC-B shows a very similar trend in the plot

as is shows more spread in the size data than SiC-SC-1RN and SiC-N and the largest pore size bin is from 2.6-2.8 μm range. The largest bar in SiC-N chart is from 0-0.75 μm range and it reaches right below 600 for the number of defects. SiC-N and SiC-SC-1RN possess similar curves and same is valid SiC-HPN and SiC-B.

Curve fitting was performed on the plots and R^2 values for all of them were above 0.90, SiC-SC-1RN with the highest value of 0.99 and SiC-HPN with the lowest value of 0.94.

5.2.2.4. Nearest Neighbor Distance Distributions

Spatial data analysis was performed once again using nearest neighbor distance distributions and plots are given in Fig. 5.19. Minor differences were observed on the plots, especially on the right side where higher values of nearest neighbor distance distributions were present. SiC-N extends up to 22 μm , which shows the highest values among all. Then, the highest value of 21 μm was observed for SiC-HPN. SiC-N and SiC-SC-1RN have lower highest values of 18 and 15 μm , respectively. These values do not mean that there are significant differences in the spatial distributions of defects; however, minor dissimilarities should be pointed for further categorization.

Q-V plots are given in Fig. 20, where the distributions that were explained above were compared to that of expected random distributions. The first graph, Fig. 20 (a) shows data points from each micrograph used in calculation of nearest neighbor distance distributions. The second graph, Fig. 20 (b) combines all data points for each sample and presents the data with the error bars. All points slightly fall into “random with clusters” region, where SiC-SC-1RN is the closest to the random point and SiC-HPN is the farthest

from the random point. This shows the same trend that was observed in the nearest neighbor distance distribution plots.

5.3. SiC Hexoloy SA Tile

5.3.1. Ultrasound Image

In this section, microstructural results from a SiC Hexoloy tile will be presented. A set of several tiles had been previously scanned and low amplitude regions, which could be a result of cluster of impurities, pores, grain size changes etc., were determined. These questionable regions were examined for one of that set of tiles by using diced pieces from those areas. Spatial distribution and size distribution of pores were determined and correlations with ultrasound results were obtained.

C-scan image of SiC Hexoloy tile is given in Fig. 5.21. The color scale represents the amplitude of ultrasound signals in millivolt (mV). The blue areas are low amplitude regions that are segregated on two sides of the tile. The tile was cut and diced from those regions as shown in Fig. 5.21. The pieces from these two cuts represent “bad” regions. Another cut was made from the middle part of the tile which had predominantly shades of yellow and red regions. The pieces from this cut represent “good” regions. The signal sent through the material provides C-scan image maps, which show the variations in the intensity of reflected signal. “Good” and “bad” areas are determined according to the signal amplitude obtained from those regions. “Bad” regions are caused by the presence of features such as pores, inclusions that instigate higher signal loss.

There were totally 12 pieces. Numbers 1 to 4 and 9 to 12 were from “bad” regions and numbers 5 to 8 were from “good” regions. Six of these of twelve pieces were studied, namely N1, N4, N5, N8, N9, and N12.

5.3.2. High Magnification Images

The micrographs from each piece are given in Fig. 5.22. There are minor differences in each one and they all look very similar qualitatively. One big round pore could be seen on the left side of the micrograph of N1. Several pores are located in the middle of the micrograph for N4. Clustering of defects seems to be present in the micrograph for N9. No significant observations are required to be emphasized for the other three micrographs which look alike.

5.3.2.1. Average Defect Size and Size Distribution

Initially, the density of the tile was measured by Archimedes' principle and all values came out to be 3.16 gr/cm^3 . The average defect size and size distributions were measured afterwards. Bar chart for the six samples is given in Fig. 5.23. The graph on the right shows each sample and the one on the left shows results based on the regional information. N5 possesses the smallest pore size of $0.92 \text{ }\mu\text{m}$ with the smallest standard deviation of $0.54 \text{ }\mu\text{m}$. N12 and N1 follow as they have average sizes of 0.98 and $0.99 \text{ }\mu\text{m}$, and standard deviations of 0.59 and $0.61 \text{ }\mu\text{m}$, respectively. The one with the largest average pore size is N4 with $1.06 \text{ }\mu\text{m}$ and with a standard deviation of $0.65 \text{ }\mu\text{m}$. It is reasonable to have N5 and N8 have smaller average pore sizes since they are from high amplitude regions or "good" regions of the tile. The results from N5 support this statement however this is not the case for N8.

Pore size distribution of each sample is given in Fig. 5.24. N5 and N8 have plots that end at roughly $4 \text{ }\mu\text{m}$ size while x-axis in plots of N4 and N9 extend to $6 \text{ }\mu\text{m}$. N1 possesses the largest sized features as the graph ends at $7 \text{ }\mu\text{m}$. This size difference between samples could provide partial explanation for the changes in ultrasound signals within the tile.

Curves were fitted as mentioned previously and FreundlichEXT function was used once more. R^2 values for all samples except N4 are 0.99. N4 has a R^2 value of 0.97, which still makes it a very good fit.

Size distributions were also plotted according to regions, given in Fig. 5.25. Region 2 has defects up to 4 μm in size while the curves for Region 1 and Region 3 extend right below 6 and 7 μm , respectively. The large-sized features could also be important in the ultrasound scans; therefore, this result is noteworthy.

5.3.2.2. Nearest Neighbor Distance Distributions

Nearest neighbor distances were calculated for all samples and no significant differences were observed among the plots given in Fig. 5.26. The largest peak for N1 reaches 150 at around 3 μm and the graph extends right above 12 μm . The values regarding the highest peak are very close to N1 for N4 and N12, while the plot goes up to a nearest neighbor distance value of 11 μm . The graph for N5 from the “good” region is not very different from the two previous plots. The largest peak reaches up to 150 at a value of around 2.5 μm . The largest nearest neighbor distance recorded is 11.4 μm for N5. The plot for N8 is narrower than the previous three plots, almost all nearest neighbor distance values are between 1 μm and 10 μm . The highest peak once again reaches 150. N9 has nearest neighbor distance values between up to 12 μm and the graph is very similar to N4.

As mentioned in the beginning, there is not a major difference among six samples. The only one that is outstanding is N8 has a plot narrower than the other five plots. Narrower nearest neighbor distance distribution graphs show more homogeneity in spatial defect distributions in the microstructure.

Fig. 5.27 looks at the distributions from the regional perspective, and probably due to the effect of N8, the graph for Region 2 shows a narrower distribution.

Q-V plots were obtained using the nearest neighbor distance data and it is given in Fig. 5.28. The data points fall very close to each other so it is hard to speculate on the spatial distribution differences between samples. The insignificant differences observed in distribution plots can be also seen here.

5.3.3. Low Magnification Results

Similar type of analysis was performed on the same samples. Optical microscopy was employed since low magnification of $100\times$ was sufficient in this part of the study and there was no need to go with scanning electron microscopy. The purpose of using lower magnification was to cover as much a larger area as possible in order to create more valid comparison with ultrasound.

The images are given in Fig. 5.29. Ten pictures from each sample were combined in the images in Fig. 5.29 and this makes the features in each image hard to spot. They are presented in this way in order to give an idea of the total area examined. It is roughly 0.5 mm^2 , which corresponds to almost half of the surface of the sample. This is a significantly larger area than the previous one at higher magnification; therefore, it might provide an insight that could have been missed in the previous examinations.

The average defect size is given in Fig. 5.30. Values are very close each other as they vary between $4.46 \text{ }\mu\text{m}$ and $4.63 \text{ }\mu\text{m}$. The one with the smallest average defect size is N12, which is from the “bad” region. However, in the order from the one with the smallest defect size to the largest one, the next two samples are N5 and N8, which are

from the “good” region. The number of defects, density calculated by image analysis, average defect size, standard deviation of defect size and the maximum defect size is all given in Table 5.4.

Defect size distributions are given Fig. 5.31. The R^2 values are all above 0.91, which signifies a very good fit. Another observation from the plots is the largest sized features found in each sample. This is also shown in Table 5.4. The largest sized features that N4, N5 and N9 possess are all in the between 20-30 μm , while that value increases gradually, reaching up to 63 μm for N1.

5.3.3.1. Nearest Neighbor Distance Distributions

Nearest neighbor distance distributions are shown in Fig. 5.32, where, broadness of the curves is important for evaluation. According to the plots and the standard deviation values, N8 shows the narrowest distribution with a standard deviation value of 12.88 μm . Although the maximum value is 136 μm , the data point decreases suddenly below 80 μm mark, while the others demonstrate nearest neighbor distance distribution values above 80 μm mark.

Q-V map, given in Fig. 5.33, shows some interesting results. The average data points for three out of six samples fall into the region of “clustering in a random background”. The samples from “good” region and N4 fall in the confidence interval of a “random” distribution. These results could be very significant in terms of explaining the differences observed in an ultrasound C-scan map. Clustering of defects could be a noteworthy factor among other possible reasons for variations.

5.3.3.2. Locating Defect Clusters

The deviations from “random” distribution have been emphasized up to this point. One further step is to actually locate these clusters. This component of the study is important since it provides the opportunity to visualize the problematic regions and further studies can be built upon this.

In order to find clusters on images, the concept of *limiting interevent distance (R)* must be established. This is the radius of a cluster which contains all the features, or events, inside a circle. All the features outside this circle of radius R , is not a part of the cluster. An illustration of the interevent distance is shown in the pictures in Fig. 5.34.

The value of R must be determined carefully in order to obtain a reasonable representation of clustering and non-clustered regions in an image. Anson and Gruzlefski [111] suggest two methods of determining the value of R . The first one is performed qualitatively, where, R is varied and the efficiency of the grouping is examined visually according to the value of R . The other technique is quantitative, where; different values are assigned to R , from zero to very large values, until all the features in the image will be a part of one cluster. If R is plotted against the number of clusters, a plateau will be observed. R value that corresponds to the start of the plateau could be accepted as the optimum R value.

The quantitative method was applied to one of the images from N9, which is given in Fig. 5.35. This sample has some degree of clustering according to the Q-V map; therefore, these clusters could be identified. Initially, the image was processed and the final form can be seen in Fig. 5.36. Then, using Image Processing Toolkit 5.0, R value was varied from zero to 100. In Fig. 5.37, the blue curve shows the number of clusters as R changes while the green curve demonstrates the number of features in clusters. The

plateau that was mentioned above can be observed between the values of 20 μm to 30 μm . Therefore, 20 μm can be accepted as the limiting interevent distance, R , according to the spatial distribution of features in this image. Fig. 5.38 shows the clusters in red, omitting the other features in the binary image that have nearest neighbor distance values above 20 μm . All defects can be seen in Fig. 5.39, where clustered defects are shown in red again. Finally, clusters are demonstrated in the original image in Fig. 5.40.

This section of the study is important since the clusters can be identified in the images. This will provide more insight in the subsequent tests, such as hardness or dynamic tests since knowing the actual location of clusters help determine the effect of them on the overall performance.

5.3.4. Serial Sectioning of Hexoloy SA Tile

In order to have more valid comparison between ultrasound and microscopy, serial sectioning was performed. Four other layers were examined in addition to the layer, results of which were presented.

The density plot from all five layers is given in Fig. 5.41. There is no clear trend as the variation between values for each sample and region is fairly high. For example, N8 seems to have the highest density value at the 4th and 5th layers while it has the second lowest density at the 1st layer. These fluctuations are observed for all samples, therefore no correlation was observed qualitatively between layers.

Since there are six different samples and five different layers from each one, it is hard to recognize trends in the plot, if any. Therefore, in order to check if there is a difference in terms of density between “good” and “bad” regions, t-tests were employed.

T-tests assess whether the means of two groups are statistically different from each other. The results are given in Table 5.5 and 5.6. P values obtained from this test are compared with α value, which represent the %95 confidence interval. In both cases where Region 2 was compared with Region 1 and Region 3 separately, P values came out to higher than α . This shows that there is not a significant difference statistically between “good” and “bad” regions in terms of density.

Fig. 5.42 shows average defect size values from all five layers. On the first look, all samples seem to have relatively close values and high standard deviation values are observed. 4th layer in N8 has the smallest average defect size of $3.87 \pm 1.87 \mu\text{m}$ among all samples while the average size value of 3rd layer in N8 is $4.49 \pm 2.05 \mu\text{m}$, which ranks among the highest values among all samples. This example summarizes the variation observed between samples. T-tests were also employed in order to reveal difference, if any. Once again, the samples were not statistically different from each other in terms of average defect size values. The t-test results are given in Table 5.7 and 5.8.

After examining the average defect size, the next parameter was the largest defect size observed in each layer. The plot is given in Fig. 5.43. Unlike the previous two graphs, this difference between samples and layers is more distinct, even qualitatively. Samples from “good” region clearly have lower values than the ones from “bad” regions. Especially N5 have consistency over five layers in terms of this parameter. In order to verify these observations; t-tests were performed once again. The results from t-tests are given in Table 5.9 and Table 5.10. P value of the one-tail distribution for the t-test between Region 1 and Region 2 is 0.021, which is smaller than α value of 0.05. This shows that the difference between Region 1 and Region 2 is statistically significant. Same

type of information is obtained in the comparison between Region 2 and Region 3. P value of the one-tail distribution is 0.042, which is smaller than α value of 0.05 once again.

The observations summarized above are relevant to the ultrasound results since any type of distinction between high amplitude and low amplitude regions is valuable. These small differences most likely contribute to the dissimilar amplitude regions observed in C-scan maps.

5.3.4.1. Nearest Neighbor Distance Distributions

In addition to the examination regarding the size of defects, their spatial distribution was studied. The plots for the five layers are given in Fig. 5.44. The first observation is that the locations of all the points are very close to each other. This is reasonable due to the fact that all samples come from a tile, which is actually an armor grade material. As a results of this, it would be logical not expect a huge difference between samples.

From all the Q-V plots shown, one common observation is that N5 and N8 fall in “random” area while some of the points fall into “clustering over random background” regions for samples from “bad” regions. Another remark could be made about the distance of the points to the random point of (1,1). It is important to mention once again that the samples can be ranked according to their location in the Q-V plot. When this parameter is also taken into account, N5 and N8 are closer to the random point in most layers, if not all, as opposed to the samples from “bad” regions that fall into “random” region of the plots.

These results show us the clustering effect present in the low amplitude regions of amplitude maps. The significance of this statement comes from the fact that cluster of defects could be misinterpreted by the transducer, depending on the maximum resolution, and therefore could come out as one large pore. Therefore, the presence of clusters could possibly cause signal loss.

In Fig. 45, Q-V graphs are plotted for each sample, showing the change in the spatial distribution of defects in each layer. The spatial distribution of defects could vary from the surface to the inside; therefore, it is worth looking at this aspect.

N1 does not show any significant pattern from the 1st layer to the 5th layer. The three layers in between the first and fifth fall into the random region while first and fifth layer values fall into the random with clusters regions.

N4 shows a different pattern from N1 where the first two layers are in random region, then the next three are in random with clusters region. According to this result, the spatial distribution of defects changes from the surface to the inner parts of a tile. This could be attributed to the more rapid pore elimination near the surface.

In the plots of N5 and N8 from the good regions, a subtle trend can be observed. The first two layers for both samples are closer to the total random case. The following three layers have data points further away from the total random case, although the difference is not very significant.

N9 shows a reverse trend observed for N4. In this case, the first two layers show random distribution with clusters while in the next three layers, the data points fall into the random regions. N12 does not show any pattern among the five layers.

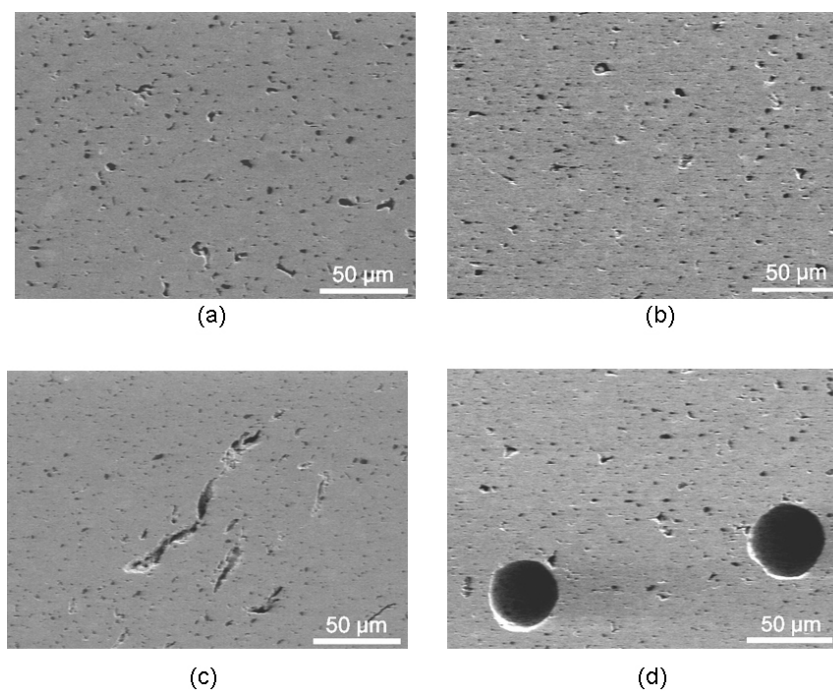


Figure 5.1. Micrographs of (a) SA-1 (b) SA-2 (c) EXT (d) SP

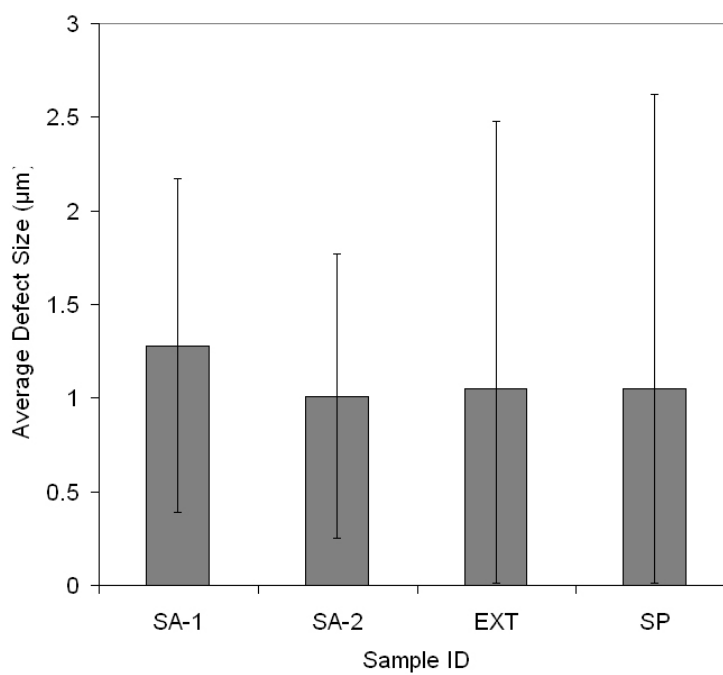
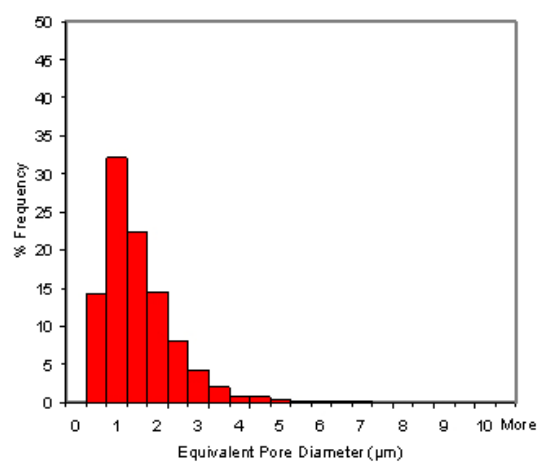
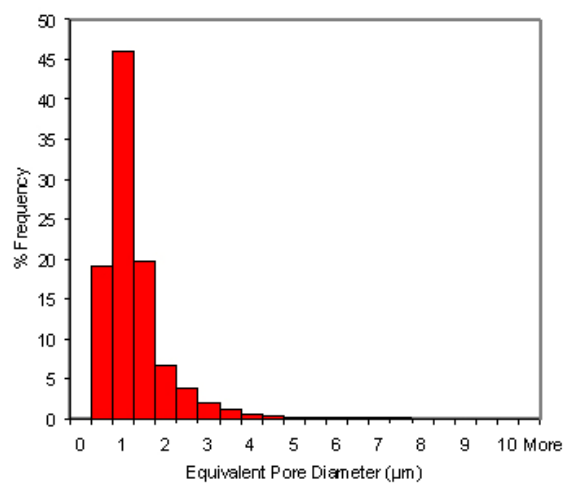


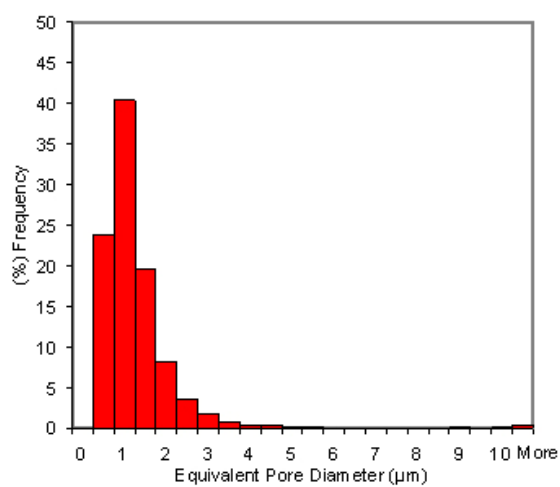
Figure 5.2. Average defect size for all samples



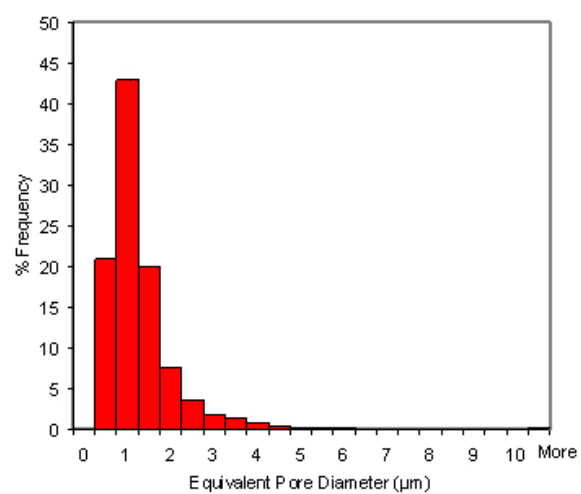
(a)



(b)



(c)



(d)

Figure 5.3. Pore size distribution (a) SA-1 (b) SA-2 (c) EXT (d) SP

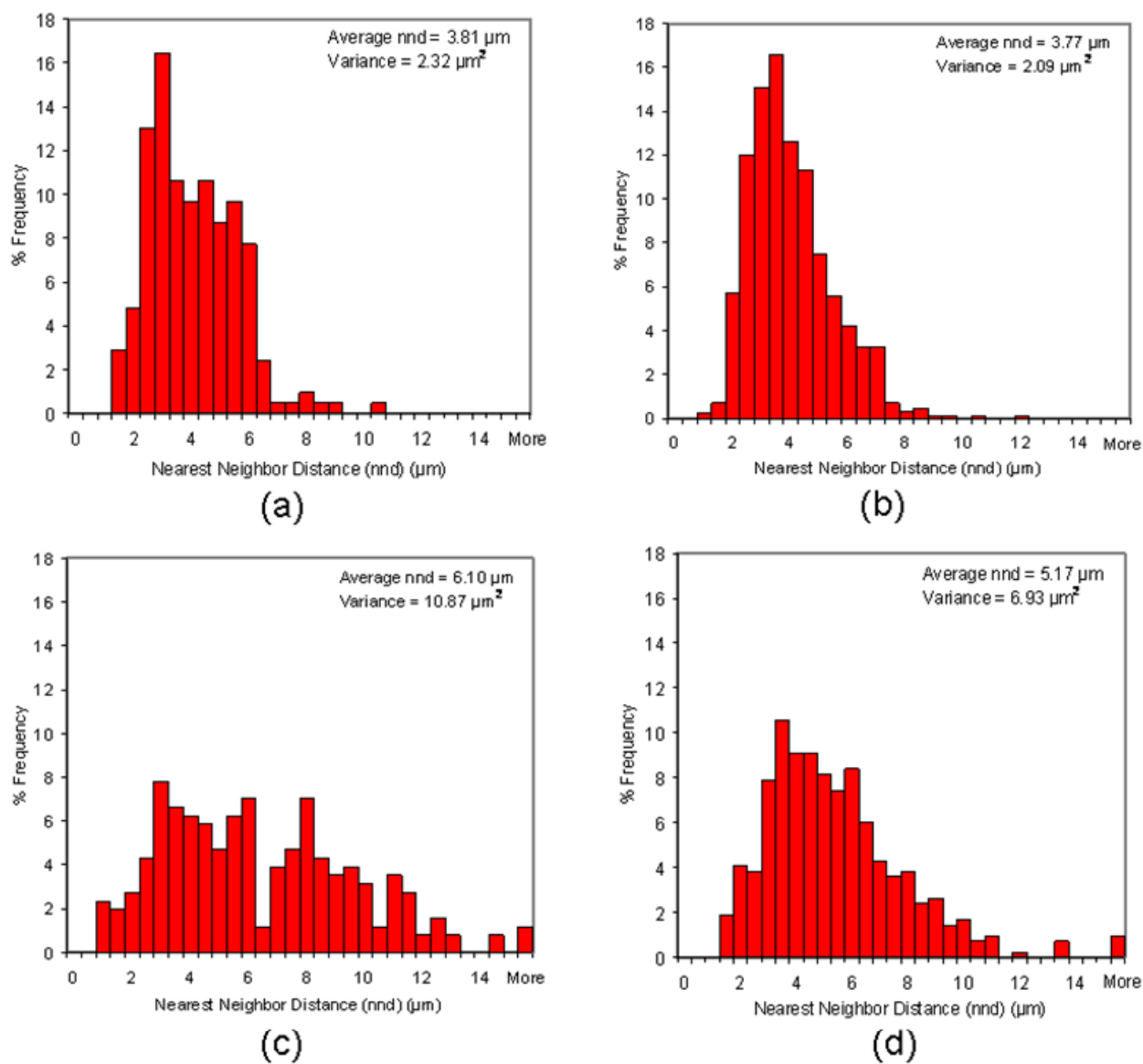


Figure 5.4. NND distribution of (a) SA-1 (b) SA-2 (c) EXT (d) SP

Table 5.1. Q and V values of off-density sintered SiC samples

	MEAN NND (μ)	VARIANCE NND	MEAN NND (RANDOM)	VARIANCE NND (RANDOM)	Q	V
SA-1	7.550	9.029	6.542	2.423	1.154	3.726
SA-2	3.769	2.103	3.262	1.208	1.155	1.174
EXT	6.093	10.798	5.753	2.131	1.059	5.068
SP	5.167	6.971	4.674	1.731	1.104	4.027

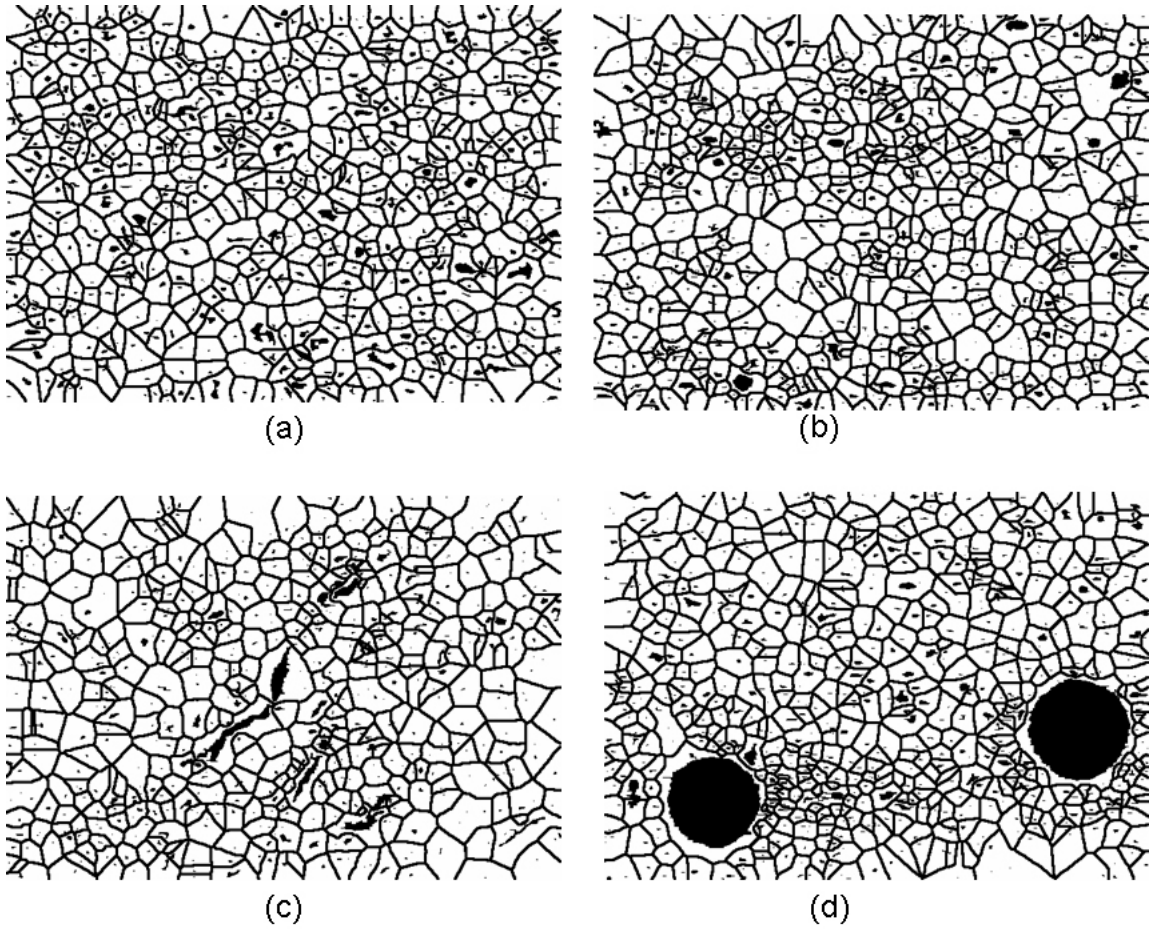


Figure 5.5. Tessellated microstructures of (a) SA-1 (b) SA-2 (c) EXT (d) SP

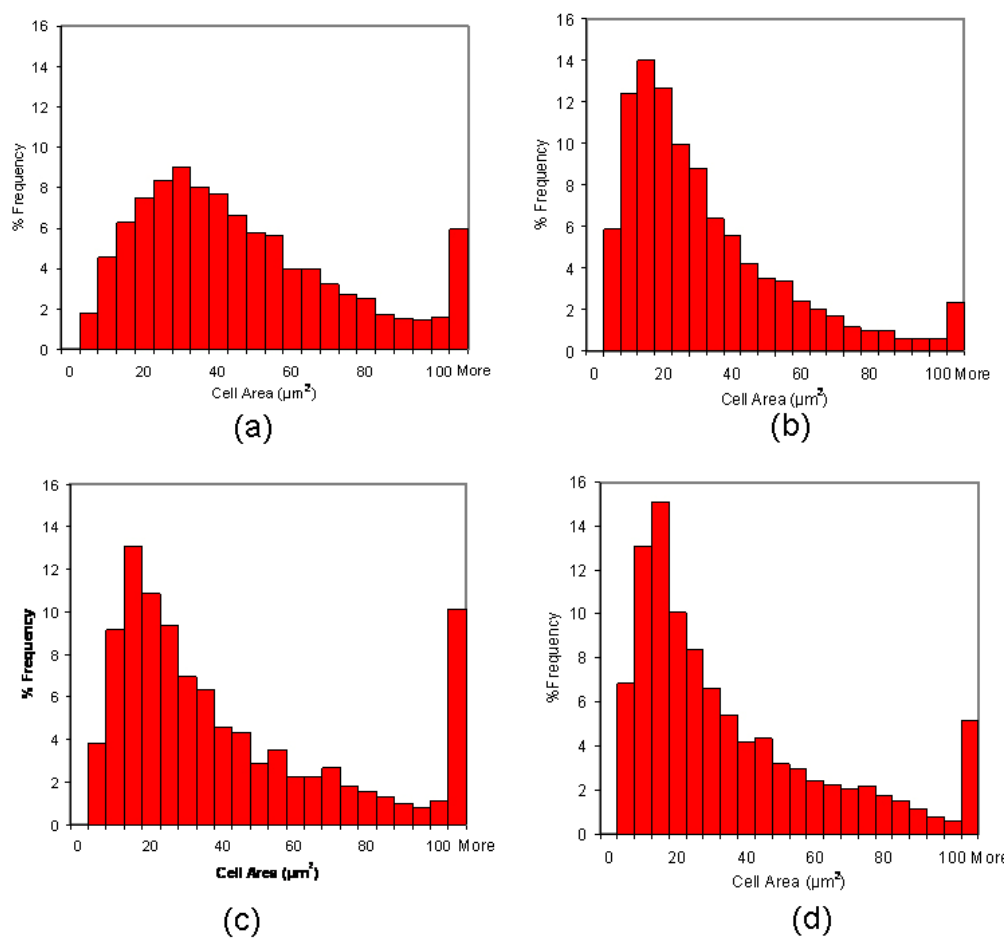


Figure 5.6. Cell area distributions of (a) SA-1 (b) SA-2 (c) EXT (d) SP

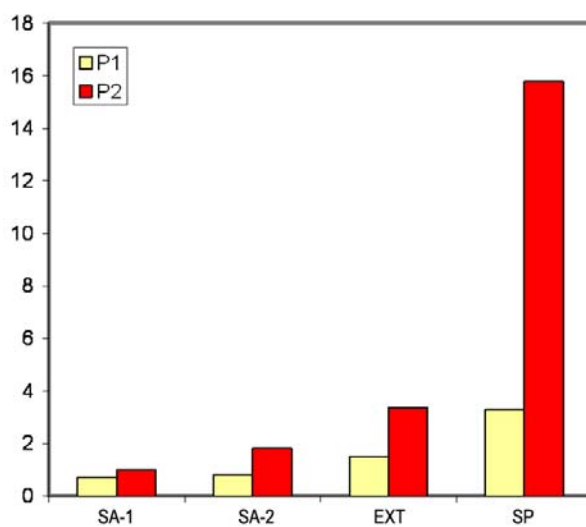
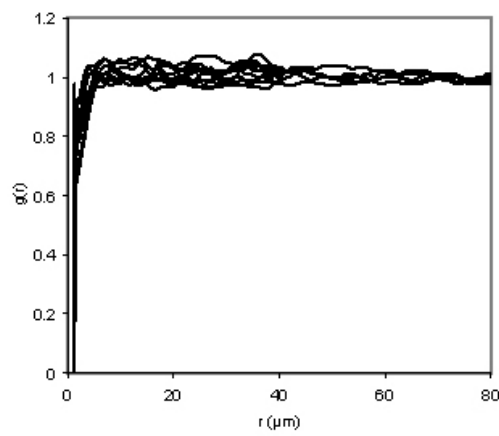


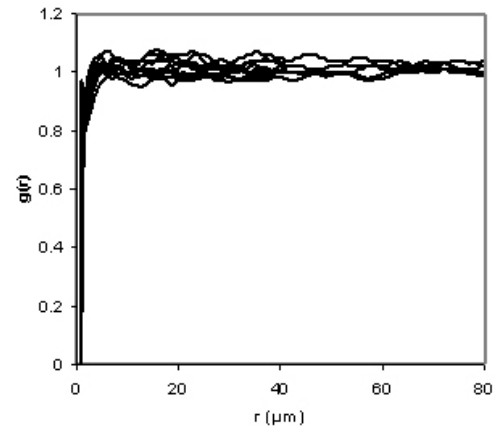
Figure 5.7. P_1 and P_2 for all four samples

Table 5.2. P_1 and P_2 values of off-density sintered SiC samples

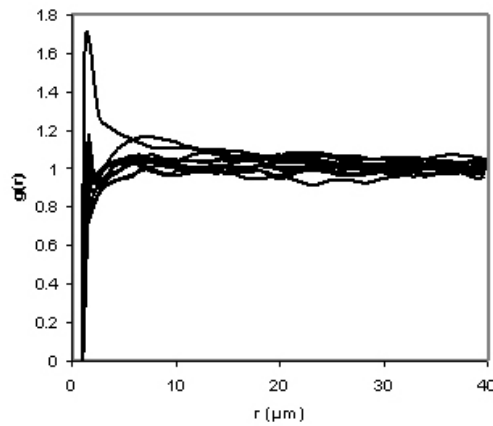
	Variance	Variance (random)	Skewness	Skewness (random)	P_1	P_2
SA-1	1011.5	1416.7	1.702	1.704	0.71	0.99
SA-2	669.3	820.2	2.28	1.27	0.82	1.80
EXT	2809.3	1855.5	4.55	1.36	1.51	3.35
SP	5443.8	1660.6	19.79	1.25	3.28	15.78



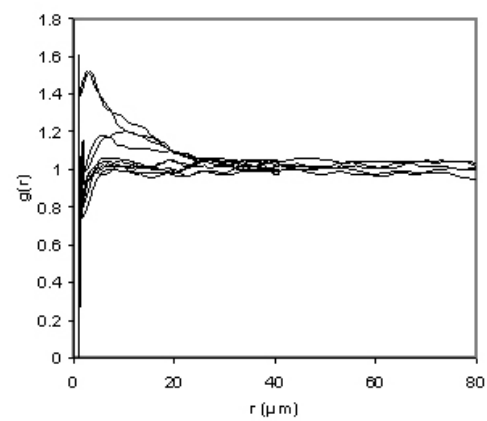
(a)



(b)

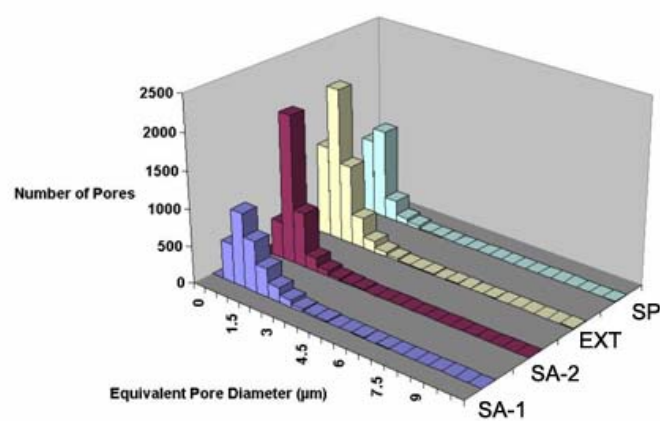


(c)

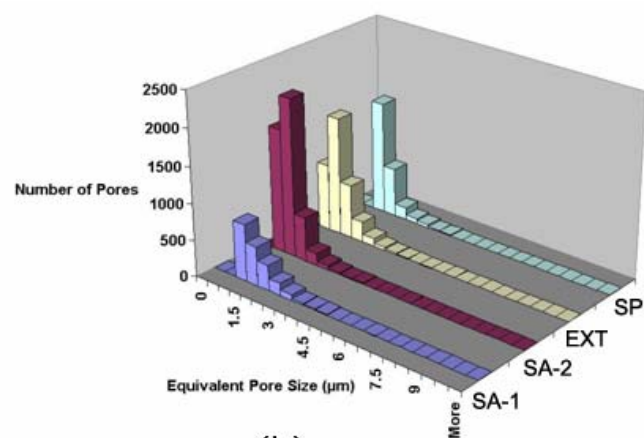


(d)

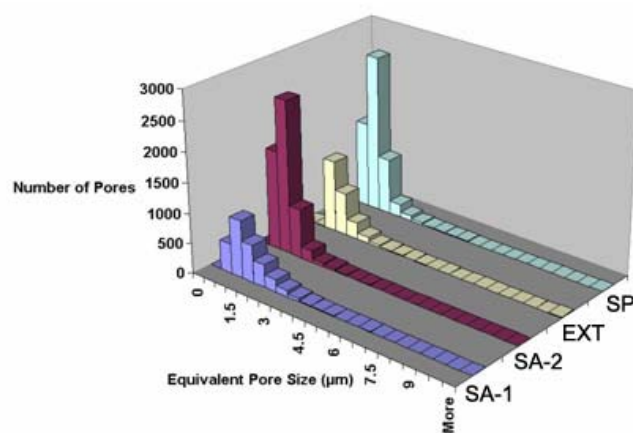
Figure 5.8. Pair correlation function plots of (a) SA-1 (b) SA-2 (c) EXT (d) SP



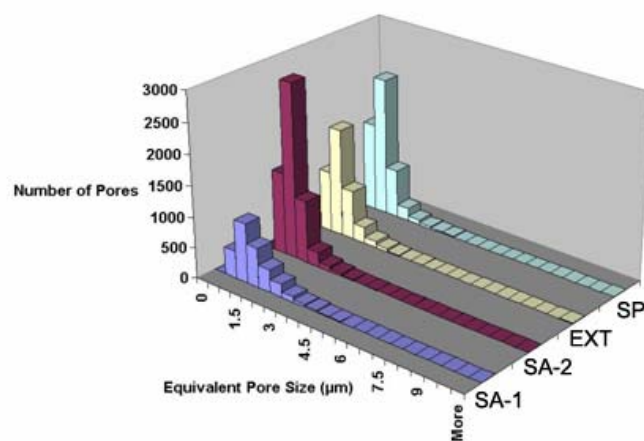
(a)



(b)



(c)



(d)

Figure 5.9. Pore size distributions from (a) 1st layer (b) 2nd layer (c) 3rd layer (d) 4th layer

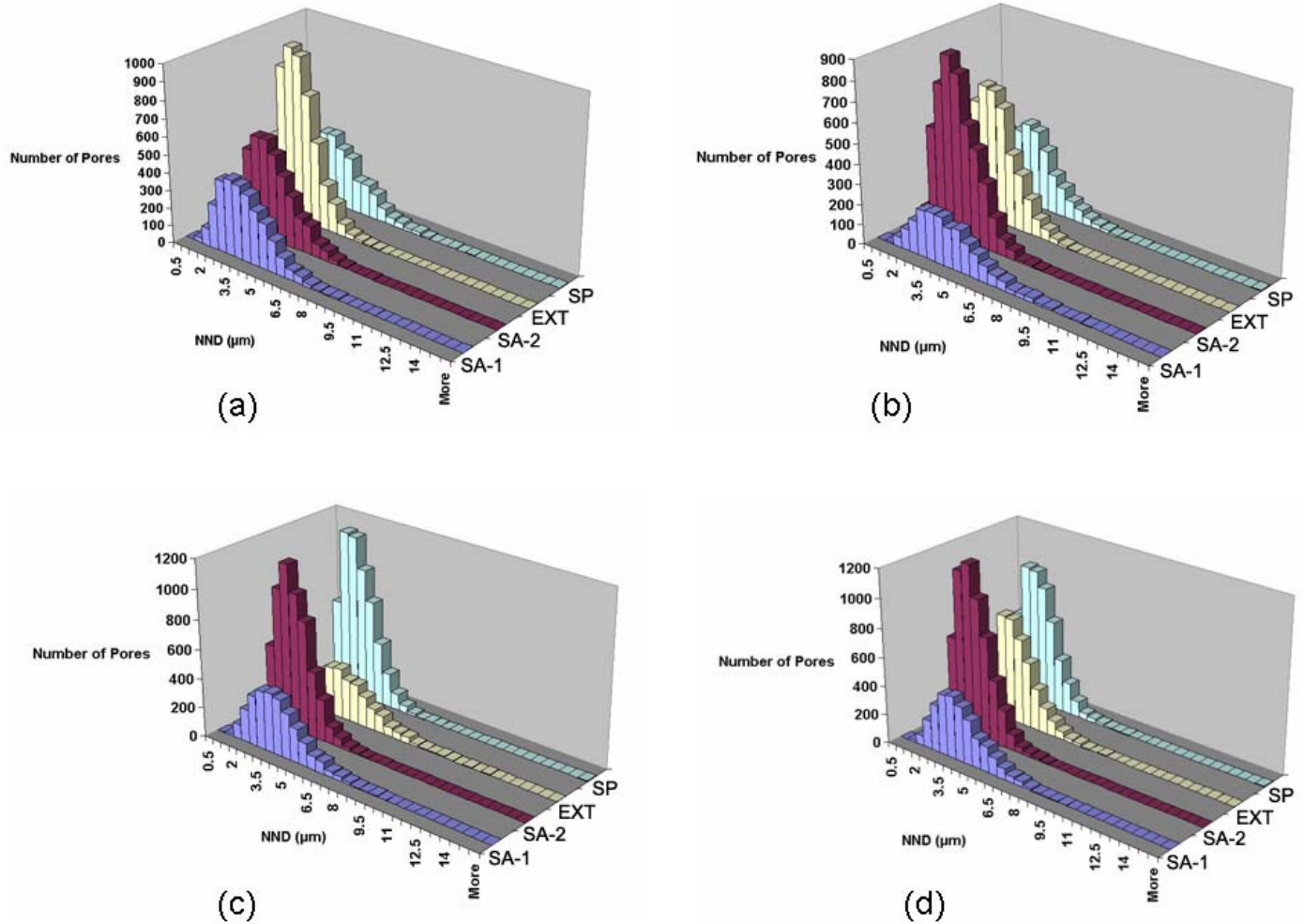


Figure 5.10. Nearest neighbor distance distribution from for (a) 1st layer (b) 2nd layer (c) 3rd layer (d) 4th layer

Table 5.3. Q and V results from each layer

	1 st layer		2 nd layer		3 rd layer		4 th layer	
	Q	V	Q	V	Q	V	Q	V
A	1.175604	3.337682	1.143111	4.488916	1.19307	3.636714	1.192785	3.414291
B	1.118401	3.190134	1.139574	2.6975	1.1657	2.348868	1.168456	2.29572
C	1.223332	2.586455	1.173615	2.675832	1.161939	4.024303	1.334786	2.795571
D	1.08343	4.308038	1.130662	3.926532	1.167692	2.727393	1.26739	3.041789

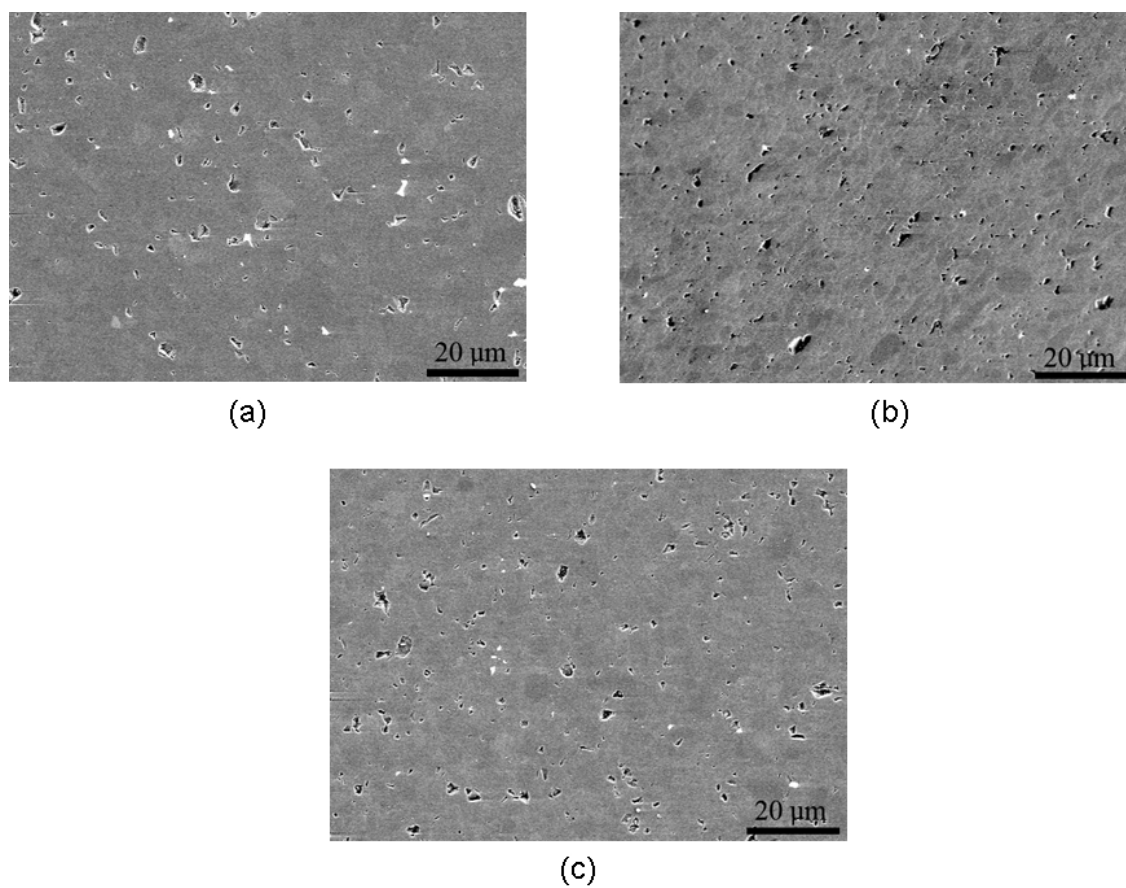


Figure 5.11. Micrographs of (a) LD (b) DEF (c) AG

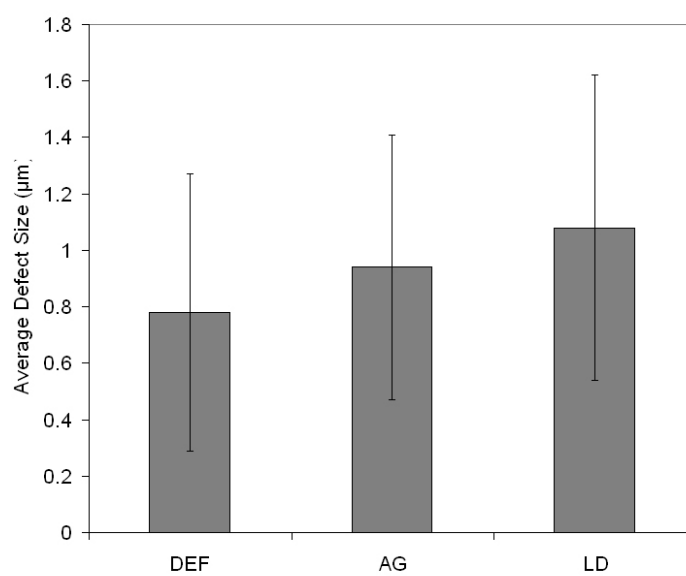


Figure 5.12. Average defect size for all three hot-pressed samples

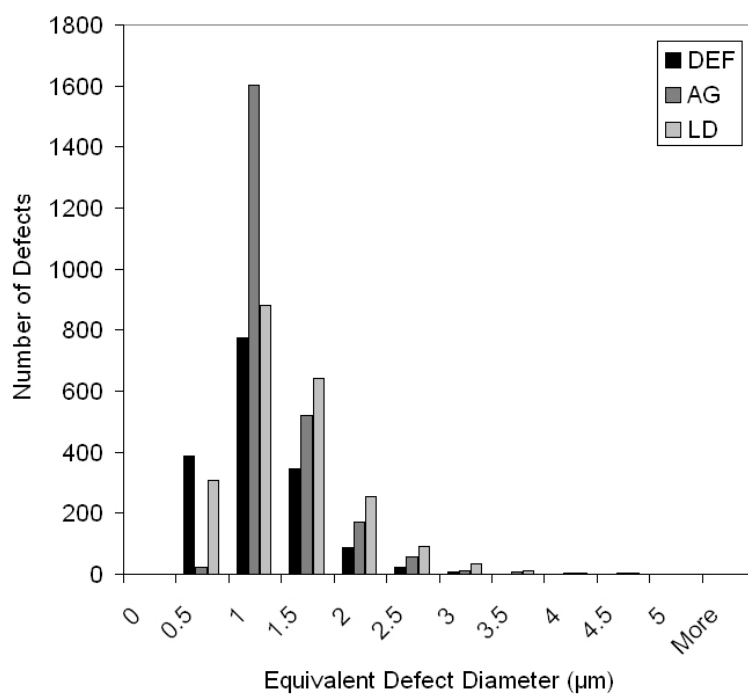


Figure 5.13. Defect size distribution of all three hot-pressed samples

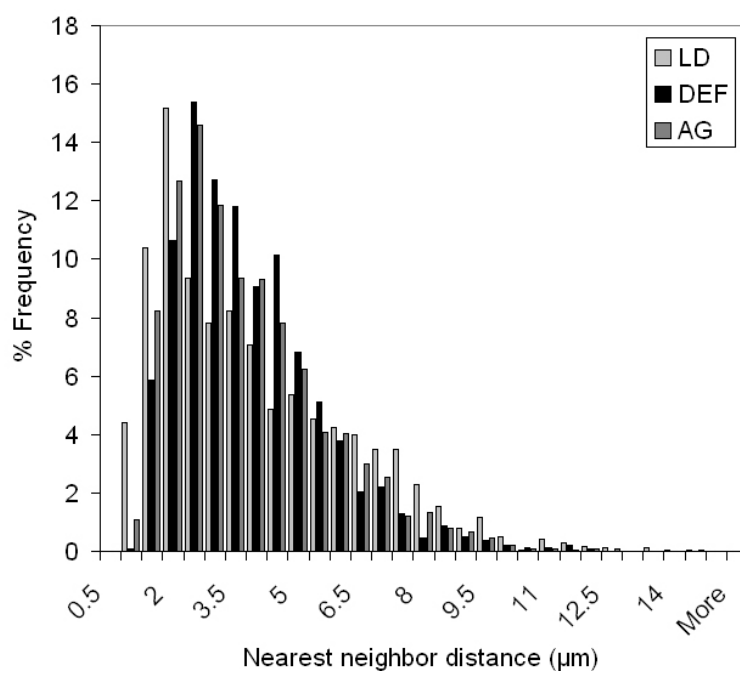


Figure 5.14. Nearest neighbor distance distributions of all three hot-pressed samples

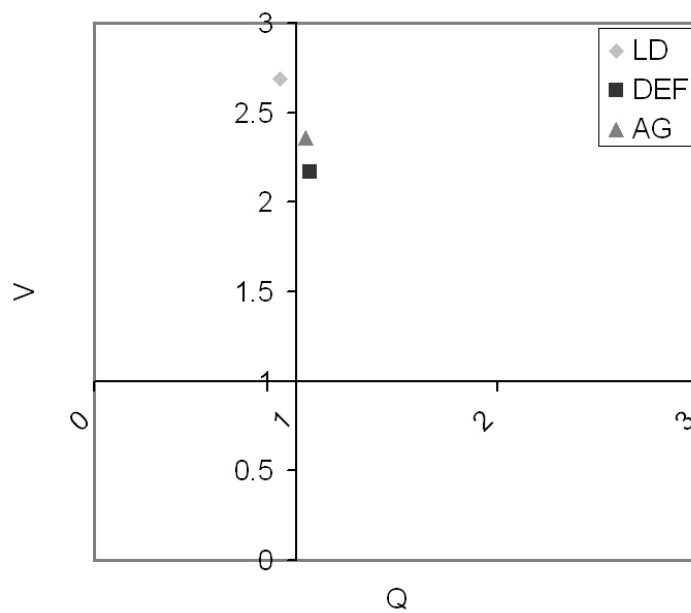
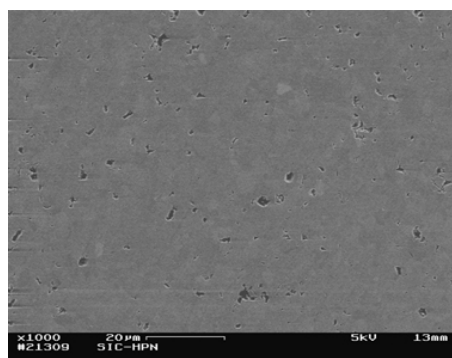
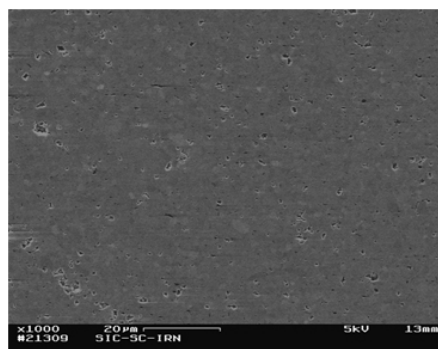


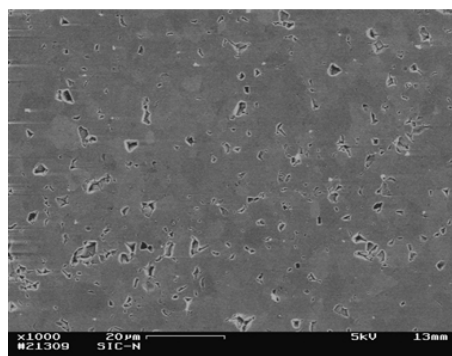
Figure 5.15. Q-V plot of all three hot-pressed samples



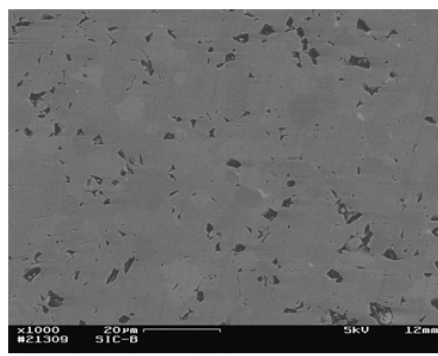
(a)



(b)



(c)



(d)

Figure 5.16. Micrographs of (a)SiC-HPN (b)SiC-SC-1RN (c)SiC-N (d)SiC-B

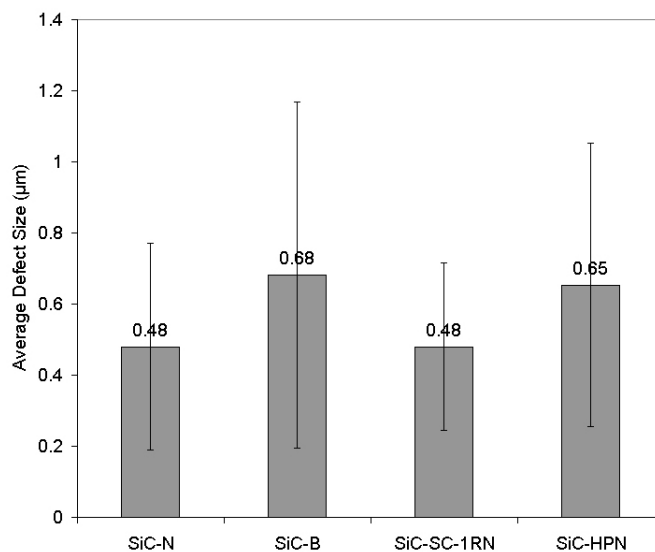


Figure 5.17. Average defect size of Lundberg samples

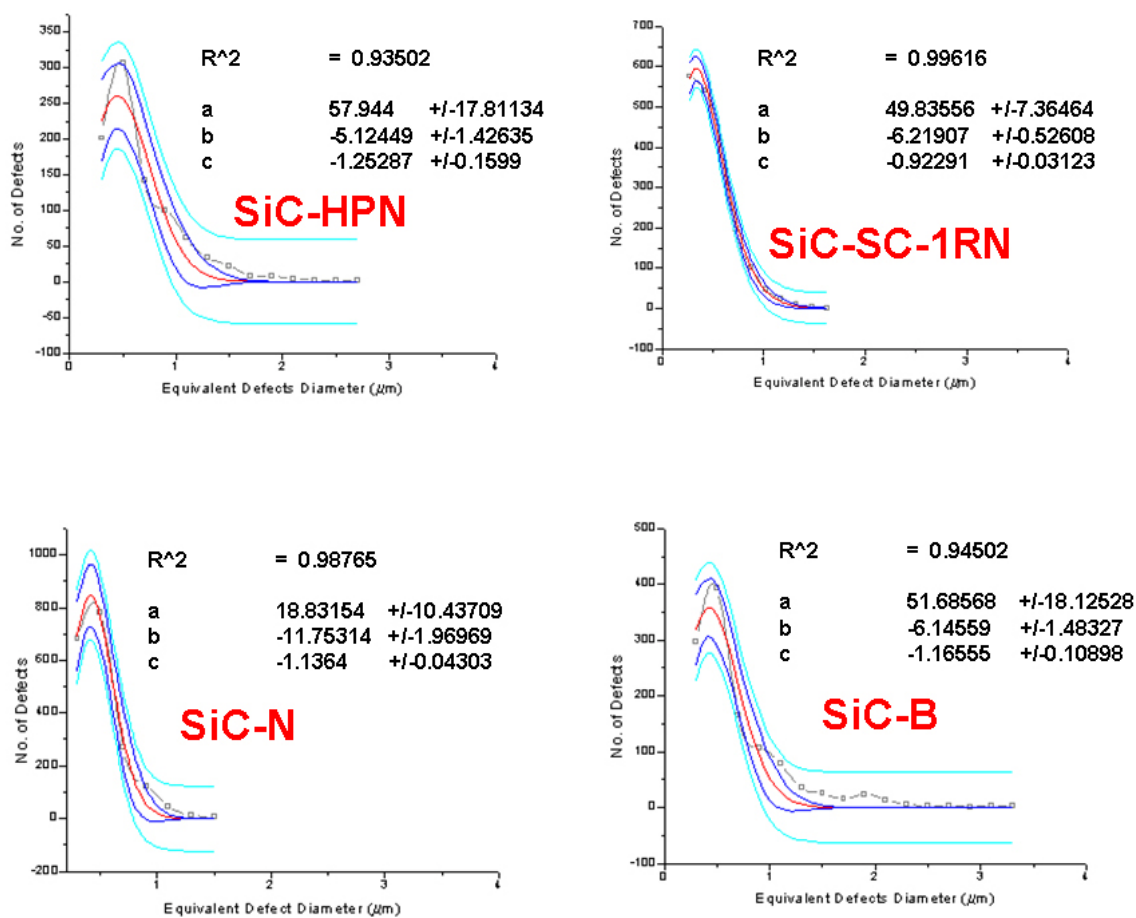


Figure 5.18. Pore size distribution of Lundberg samples

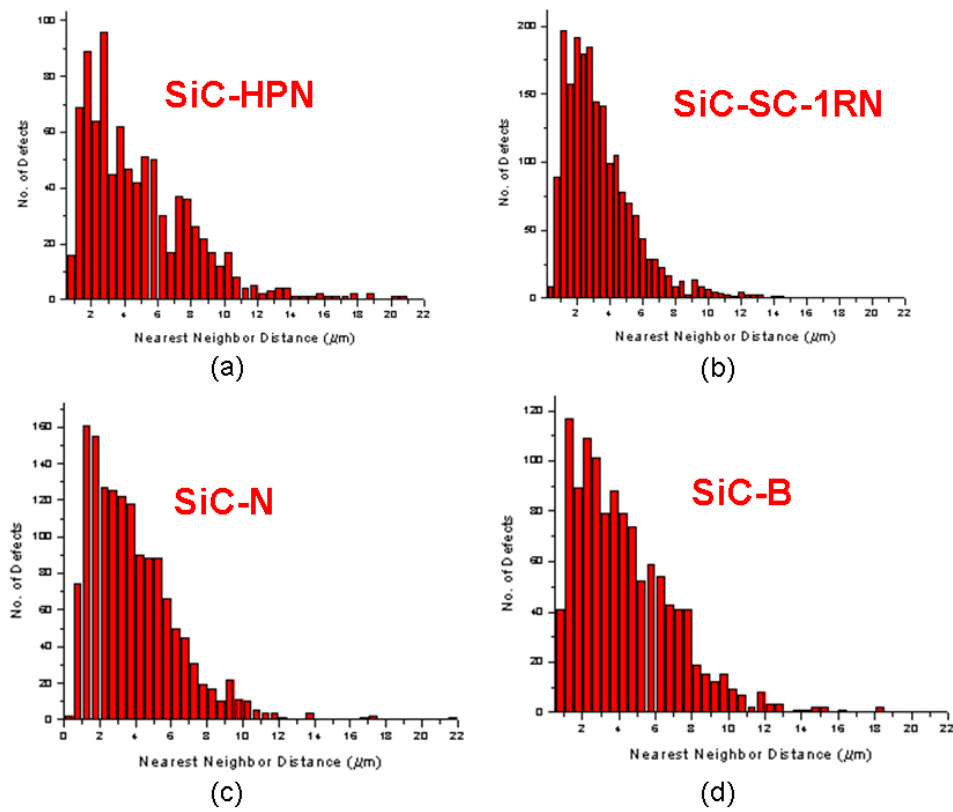


Figure 5.19. Nearest neighbor distance distribution of (a)SiC-HPN (b)SiC-SC-1RN (c)SiC-N (d)SiC-B

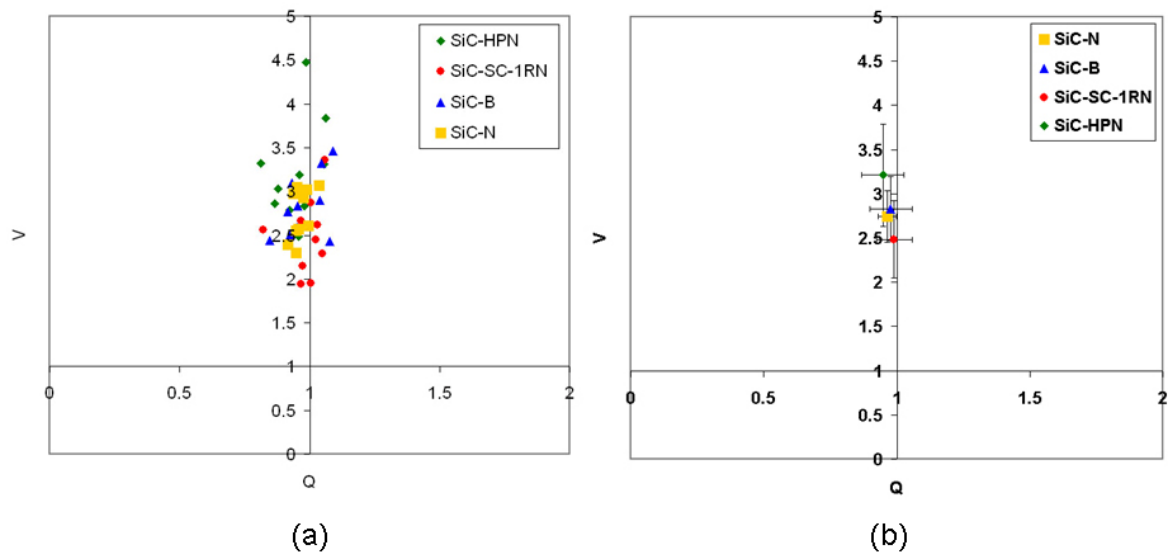


Figure 5.20. Q-V map showing (a) each individual point (b) all points combined

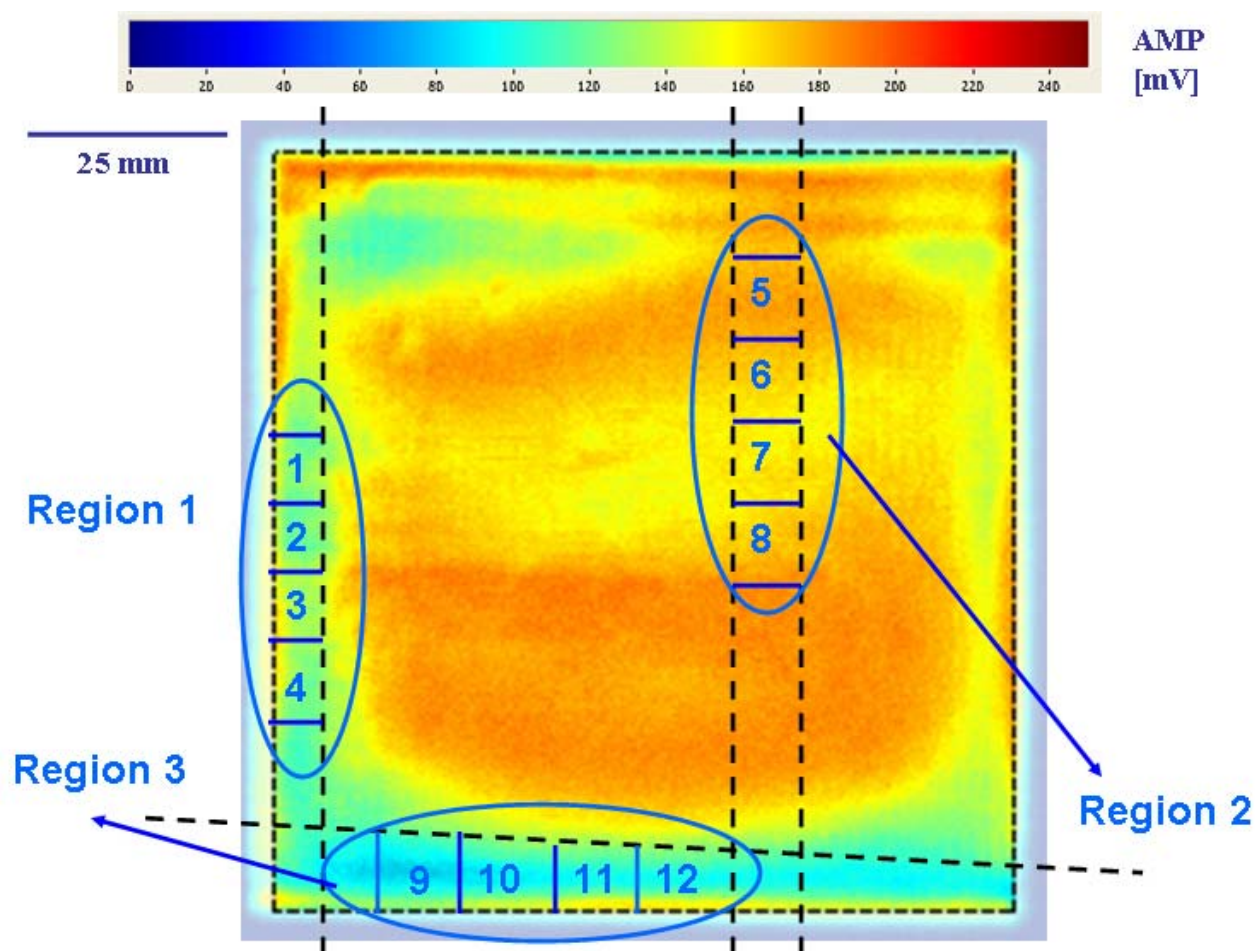


Figure 5.21. C-scan image by ultrasound of Hexoloy SA3

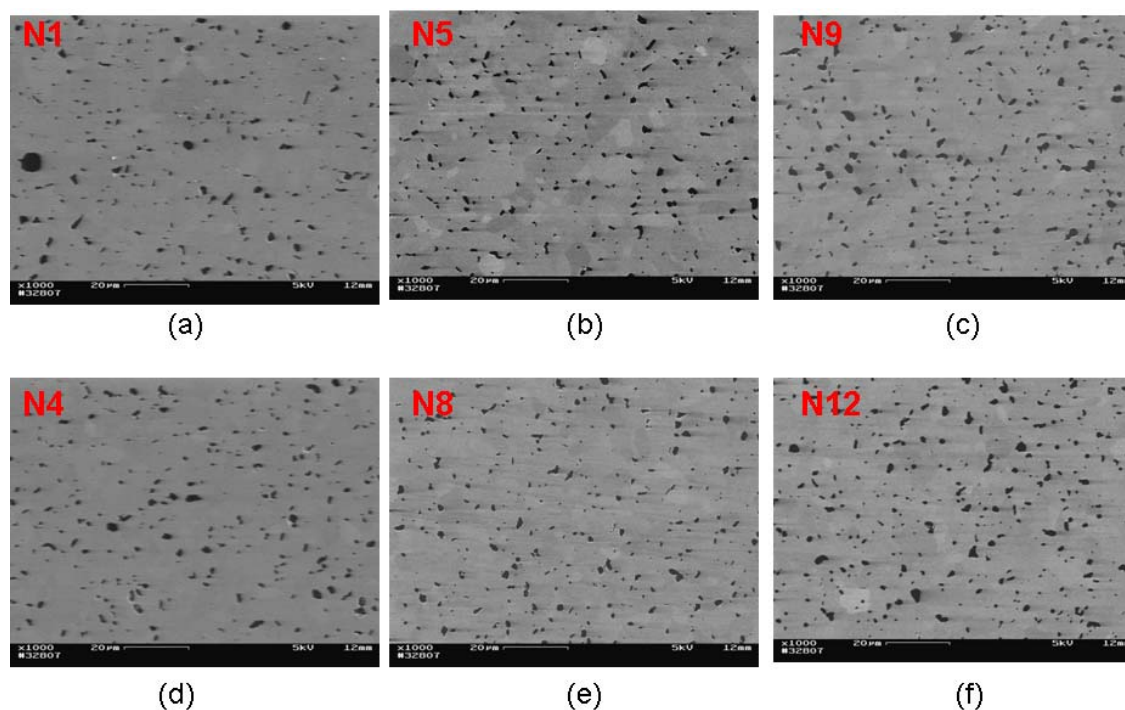


Figure 5.22. Representative micrographs of (a) N1 (b) N4 (c) N5 (d) N8 (e) N9 (f) N12

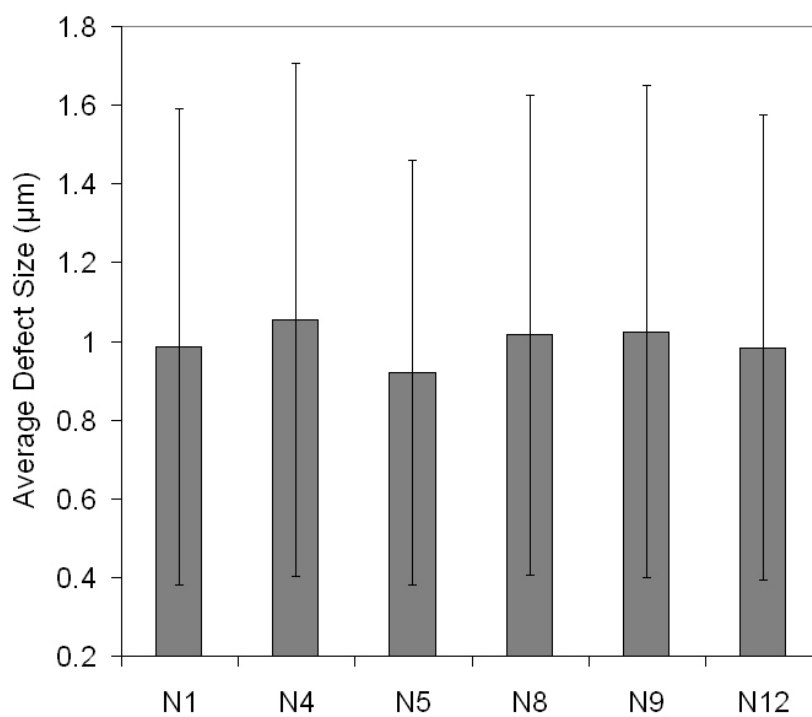


Figure 5.23. Average defect size of each sample

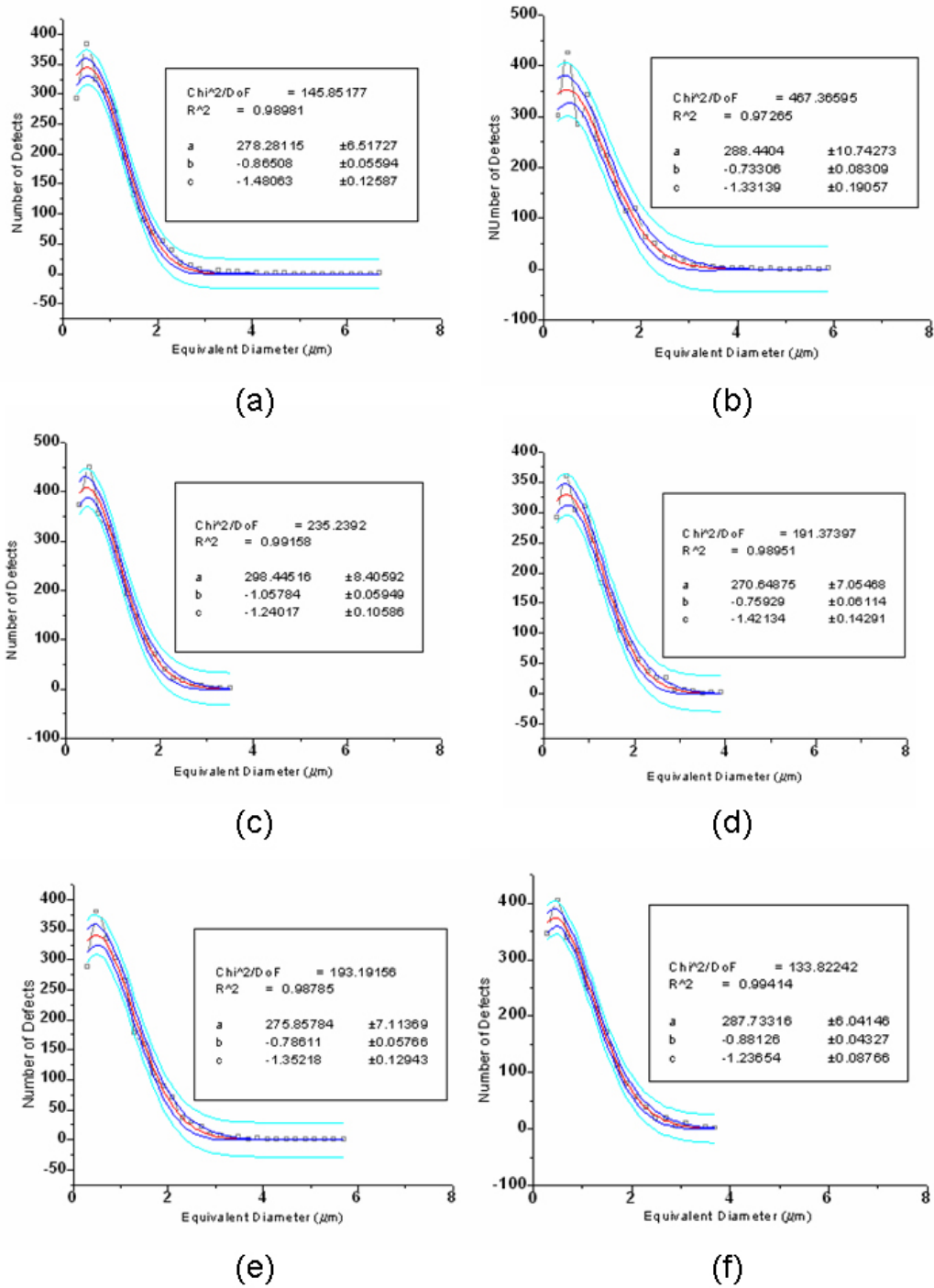
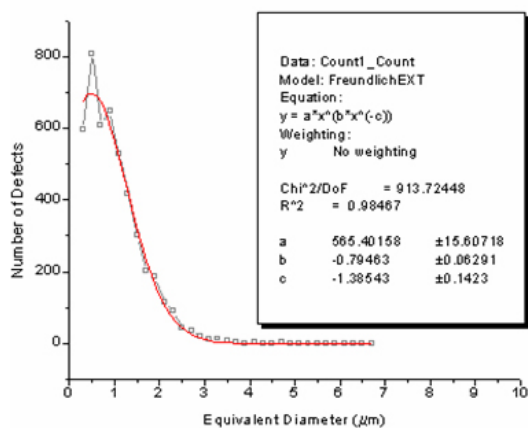
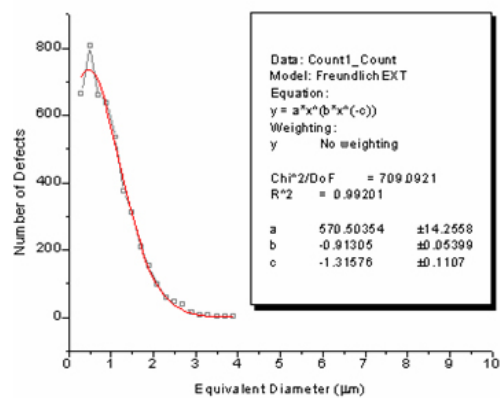


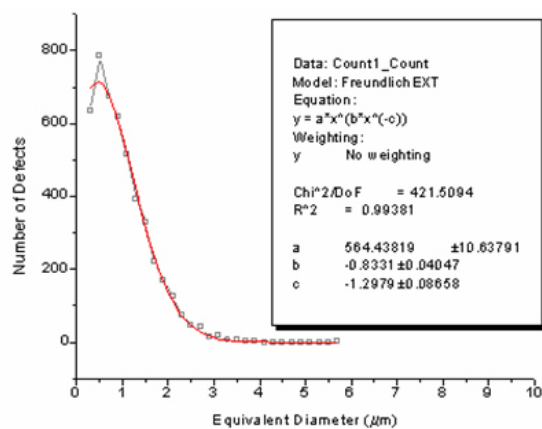
Figure 5.24. Defect size distribution of (a) N1 (b) N4 (c) N5 (d) N8 (e) N9 (f) N12



(a)



(b)



(c)

Figure 5.25. Defect size distribution of (a) Region 1 (b) Region 2 (c) Region 3

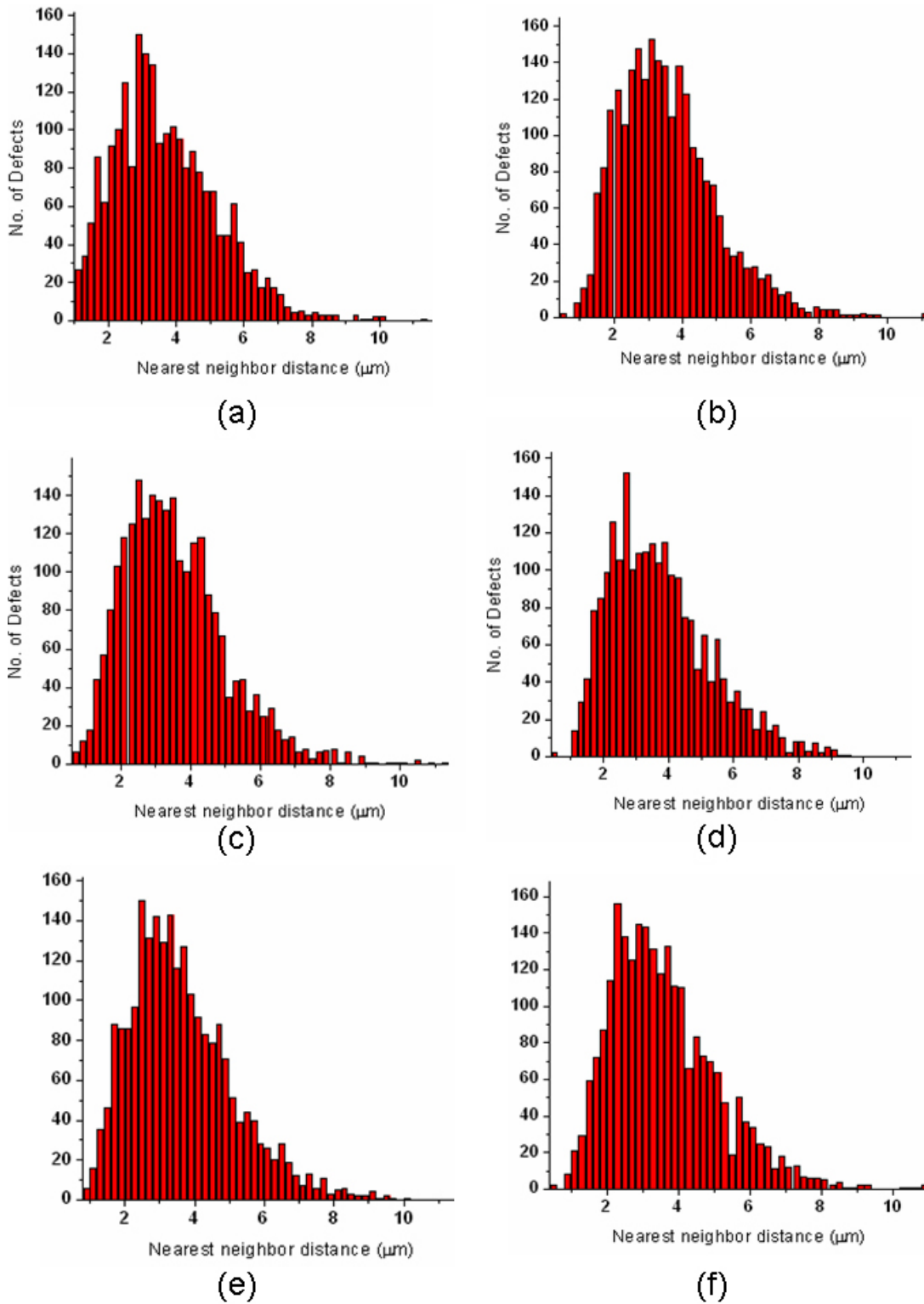


Figure 5.26. Nearest neighbor distance distributions of (a) N1 (b) N4 (c) N5 (d) N8 (e) N9 (f) N12

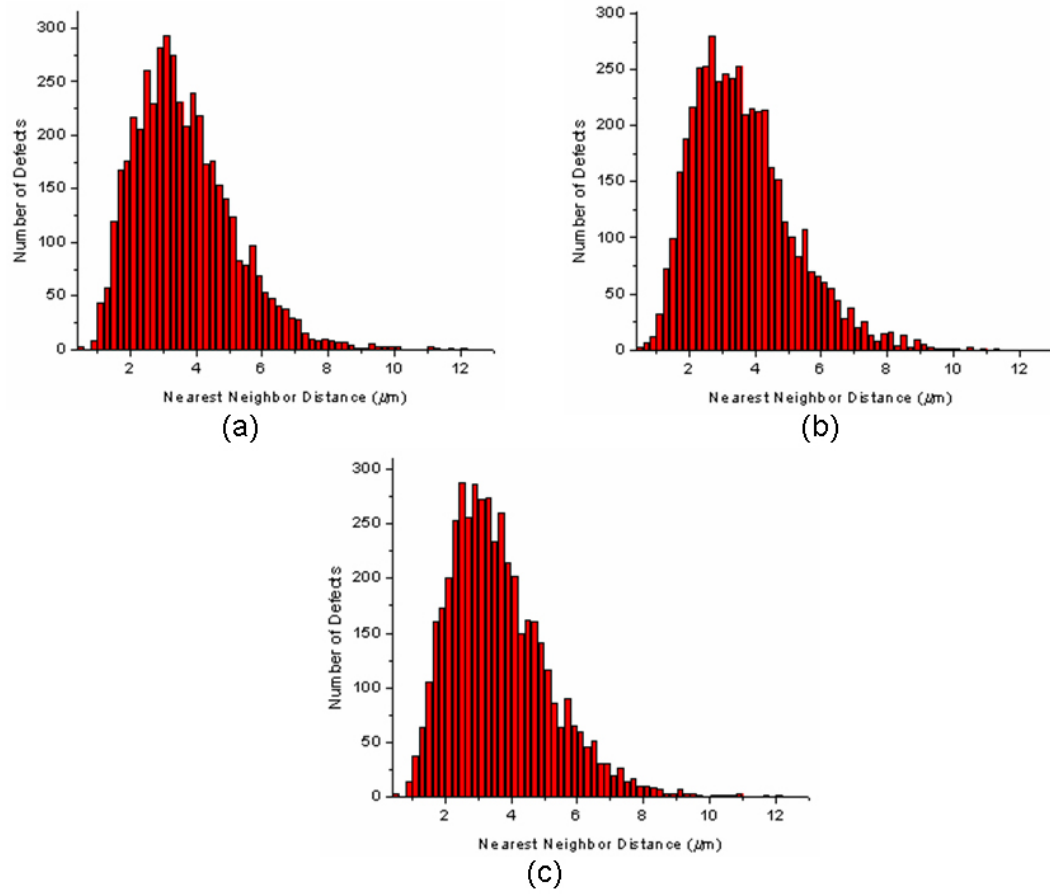


Figure 5.27. Nearest neighbor distance distributions of each region

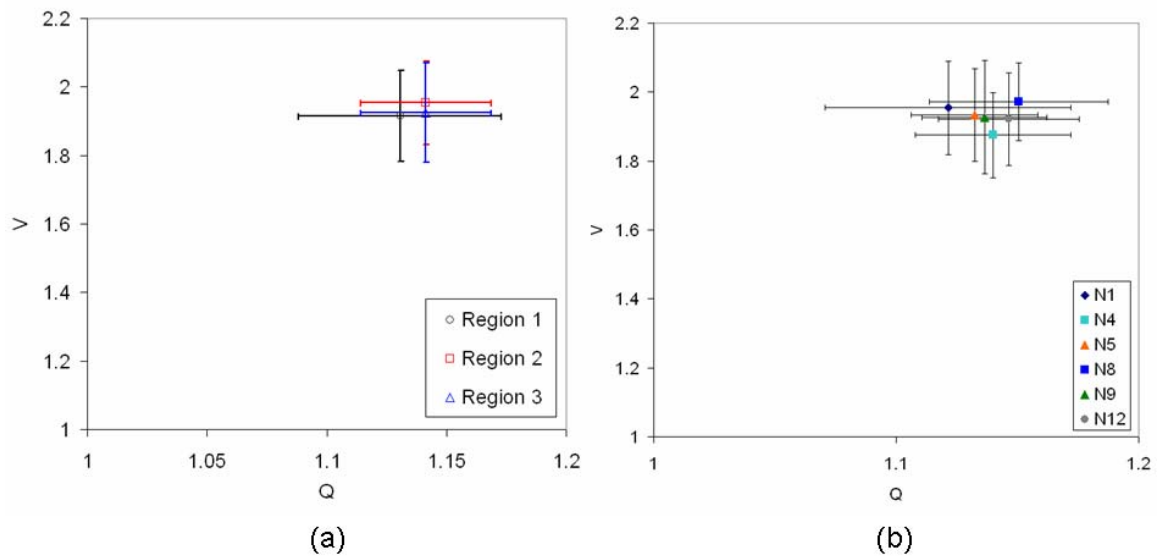


Figure 5.28. Q-V plots based on (a) region (b) sample

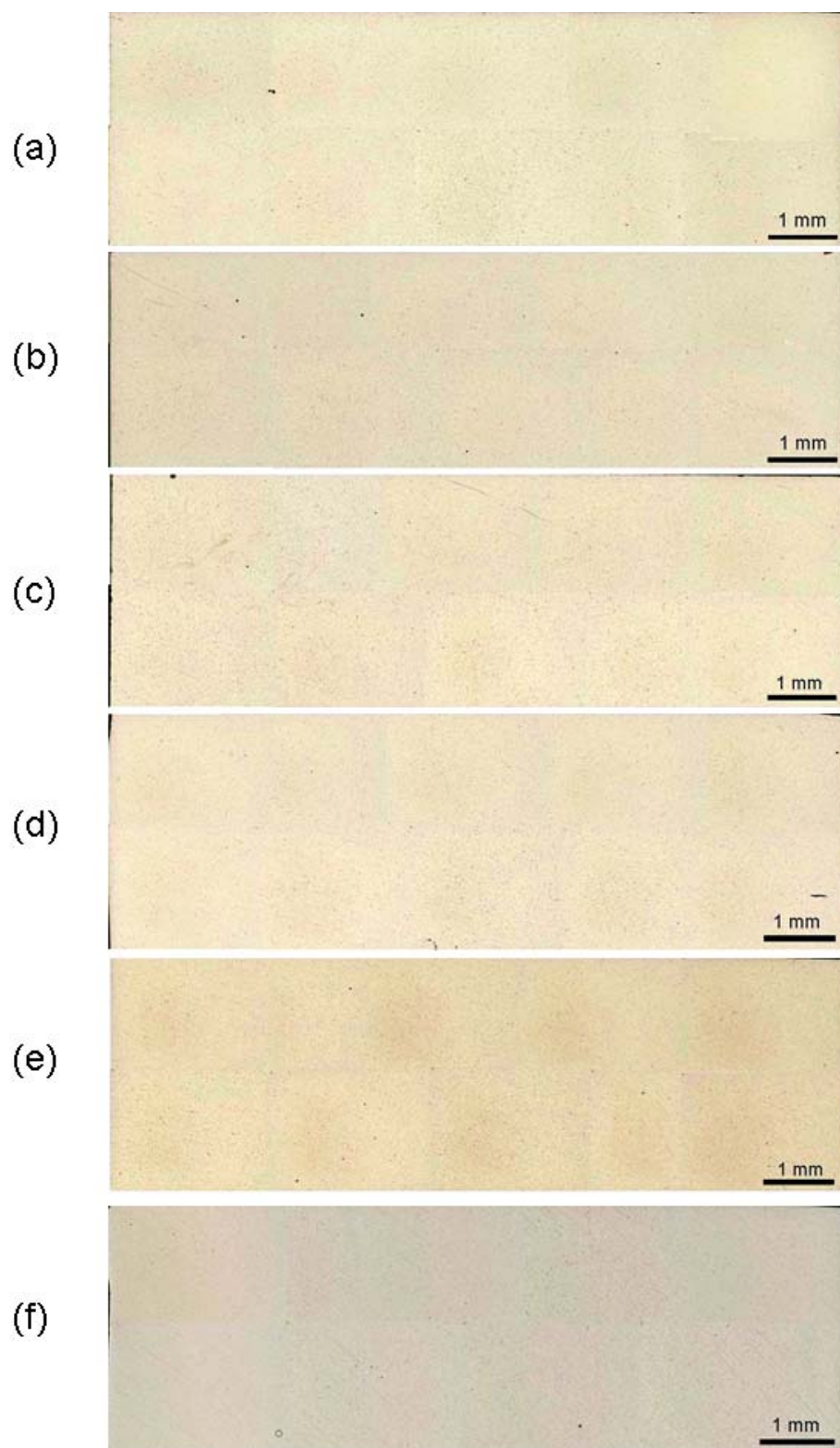


Figure 5.29. Low magnification images of (a) N1 (b) N4 (c) N5 (d) N8 (e) N9 (f) N12

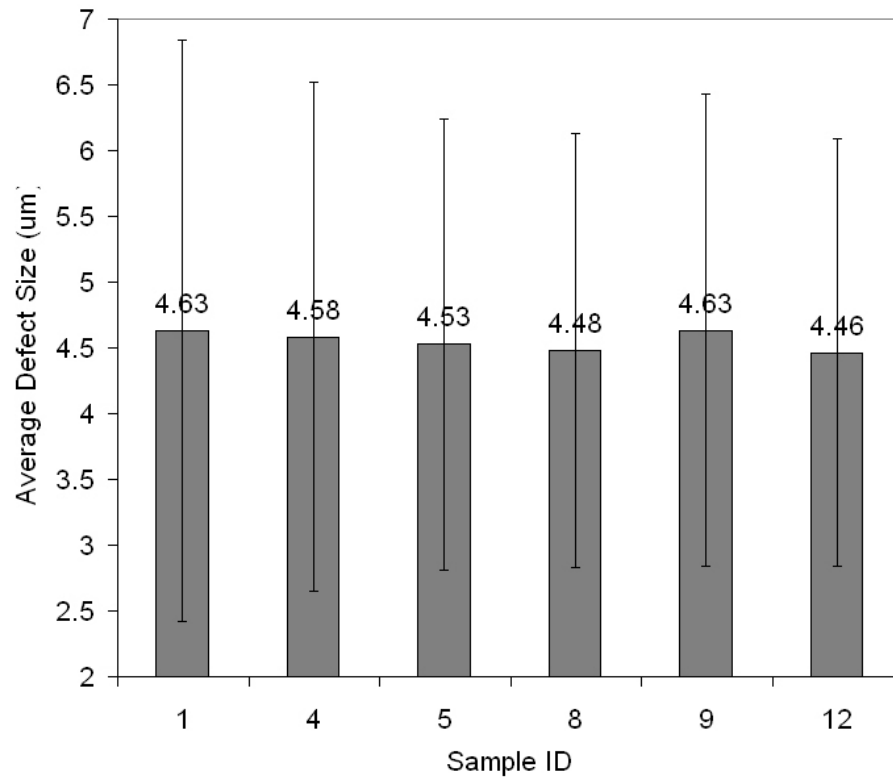


Figure 5.30. Average defect size of all examined samples

Table 5.4. Image analysis results from all examined samples

	N1	N4	N5	N8	N9	N12
No. of defects	14754	14455	15452	16445	14615	15359
Density (gr/cm³)	3.185	3.187	3.187	3.187	3.188	3.188
Ave. Def. Size (μm)	4.63	4.58	4.52	4.47	4.63	4.46
Std. Dev.	2.20	1.93	1.71	1.65	1.79	1.62
Max. Def. Size (μm)	63.10	35.58	25.54	21.95	27.76	38.41

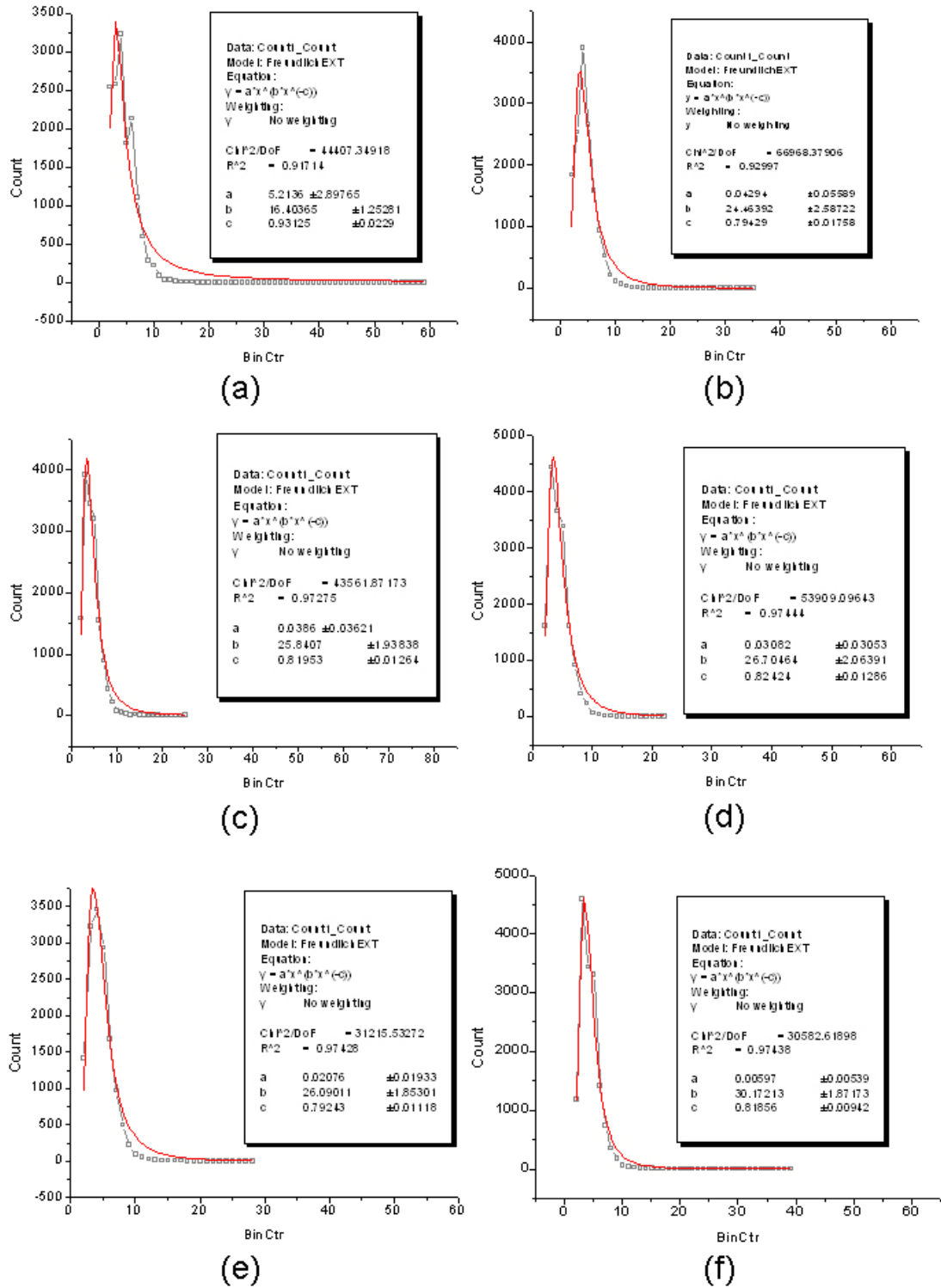


Figure 5.31. Defect size distributions of (a) N1 (b) N4 (c) N5 (d) N8 (e) N9 (f) N12

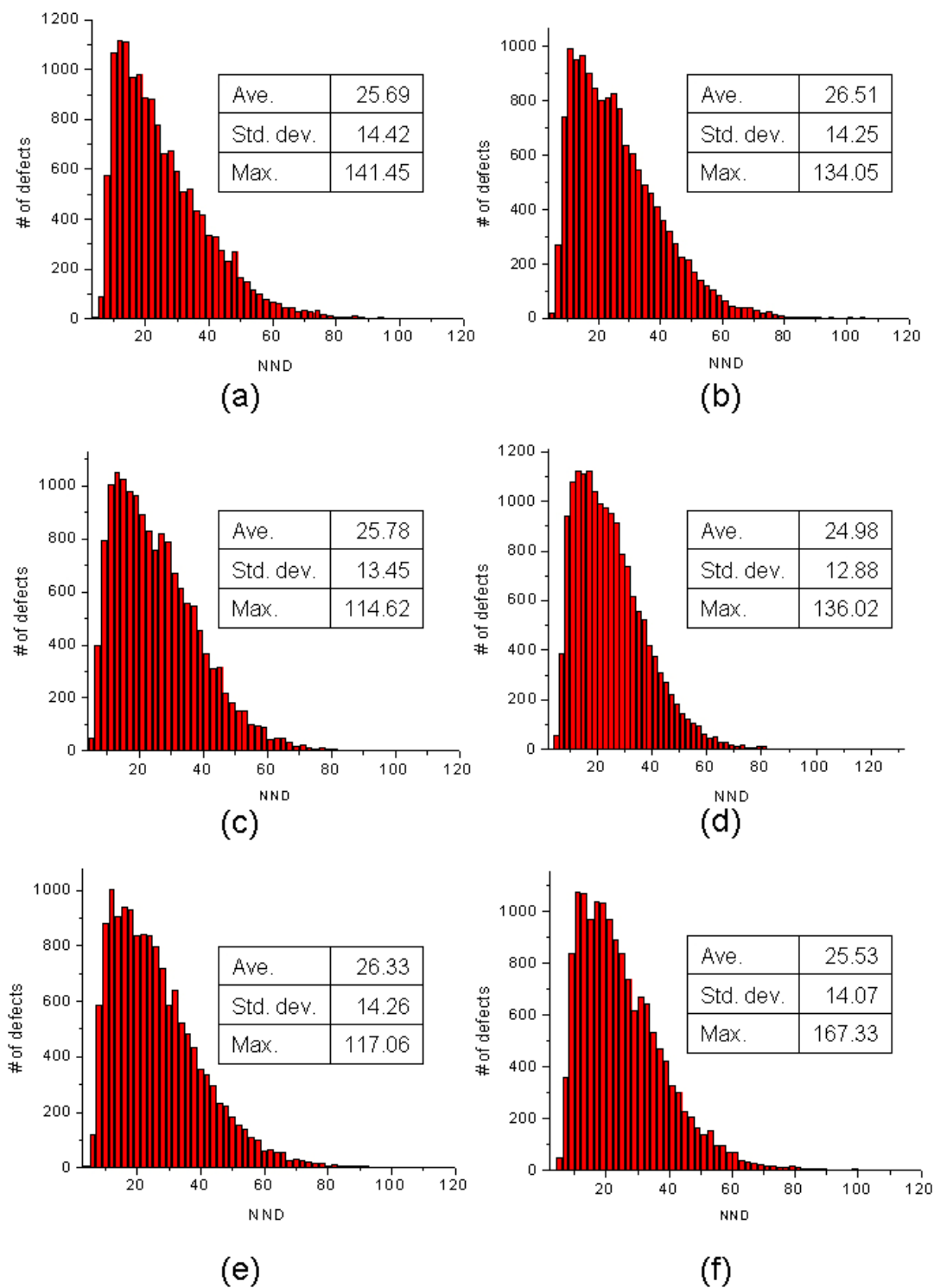


Figure 5.32. Nearest neighbor distance distributions of (a) N1 (b) N4 (c) N5 (d) N8 (e) N9 (f) N12

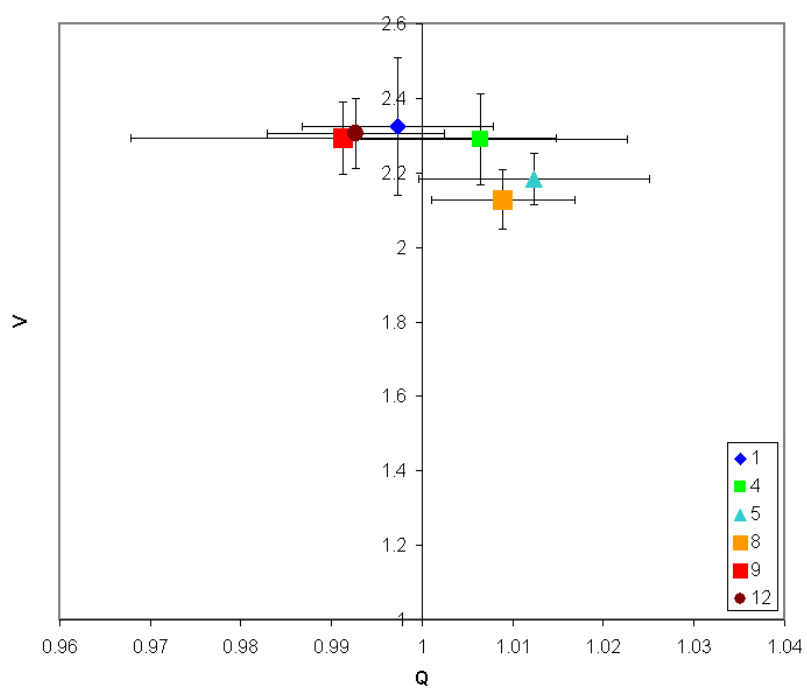


Figure 5.33. Q-V plot according to the low magnification images

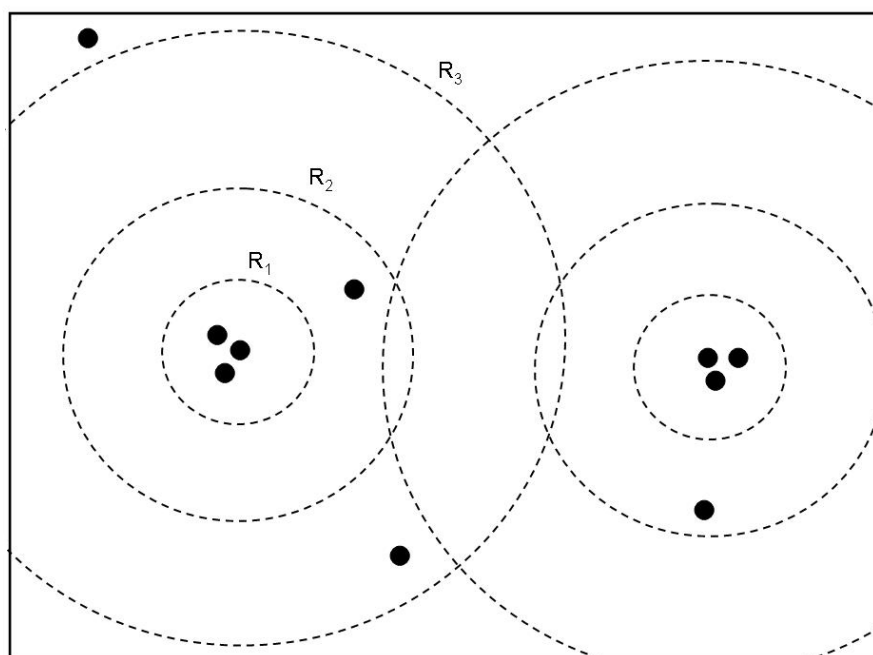


Figure 5.34. An illustration of the interevent distance



Figure 5.35. One of the ten images from N9

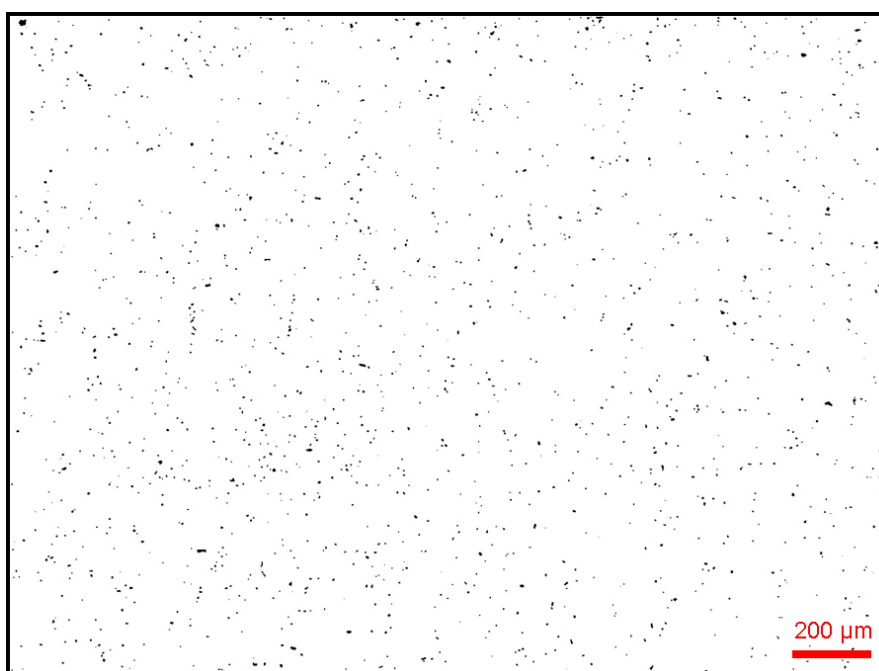


Figure 5.36. Binary image of N9

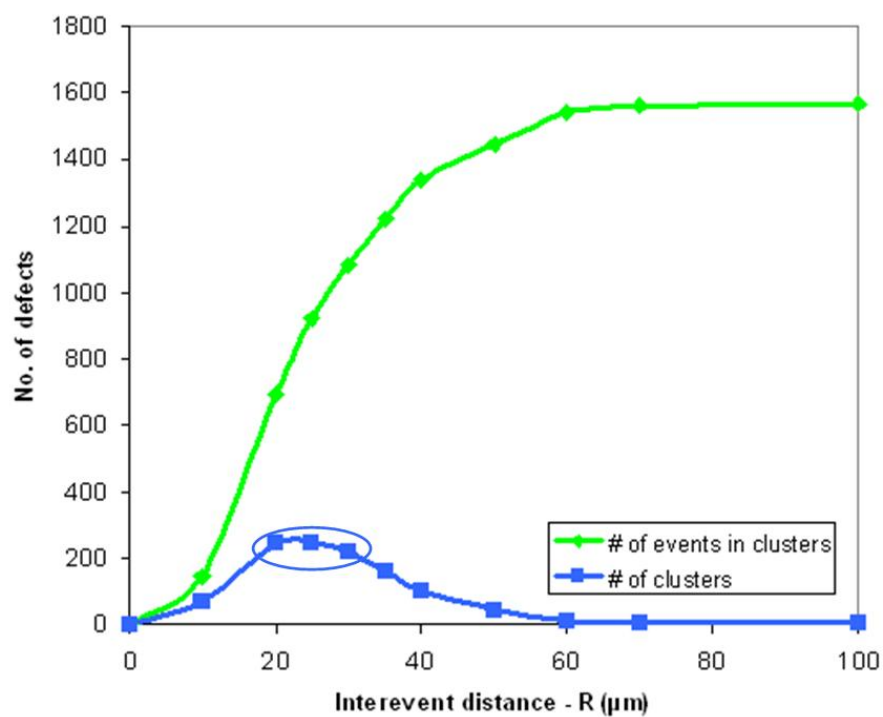


Figure 5.37. Optimum limiting interevent distance determination

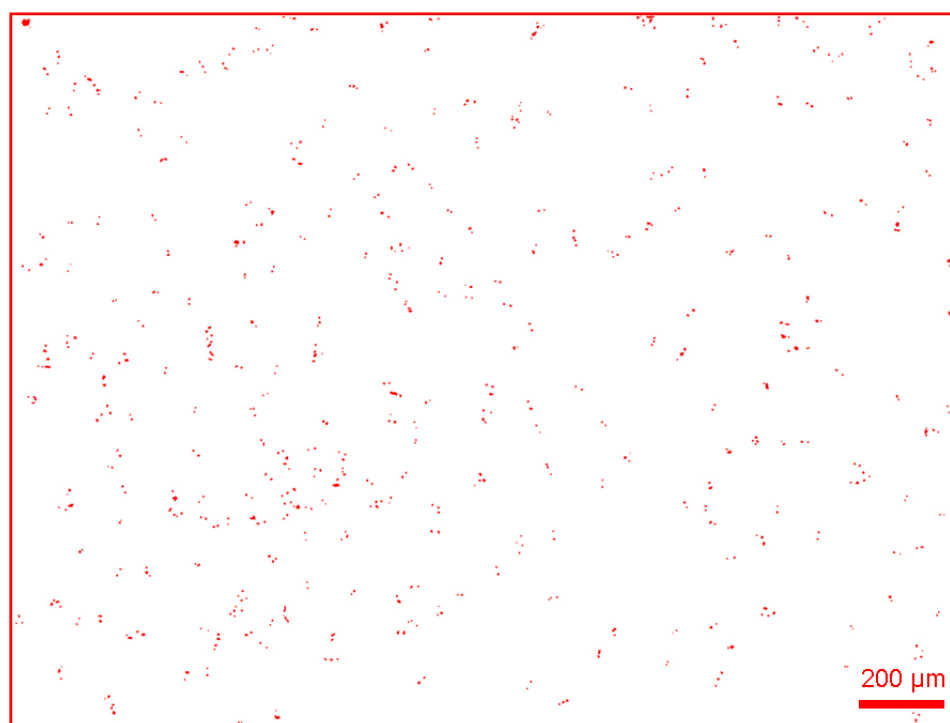


Figure 5.38. Demonstration of clusters when $R=20 \mu\text{m}$

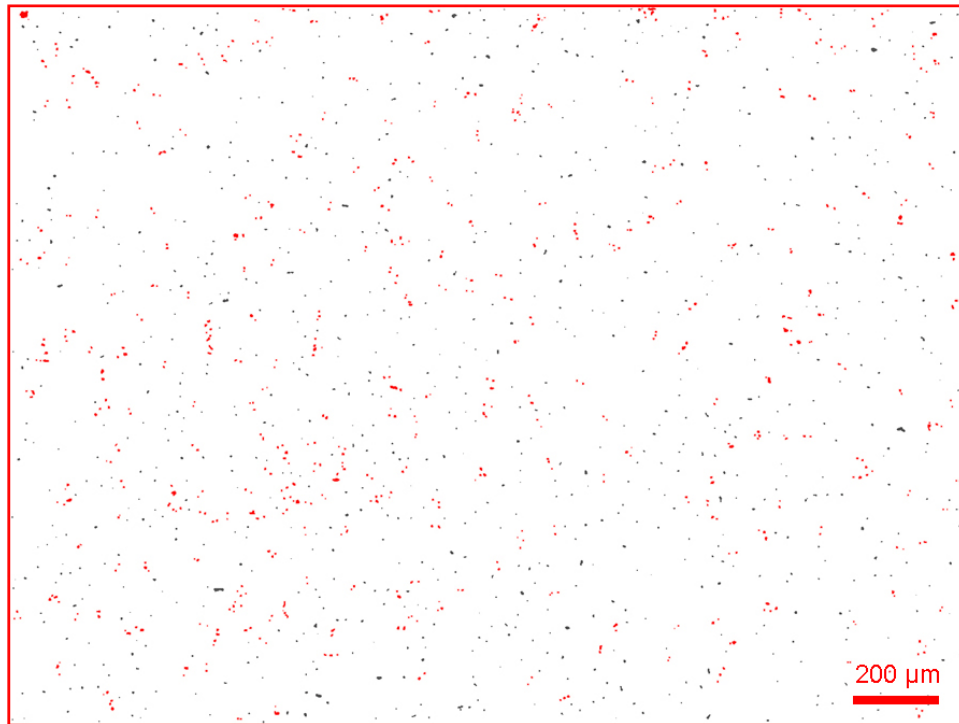


Figure 5.39. Demonstration of clusters and random background when $R=20\text{ }\mu\text{m}$



Figure 5.40. Demonstration of clusters in the original image

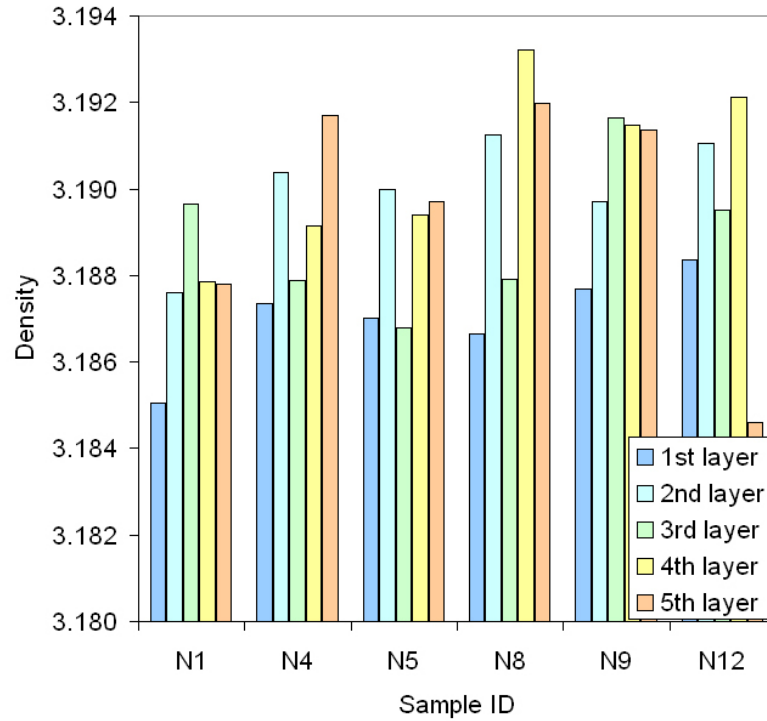


Figure 5.41. Density values from 5 layers obtained by serial sectioning

Table 5.5. T-test results of density between Region 1 and Region 2

t-Test: Two-Sample Assuming Unequal Variances	<i>region 1</i>	<i>region 2</i>
Mean	3.188	3.189
Variance	3.42E-06	5.25E-06
Observations	10	10
df	17	
t Stat	1.026	
P(T<=t) one-tail	0.159	
t Critical one-tail	1.739	

Table 5.6. T-test results of density between Region 3 and Region 2

t-Test: Two-Sample Assuming Unequal Variances	<i>region 3</i>	<i>region 2</i>
Mean	3.189	3.189
Variance	5.45E-06	5.25E-06
Observations	10	10
df	18	
t Stat	0.347	
P(T<=t) one-tail	0.366	
t Critical one-tail	1.734	

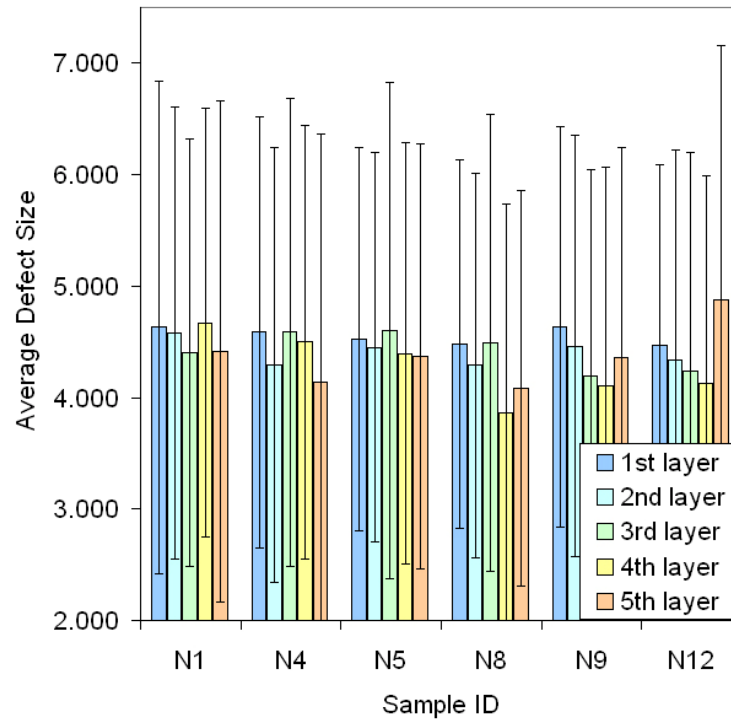


Figure 5.42. Average defect size values from 5 layers obtained by serial sectioning

Table 5.7. T-test results of average defect size between Region 1 and Region 2

t-Test: Two-Sample Assuming Unequal Variances	<i>region 1</i>	<i>region 2</i>
Mean	4.479	4.355
Variance	0.028	0.049
Observations	10	10
df	17	
t Stat	1.404	
P(T<=t) one-tail	0.089	
t Critical one-tail	1.739	

Table 5.8. T-test results of average defect size between Region 3 and Region 2

t-Test: Two-Sample Assuming Unequal Variances	<i>region 3</i>	<i>region 2</i>
Mean	4.380	4.355
Variance	0.057	0.049
Observations	10	10
df	18	
t Stat	0.237	
P(T<=t) one-tail	0.407	
t Critical one-tail	1.734	

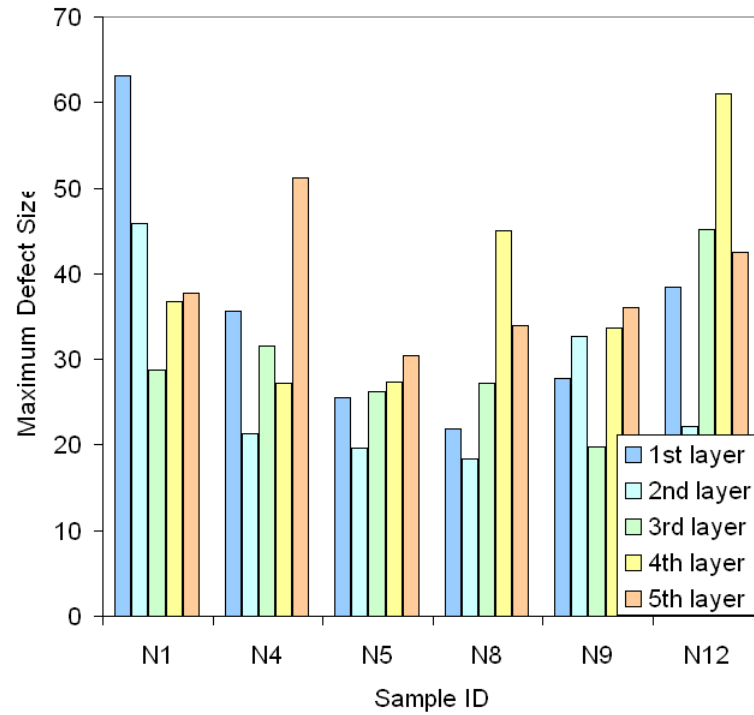


Figure 5.43. Largest defect observed at 5 layers obtained by serial sectioning

Table 5.9. T-test results of largest defect size observed between Region 1 and Region 2

t-Test: Two-Sample Assuming Unequal Variances	<i>region 1</i>	<i>region 2</i>
Mean	37.894	27.564
Variance	154.650	59.801
Observations	10	10
df	15	
t Stat	2.230721461	
P(T<=t) one-tail	0.020695494	
t Critical one-tail	1.753050325	

Table 5.10. T-test results of largest defect size observed between Region 3 and Region 2

t-Test: Two-Sample Assuming Unequal Variances	<i>region 3</i>	<i>region 2</i>
Mean	35.915	27.564
Variance	143.874	59.801
Observations	10	10
df	15	
t Stat	1.850	
P(T<=t) one-tail	0.042	
t Critical one-tail	1.753	

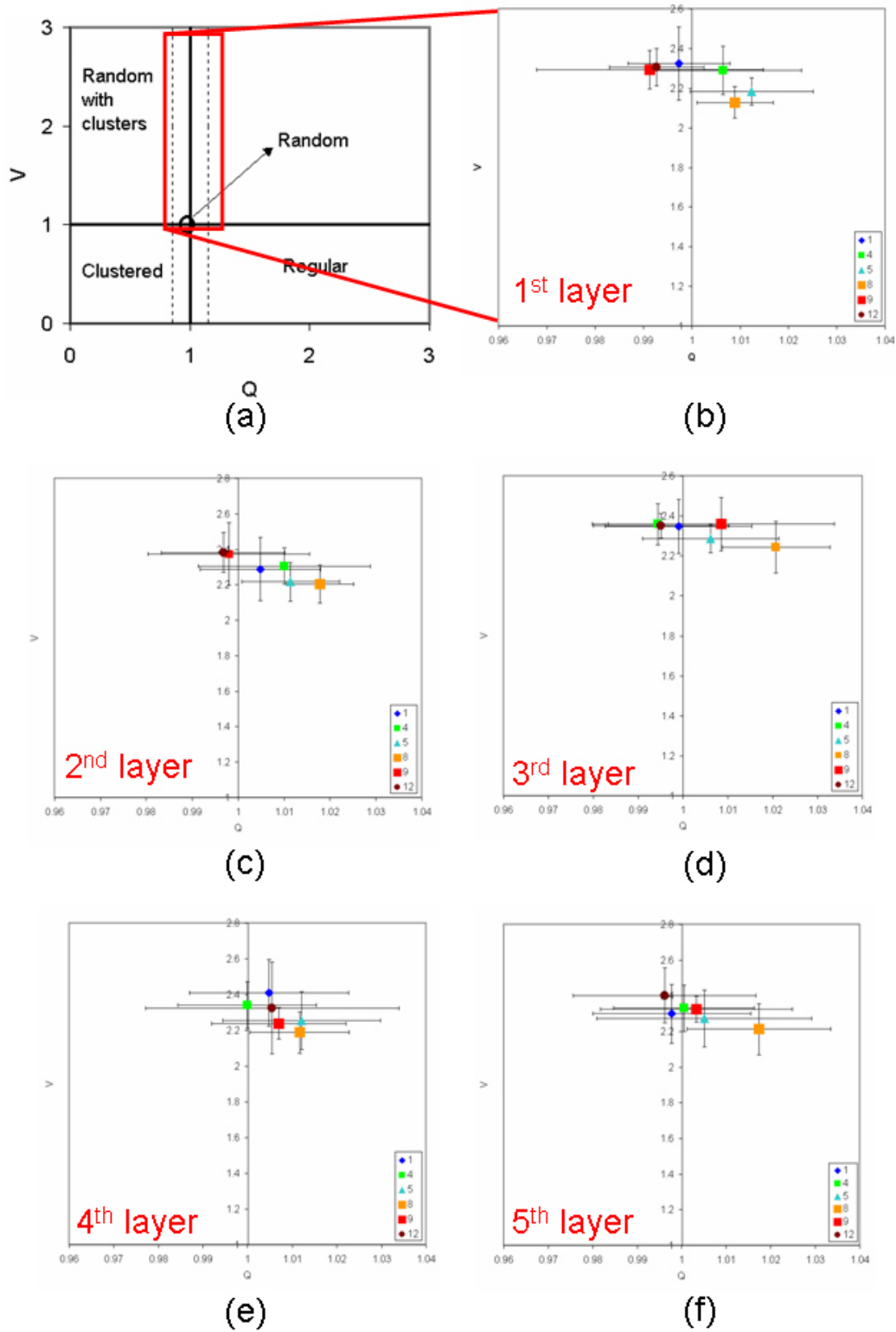


Figure 5.44. Q-V maps showing (a) The identified regions (b) 1st layer (c) 2nd layer (d) 3rd layer (e) 4th layer (f) 5th layer

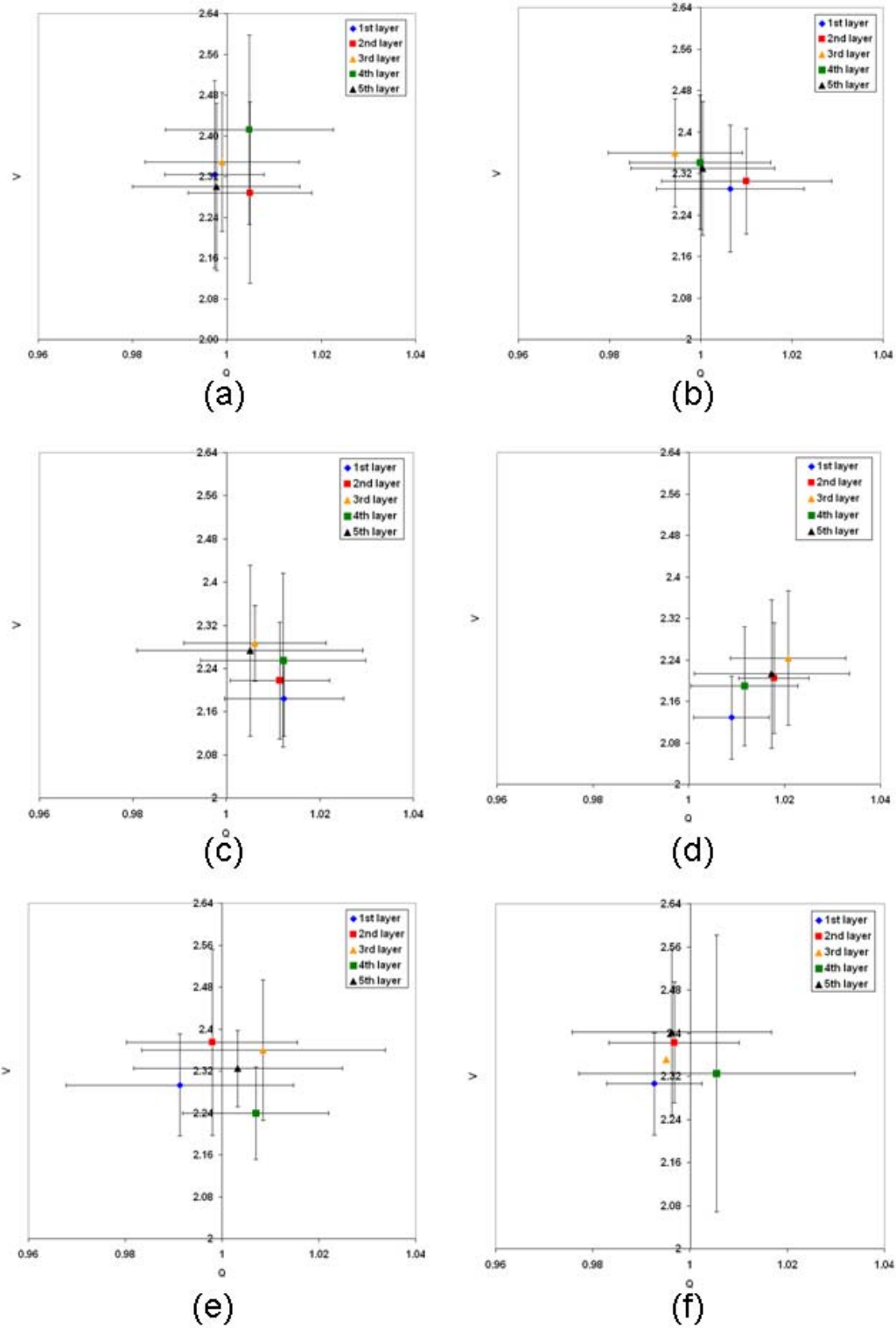


Figure 5.45. Q-V maps of all five layers from (a) N1 (b) N4 (c) N5 (d) N8 (e) N9 (f) N12

5.4. Property Measurements

Completion of the microstructural investigation was followed by mechanical analyses. Hardness was chosen as the primary method for obtaining property data. The selection criteria for hardness were explained extensively in Literature Review chapter. In a few words, it is a relevant and convenient method to obtain volumetric information regarding the homogeneity of microstructures. Additionally, there has been an agreement in armor community that hardness is one of the key parameters on prediction of ballistic performance [136-142].

5.4.1. Off-density Hexoloy SiC

5.4.1.1. Average Hardness

As mentioned in the previous section, off-density SiC samples consist of SA-1, SA-2, EXT and SP. Hardness tests were performed according to the procedure presented in the Experimental chapter. Measurements were carried out at five different loads, which start from 2 Kg down to 0.1 Kg. The intermediate loads were 1 Kg, 0.5 Kg and 0.3 Kg.

Fig. 5.46 shows the average hardness value against the load applied. The curve shapes are as expected, which obeys indentation size effect (ISE) [119]. At intermediate loads, SA-1 exhibits the highest values while SA-2 possesses higher average hardness at 2 Kg and 0.1 Kg. Also, it can be seen that SA-2 has the smallest standard deviation for majority of the indentation loads.

The bar chart for 2 Kg load is given Fig. 5.47 (a). SA-2 possesses the highest hardness values with an average value of $1615.5 \pm 214.3 \text{ Kg/mm}^2$. Another observation from the plot is that EXT and SP have significantly high standard deviation values. This could be attributed to the presence of large elongated defects in EXT and large circular

defects in SP. It is reasonable to say that the effect of these defects will be lessened with load as the smaller indent size will reduce the likelihood that these defects will fall within the indented volume and will affect the indentation results.

The indent size changes considerably as the indentation load varies, which will enable covering areas of different sizes. Typical indent size at 2 Kg load is approximately 120 μm . At 1 Kg, this value decreases to 90 μm . At the succeeding loads of 0.5 Kg, 0.3 Kg and 0.1 Kg, the indent size goes down to 60 μm , 45 μm and 25 μm , respectively. It should be noted that these values are approximate but, they provide a rough estimate on the extent of area covered by an indent.

Fig. 5.47 (b) provides the bar chart at 1 Kg. SA-1 has the highest hardness value with 2237.0 \pm 162.8 Kg/mm^2 . EXT has the lowest hardness value at this indentation load. The effect of indent size on the hardness is also shown here as 1 Kg load covers an area 3.6 times that of covered with a 0.1 Kg indenter. This increases the likelihood that an indent will interact with the large elongated defects in EXT or the clusters of defects, which will reduce the average hardness.

Fig. 5.47 (c) and Fig. 5.46 (d) show bar charts for 0.5 Kg and 0.3 Kg, respectively. SA-1 has the highest values again and SA-2 has the smallest standard deviation at both indentation loads. Fig. 5.47 (e) shows the results from smallest indentation load at 0.1 Kg. SA-2 possesses the highest hardness value with 4037.8 \pm 414.3 Kg/mm^2 . This sample also has the smallest standard deviation value among these four samples, following the trend, exhibited at previous indentation loads. Hardness values from all samples seem to get closer to each other at lower loads, although the standard deviation is still high for EXT and SP even at 0.1 Kg load.

5.4.1.2. Comparison of Hardness Results with Rice's model

Rice demonstrated that the presence of defects leads to lower hardness values. He exhibited a change in hardness with porosity. The following equation is used for the calculations:

$$H_V = H_0 \exp(-bP) \quad 5.2$$

where H_V is the measured Vickers hardness, H_0 is the Vickers hardness value corresponding to a specimen with zero porosity, b is a material dependence constant and P is the volume fraction porosity of the specimen [131,134,135]. Reynaud and Thevenot used this model and tested its validity for SiC [131]. SiC samples were indented using 0.5 Kg load. After performing curve fits for the samples with varying levels of porosity, the preexponential factor, b , was found to be 3.89. H_0 was calculated to be 2059.8 Kg/mm² after the plots were extrapolated at $P = 0$.

These parameters were used for calculation of hardness values at 0.5 Kg load. The values for SA-1, SA-2, EXT and SP were found to be 1824.3, 1846.7, 1738.6 and 1780 Kg/mm², respectively. The actual measured values at 0.5 Kg are 2128.0, 1925.0, 1676.0, and 2016.9 Kg/mm². The discrepancy between calculated values and measured values is quite obvious. It is especially pronounced for SA-1 and SP with significant differences between the measured and calculated values. This example clearly shows that the likelihood of indent interaction with pores changes the expected hardness results considerably. This subject will also be discussed in the next section of contour maps where local variations are examined.

5.4.1.3. Hardness Contour Maps

Hardness contour maps were obtained by indenting the samples in an array of 10×10 square. The procedure was explained in details in Experimental chapter.

The contour maps at each load are given between Figures 5.48-5.52. Among the four samples, SA-2 shows more uniformity compared to the other three at the 2 Kg load. SA-1 has a fairly homogenous distribution of hardness data, with most data points in the range of 1000-1500 Kg/mm². Whereas in SA-2, they are in 1500-2000 Kg/mm² range. EXT and SP show regions of extreme high and low values. This outcome is predictable for EXT and SP since strong deviation from random case was observed previously in their respective spatial defect distribution patterns. Overall, the trends observed in the microstructures data can be seen in the hardness data as well.

For the 1 Kg load, SA-1 has the highest average hardness but the spread in the data is apparent in the map containing all colors representing different hardness ranges. SA-2 contains values almost only between 1600 and 2000 Kg/mm², therefore showing the narrowest spread among the hardness maps for 1 Kg. EXT contains large amount of area with very low values while SP possesses high and low hardness regions together, showing a large spread.

At the 0.5 Kg load, SA-1 displays regions of high and low values. The difference between SA-1 and SA-2 is also not as apparent as the 1 Kg load. Hardness values of SA-2 are more consistent in the range of 1800-2200 Kg/mm². The hardness map of EXT exhibits low hardness areas once again. SP has regions of high values in 2600-2800 Kg/mm² range.

SA-1 and EXT have regions that show values above 3000 Kg/mm² at 0.3 Kg load. Unlike the previous loads, EXT has the largest area in the highest color range, which is

3000 Kg/mm² and above. SA-2 has the largest area in the 2000-2200 Kg/mm² range, which is on lower part of the scale. SP has a significant portion of the map in 2200-2400 Kg/mm² range, which is uncharacteristically higher than that of SA-2 when compared to the previous three loads.

At the final indentation load of 0.1 Kg, highest hardness values are observed for SA-2 and SP, with both samples having areas in 4600 Kg/mm² and above range. However, SA-2 does not have low hardness regions like SP does, which is in the 2600-2200 Kg/mm² range. SA-1 and EXT have areas in the 4200-4600 Kg/mm² range. Especially EXT possesses a significant amount of low hardness regions as in the previous loads.

Consequently, the following trends were observed. SA-2 showed fairly high values and more importantly, values on a very narrow range. SA-1 has the largest areas of high hardness especially at 1 Kg, 0.5 Kg and 0.300 Kg loads. EXT and SP show large variations in the areas tested almost at every indentation load.

As indicated previously, apart from the pore size and volume fraction, the spatial arrangements of pores are just as important for microhardness. With the change in indent size, the area that an indent can cover changes considerably. The lower indentation loads produced average hardness values that closer to each other for each sample. This result could be attributed to that fact that smaller areas are covered at low indentation loads.

The starting point for the indent arrays in this study are chosen randomly, although a constant distance was maintained between indents. Therefore, it can be accepted that the area is chosen totally random and in that case, the likelihood that an indent falls on a pore, a group or cluster of pores or on the matrix changes significantly

with the indent size. Large indents will naturally cover a larger area and this will increase the likelihood that the indent falls partially or completely on large defects or clusters of defects. As the indentation loads decreases, the likelihood between an indent and a defect interaction is lessened.

The theoretical hardness values calculated at 0.5 Kg load using Rice's model are worth mentioning here. It was shown above that the calculated values, which are 1824.3, 1846.7, 1738.6 and 1780 Kg/mm² for SA-1, SA-2, EXT and SP, respectively, do not match up well with the measured average values. The calculated values could be used in a comparison with the contour maps. Since these values were obtained at 0.5 Kg, the contour maps at 0.5 Kg must be taken into account. Only a small part in the middle parts of the contour map of SA-1 corresponds to the calculated value of 1824.3 Kg/mm². For SA-2, a better match could be observed as hardness numbers close to the calculated value could be seen at almost 60 % of the map. In the map of EXT, a significant amount of data below 1800 Kg/mm² can be observed. These values are lower than the calculated one. The influence of defects is strictly observed in this map due the values much lower than the predicted value. The discrepancy is not that pronounced for SP as higher hardness regions than the predicted value are common. Apart from the average hardness, contour maps show the influence of defects by using Rice's model of hardness as a function of porosity.

5.4.1.4. Weibull Analysis

Statistics and probability functions are commonly used in property determination of brittle materials due to the presence of flaws and their influence on mechanical

properties [144,145]. The normal, lognormal and Weibull distributions are the most common ones employed for statistical examination of experimental data [146,147].

Weibull distribution is based on the weakest link approach, in which the property of material is dictated by the most serious flaws [151-154]. Although advanced processing techniques are employed and high apparent densities are achieved in armor ceramics, the presence of defects such as pores and inclusions are common. Their presence creates the highest probability of reducing hardness. As a result, Weibull distribution would be valuable in describing statistical interpretation of hardness data [44,159,160].

It was clearly shown in the Literature Review chapter that Weibull statistics are effective in studying hardness results. Weibull analysis was chosen to study the variability and the extent of spread in hardness data. It was also employed in order to get a representative number out of the quasi-static tests so that a correlation between microstructural data and hardness data can be drawn [146,147].

The Weibull plot for each load is given in Fig. 5.53 and Weibull modulus values are provided in Table 5.11. SA-2 has the highest modulus value 18.92, preceding SA-1 with 9.35. EXT and SP have much lower values compared to those of SA-1 and SA-2 at 2 Kg of load. Same trend is observed at 1 Kg load except that a bimodal distribution is apparent for SP. The results from 0.5 Kg load show the same trend as SA-2 has the highest values, followed by SA-1, SP comes third and EXT has a bimodal distribution and the lowest values with 1.98 and 7.42. The order does not change for 0.3 Kg of load. At 0.1 Kg load, SA-1 and SP have values very close to each other. SA-2 once again has the highest value with 11.81 among all four samples.

5.4.1.5. Interpretation of Weibull plots

Ideally, in the case where the distribution of all phases is homogeneous, Weibull plot will be indicative of that, having a linear distribution. When the phases in a microstructure are evenly spread, each indentation samples all phases at the same time; therefore, no individual phase will dominate hardness results. However, the regions exhibiting higher degree of homogeneity would probably present higher Weibull modulus values and less data scattering than those regions with lower degree of homogeneity, thereby giving rise to the bimodal distribution. The bimodal distribution characteristic is a clear indication that different phases are present in the material. In the case of these Hexoloy SiC samples, other than the matrix and pores, carbon inclusions are present in the microstructure. These inclusions could very well contribute to the bimodal distribution in these samples.

It is reasonable to predict that as the defect concentration decreases or when the defect distribution is more uniform at the same concentration, the length of the upper slope increases and the lower slope tends to be minimized. From this observation, it can be inferred that if the second phase content decreases to lower values or it becomes more evenly spread, the bimodal distribution will tend to disappear.

When Table 5.11 is examined carefully, it is obvious that bimodal distributions are observed at higher loads of 1 Kg and 0.5 Kg. The plots at 0.3 Kg and 0.1 Kg loads have single modes for all samples. At low indentation loads, only a small volume of materials is analyzed. However, at higher indentation loads, defects affect the hardness results significantly since the likelihood that the indents interact with defects increases with the increasing defect size. As mentioned in the beginning of this chapter, a typical indent size for SiC at 2 Kg load is roughly 120 μm while this number decreases to 25 μm

at 0.1 Kg load, so the indent size for 0.1 Kg is approximately five times smaller than that of 2 Kg. The mean nearest neighbor distance values give an idea of spacing between pores, with the corresponding values for SA-1, SA-2, EXT, SP are 3.81 μm , 3.77 μm , 6.10 μm , 5.17 μm , respectively. Even at low loads such as 0.1 Kg, an indent with a size of 25 μm will likely interact with a minimum number of four or five defects. As the indent size increases to 120 μm , this number will reach up to 30. High load indents will also have higher probability that there are large defects or defect clusters under the indent, leading to more variability in the data. This will be reflected in the slopes of Weibull plots.

5.4.1.6. Crack Paths

Latest part regarding off-density samples involves taking a close look at the fracture path of indentation cracks. Indentation causes cracking to a certain degree, especially at the higher loads. Fracture mode of cracking is strongly dependent on the grain boundary strength of ceramics and it can provide information in that microstructural aspect. In addition, fracture mode was used as a tool to speculate on ceramic armor performance. Viechnicki et al. studied the fracture mode in armor ceramics and reported that transgranular fracture was associated with superior armor performance rather than intergranular fracture [136]. However, intergranular fracture has its own benefits in providing crack deflection along grain boundaries, which prolongs the route of crack expansion, leading to increased fracture toughness. This argument was put forward in a study by Shih et al, who claimed that intergranular fracture was favored in armor ceramics due to more energy consumption during this type of fracture [181]. In a study by Ray et al., fracture modes of several hot-pressed SiC were examined, where; quasi-

static fracture modes varied from mainly transgranular to largely intergranular, leading to a significant increase in the single-edged pre-cracked beam (SEPB) fracture toughness [182].

The cracks resulting from high load indentation of 2 Kg in these four SiC samples were investigated. Both intergranular and transgranular cracking was observed, along with no cracking cases at some of the indents.

The results are given in Table 5.12 as the type of fracture mode is represented in terms of percentage. SA-2 has the highest percentage of intergranular mode with 14%, and the lowest number for transgranular mode with 46%. Also, 40% of the indents examined show no cracking for SA-2, which is the highest “no cracking” percentage among all. Intergranular mode was rarely observed in EXT and SP as both samples have 2% of all cracks in this mode. SP has 92% of the cracks examined in transgranular fracture mode. SA-1 has intermediate values for all three cases.

A certain degree of distinction in fracture modes between these four samples is clearly apparent. However, their interpretation is somewhat difficult due to explanations made above on the fracture modes of ceramics. To be able to understand what contributes to these results, the components in these materials must be known. Hexoloy SA was doped with boron and carbon and the major secondary phase observed in this material was graphite, as particulates within SiC grains and at large triple junctions. According to Moberlychan et al., the crack paths in Hexoloy SA exhibited strictly transgranular fracture [183]. Although transgranular fracture is still dominant at 46%, intergranular fracture is significantly observed at a value of 14%. It is reasonable that cracks are

deflected from the carbon inclusions/SiC matrix interfaces and consequently, a significant amount of intergranular fracture mode could be seen.

As a result of this analysis, SA-2 came out to be the sample with higher hardness numbers, superior microstructural data and with the highest amount of intergranular fracture, which indicates higher fracture toughness.

5.4.2. Cercom Hot-Pressed SiC Samples

5.4.2.1. Average Hardness

Fig. 5.54 (a) shows average hardness values at 2 Kg for this set of samples. AG and DEF have average hardness values close to each other with $2009.1 \pm 44.5 \text{ Kg/mm}^2$ and $2026.2 \pm 59.8 \text{ Kg/mm}^2$, respectively. An important observation from this graph is the significantly low average hardness value of $1759.7 \pm 43.9 \text{ Kg/mm}^2$ observed in LD. This is a promising result in terms of supporting ultrasound data and how low amplitude regions provide important information without destructive evaluation of tiles.

Average hardness values are shown at the other four loads from Fig. 5.54 (b) through Fig. 5.54 (e). Results from 1 Kg and 0.5 Kg do not follow the trend that is observed at 2 Kg load. However, as the measurements proceed to lower loads, LD shows inferiority to the other two samples. At 0.3 Kg, the average hardness values for LD, DEF and AG are $2115.0 \pm 200.6 \text{ Kg/mm}^2$, $2220.3 \pm 183.3 \text{ Kg/mm}^2$ and $2201.3 \pm 194.6 \text{ Kg/mm}^2$. DEF and AG have roughly equal values while the results from LD are one notch below DEF and AG. Hardness data from 0.1 Kg load shows more distinct results as AG has an average hardness value of $4010.8 \pm 533.3 \text{ Kg/mm}^2$, which is significantly higher than the other two samples. LD has the lowest average value among the three with

3444.9 +/- 658.7 Kg/mm². DEF has an average value in between AG and LD with 3594.7 +/- 581.6 Kg/mm².

Although some inconsistencies are present at intermediate loads, it can be concluded that lower average hardness results are observed for LD for majority of the measurements. Ultrasound results are significantly affected by inhomogeneities, defects, or anything that is abnormal to the matrix of a ceramic, as they could cause low signal amplitude. Hardness is also affected considerably by the presence of defects as mentioned previously. When the density values, which are 3.18 g/cm³, 3.19 g/cm³ and 3.20 g/cm³ for LD, DEF and AG, respectively, are considered, these hardness findings become especially reasonable. Off-density values are typical reasons for low amplitude signals in ultrasound. Off-density values would also cause lower hardness outputs; therefore, the current findings are not surprising.

5.4.2.2. Weibull Analysis

First, Weibull plot for 2 Kg is given in Fig. 5.55. LD and DEF present single mode of distribution while AG has a bimodal Weibull distribution. The number of data points for the first mode is considerably large as 85 data points were grouped into the first mode and 15 data point were grouped into the second. Therefore, the dominant mode in this distribution is the first one, which provides an appreciably greater Weibull modulus value with 90.7 at R² value of 0.988. Modulus values are considerably smaller for LD and DEF with values 49.2 at R² value of 0.982 and 41.3 at R² value of 0.972.

As mentioned previously, AG has the highest density with a value of 3.20 g/cm³ among all three samples and it also has the highest Weibull modulus value. According to

these results, the high density is confirmed by the Weibull plot, which shows the degree of variability in the hardness data.

Weibull plots of AG, DEF and LD are given in Fig. 5.56 at all five loads. Bimodal Weibull distributions can be observed in the plots for all three samples and at most of the indentation loads except at 0.1 Kg for AG, at 2 Kg and 0.1 Kg for LD, at 2 Kg and 0.5 Kg for DEF. AG has the highest Weibull modulus with 90.7 at 2 Kg load. The trend is reversed at 1 Kg, with LD having the highest value of 67.9. DEF has the highest value at 0.5 Kg with 57.3 while LD and AG have very close modulus values with each other, at 34.3 and 35.7, respectively. At 0.3 Kg, DEF possesses the highest value again with 32.5. DEF has the largest Weibull modulus once again with 18.7 at 0.1 Kg. No definite trend was apparent according to these results.

However, one important observation from these plots is that as the indentation load decreases, the slopes of the curves tend to decrease accordingly. Lower indentation loads affect smaller areas. Due to the less likelihood of the tip to come across with pores, or clusters of pores, a larger spread is obtained at the end. It might be mentioned that as the indent size decreases, the hardness value depends very much on the number of present pores under the indent. However, with higher indentation loads, the effective area under the indent is much larger. Therefore, a small change in the number of defects does not affect the results drastically. Again, probability is an important factor in the variation of hardness values. The likelihood that an indent falls partially or completely on a defect or a group of defects affects the hardness value drastically. Especially at low indentation loads, the probability of an indent and a defect interaction is lessened. Since the spatial arrangement of defects is one of the focal points of this study, comparison between the

scales of homogeneity of the defects against the scale of indenters will provide insight to the spatial arrangement. This will be discussed in the last part of this chapter, where results from hardness tests and microstructural analysis will be correlated.

5.4.2.3. Grain Size Distribution around High and Low Density Regions

Grain size has a considerable contribution to measured hardness [118]. In order to test if grain size distribution contributes to the variations in hardness maps, certain regions from 2 Kg load map were examined more closely after etching. Fig. 5.57 shows the selected areas in the hardness map, which are from low and high hardness regions. Fig. 5.58 shows grain size distribution from both high and low hardness areas. Average grain size for LD on the low hardness region and high hardness region are 1.73 μm and 3.60 μm , respectively. Materials with smaller grain sizes typically exhibit higher hardness values, however this trend was not observed in this sample. Same procedure was repeated for DEF. The average grain size values are 1.72 μm and 1.92 μm from low hardness and high hardness regions, respectively. The values are much closer to each other for DEF while it also has no correlation with the trend explained above. The only sample that higher hardness regions have smaller grain size is sample AG. However, when the results are assessed entirely, it can be concluded that hardness value changes cannot be attributed to grain size variations in each sample. Therefore, the presence of defects, on the surface or underneath, plays an important role in the indentation process without a significant effect from grain size for these particular samples.

Apart from grain size distribution around these specified regions, grain size clustering was also examined. This is important due to the fact that carbon inclusions

could affect the grain size distribution around themselves. By performing nearest neighbor distance distributions to this data, spatial distribution of grains was studied. Fig. 5.59 shows the Q-V plot from grains around low and high hardness regions again. A significant difference between two cases was observed although none of the points fall into the “clustering on a random background” region. As mentioned previously, (1,1) point is the totally random case. The data point for the low hardness region is much closer to the random point than the one from high hardness region, therefore, a strong deviation from random distributions is valid for the second one. Carbon inclusions could be the main reason for this result, which shows another variation in the microstructure apart from nonuniform spatial distribution of defects.

5.4.3. SiC Hexoloy SA Tile

5.4.3.1. Average Hardness

The indents for each sample can be seen in Fig. 5.60. Knoop indenter was used to indent the samples as usual. The distance between each indent was kept at 0.5 mm. N2 represents Region 1, N6 represents Region 2 and N10 represents Region 3. Average hardness data is given in Fig. 5.61. Average hardness for Region 2 (N6) is slightly higher than the other two regions.

5.4.3.2. Hardness Contour Maps

Contour maps are given Fig. 5.62 and the percentage of hardness values in each hardness range is given in Table 5.13 for each sample. The contour maps for N6 and N10 show more homogeneity while N2 seems to possess significant amount of hardness

values from all the ranges given in the scale. As it is shown in Table 5.13, Region 2 has the highest percentage of hardness data with 84.69% in the most dominant data range, 1800-1900 Kg/mm², represented by "light green" color. Region 3 is close with 83.20%. However, for the higher range, 1900-2000 Kg/mm², it is much lower to Region 2 with 5.99 % to Region 2's 9.16%. Region 1 has a wide large spread as this is quantified in Table 5.13.

The percentage values are shown against the hardness range in Fig. 5.63. The uniformity is more easily observed in this plot as Region 2 has the largest peak in 1800-1900 Kg/mm² range and relatively smaller peaks in the other hardness ranges.

5.4.3.3. Weibull Analysis

Weibull plot is given in Fig. 5.64. Modulus values are written on the graph. Bimodal distributions were observed for Region 1 and Region 2 while a single mode was observed for Region 3. Highest modulus was obtained from Region 2 with a value of 56.1. Region 1 and Region 2 are close second and third with values of 40.8 and 38.8, respectively.

Consequently, the difference observed in amplitude of ultrasound signals was also obtained using hardness test. This is an encouraging step towards interpretation of ultrasound scans and how they could be utilized.

5.4.4. Lundberg Samples

Static and dynamic test results from the literature [14,184] are given in Table 5.14. SiC-SC-1RN possesses the highest hardness while SiC-HPN has the highest

fracture toughness among all four. Elastic modulus values are close, with SiC-N slightly having the highest modulus value. Transition velocity is the highest for SiC-HPN with 1625 ± 12 m/s while penetration velocity shows the ideal lowest value for this parameter with 370 m/s.

5.4.4.1. Average Hardness

In addition to the results obtained from literature, hardness tests were performed to this sample set using the same procedure which provides contour maps. First, average hardness values are given in Fig. 5.65. As shown in Table 5.14, SiC-SC-1RN has the highest Vickers hardness value 28.85 ± 1.92 GPa while SiC-B has the lowest value with 25.20 ± 1.74 GPa. SiC-HPN is a close second with an average value of 25.32 ± 2.02 GPa. Exact same trend was obtained in the measurements performed in this thesis. SiC-SC-1RN is the hardest material among all with 2159.6 ± 76.6 Kg/mm² while SiC-B and SiC-HPN possess the lowest values with 1890.3 ± 61.1 Kg/mm² and 1956.1 ± 93.8 Kg/mm², respectively.

5.4.4.2. Weibull Analysis

Weibull plots were obtained from the hardness data and they are given in Fig. 5.66. All samples except SiC-N display bimodal distribution. SiC-N, SiC-B and SiC-SC-1RN have very close moduli values with 47.7, 51.2 and 49.7, respectively. SiC-HPN has a modulus value of 36.9, which is moderately different from the grouping observed with the other three samples. Moduli values from the second modes for SiC-B, SiC-HPN and SiC-SC-1RN are 12.4, 19.0 and 25.5, respectively. None of the samples show any great

difference to the others in terms Weibull modulus. This could be attributed to the high density/low defect population of all samples in this set. Although ballistic tests showed differences between samples, this was not observed distinctively in hardness tests. More thorough examination of hardness results will be presented in next section where they are compared to the microstructural findings.

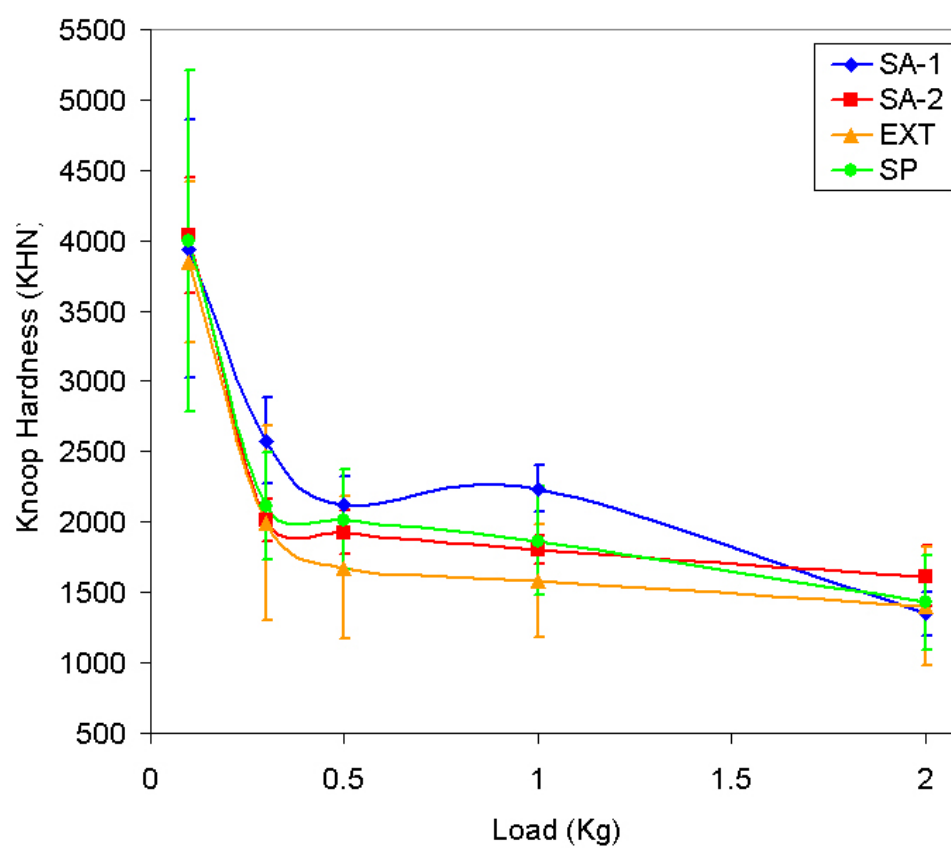


Figure 5.46. Average hardness vs. load for off-density SiC samples

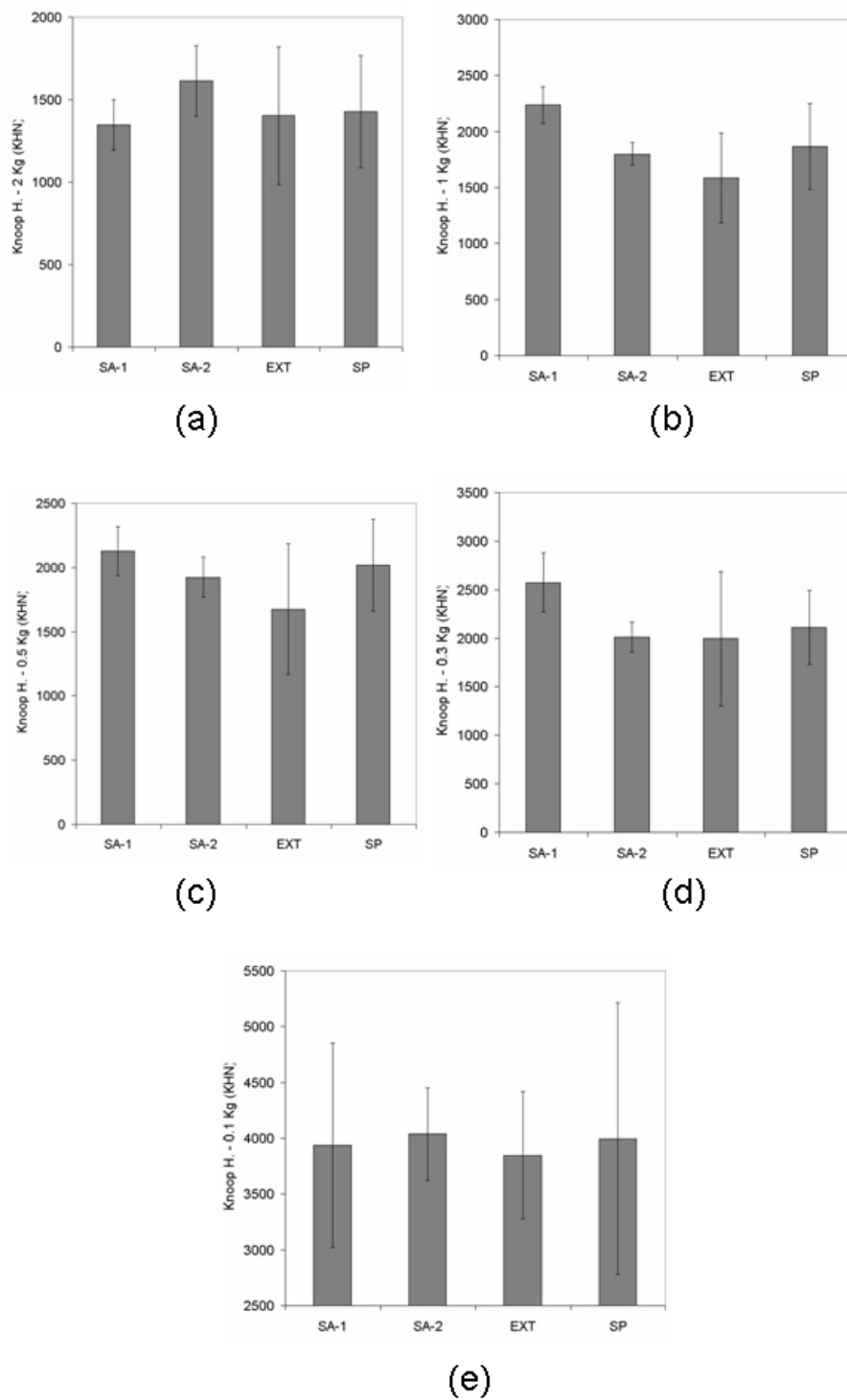


Figure 5.47. Average hardness values of off-density SiC samples (a) 2 Kg (b) 1 Kg (c) 0.5 Kg (d) 0.3 Kg (e) 0.1 Kg

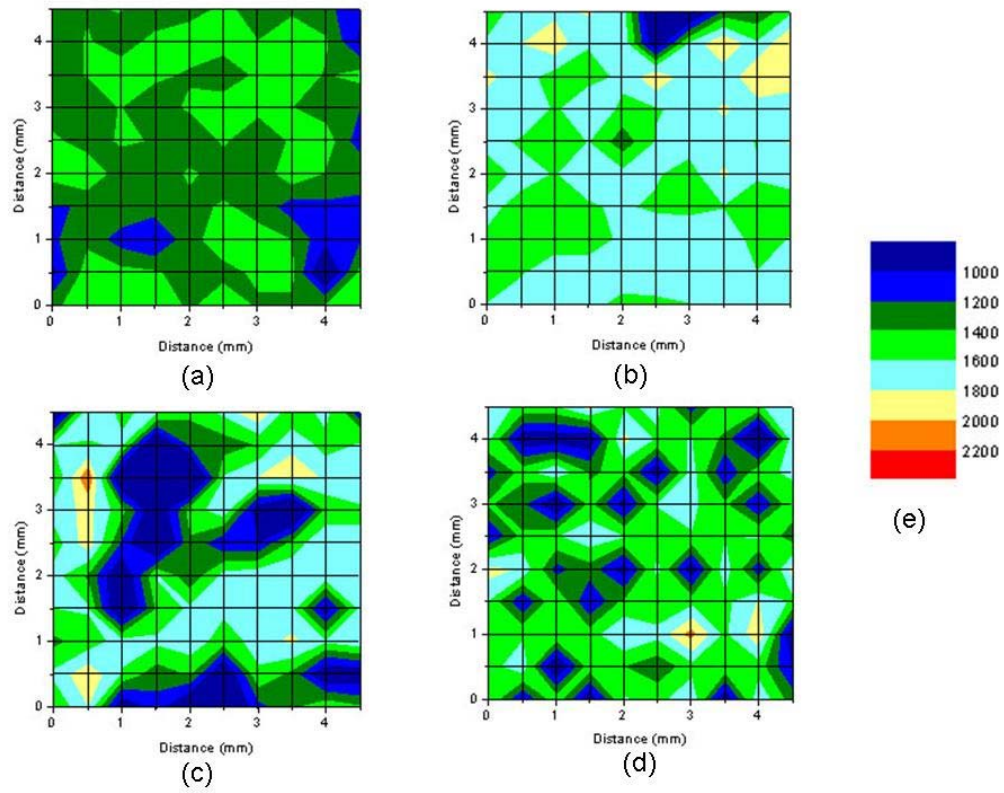


Figure 5.48. Contour maps at 2 Kg for (a) SA-1 (b) SA-2 (c) EXT (d) SP

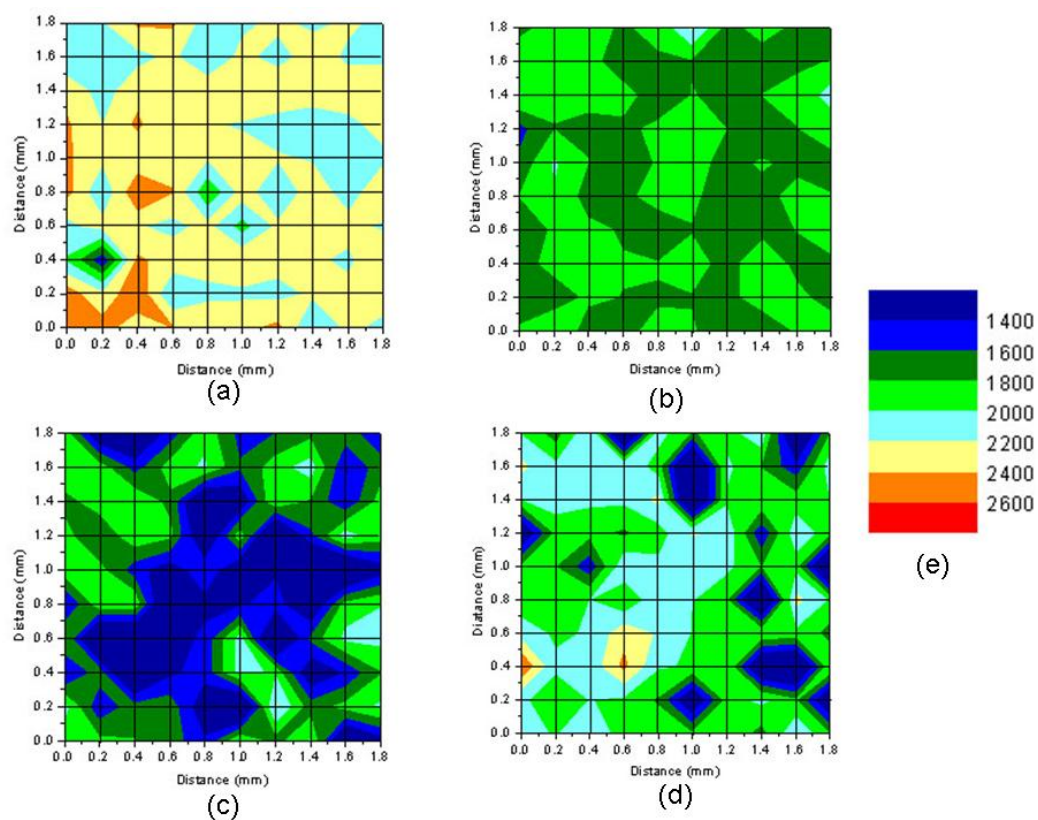


Figure 5.49. Contour maps at 1 Kg for (a) SA-1 (b) SA-2 (c) EXT (d) SP

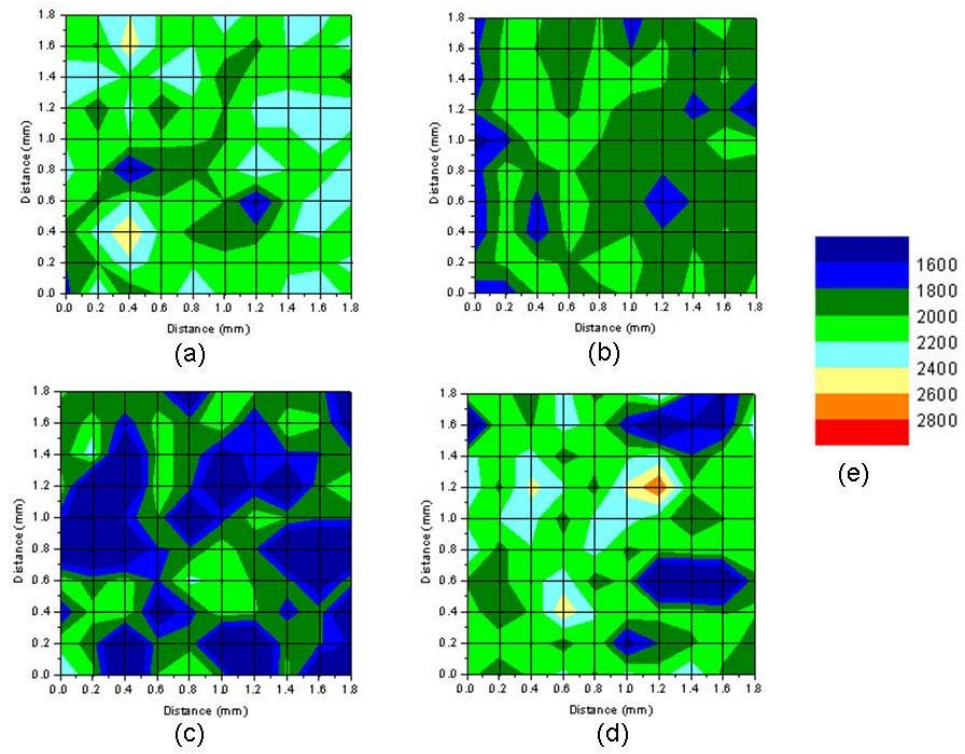


Figure 5.50. Contour maps at 0.5 Kg for (a) SA-1 (b) SA-2 (c) EXT (d) SP

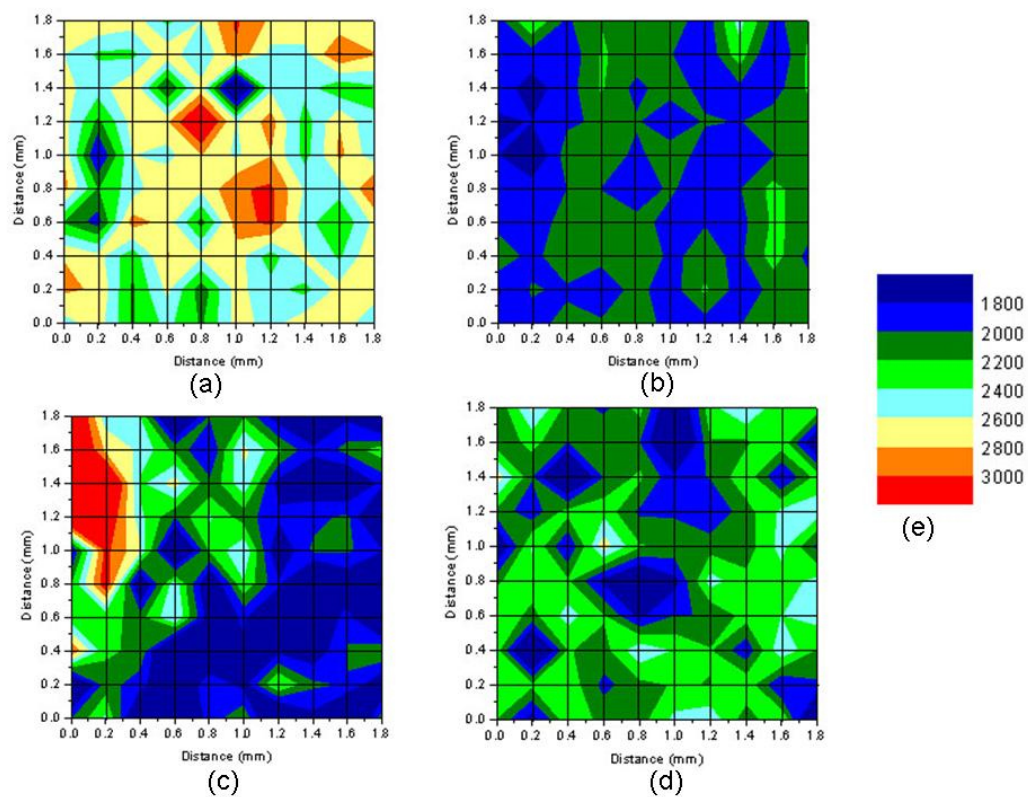


Figure 5.51. Contour maps at 0.3 Kg for (a) SA-1 (b) SA-2 (c) EXT (d) SP

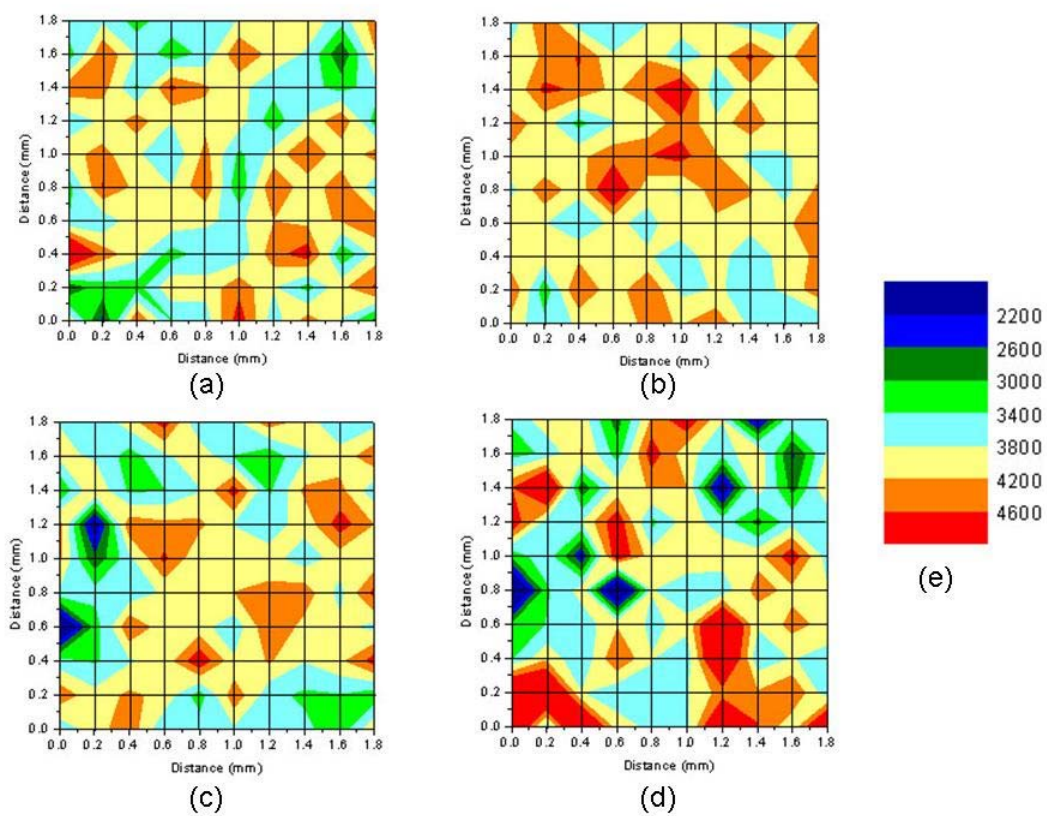


Figure 5.52. Contour maps at 0.1 Kg for (a) SA-1 (b) SA-2 (c) EXT (d) SP

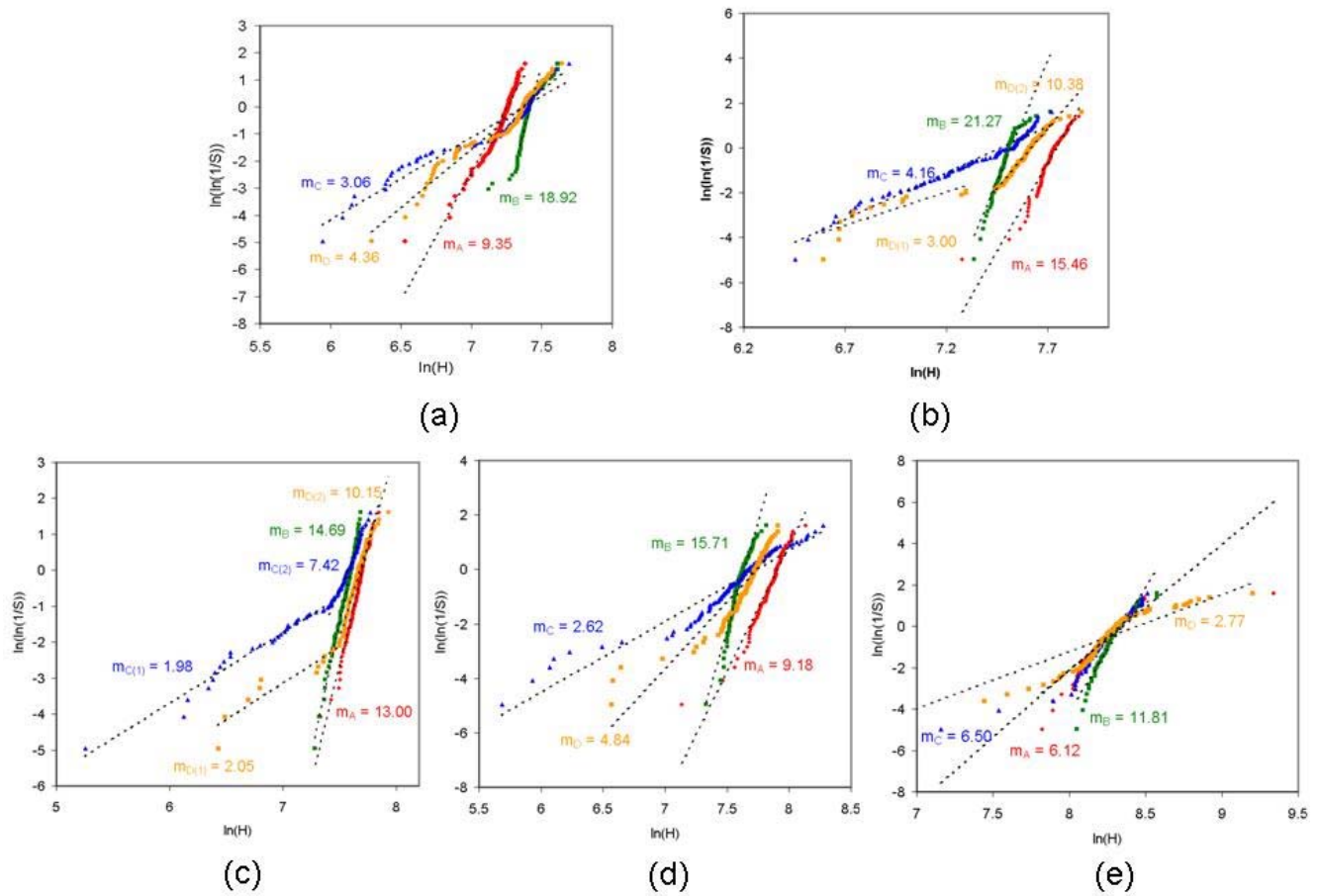


Figure 5.53. Weibull plot at (a) 2 Kg (b) 1 Kg (c) 0.5 Kg (d) 0.3 Kg (e) 0.1 Kg where A = SA-1, B = SA-2, C = EXT, D = SP

Table 5.11. Weibull modulus values for different loads

	m	2 Kg	1 Kg	0.5 Kg	0.300 Kg	0.1 Kg
SA-1	m_1	9.35	15.46	13.00	9.18	6.12
	m_2	-	-	-	-	-
SA-2	m_1	18.92	21.27	14.69	15.72	11.81
	m_2	-	-	-	-	-
EXT	m_1	3.06	4.16	1.98	2.62	2.77
	m_2	-	-	7.42	-	-
SP	m_1	4.36	3.00	2.05	4.84	6.12
	m_2	-	10.38	10.15	-	-

Table 5.12. Percentage of fracture modes

	Transgranular (%)	Intergranular (%)	No cracking (%)
SA-1	78	10	12
SA-2	46	14	40
EXT	68	2	30
SP	92	2	6

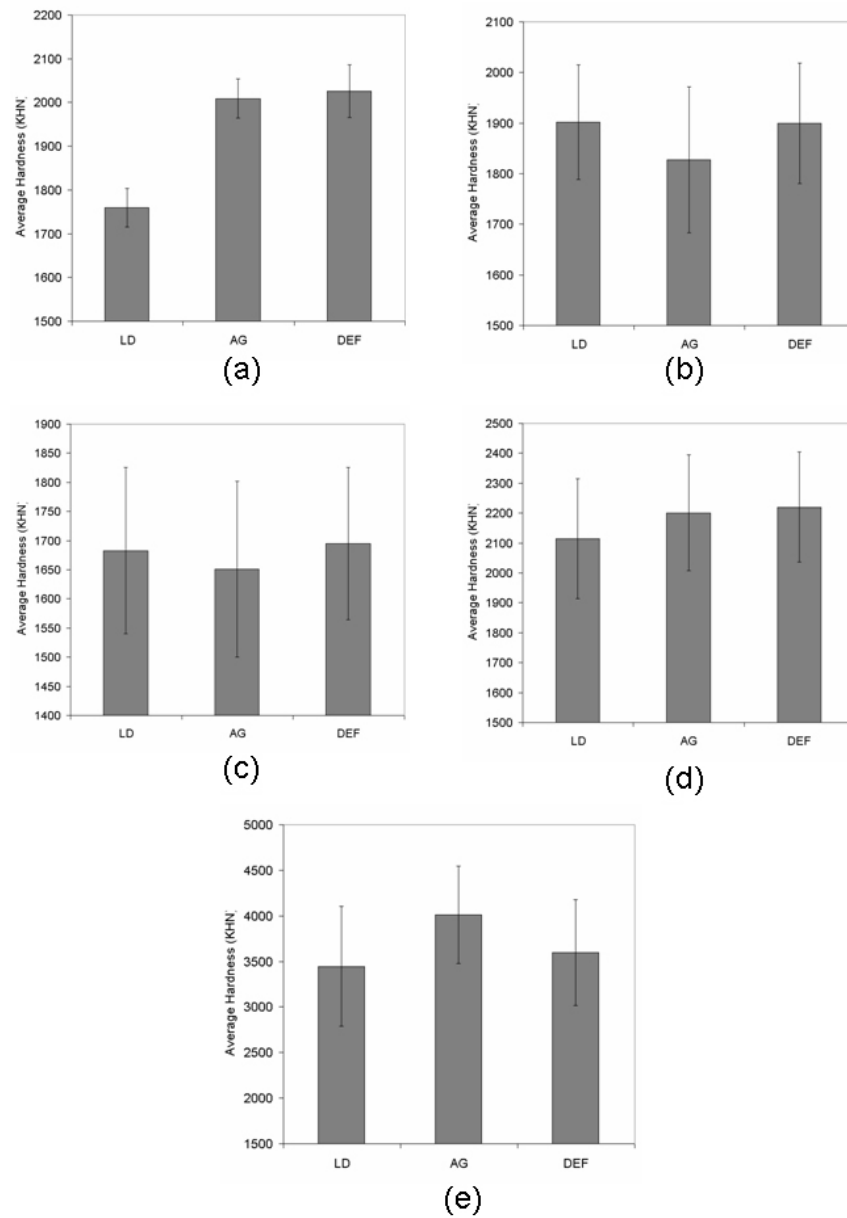


Figure 5.54. Average hardness at (a) 2 Kg (b) 1 Kg (c) 0.5 Kg (d) 0.3 Kg (e) 0.1 Kg

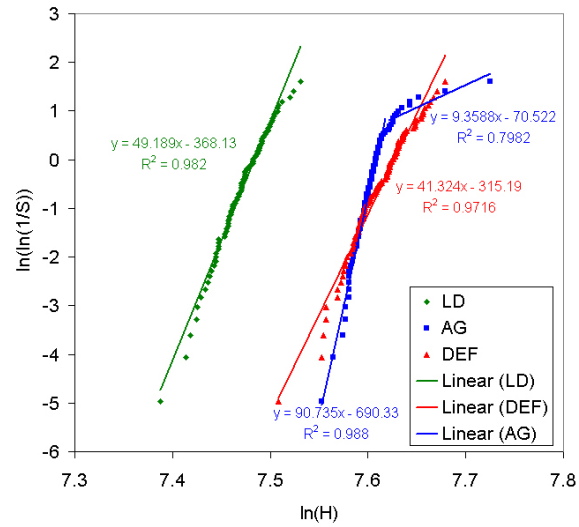


Figure 5.55. Weibull plot at 2 Kg for Cercom SiC samples

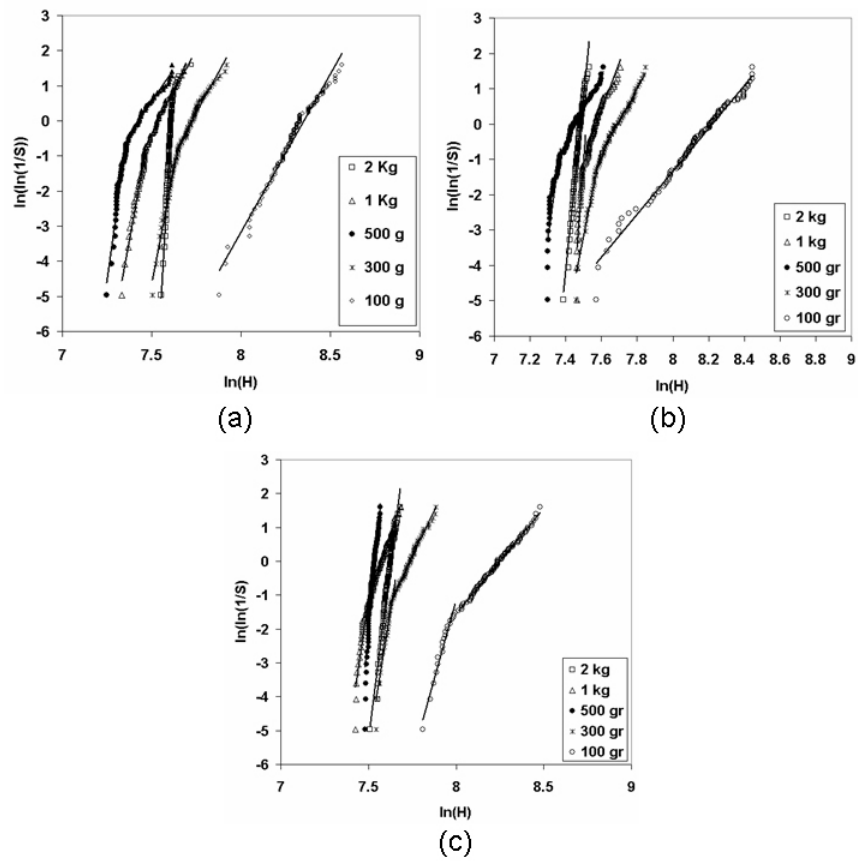


Figure 5.56. Weibull plots of (a) AG (b) LD (c) DEF at all loads

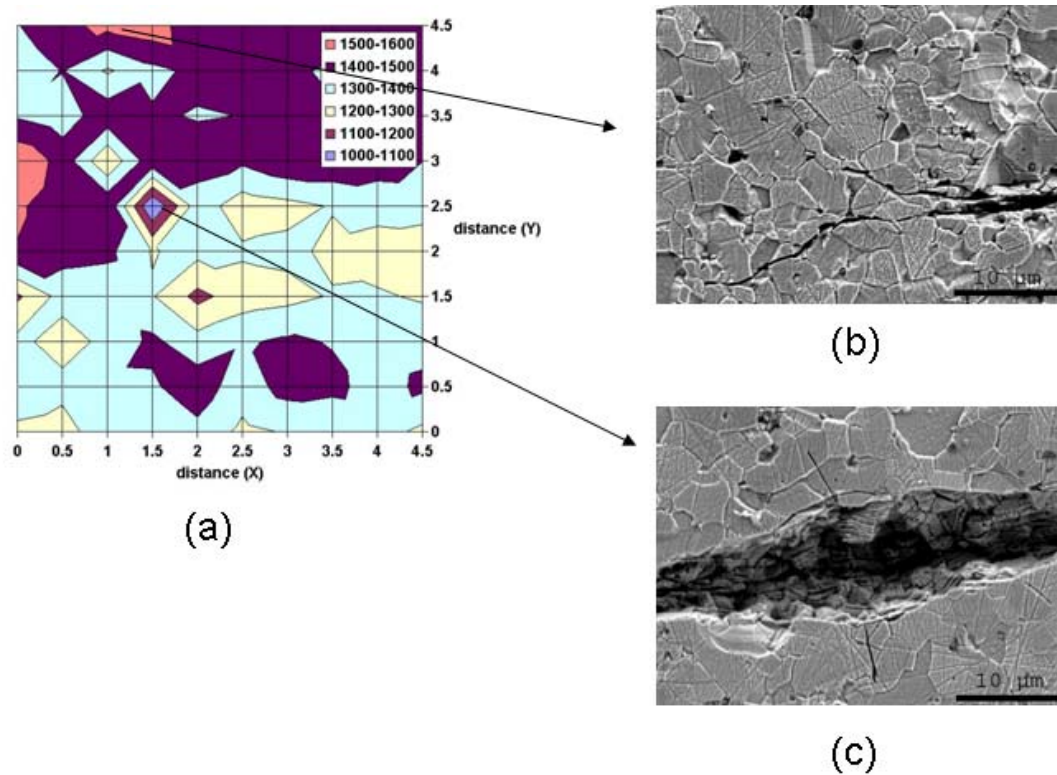


Figure 5.57. (a) Selected areas in the contour map of Cercom SiC samples (b) a micrograph from high hardness region (c) a micrograph from low hardness region

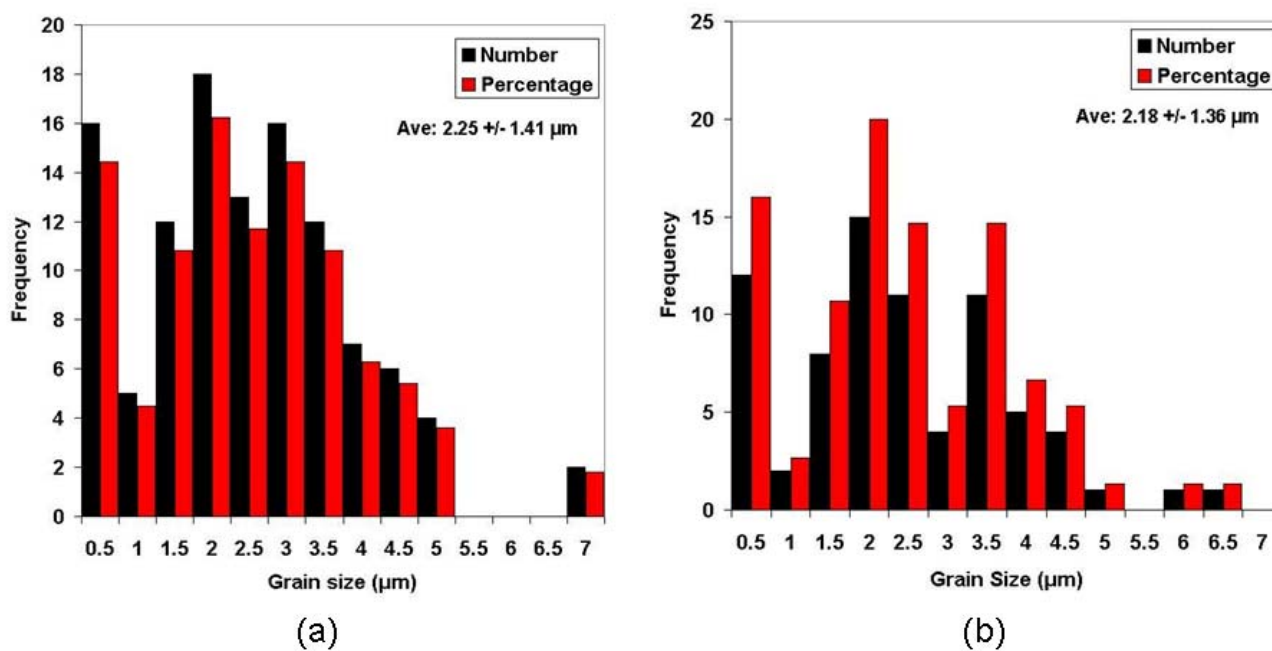


Figure 5.58. Grain size distribution around (a) high hardness region (b) low hardness region

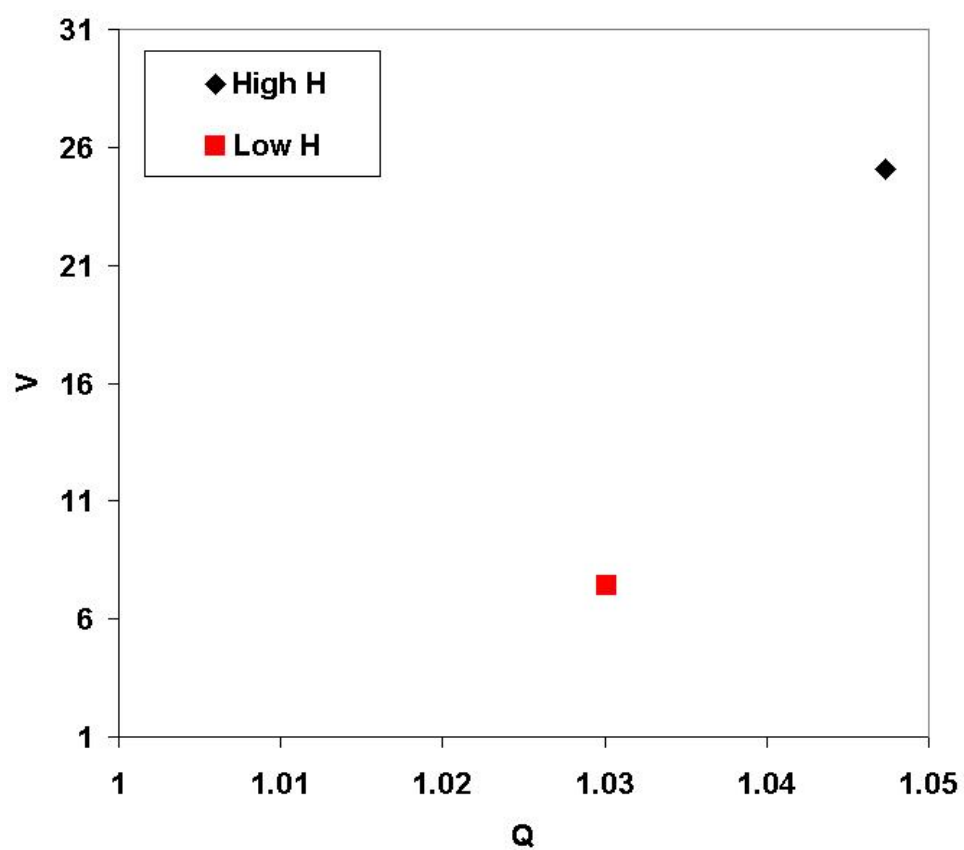


Figure 5.59. Grain size clustering around high and low hardness regions

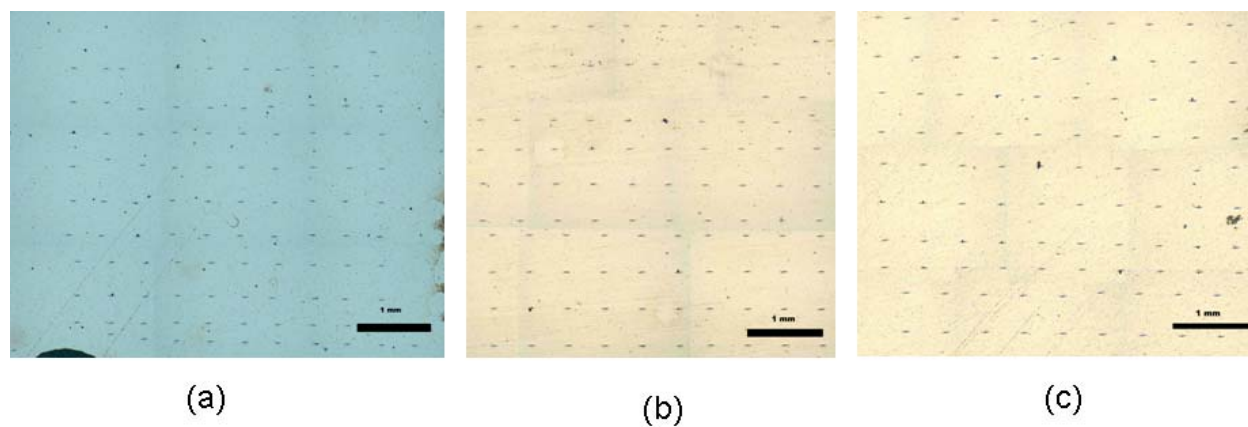


Figure 5.60. Indents from Hexoloy samples of (a) N2 (Region 1) (b) N6 (Region 2) (c) N10 (Region 3)

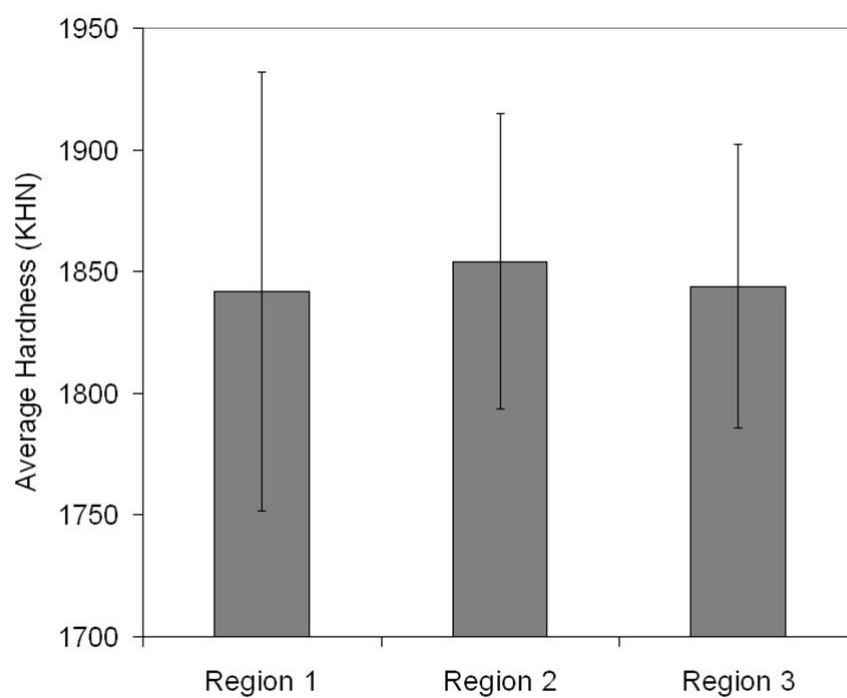


Figure 5.61. Average hardness of Hexoloy samples (N2, N6 and N10)

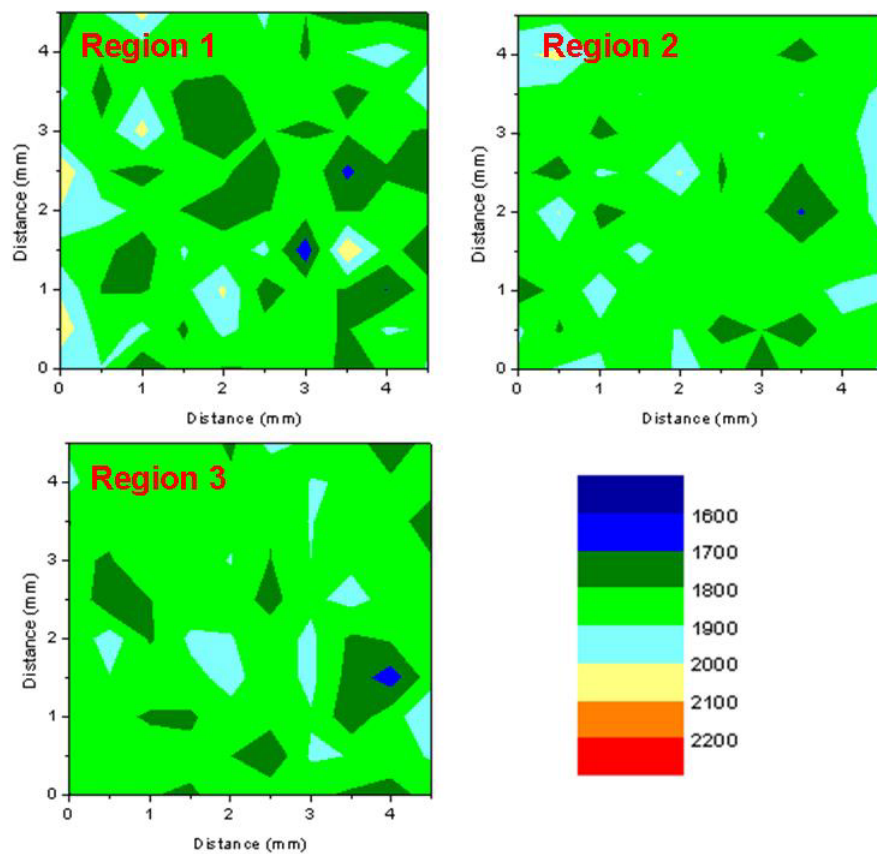


Figure 5.62. Contour maps of Hexoloy samples N2, N6 and N10

Table 5.13. Percentage of hardness values in each hardness range

%	<1600	1600-1700	1700-1800	1800-1900	1900-2000	2000-2100	2100-2200	2200<
Region 1	0	0.23	20.77	68.35	9.67	0.98	0	0
Region 2	0	0.02	5.95	84.69	9.16	0.18	0	0
Region 3	0	0.27	10.54	83.20	5.99	0	0	0

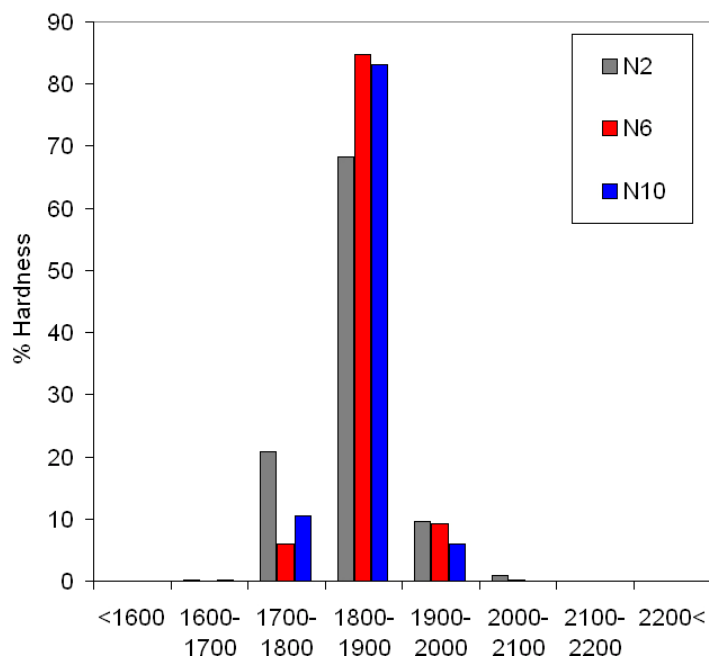


Figure 5.63. % Hardness vs. hardness range

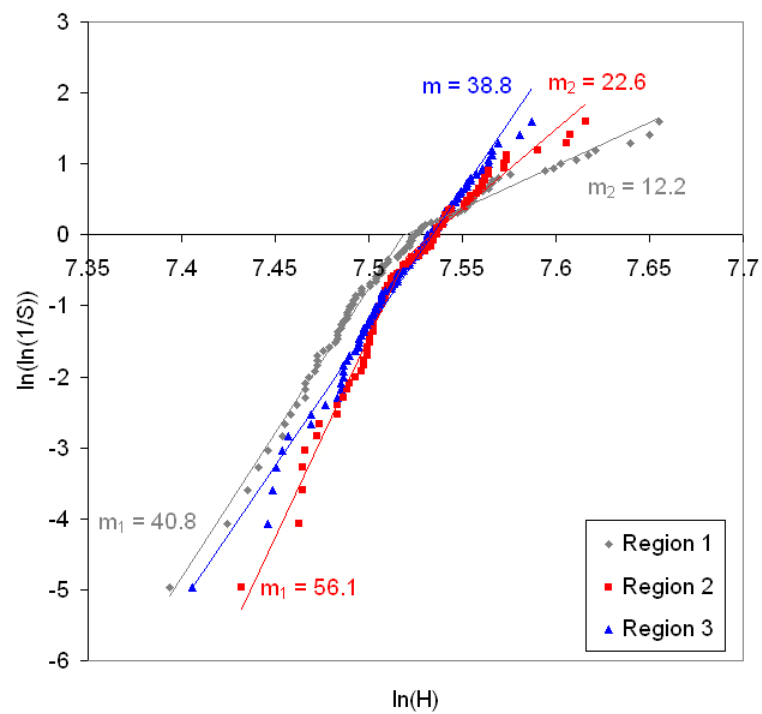


Figure 5.64. Weibull modulus of each Hexoloy sample at 2 Kg

Table 5.14. Quasi-static and dynamic properties of Lundberg samples [14,183]

	Vickers H (GPa)	KIc (MPam^{1/2})	E (GPa)	Transition Velocity (m/s)	Penetration Velocity (m/s)	Ave. Norm. Projectile Erosion V.
SiC-SC-1RN	28.85 +/- 1.92	2.84 +/- 0.22	440	1526 +/- 25	480	0.67 +/- 0.05
SiC-HPN	25.32 +/- 2.02	3.17 +/- 0.13	448	1625 +/- 12	600	0.57 +/- 0.04
SiC-N	27.16 +/- 1.76	2.75 +/- 0.32	449	1507 +/- 5	580	0.64 +/- 0.03
SiC-B	25.20 +/- 1.74	3.00 +/- 0.44	441	1549 +/- 19	370	0.58 +/- 0.08

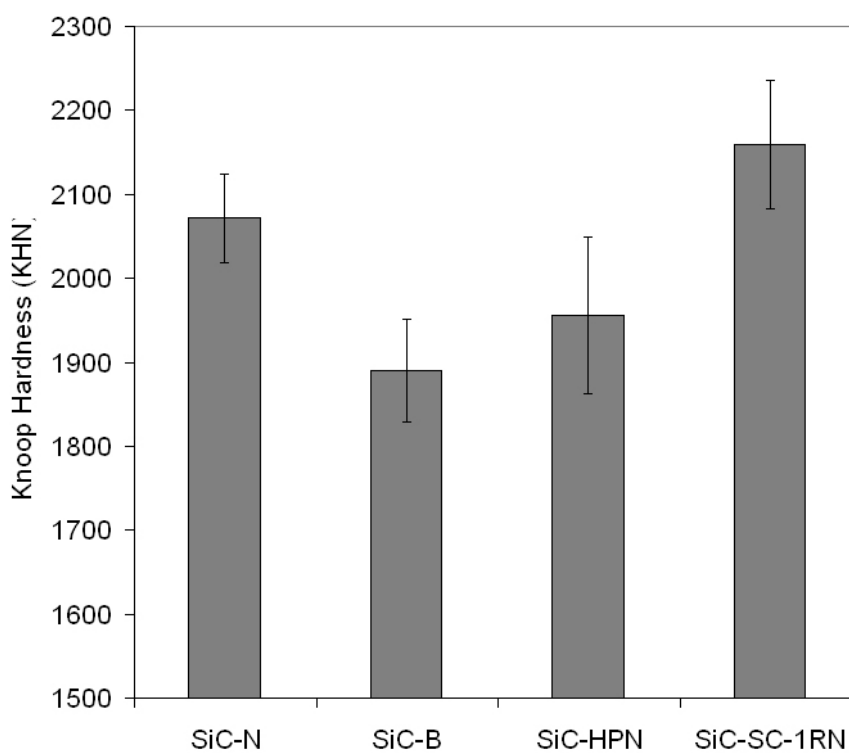


Figure 5.65. Average hardness of Lundberg samples at 2 Kg

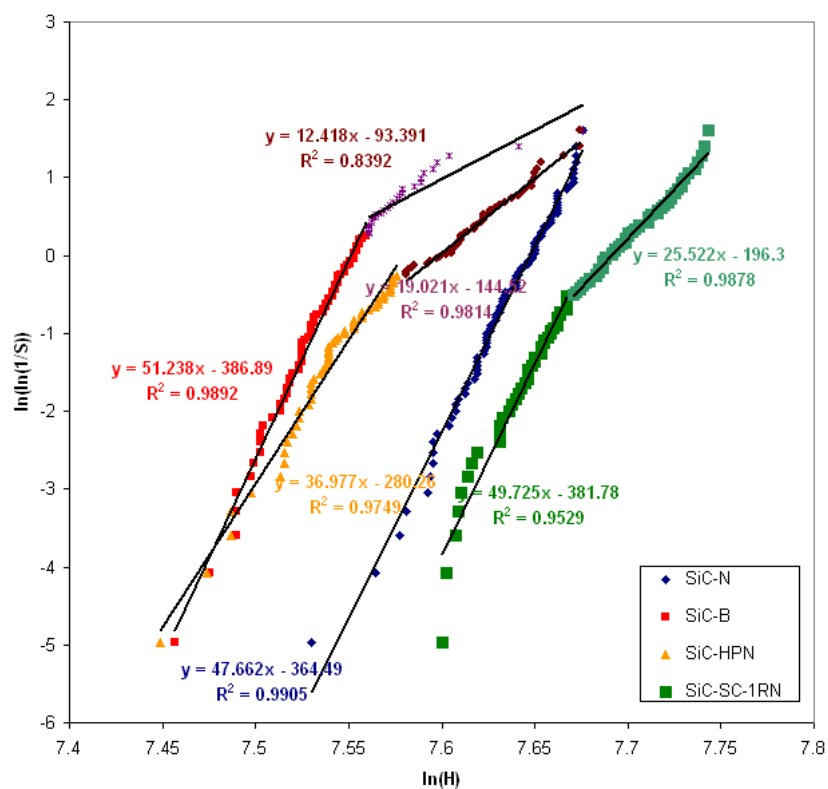


Figure 5.66. Weibull plots for each sample

5.5. Correlation between Microstructural Findings and Property Data

Microstructural results do not mean a lot when there is not enough property information that can be correlated with. Therefore, the information from these two sources will be tested to see if there is any link in between. This will be applied to all the samples that were discussed up to this point. Lundberg samples have the additional information of ballistic data which provides the opportunity to test any correlation between microstructure and ballistic performance.

5.5.1. Off-Density Hexoloy Samples

Initially, average hardness values at 2 Kg were plotted against $[(Q-1)^2 + (V-1)^2]^{1/2}$ parameter, which can also be called $d(1,1)$. This parameter was obtained from nearest neighbor distance distribution to gauge the distance to the random point, (1,1). The plot is given in Fig. 5.67. Q and V values were averaged from the four layers that were analyzed. $d(1,1)$ parameter was calculated for SA-1, SA-2, EXT and SP as 2.73, 1.64, 2.03 and 2.51, respectively. According to the plot, as the spatial distribution of defects approaches random ideal random point, an increase in hardness is observed. The R^2 value was reasonably high with 0.74.

Another factor that should be considered was the average defect size. This parameter was plotted against average hardness value at 2 Kg. The combined results from all layers are given in Fig. 5.68. The plot shows fairly good correlation between average defect size and average hardness with R^2 value of 0.70. Overall, both average defect size and spatial distribution of defects generate an interesting link with hardness. It is hard to separate which one is more important in affecting hardness data; however, it could be

likely that each one contributes to the result significantly. As discussed earlier, hardness has a close correlation with ballistic performance; therefore, we can extrapolate the current results and conclude that spatial distribution of defects is as important as the size of the defects present in the material, which can impact the ballistic performance of a material.

5.5.2. SiC Hexoloy SA Tile

Correlations with microstructure and hardness data were performed using the data from the pieces of SiC Hexoloy SA tile. The first graph is given in Fig. 5.69 where average hardness was plotted against average defect size. As mentioned previously, the “good” area, which is Region 2, possesses slightly lower average defect size and again, somewhat higher hardness. This produces a trend shown in Fig. 5.69 as the defect size decreases; there is an increase in the average hardness. The R^2 value is quite high with 0.94. This result is consistent with some of the data presented previously.

Fig. 5.70 looks at the link between the average defect size and Weibull modulus. There is again a positive correlation between these two parameters with R^2 value of 0.76.

Fig. 5.71 displays the link between distance to the random point and average hardness. The R^2 number is significantly high with a value of 0.99. However, it should be mentioned that this is a correlation that is counterintuitive. As discussed previously in the microstructure section, smaller numbers indicate proximity to the random case where larger numbers show deviation from this. As a result, this high R^2 value is misleading and it does not present a positive correlation.

Similar trend was observed in Fig. 5.72 where $d(1,1)$ was plotted against Weibull modulus. The argument made in the previous paragraph is still valid with R^2 of 0.87. This is contradictory to what is expected. On the other hand, differences between these three values regarding the spatial distribution of defects are minor. It is actually showing a very small difference, therefore, it does not really demonstrate that spatial distribution of defects is not important in terms of its effect on properties. It just shows that differentiation among very similar samples is not enough to comment on this aspect of a microstructure.

Fig. 5.73 shows another link between hardness data and microstructural properties where percentage hardness data was plotted against average defect size. The homogeneity of the hardness contour map was linked with the average defect size, which shows a positive correlation. The R^2 value is reasonably high with 0.72. This translates into the notion that smaller defect sizes produce uniformity in the hardness data.

The homogeneity of the hardness values were plotted against the microstructural spatial distribution parameter, which is given in Fig. 5.74. The R^2 coefficient is considerably low with a value of 0.58. If the results in Fig. 5.73 and Fig. 5.74 are considered, it implies that size is a more important factor in terms of hardness homogeneity than the spatial distribution of defects for this particular set of samples.

5.5.3. Cercom Hot-Pressed Samples

Microstructure and hardness results are also correlated using the data on three hot-pressed samples from Cercom. First, the distance of data points to the random point (1,1) in the Q-V plot is obtained. The values for LD, AG and DEF are 2.85, 1.85 and 1.38,

respectively. These values are plotted against average hardness values. Fig. 5.75 shows $d(1,1)$ against average hardness value at 2 Kg. The graph has a negative slope as AG and DEF have lower $d(1,1)$ values and higher hardness averages with respect to LD. The fit value for this plot is reasonably high with 0.93.

Same graph was plotted for hardness data at 0.3 Kg in Fig. 5.76. This looks very much like the previous graph where hardness data at 2 Kg was used. The fit value is higher in this case with a value of 0.98. These results are consistent with the thought that presence of pore clusters might cause lower hardness values as opposed to the situation of more uniform spatial distribution of defects.

One of the correlations that should be performed is the link between average defect size and average hardness, which is plotted in Fig. 5.77. The fit value is fairly high with 0.77; however, it is not as high as the values observed on the previous two graphs that show the link between hardness and spatial distribution of defects. The contribution of each parameter to hardness results could not be determined as mentioned previously since it is impossible to separate the effect of each one. Demonstrated earlier by using the off-density samples, similar outcome is obtained in this set of hot-pressed samples.

Weibull modulus values were also utilized to make a correlation between microstructure data and hardness data. Fig. 5.78 shows Weibull modulus at 0.1 Kg against average defect size. Linear dependence was observed in the plot with a fit value of 0.93. According to this plot, there is a good correlation between Weibull modulus at 0.1 Kg and average defect size.

The link between Weibull modulus and spatial distribution of defects was also examined using the plot in Fig. 5.79. A positive correlation was observed as the sample

with a microstructure closer to a random distribution produced higher modulus values. The fit value was 0.76. The results regarding Weibull modulus provide reasonable outcome as smaller average defect size and low $d(1,1)$ values were shown to lead to higher uniformity and therefore, higher, Weibull modulus values. This outcome is rational as random distribution of defects would yield more consistency in the property data.

5.5.4. Lundberg Samples

Correlation between spatial data and dynamic and static properties were obtained using the previously mentioned data and the microstructural results. Average defect size and $[(Q-1)^2 + (V-1)^2]^{1/2}$ parameters were used to test the degree of correlation between the two groups of data. The distances to the random point, $d(1,1)$, are 1.75, 1.83, 1.48 and 2.21 for SiC-N, SiC-B, SiC-SC-1RN and SiC-HPN, respectively.

Fig. 5.80 shows two plots of microstructural data against hardness. As it can be observed from both graphs, there is a certain degree of correlation with R^2 values of 0.84 and 0.71, for average defect size and $d(1,1)$, respectively. These results are reasonable since smaller defect sizes and more homogenous distribution of defects provide higher hardness values.

Elastic modulus was correlated with microstructural findings in Fig 5.81. There is not any correlation observed either between elastic modulus and defect size or with the spatial distribution of defects.

A certain degree of correlation was observed in Fig. 5.82 between fracture toughness and microstructural data with R^2 values of 0.74 and 0.69, for size and spatial

distribution, respectively. However, this is contradictory to the expected, where larger defect sizes and higher $d(1,1)$ values give higher fracture toughness values.

As it comes to the dynamic results in Fig.5.83, transition velocity does not show any correlation with average defect size with low R^2 value of 0.52. On the second plot, SiC-HPN, the sample with the highest transition velocity, shows the largest deviation from the random case.

Fig. 5.84 shows the plots of penetration velocity against average defect size and spatial distribution of defect size. There is no correlation observed for this parameter with the microstructural parameters.

The correlation between defects and average normalized projectile erosion rate was tested in Fig. 5.85. High R^2 values were obtained both for size and spatial distribution data, 0.90 and 0.79, respectively.

To sum up, it can be concluded that only small differences in the size distributions and spatial distributions of defects were observed due to the high quality of Lundberg samples. These findings were correlated with previously published and presented property data. Certain degree of correlation was observed between hardness and defect size and along with its spatial distribution. Other static property data, K_{Ic} and E , did not match up well with defect size and its spatial correlation results. Out of the dynamic properties, average normalized projectile erosion rate produced positive correlation with spatial distribution of defects and their size.

5.5.5. Comparison between hot-pressed and sintered

Since several sintered and hot-pressed samples were studied, it is reasonable to make an evaluation between the samples from two different processing routes. Two samples that seem to represent the good qualities of each processing technique will be used for evaluation. SiC-SC-1RN was chosen from Lundberg samples representing the hot-pressed samples and N5 from Region 2 was chosen from the Hexoloy tiles representing the sintered samples. The initial assessment will be based on the number of defects and the average size of defects observed in each sample. It should be mentioned once again the results were obtained from 10 images at $\times 1000$.

The number of defects and the average defect size is compared in Table 5.15. The number of defects for SiC-SC-1RN is 1923 while this number is reasonably high for Hexoloy SiC-N5 with a value of 2402. The values are also considerably different in terms of average defect size as hot-pressed SiC-SC-1RN has an average defect size value of $0.48 \pm 0.24 \mu\text{m}$. As opposed to this value, sintered Hexoloy SiC-N5 has an average defect size value of $0.91 \pm 1.15 \mu\text{m}$. The striking difference can be observed here as the value for the sintered sample is doubled by that of hot-pressed SiC.

Defect size distribution is another aspect that should be taken into account during comparison between the samples from two processing routes. Although it was presented earlier, the defect size distributions are given here side by side in Fig. 5.86. The curve for the sintered material reaches up to $4 \mu\text{m}$ in size while the plot of hot-pressed material ends below $2 \mu\text{m}$. This is natural result of processing technique differences and the superiority of hot-pressed samples both in average defect size and defect size distribution could be predicted. However, these results validate the predictions based on the processing routes of samples.

The next aspect in comparison is the spatial distribution of defects. Nearest neighbor distance distributions are given in Fig. 5.87. The plot for the hot-pressed SiC-SC-1RN is significantly narrower than that of sintered Hexoloy SiC. Sintered SiC shows more of a bell-shaped curve while SiC-SC-1RN has several large peaks followed by a tail showing very low values. The maximum peaks correspond to 200 on y-axis for hot-pressed SiC. Sintered SiC has a maximum value of 145. This difference makes it easy to explain the spread in the data of the sintered sample. Considering the fact that sintered sample has significantly higher number of defects and a lower maximum peak numbers, the spread in the data is quite reasonable.

A Q-V plot for the sintered and hot-pressed sample is given Fig. 5.88. The difference between two samples is not very significant, as the data point for hot-pressed SiC fall right by the y-axis with coordinate values of 0.99 and 2.48, for Q and V, respectively. The coordinates of the data point for sintered SiC is 1.13 and 1.93, for Q and V, respectively. Q value for the hot-pressed sample is almost 1, which is the ideal random value whereas that value is 1.13 for the sintered sample. In that case, hot-pressed sample is clearly closer to the ideal “random” case than the sintered sample. When it comes to V values, which is the ratio of variances between the calculated value and the expected value, there is a minor difference between the two samples. The variance value is higher for hot-pressed which puts the data point in Q-V map farther from (1,1) point than that of sintered sample. The reason behind this could possibly be the number of data points examined for both samples. This is considerably low for the hot-pressed sample. This relates to the fact that application of this spatial data analysis techniques depends a lot on the number of features in the field of view. Small changes could be accepted,

however, deviations from this might lead to higher variance numbers. However, it is still reasonable to say that sintered sample possesses more uniformity in terms spatial defect distributions.

In addition to microstructural differences between sintered and hot-pressed samples, property differences will also be presented. As mentioned before, hardness results are based one hundred indentations performed as a square array of indents using a Knoop indenter.

The average hardness values at 2 Kg for sintered and hot-pressed samples are given in Fig. 5.89. Sintered Hexoloy SiC has an average hardness value of 1854.2 +/- 60.8 KHN, whereas, hot-pressed SiC has an average value of 2159.6 +/- 76.6 KHN, which is a considerable difference. The defect size and number could be attributed to the difference between hot-pressed and sintered sample.

Uniformity of hardness values across the sample was examined, as explained previously, and is compared between sintered and hot-pressed samples. Hot-pressed SiC has data in three ranges in the contour map, starting from 2000-2100 KHN up to 2200-above. The major one is 2100-2200 KHN, where 60.8 % of the area is in this range. For the sintered sample, the maximum percentage is 84.7 % in the data range of 1800-1900. Hardness data for the sintered sample scatters into four ranges as opposed to hot-pressed sample's three, starting from 1700-1800 KHN up to 2000-2100 KHN. According to these results, sintered SiC displays more homogeneity. However, there is a significant difference in the contour maps since the highest range in sintered is the lowest for the hot-pressed material. Therefore, uniformity is probably inferior to absolute average in the

case of ballistic environment. The uniformity in hardness of sintered samples could be attributed to the more uniform spatial distribution of the sintered sample.

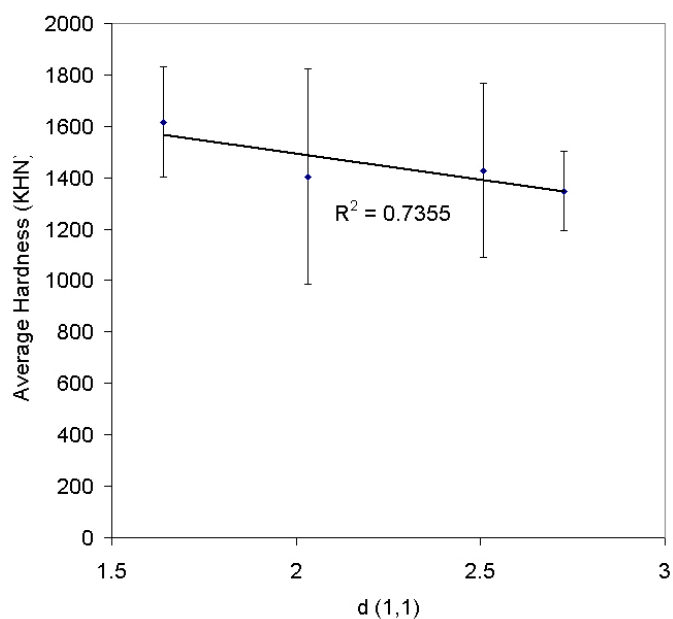


Figure 5.67. Average hardness vs. $d(1,1)$ for off-density SiC density samples

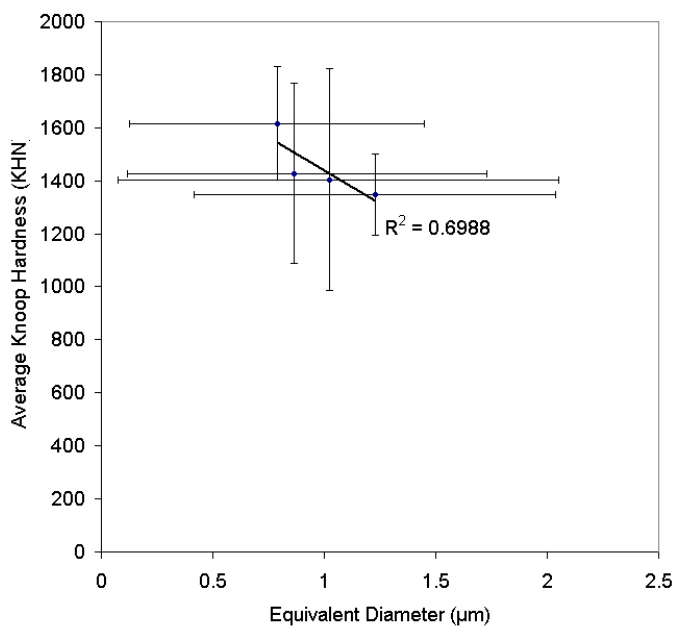


Figure 5.68. Average hardness vs. average defect size for off-density SiC samples

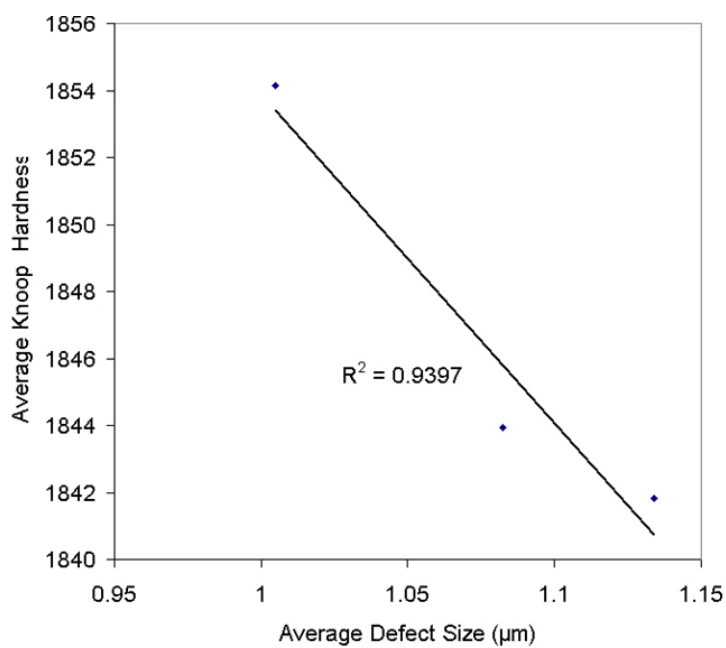


Figure 5.69. Average hardness vs. average defect size for SiC Hexoloy tile

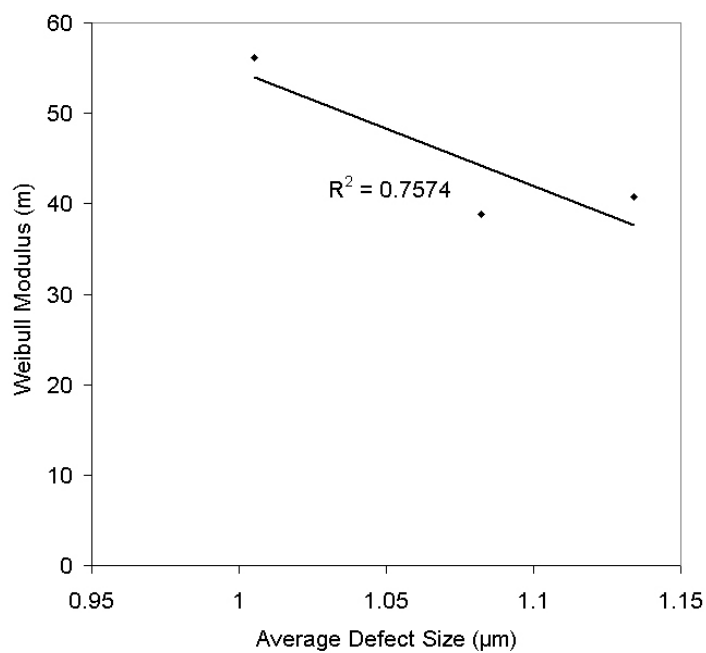


Figure 5.70. Weibull modulus vs. average defect size for SiC Hexoloy tile

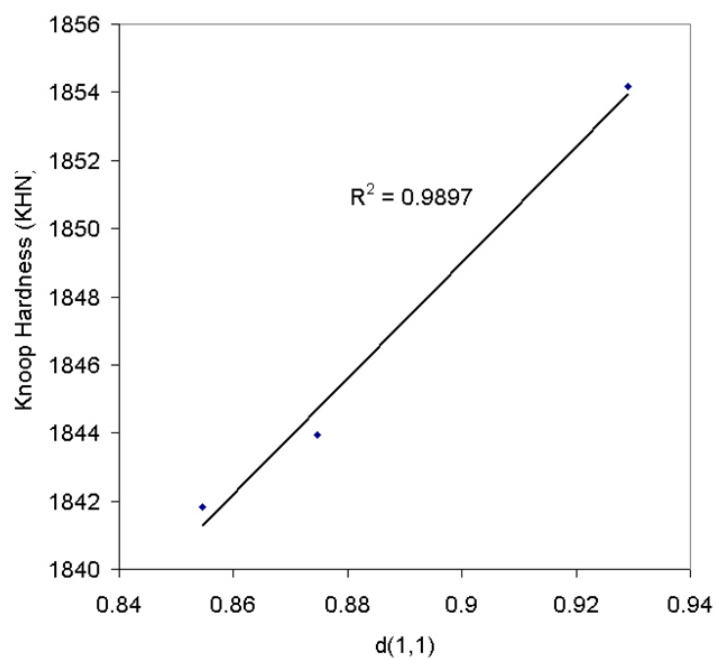


Figure 5.71. Average hardness vs. $d(1,1)$ for SiC Hexoloy tile

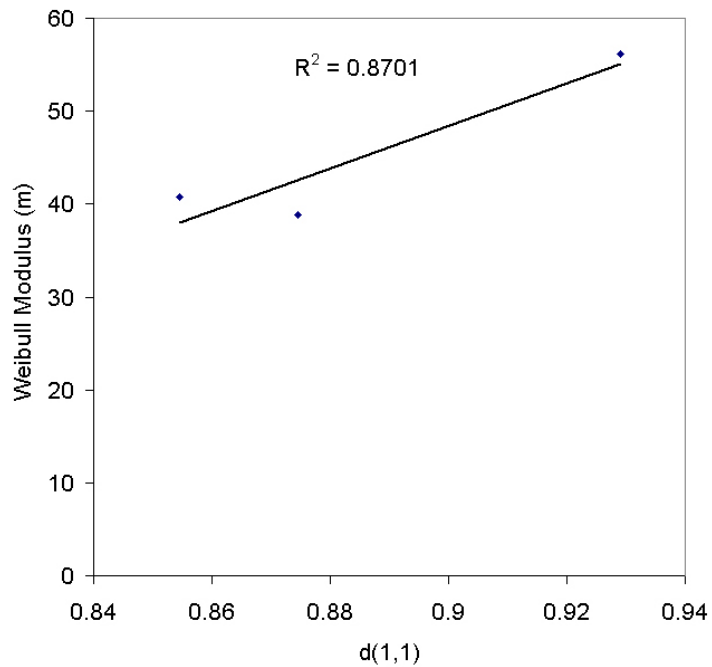


Figure 5.72. Weibull modulus vs. $d(1,1)$ for SiC Hexoloy tile

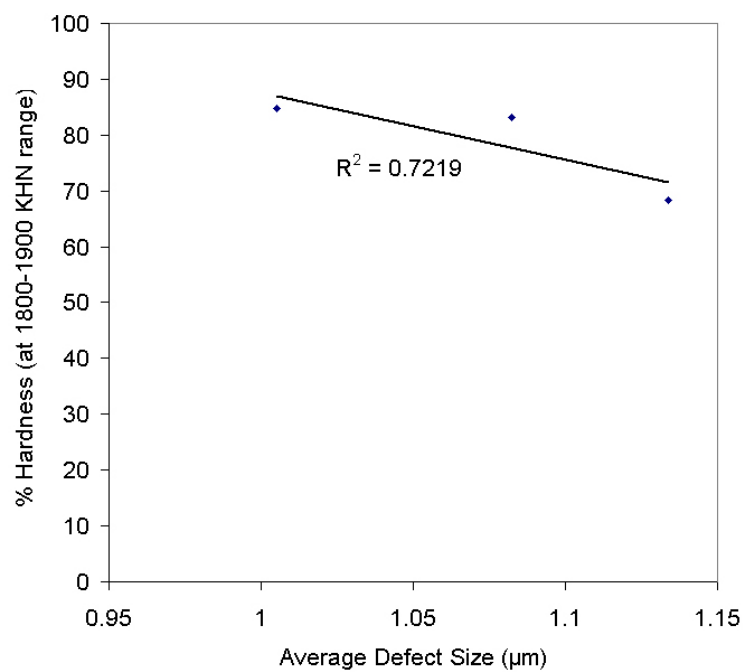


Figure 5.73. % Hardness vs. average defect size for SiC Hexoloy tile

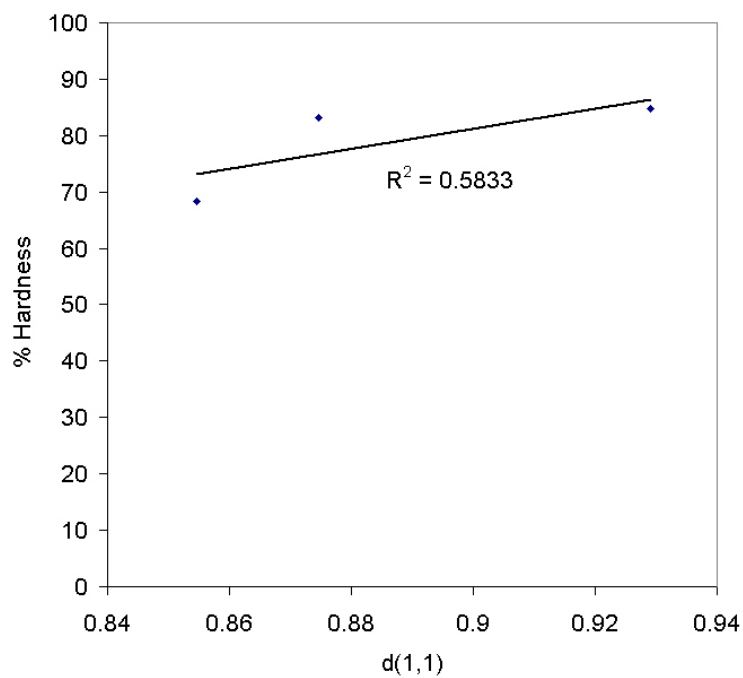


Figure 5.74. % Hardness vs. d(1,1) for SiC Hexoloy tile

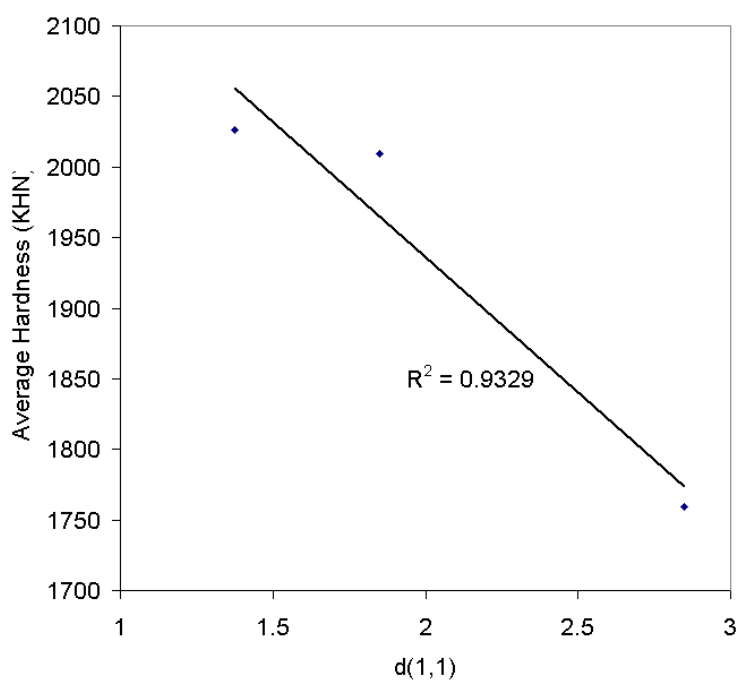


Figure 5.75. Average hardness at 2 Kg vs. $d(1,1)$ for hot-pressed SiC samples from Cercom

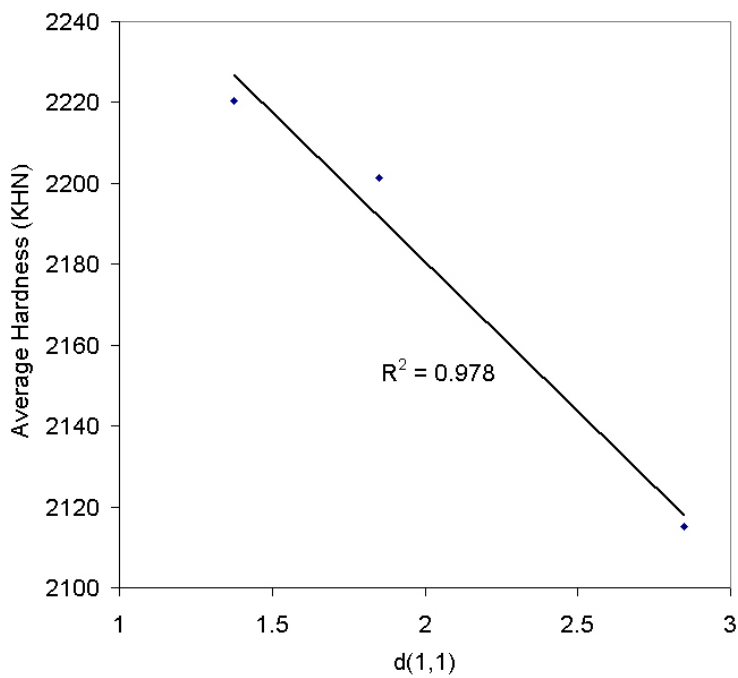


Figure 5.76. Average hardness at 0.3 Kg vs. $d(1,1)$ for hot-pressed SiC samples from Cercom

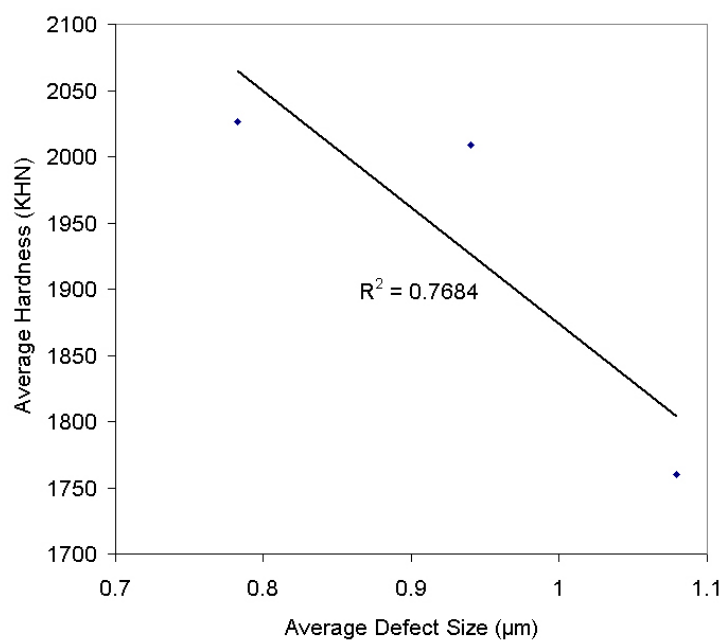


Figure 5.77. Average hardness vs. average defect size for hot-pressed SiC samples from Cercom

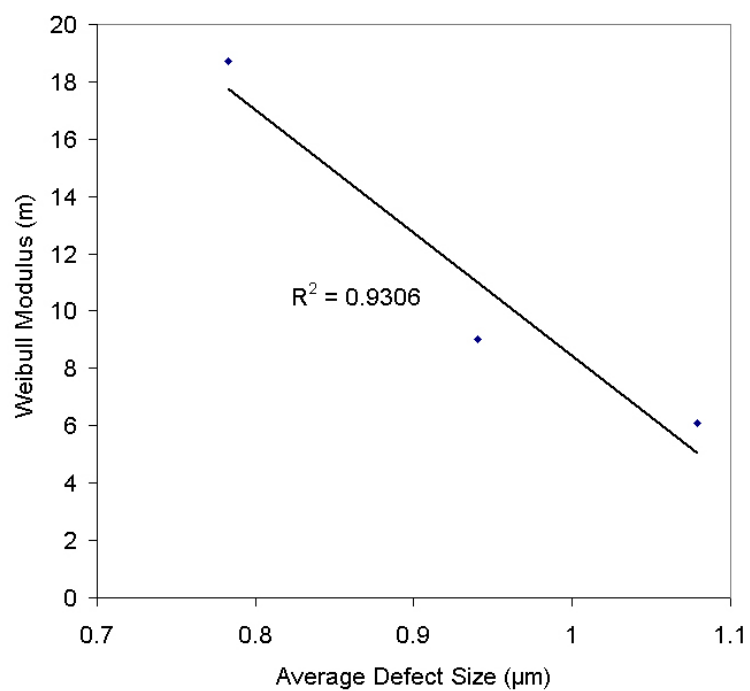


Figure 5.78. Weibull modulus at 0.1 Kg vs. average defect size for hot-pressed SiC samples from Cercom

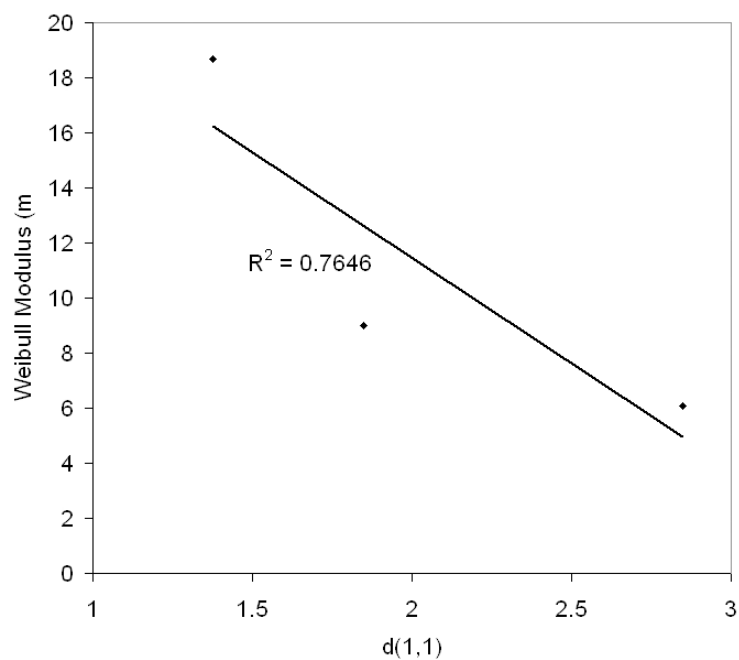


Figure 5.79. Weibull modulus at 0.1 Kg vs. $d(1,1)$ for hot-pressed SiC samples from Cercom

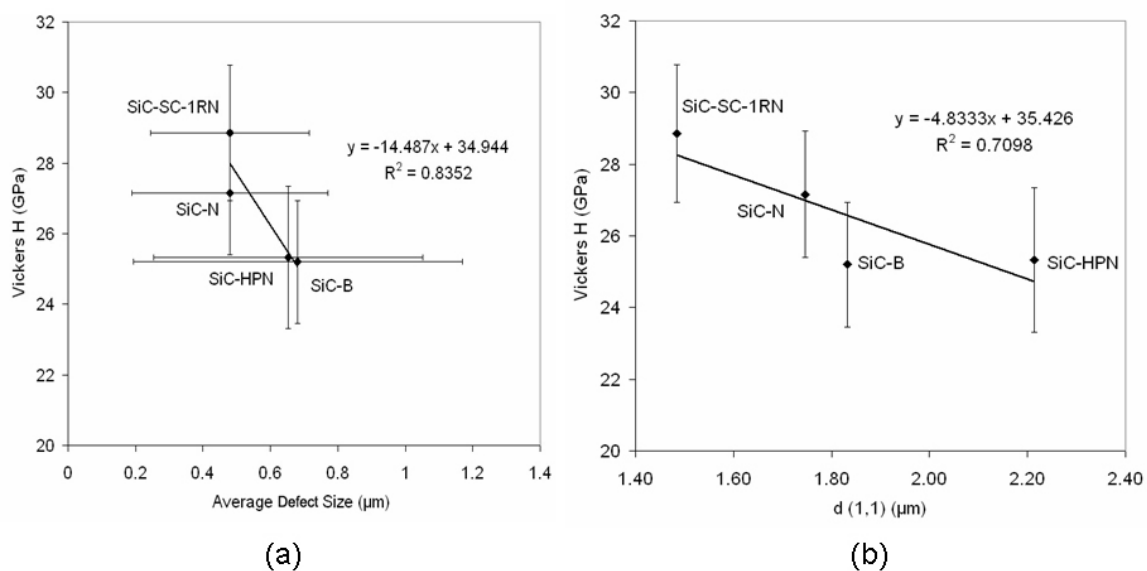


Figure 5.80. (a) Average hardness vs. average defect size (b) Average hardness vs. $d(1,1)$ for Lundberg samples

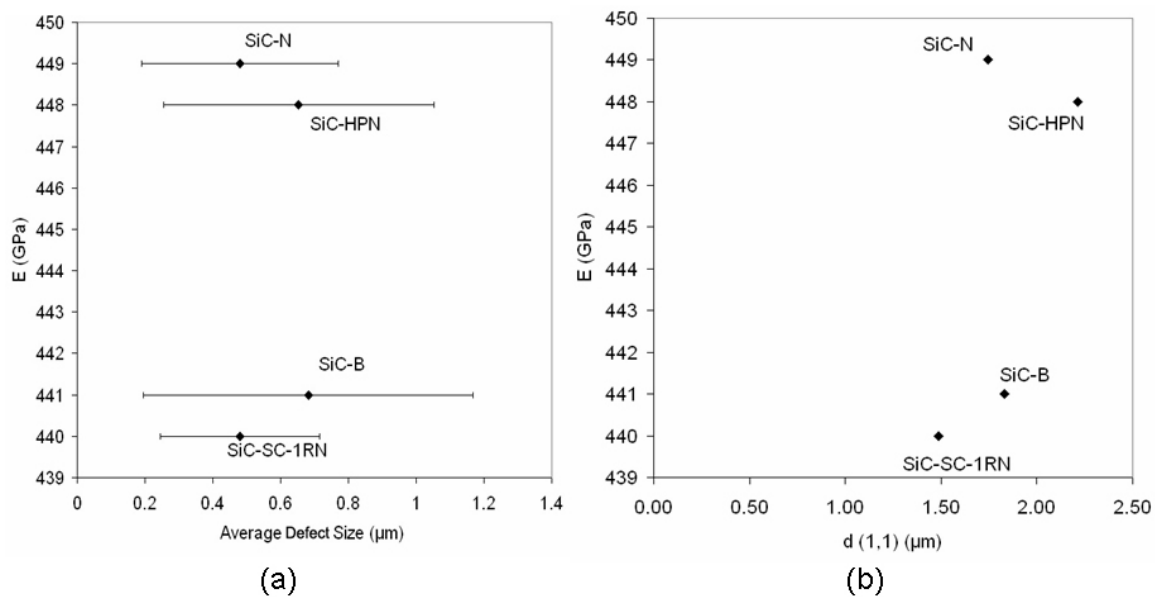


Figure 5.81. (a) Elastic modulus vs. average defect size (b) Elastic modulus vs. $d(1,1)$ for Lundberg samples

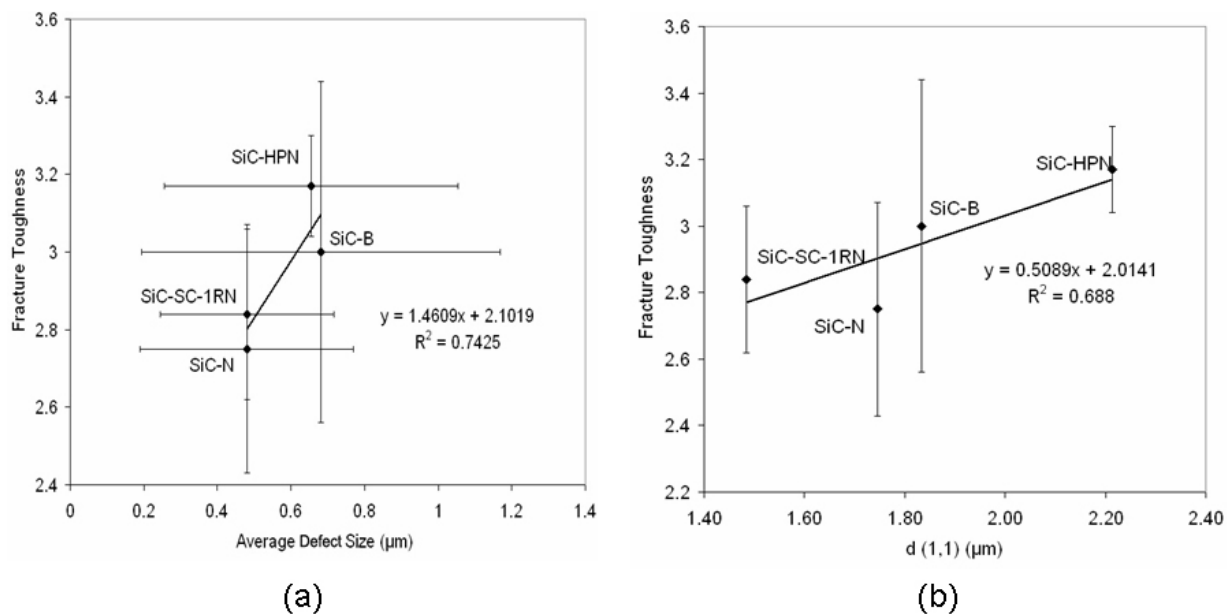
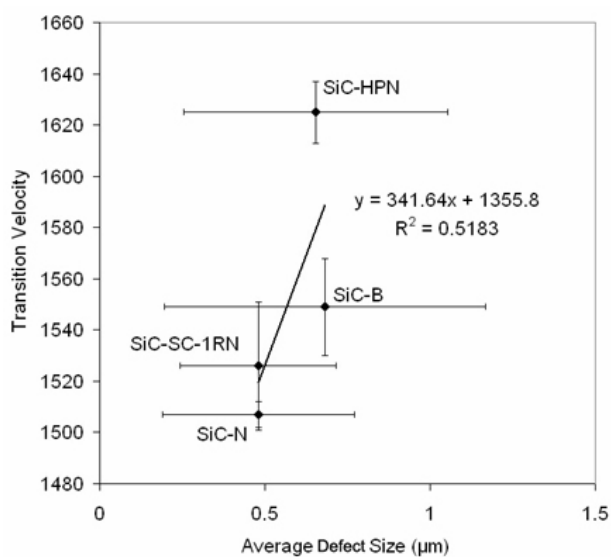
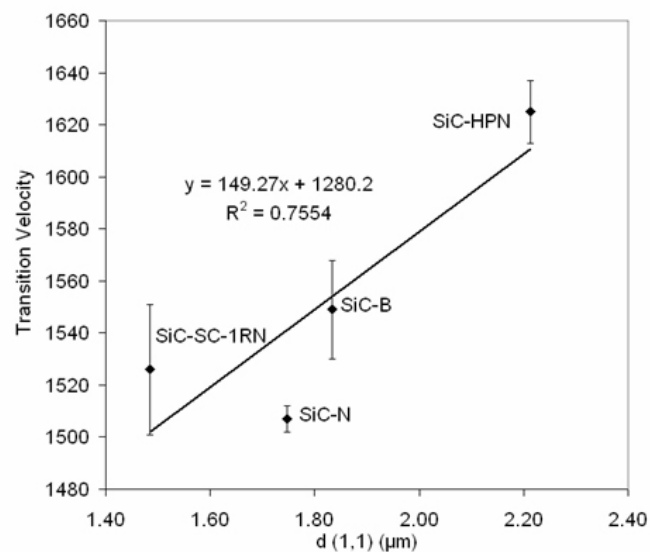


Figure 5.82. (a) Fracture toughness vs. average defect size (b) Fracture toughness vs. $d(1,1)$ for Lundberg samples

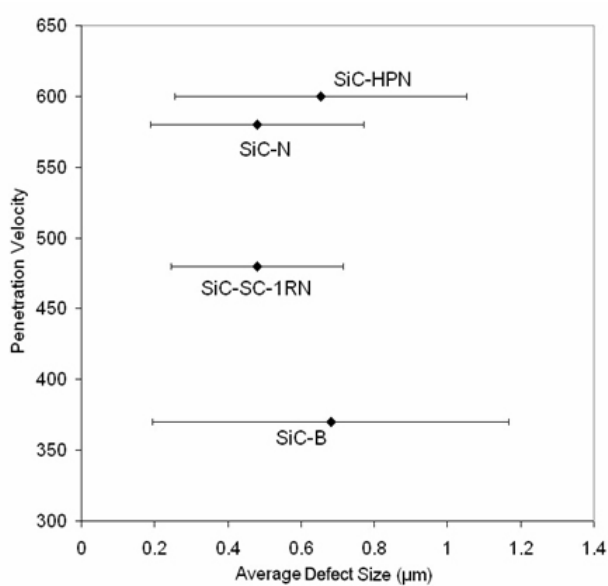


(a)

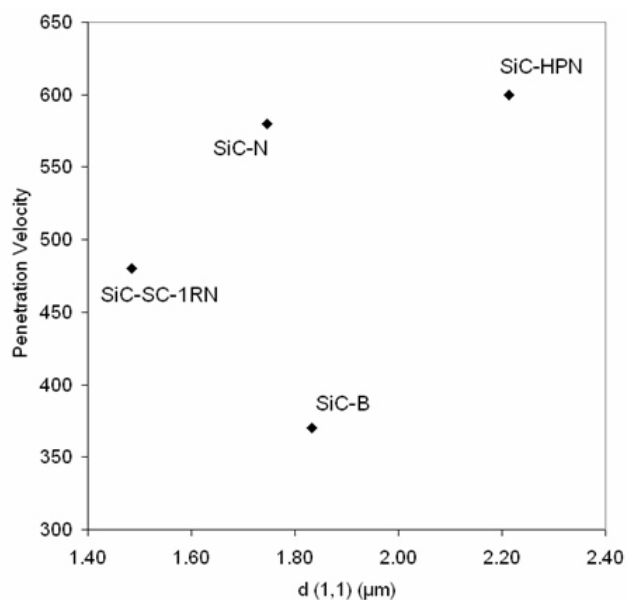


(b)

Figure 5.83. (a) Transition velocity vs. average defect size (b) Transition velocity vs. $d(1,1)$ for Lundberg samples



(a)



(b)

Figure 5.84. (a) Penetration velocity vs. average defect size (b) Penetration velocity vs. $d(1,1)$ for Lundberg samples

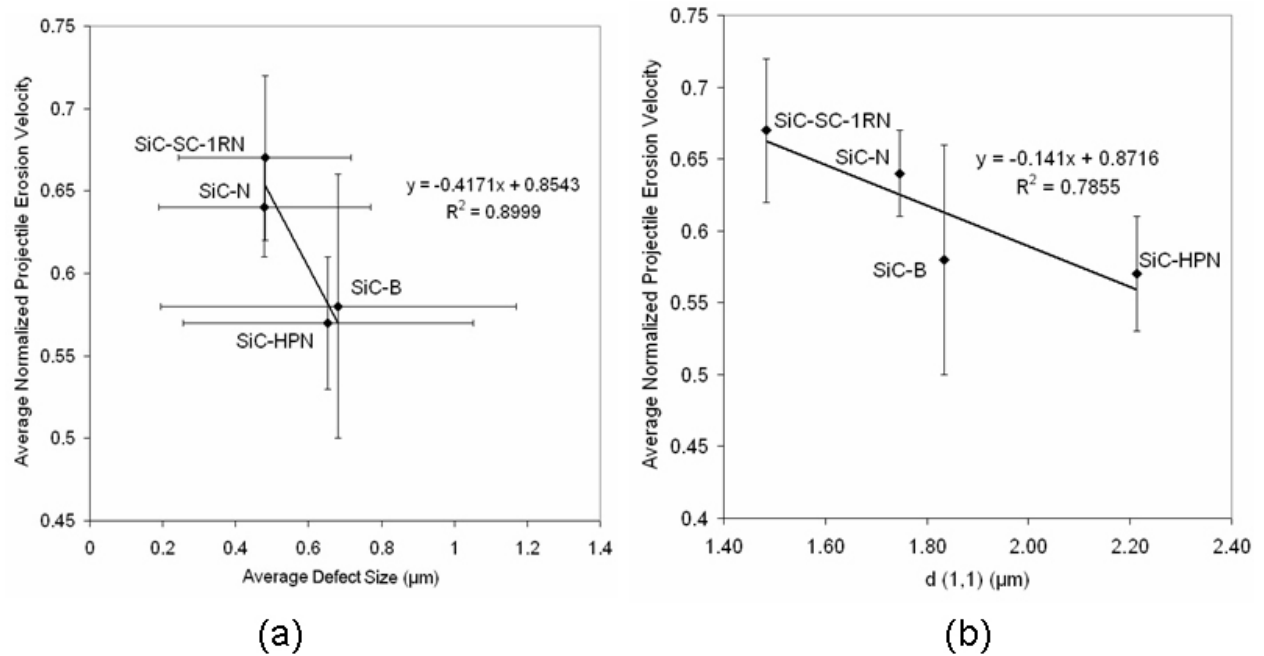


Figure 5.85. (a) Average normalized projectile erosion rate vs. average defect size (b) Average normalized projectile erosion rate vs. $d(1,1)$ for Lundberg samples

Table 5.15. Number of defects and average defect size for sintered and hot-pressed SiC

	Sintered SiC	Hot-pressed SiC
Number of defects	2402	1923
Average defect size (μm)	0.91	0.48
Standard deviation (μm)	1.15	0.24

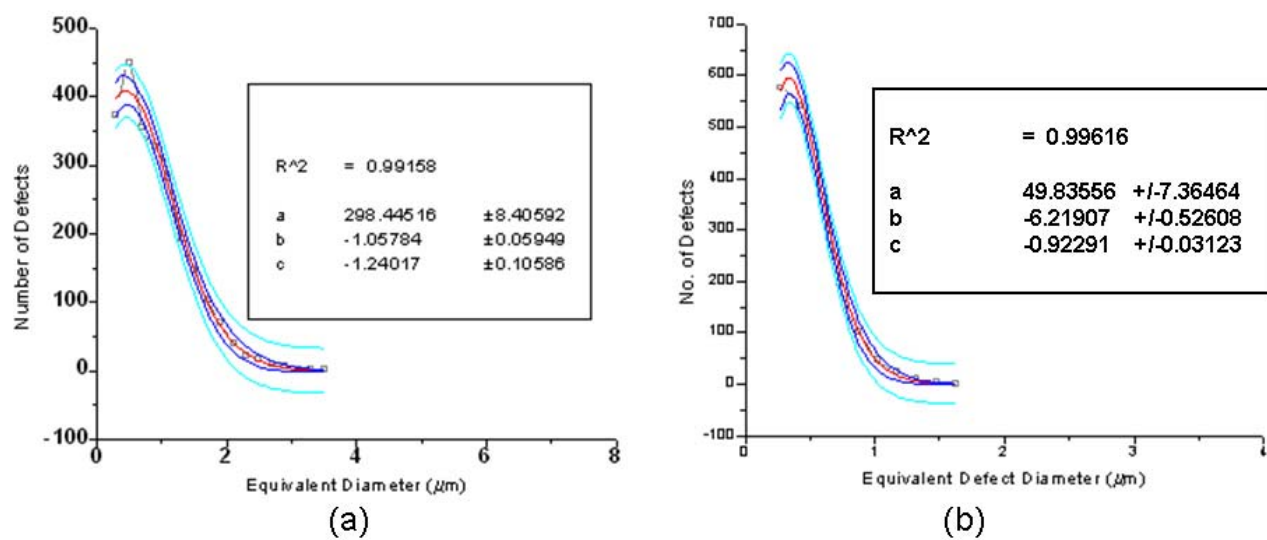


Figure 5.86. Defect size distribution of (a) sintered (b) hot-pressed SiC

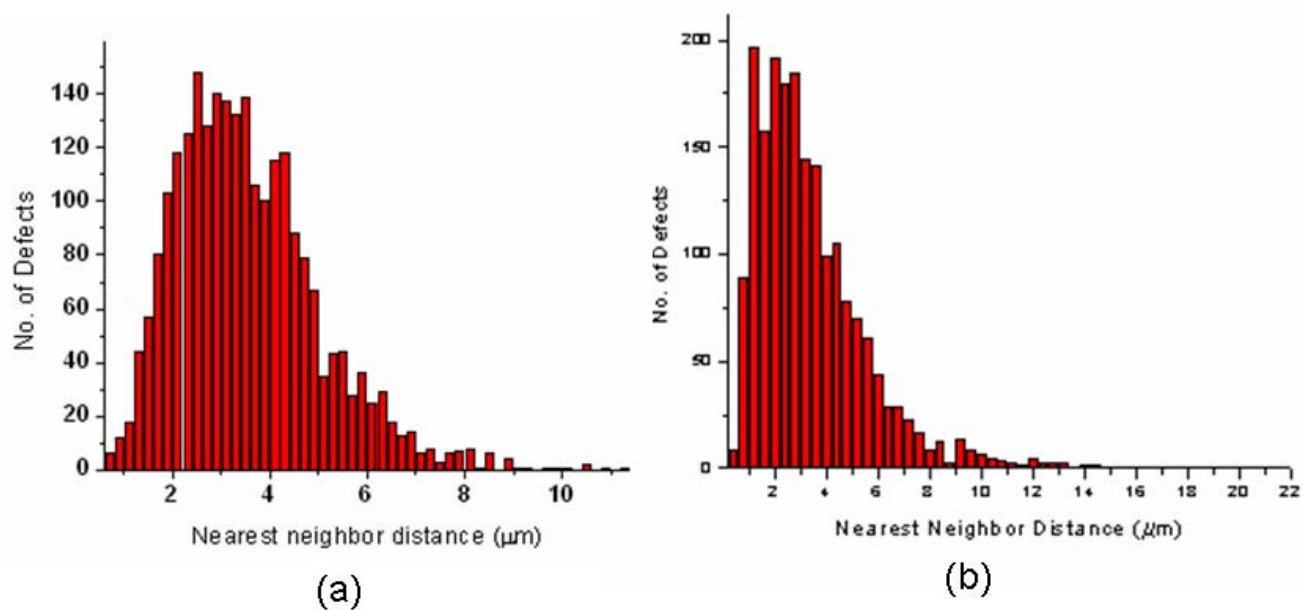


Figure 5.87. Nearest neighbor distance distributions of sintered and hot-pressed SiC

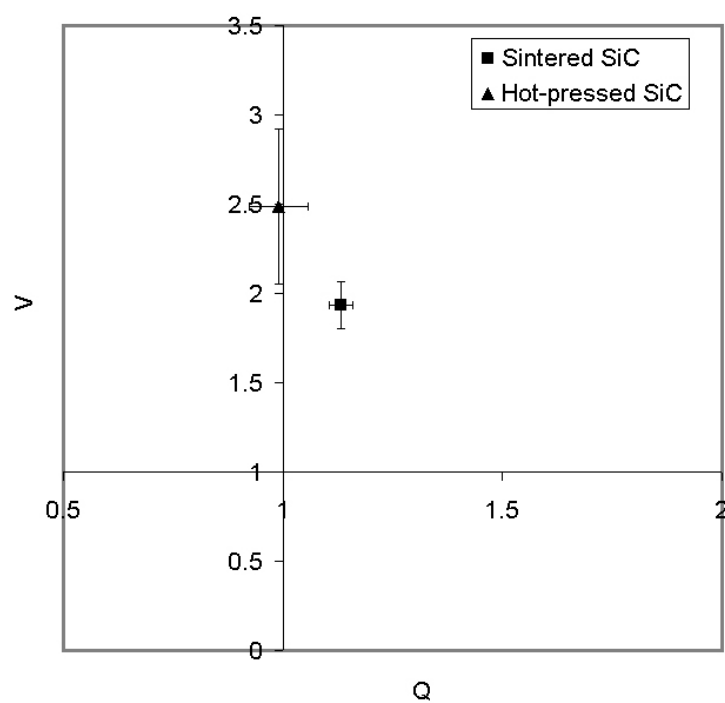


Figure 5.88. Q-V plot for sintered and hot-pressed SiC

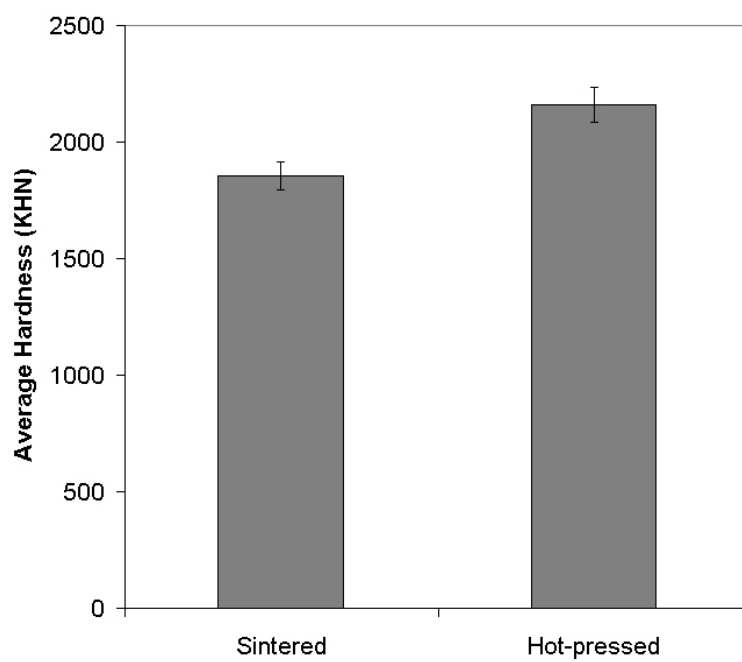


Figure 5.89. Average hardness for sintered and hot-pressed SiC

5.6. Practical Implications of This Thesis

This thesis provides a methodology for utilizing spatial data analysis in materials science. Microstructural characterization focused on the spatial arrangement of defects was performed due to its importance in the performance of the final product. Quasi-static property determination was used to obtain volumetric information regarding the homogeneity of microstructures. Possible implications of this methodology include four distinct applications including green body examination, final part examination in manufacturing, at decision making during purchasing of parts, and on investigation of different material subgroups other than bulk ceramics.

Uniformity in green bodies is essential since characteristics before sintering are carried over to the final product after sintering. The methodology used in this thesis could be applied to green bodies, where defect distribution uniformity is assessed, and parts that do not match preset standards could be rejected. The integrity of green bodies could be achieved by epoxy impregnation, which would hold the material together. Assessment on green bodies is particularly important due to conservation of time and energy by avoiding the unnecessary sintering of poor quality green bodies that would eventually provide poor quality materials. If lower-than-standard green bodies could be detected before sintering, the yield at the end of product line would be higher. In addition, recycling of rejected green bodies is technically much more feasible than rejected sintered bodies.

The second application could be in manufacturing line where pass/fail criteria are required in armor ceramics. The absolute density is used as a threshold value for accepting or rejecting parts, however, density variation within a part could be just as important as explained throughout this thesis. The destructive nature of this technique could be a drawback in manufacturing since quick assessment is important; however, this

method could be coupled with ultrasound to obtain a better assessment on sample uniformity. This method could also be valuable for the customer as much as the manufacturer. It could be used as a decision making criteria during purchasing.

Although, this thesis was focused in silicon carbide armor ceramics, same type of analysis could be very valuable regardless of the material of interest and the field of study. The methodology used in this thesis could be applicable to any material where homogeneity of microstructure plays an important role and uniformity is a desired attribute. Research on coatings, particle reinforced or fiber composites could be potential areas since homogeneity is a key attribute.

6. CONCLUSION

A means of quantifying microstructures were established in order to develop the criterion for good/bad armor. Quasi-static tests were conducted to correlate the results from microstructural analysis. Serial sectioning has been carried out to examine the degree of variability between layers. Nondestructive ultrasound results and spatial data analysis were combined in order to assess uniformity in SiC armor ceramics.

6.1. Off-Density Hexoloy Samples

Initially, three different techniques, nearest neighbor distance distributions, tessellation analysis, and pair correlation functions, were used to examine spatial distribution of pores in SiC. This sample set was used as a standard to test the feasibility of different spatial analysis methods

According to the nearest neighbor distance distributions, Q values for all four samples are approximately equal to 1; however the V values differ strongly from the random case. SA-2 is the only one whose V value is roughly 1. Tessellation analysis results produced close values as P_1 and P_2 parameters were calculated for all samples. SP has a strong deviation from the random case with the P_1 and P_2 values of 3.28 and 15.78, respectively, as opposed to 1, which is the expected value for random distribution of particles. Pair correlation functions provided plots of EXT and SP that have sharp peaks very close to the y-axis. Strong first peak at a distance well below the mean interparticle distance (r_0) followed by a weak minimum at about this distance is an indication of clustering. The curves for SA-1 and SA-2 were typical random distribution curves.

As summarized above, similar trends were observed in each technique and no significant difference was observed among the three. Therefore, nearest neighbor distance

distributions was established as a convenient method to evaluate spatial distribution of defects.

Hardness tests were then used to obtain volumetric information regarding the homogeneity of microstructures. Theoretical values according to Rice's model and calculated values were compared. The calculated values for SA-1, SA-2, EXT and SP were found to be 1824.3, 1846.7, 1738.6 and 1780 Kg/mm², respectively. The actual measured values at 0.5 Kg were 2128.0, 1925.0, 1676.0, and 2016.9 Kg/mm². The discrepancy between calculated values and measured values was attributed to the inhomogeneity of microstructures and nonuniform defect distribution.

Weibull analysis showed bimodal Weibull distributions at multiple indentation loads. This observation was attributed to the presence of different phases in SiC. In the case of these Hexoloy SiC samples, other than the matrix and pores, carbon inclusions are present in the microstructure. According to the results, these inclusions contribute to the bimodal distribution in these samples.

The crack paths were examined after indentation at 2 Kg load. Intergranular fracture was seen at 14% of all the indentations observed. This was due to the cracks being deflected from the carbon inclusions/SiC matrix interfaces and consequently, a significant amount of intergranular fracture mode was observed.

Microstructure and hardness correlations were performed. According to the plots, as the spatial distribution of defects approaches random point, an increase in hardness was observed. The average defect size was tested by plotting it against average hardness value at 2 Kg. The plot showed fairly good correlation between average defect size and

average hardness. Both average defect size and spatial distribution of defects generated a strong correlation with hardness.

6.2. Cercom Hot-pressed SiC samples

Microstructural and property determination analyses were performed on three hot-pressed SiC samples that had low density region (LD), a white spot that caused rejection of the tile (DEF), and an armor grade material (AG). Among the three samples, DEF has the smallest pore size. LD has the largest pore size and also the highest standard deviation. In terms of defect size distributions, LD has the broadest distribution among the three, which is consistent with the previously ultrasound results.

AG and DEF show relatively narrow nearest neighbor distance distributions with the variance values of 3.47 and 2.94 μm^2 , respectively, while LD shows a higher variance value with 5.51 μm^2 and broader distribution compared to the other two samples. This is an indication of inhomogeneous distribution of defects that LD possesses. In Q-V plots, all points fall in between the two lines that could be labeled as “random”. However, there is a minor difference between LD and the other two samples where LD is in the region of random distribution with clusters while AG and DEF do not show any clustering according to the plot. In addition to the larger average defect size, clustering of defects were also observed, which contributed to the lower ultrasound signal.

Lower average hardness results were observed for LD for most indentation loads. Off-density values would cause lower hardness outputs so, when the density values, which were 3.18 g/cm³, 3.19 g/cm³ and 3.20 g/cm³ for LD, DEF and AG, respectively, were considered, these hardness findings become especially reasonable.

A change in indentation load lead to a decrease in slopes at Weibull plots. Lower indentation loads affected smaller areas. Due to the less likelihood of the indenter coming in contact with pores, or clusters of pores, a larger statistical spread was obtained at the end. The likelihood that an indent fell partially or completely on a defect or a group of defects affected the hardness value drastically. Especially at low indentation loads, the probability of an indent and a defect interaction was lessened.

According to grain size distributions around high and low hardness regions, it can be concluded that hardness value changes cannot be attributed to grain size variations in each sample. The conclusion was that the presence of defects, on the surface or underneath, plays an important role in the indentation process without a significant effect from grain size for these particular samples. Apart from grain size distribution around these specified regions, grain size clustering was also examined. A strong deviation from random distributions was observed around the area of low hardness regions. According to this result, carbon inclusions are the main reason of grain size variation in the microstructure.

Positive correlations were found between average hardness values and $d(1,1)$, Weibull modulus and average defect size. R^2 values up to 0.98 were reached in these correlations. The effect of defect size and homogeneity of distribution was verified with these results.

6.3. Lundberg Samples

This sample set showed small differences regarding the size of defects. This could be attributed to the fact that all samples were high quality, armor grade SiC ceramics.

Curve fitting was performed on the defect size distribution plots. It was observed that the function used for the fit was a version of inverse power law. Defect size distributions were found to obey inverse power law according to numerous studies, therefore, the current observation noteworthy. R^2 values for all of them were above 0.90, SiC-SC-1RN with the highest value of 0.99 and SiC-HPN with the lowest value of 0.94.

Weibull analysis data showed close values with SiC-N, SiC-B and SiC-SC-1RN having 47.7, 51.2 and 49.7, respectively. SiC-HPN has a modulus value of 36.9, which is moderately different from the grouping observed with the other three samples. None of the samples showed any significant difference to the other, which could again be attributed to the high quality of the samples, although ballistic tests displayed a certain degree of difference.

Correlation between spatial data and dynamic and static properties were obtained. Average defect size and, $[(Q-1)^2 + (V-1)^2]^{1/2}$ or $d(1,1)$, parameters were used to test the degree of correlation between the two groups of data. In the plots of microstructural data against hardness, there is a certain degree of correlation with R^2 values of 0.84 and 0.71, for average defect size and $d(1,1)$, respectively. These results are reasonable since smaller defect sizes and more homogenous distribution of defects provide higher hardness values.

One of the dynamic properties, the transition velocity does not show any correlation with average defect size with low R^2 value of 0.52. On the second plot, SiC-HPN, the sample with the highest transition velocity, shows the largest deviation from the random case. There is also no correlation observed for this parameter with the microstructural parameters in the plots of penetration velocity against average defect size and spatial distribution of defect size. However, the correlation between defects and

average normalized projectile erosion rate was tested and high R^2 values were obtained both for size and spatial distribution data, 0.90 and 0.79, respectively.

It can be concluded that only small differences in the size distributions and spatial distributions of defects were observed due to the high quality of Lundberg samples. These findings were correlated with previously published and presented property data. Certain degree of correlation was observed between hardness and defect size and along with its spatial distribution. Other static property data, K_{Ic} and E , did not match up well with defect size and its spatial correlation results. Out of the dynamic properties, average normalized projectile erosion rate produced positive correlation with spatial distribution of defects and their size.

6.4. Hexoloy SA Tile

A lot of eight SiC Hexoloy tiles were scanned using ultrasound. Low and high amplitude regions were identified and one tile from that lot was selected for further microstructural evaluation by using diced pieces from those regions. Initially, high magnification assessment was performed. In the pore size distribution plots, N5 and N8 have graphs that end at roughly 4 μm size while x-axis in plots of N4 and N9 extend to 6 μm . N1 possesses the largest sized features as the graph ends at 7 μm . This size difference between samples could provide partial explanation for the changes in ultrasound signals within the tile. High R^2 values were obtained once again using a version of inverse power law for all samples. Regional information showed that Region 2 has defects up to 4 μm in size while the curves for Region 1 and Region 3 extend right below 6 and 7 μm , respectively. Again, the large-sized features could also be important in

the signal loss observed in certain parts of the tile. In the low magnification examinations, the largest sized features that N4, N5 and N9 possess were all in the between 20-30 μm , while that value increased gradually, reaching up to 63 μm for N1.

The Q-V map showed remarkable results as the average data points for three out of six samples fell into the region of “clustering in a random background”. The samples from “good” region and N4 fall in the confidence interval of a “random” distribution. These results are very significant in terms of explaining the differences observed in an ultrasound C-scan map. Clustering of defects is a considerable factor among other possible reasons for variations.

A method for identification of clusters was established by defining a parameter called *limiting interevent distance*, which was described as the radius of a cluster which contains all the features, or events, inside a circle. This value was found to be equal to 20 μm after rigorous iterations. This method is particularly important for assessing the effect of clusters in dynamic tests.

Serial sectioning was performed for all SiC samples in this set. Although, no significant difference was observed in terms of density and average defect size, t-tests showed that the difference in the largest defect size observed in “good” and “bad” regions was statistically significant. The signal loss observed in ultrasound C-scans could partially be attributed to this fact.

The correlation between high amplitude regions of ultrasound and hardness data was observed in contour maps as Region 2 has the highest percentage of hardness data with 84.69% in the most dominant data range, 1800-1900 Kg/mm^2 . Region 3 is a close second with 83.20%. However, for the higher range, 1900-2000 Kg/mm^2 , it is much

inferior to Region 2 with 5.99 % to Region 2's 9.16%. The difference in ultrasound signals in the sintered Hexoloy SA tile was conformed by hardness contour maps.

6.5. Overall Conclusions

Microstructure homogeneity was spatially assessed using tessellations, nearest-neighbor distance distributions and pair correlation functions. Numerical quantification of spatial defect patterns was obtained by these three techniques. Trends that were observed in one technique were validated by another and consequently, no significant difference was observed among the three. Therefore, nearest neighbor distance distributions was established as the most convenient technique to evaluate spatial distribution of defects.

Hardness tests were then used to obtain volumetric information regarding the homogeneity of microstructures. Weibull distributions were used for studying variability of hardness data. Bimodal Weibull distributions were noticed at multiple indentation loads, which were attributed to the presence of different phases such as pores and carbon inclusions common in sintered SiC. Decrease in indentation load led to a decrease in slopes of Weibull plots. Especially at low indentation loads, the probability of an indent and a defect interaction was found to be lessened, which is the reason for change in slopes.

According to the crack path observations, a significant amount of intergranular fracture was attributed to the cracks being deflected from the carbon inclusions/SiC matrix interfaces.

Positive correlations were found between average hardness values and $d(1,1)$, Weibull modulus and average defect size. R^2 values up to 0.98 were reached in these

correlations. The effect of defect size and homogeneity of distributions on hardness was verified with these results.

Regarding Lundberg samples with the ballistic data, a certain degree of correlation was observed between hardness and defect size and along with its spatial distribution. K_{Ic} and E did not produce any positive correlation with defect size and spatial analysis results. Average normalized projectile erosion rate was the only property that produced positive correlation with spatial distribution of defects and their size.

Serial sectioning was performed on pieces from a Hexoloy SiC tile. Although, no significant difference was observed in terms of density and average defect size, t-tests showed that the difference in the largest defect size observed in “good” and “bad” regions was statistically significant. The signal loss that was observed in ultrasound C-scans is partially attributed to this fact.

Particularly high degree of correlation was observed between average defect size, spatial distributions parameters and hardness data. These findings exhibit the strong effect of microstructure on the quasi-static properties, and ultimately, ballistic performance.

7. FUTURE WORK

This study laid the groundwork on microstructural assessment concentrated on the spatial distribution of defects and its correlation with the quasi-static property measurements. Although it is difficult to obtain ballistic data or have ballistic tests done due to regulations, ballistic tests should be incorporated in order to assess the type of correlation using the data obtained throughout this study. Sphere-on-plate impact evaluation would be valuable in order to acquire dynamic properties for the studied samples.

The interaction between defects and indents could be studied more extensively since clusters of defects were identified using nearest neighbor distance distributions. Knowing the exact location of clusters could also be important during the dynamic tests as their effect on the performance could be quantified.

The database created on different sets of sintered and hot-pressed samples could be used as input for Finite Element Modeling (FEM). The effect of clustering on the ballistic performance could be simulated by FEM. This would provide the insight to determine local stress and strain fields in the microstructures made up of clusters of defects as opposed a random distribution of defects.

In addition to the destructive characterization techniques, nondestructive evaluation by ultrasound could be performed on the same set of samples and the amount of collaboration between these two techniques shown in this thesis could be extended further.

This study concentrated mainly on silicon carbide; however, the same type of analysis could be performed on different armor materials. The technique introduced in

this thesis could even be valuable for evaluating materials other the field of armor ceramics.

Eventually, the results from microscopy, property analysis, FEM modeling and ultrasound could be correlated for a better ballistic assessment of armor ceramics.

8. REFERENCES

- [1] H. Luo, W. W. Chen, A. M. Rajendran, "Dynamic compressive response of damaged and interlocked SiC-N ceramics", *Journal of the American Ceramic Society* 89
- [2] D. E. Grady, "Shock-wave compression of brittle solids", *Mechanics of Materials* 29 (1998) 181-203
- [3] N. Bourne, J. Millett, Z. Rosenberg, N. Murray, "On the shock induced failure of brittle solids", *J. Mech. Phys. Solids*, Vol. 46. No. 10, pp. 1887-1908 (1998)
- [4] B.R. Lawn, T.R. Wilshaw, "Dynamic Processes in Fracture", *Fracture of Brittle Solids*, pp. 91-108, 1975
- [5] D.E. Grady, "Shock-wave Compression of Brittle Solids", *Mechanics of Materials*, Vol. 29, pp. 181-203, 1998
- [6] Z.X. Zhang, S.Q. Kou, J. Yu, Y. Yu, L.G. Jiang, P.A. Lindqvist, "Effects of Loading Rate on Rock Fracture," *International Journal of Rock Mechanics and Mining Sciences* Vol. 36, pp.597-611, 1999
- [7] D.E. Grady, T.G. Trucano, "Impact shock and penetration fragmentation in porous media", *International Journal of Impact Engineering*, 17 (4-6): 861-872 Part 2 1995
- [8] D.E. Grady, M.E. Kipp, "The Micromechanics of Impact Fracture of Rock", *International Journal of Rock Mechanics and Mining Sciences*, and *Geomechanics Abstracts*, Vol. 16, pp 293-302 1979
- [9] Z.X. Zhang, S.Q. Kou, L.G. Jiang, P.A. Lindqvist, "Effects of Loading Rate on Rock Fracture: Fracture Characteristics and Energy Partitioning" *International Journal of Rock Mechanics and Mining Sciences* Vol. 37, pp.745-762, 2000
- [10] S.H. Cho, Y. Ogata, K. Kaneko, "Strain-rate Dependency of the Dynamic Tensile Strength of Rock", *International Journal of Rock Mechanics and Mining Sciences*, Vol. 40, pp. 763-777, 2003
- [11] Zhang ZX, Kou SQ, Yu J, Yu Y, Jiang LG, Lindqvist PA, "Effects of loading rate on rock fracture", *Int. J. Rock Mech. Min. Sci.*, 36 (5):597-611 (1999)
- [12] Jaeger Z, Englman R, Gur Y, Sprecher A., "Internal damage in fragments", *J Mater Sci. Lett.* 1986 (5) 577-579
- [13] P. Lundberg, R. Renstrom, B. Lundberg, "Impact of metallic projectiles on ceramic targets: transition between interface defeat and penetration", *International Journal of Impact Engineering* 24 (2000) 259-275
- [14] P. Lundberg, B. Lundberg, "Transition between interface defeat and penetration for tungsten projectiles and four silicon carbide materials", *International Journal of Impact Engineering* 31 (2005) 781-792
- [15] C. E. Anderson Jr., J. D. Walker, "An analytical model for dwell and interface defeat", *International Journal of Impact Engineering* 31 (2005) 1119-1132
- [16] Chen, X. W., and Li, Q. M., "Deep penetration of a nondeformable projectile with different geometrical characteristics", *Int. J. Impact Eng.*, 27 (6), 619-637 (2002)
- [17] Li, Q. M., and Chen, X. W., "Dimensionless formulae for penetration depth of concrete target impacted by a nondeformable projectile", *Int. J. Impact Eng.*, 28 (1), 93-116 (2003)
- [18] J. Cinnamon, S. E. Jones, J. House, L. L. Wilson, "One-dimensional analysis of rod penetration", *International Journal of Impact Engineering*, Vol. 12 (2) pp. 145-166 (1992)

- [19] Chen, X.W., Li, Q.M., "Transition from nondeformable projectile penetration to semihydrodynamic penetration", *Journal of Engineering Mechanics*, Jan2004, Vol. 130 Issue 1, pp. 123-127
- [20] C. Denoual, F. Hild, "Dynamic fragmentation of brittle solids: a multi-scale model", *European Journal of Mechanics A/Solids* 21 (2002) 105–120
- [21] B. Paliwal, K. T. Ramesh, "An interacting micro-crack damage model for failure of brittle materials under compression", *Journal of the Mechanics and Physics of Solids*, x (xxxx) xxx–xxx
- [22] F. Zhou, J. Molinari, "On the rate-dependency of dynamic tensile strength of a model ceramic system", *Comput. Methods Appl. Mech. Engrg.* 194 (2005) 1693–1709
- [23] F. Zhou, J. Molinari, "Stochastic fracture of ceramics under dynamic tensile loading", *International Journal of Solids and Structures* 41 (2004) 6573-6596
- [24] D.H. Warner and J.F. Molinari, "Micromechanical finite element modeling of compressive fracture in confined alumina ceramic", *Acta Materialia*, Volume 54, Issue 19, November 2006, Pages 5135-5145
- [25] F.H. Zhou, J.F. Molinari, K. T. Ramesh, "Effects of material properties on fragmentation of brittle materials", *International Journal of Fracture* 129 (2): 169-196 May 2006
- [26] F. Zhou, J. F. Molinari, K. T. Ramesh, "A cohesive model based fragmentation analysis: Effects of strain and initial defects distribution", *International Journal of Solids and Structures*, Vol 42, Issue 18-19 (2005) 5181-5207
- [27] *Introduction to Ceramics*, 2nd Edition, by W.D. Kingery, H.K. Bowen and D.R. Uhlmann, John Wiley and Sons, New York, 1976
- [28] A.G. Evans, "Structural Reliability: A Processing-Dependent Phenomenon", *Journal of the American Ceramic Society*, Vol. 65, No. 3, pp 127-137
- [29] T.-S. Yeh and M. D. Sacks, "Effect of Particle-Size Distribution on the Sintering of Alumina," *J. Am. Ceram. Soc.*, **71** [12] C-484–C-487 (1988).
- [30] J. Zhao and M. P. Harmer, "Effect of Pore Distribution on Microstructure Development: I, Matrix Pores," *J. Am. Ceram. Soc.*, **71** [2] 113–20 (1988)
- [31] M. A. Occhionero and J. W. Halloran, "Influence of Green Density upon Sintering"; pp. 89–102 in *Sintering and Heterogeneous Catalysis*, edited by G. C. Kuczynski, A. E. Miller, and G. A. Sargent. Plenum Press, New York, 1984.
- [32] A. V. Galakchov and V. J. Shevchenko, "Influence of Pore Structure Inhomogeneities in Green Compacts on Strength and Reliability of Y-TZP," *J. Eur. Ceram. Soc.*, **6** [5] 317–22 (1990)
- [33] D.-M. Liu, "Influence of Pore Structure in Green Compacts on the Densification of SiC–Al₂O₃–Y₂O₃," *Ceram. Int.*, **22** [5] 403–406 (1996)
- [34] J. Zheng and J. S. Reed, "Study of the Bimodal Pore Structure of Ceramic Powder Compacts by Mercury Porosimetry," *J. Am. Ceram. Soc.*, **75** [12] 3498–50 (1992). [x-ray tomographyde 8-11dedigi yerden]
- [35] M. J. Cima, J. A. Lewis, and A. D. Devoe, "Binder Distribution in Ceramic Greenware during Thermolysis," *J. Am. Ceram. Soc.*, **72** [7] 1192–99 (1989)
- [36] P. K. Lu, J. J. Lannutti, "Effect of density gradients on dimensional tolerance during binder removal", *J. Am. Ceram. Soc.*, **83** [10] 2536–42 (2000)
- [37] Jennifer A. Lewis, "Binder removal from ceramics", *Annual Review of Materials Science* (27) 1997 pp.147-173

- [38] R.W. Rice, "Fractographic Identification of Strength-Controlling Flaws and Microstructure", *Fracture Mechanics of Ceramics*, Vol 1, pp. 323-344, 1974
- [39] R.W. Rice, "Processing Induced Sources of Mechanical Failure in Ceramics", *Processing of Crystalline Ceramics*, pp. 303-319, 1978
- [40] A.G. Evans, "Structural Reliability: A Processing-Dependent Phenomenon", *Journal of the American Ceramic Society*, Vol. 65, No. 3, pp 127-137 [36yla ayni, kaldir]
- [41] M.G. Gee, R. Morrell, "Fracture Mechanics and Microstructures", *Fracture Mechanics of Ceramics*, Vol. 8 Microstructure, Methods, Design, and Fatigue, pp. 1-22, 1986
- [42] F.F. Lange, "Fracture Mechanics and Microstructural Design", *Fracture Mechanics of Ceramics* Vol. 4, pp. 799-819, 1978
- [43] M.J. Normandia, J.C. LaSalvia, W.A. Gooch, J.W. McCauley, A.M. Rajendran, "Protecting the Future Force: Ceramics Research Leads to Improved Armor Performance", *AMPTIAC Quarterly*, 8(4), pages 21-27, 2004
- [44] Jayatilaka A, Trustrum K. Statistical approach to brittle fracture. *J Mater Sci* 12:1426-30 (1977)
- [45] Y. Zhang, M. Inoue, N. Uchida, K. Uematsu, "Characterization of processing pores and their relevance to the strength of alumina ceramics", *Journal of Materials Research*, Vol. 14, No. 8, 1999
- [46] K. Uematsu, H. Abe, M. Naito, T. Hotta, N. Shinohara, "Flaw Size Distribution in High-Quality Alumina", *Journal of the American Ceramic Society*, Vol. 86, No. 6, pp. 1019-1021, 2003
- [47] K. Uematsu, M. Sekiguchi, J-Y. Kim, K. Saito, Y. Mutoh, M. Inoue, Y. Fujino, and A. Miyamoto, "Effect of processing conditions on the characteristics of pores in hot isostatically pressed alumina", *Journal of Material Science* 28, 1788 (1993)
- [48] M.G. Gee and R. Morrell, in *Fracture Mechanics of Ceramics*, edited by R.C. Bradt, D.P.H. Hasselman, and F.F. Lange (Plenum Press, New York, 1986), Vol. 8, p. 1.
- [49] H. Takahashi, N. Shinohara, K. Uematsu, and J. Tsubaki, "Influence of Granule Character and Compaction on the Mechanical Properties of Sintered Silicon Nitride", *Journal of the American Ceramic Society* 79, 843 (1996)
- [50] M.G. Gee, "Brittle fracture of hardmetals: Dependence of strength on defect size distribution", *Int. J. Mech. Sci.* 26, 85 (1984)
- [51] M. P. Bakas, "Analysis of Inclusion Distributions in Silicon Carbide Armor Ceramics", Ph.D. Thesis, Rutgers University, 2006
- [52] M.P. Bakas, V.A. Greenhut, D.E. Niesz, G.D. Quinn, J.W. McCauley, A.A. Wereszczak, and J.J. Swab, "Anomalous Defects and Dynamic Material Properties in the Performance," *International Journal of Applied Ceramic Technology*, Vol.1 [3] 211(2004)
- [53] C. Ziccardi, M.V. Demirbas, R. A. Haber, D. E. Niesz and J. McCauley, "Means of Using Advance Processing to Eliminate Anomalous Defects on SiC Armor", *Advances in Ceramic Armor, Cer. Eng. Sci. Proc.*, Vol.26, No.7, p. 271-277, 2005
- [54] R. Hamminger, "Carbon inclusions in sintered silicon carbide", *Journal of the American Ceramic Society* 72 [9] (1989) 1741-1744
- [55] T. Nagano, K. Kaneko, G. Zhan, M. Mitomo, "Effect of atmosphere on weight loss in sintered silicon carbide during heat treatment", *Journal of the American Ceramic Society*, 83 [11] 2781-2787 (2000)

- [56] R. M. Williams, B. N. Juterbock, S. S. Shinozaki, C. R. Peters, T. J. Whalen, "Effects of sintering temperatures on the physical and crystallographic properties of β -SiC", American Ceramic Society Bulletin 64 [10] 1385-1389 (1985)
- [57] J. W. Fergus, W. L. Worrell, "Effect of carbon and boron on the high-temperature oxidation of silicon carbide", Journal of the American Ceramic Society, 78 [7] 1961-1964 (1995)
- [58] S. Shinozaki, R. M. Williams, B. N. Juterbock, W. T. Donlon, J. Hangan, C. R. Peters, "Microstructural development in pressure-sintered β -SiC materials with Al, B and C additions", American Ceramic Society Bulletin 64 [10] 1389-1393 (1985)
- [59] S. Prochazka, R. M. Scanlan, "Effect of boron and carbon on sintering of SiC", Journal of the American Ceramic Society, Vol. 58, No. 1-2, 72 (1975)
- [60] F.F. Lange, "Strong, High-Temperature Ceramics", Annual Review of Materials Science, August 1974, Vol. 4, Pages 365-390
- [61] W. J. Clegg, "Role of carbon in the sintering of boron-doped SiC", Journal of the American Ceramic Society, 83 [5] 1039-1043 (2000)
- [62] W. van Rijswijk, D. J. Shanefield, "Effects of carbon as a sintering aid in silicon carbide", Journal of the American Ceramic Society, 73 [1] 148-149 (1990)
- [63] L. Stobierski, A. Gubernat, "Sintering of silicon carbide, I. Effect of carbon", Ceramics International 29 (2003) 287-292
- [64] R. Hamminger, G. Grathwohl, F. Thummler, "Microanalytical investigation of sintered SiC, Part 2: Study of the grain boundaries of sintered SiC by high resolution Auger electron spectroscopy", Journal of Materials Science 18 (1983) 3154-3160
- [65] F. F. Lange, "Hot-pressing behaviour of silicon carbide powders with additions of aluminium oxide", Journal of Materials Science, Vol. 10, No. 2 (1975) 314-320
- [66] X. F. Zhang, M. E. Sixta, L. C. De Jonghe, "Grain boundary evolution in hot-pressed ABC-SiC", Journal of the American Ceramic Society 83 (11), 2813-2820, 2000
- [67] T. Sakai, "Hot-Pressing of SiC with Additions of BaO and C", Journal of the American Ceramic Society 68(8) (1985), pp. 191-193
- [68] B. Lin, M. Imai, T. Yano, T. Iseki, "Hot-pressing of β -SiC powder with Al-B-C additives", Journal of the American Ceramic Society 69 (4), pp. 67-68, 1986
- [69] T. Iseki, K. Arakawa, H. Suzuki, "Joining of dense silicon carbide by hot-pressing", Journal of Materials Science, Vol. 15, No.4 (1980), pp. 1049-1050
- [70] N. Hidaka, Y. Hirata, X. H. Wang, S. Tabata, "Aqueous processing, hot-pressing and mechanical properties of silicon carbide with Al_2O_3 and Y_2O_3 ", Journal of the Ceramic Society of Japan 113 (2) 143-148 (2005)
- [71] K. L. More, C. H. Carter, Jr., J. Bentley, W. H. Wadlin, L. LaVanier, R. F. Davis, "Occurrence and Distribution of Boron-Containing Phases in Sintered α -Silicon Carbide", *J Am. Ceram. Soc.*, 69 [9] 695-98 (1986)
- [72] R.W. Carpenter, W. Braue, R. A. Cutler, "Transmission electron microscopy of liquid phase densified SiC", Journal of Materials Research, Vol. 6, No.9, pp. 1937-1944 (1991)
- [73] X. F. Zhang, M. E. Sixta, L. C. De Jonghe, "Secondary Phases in Hot-Pressed Aluminim-Boron-Carbon-Silicon Carbide", *J. Am. Ceram. Soc.*, 84 [4] 813-20 (2001)
- [74] B. W. Lin, M. Imai, T. Yano, and T. Iseki, "Hot Pressing of β -SiC Powder with Al-B-C Additives," *J. Am. Ceram. Soc.*, 69 [4] C-67-C-68 (1986)
- [75] J. J. Cao, W. J. Moberly Chan, L. C. De Jonghe, C. J. Gilbert, and R. O. Ritchie,

- “*In Situ*-Toughened Silicon Carbide with Al-B-C Additions,” *J. Am. Ceram. Soc.*, **79** [2] 461–69 (1996).
- [76] D. Chen, C. J. Gilbert, X. F. Zhang, and R. O. Ritchie, “High-Temperature Cyclic Fatigue-Crack Growth Behavior in an *in Situ*-Toughened Silicon Carbide,” *Acta Mater.*, **48** [3] 659–74 (2000).
- [77] T. E. Mitchell Jr., L. C. De Jonghe, W. J. Moberly Chan, and R. O. Ritchie, “Silicon Carbide Platelet/Silicon Carbide Composites,” *J. Am. Ceram. Soc.*, **78** [1] 97–103 (1995)
- [78] W. J. Moberly Chan, J. J. Cao, and L. C. De Jonghe, “The Role of the Amorphous Grain Boundaries and the b– a Transformation in Toughening SiC,” *Acta Mater*, **46** [5] 1625–35 (1998).
- [79] R. Sherman, “Auger analysis of hot-pressed and sintered SiC”, *Journal of the American Ceramic Society*, 68 (1) C-7-C-10 (1985)
- [80] M. N. Rahaman, “Ceramic Processing”, Taylor & Francis, Boca Raton, 2007
- [81] C. A. Handwerker, J. M. Dynys, R. M. Cannon, R. L. Coble, “Dihedral angles in magnesia and alumina: distributions from thermal surface grooves”, *Journal of the American Ceramic Society*, 73, 1371 (1990)
- [82] W. D. Kingery and B. Francois, “Sintering of crystalline oxides: I. Interactions between grain boundaries and pores”, *Sintering and Related Phenomena*, G.C. Kuczynski, N.A. Hooton, G.F. Gibbon, Gordon and Breach, New York, 1967
- [83] F. J. Lino, “Pull-out During Grinding of Ceramics Containing an Amorphous Phase”, *Struers Journal of Materialography, Structure* (2000)
- [84] J. F. Li, J. X. Ding, “Fractal character of circumferences of polishing-induced pullouts of plasma sprayed Cr₃C₂-NiCr coatings”, *Thin Solid Films*, 376 (2000) pp. 179-182
- [85] J. Li, H. Liao, X. Wang, C. Coddet, “Fractal perimeters of polishing-induced pullouts present on polished cross sections of plasma sprayed yttria-stabilized zirconia coatings”, *Journal of the American Ceramic Society*, 86 [11] 1906-1910 (2003)
- [86] S. Desphande, A. Kulkarni, S. Sampath, H. Herman, “Application of image analysis for the characterization of porosity in thermal spray coatings and correlation with small angle neutron scattering”, *Surface and Coatings Technology*, 187 (2004) pp. 6-16
- [87] John C. Russ, “Computer-Assisted Microscopy”, 1990 Plenum Press, New York
- [88] G. F. Vander Voort: *Computer-aided microstructural analysis of specialty steels. Mater. Charact.* 27: 241–260 (1991).
- [89] P. J. Wray, O. Richmond, and H. L. Morrison: Use of the dirichlet tessellation for the characterizing and modeling nonregular dispersions of secondphase particles. *Metallography* 16:39–58 (1983).
- [90] J. B. Parse and J. A. Wert: A geometrical description of particle distributions in materials. *Modell. Simul. Mater. Sci. Eng.* 1:275–296 (1993)
- [91] E. A. Gulliver, “Simulation of mixture microstructures via particle packing models and their direct comparison with real mixtures”, Ph.D Thesis (2003), Rutgers University
- [92] S. Torquato, “Random Heterogeneous Materials, Microstructure and Macroscopic Properties”, Springer-Verlag New York (2002)
- [93] W. A. Spitzig, J. F. Kelly, and O. Richmond: Quantitative characterization of second-phase populations. *Metallography* 18:235–261 (1985).

- [94] A. Olszowka-Myalska, J. Szala, J. Cwajna, "Characterization of reinforcement distribution in $\text{Al}/(\text{Al}_2\text{O}_3)_p$ composites obtained from composite powder", *Materials Characterization* 46, 189-195 (2001)
- [95] K. J. Kurzydowski, J. Bystrzycki, and T. Czujko, "Applications of cluster analysis in the quantitative estimation of similarities in geometrical characteristics of grains in polycrystalline materials' *Mater. Charact.* 32:105–118 (1994)
- [96] N. Yang, J. Boselli, P. J. Gregson, I. Sinclair, "Simulation and Quantitative Assessment of Finite-size Particle Distributions in Metal Matrix Composites", *Journal of Microscopy* 175, 195-204 (1994)
- [97] J. M. Missiaen, J. M. Chaix, "The homogeneity of phase repartition in TiB_2 -Fe composites using variance and covariance analysis", *Journal of Microscopy*, Vol.. 175, pp. 195-204 (1994)
- [98] J. Zhang, M. A. Przystupa, and A. J. Luevano: Characterization of pore and constituent particle populations in 7050-T7451 aluminum plate alloys. *Metall. Trans.* 29A:727–737 (1998)
- [99] A. Tewari, M. Dighe, and A. M. Gokhale: Quantitative characterization of spatial arrangement of micropores in cast microstructures. *Mater. Charact.* 40:119–132 (1998)
- [100] I. Kadashevich, H. Schneider, D. Stoyan, "Statistical modeling of the geometrical structure of the system of artificial air pores in autoclaved aerated concrete", *Cement and Concrete Research* xx (2004) xxx-xxx
- [101] H. Schwarz and H. E. Exner: The characterization of the arrangement of feature centroids in planes and volumes. *J. Microsc.* 129:155–169 (1983).
- [102] J. Hubalkova, D. Stoyan, "On a qualitative relationship between degree of inhomogeneity and cold crushing strength of refractory castables", *Cement and Concrete Research* 33, 747-753 (2003)
- [103] D. Stoyan, W. S. Kendall, J. Mecke, *Stochastic Geometry and its Applications*, 2nd edition, Wiley, Chichester, (1995)
- [104] P. J. Diggle, "Statistical Analysis of Spatial Point Patterns", 2nd edition, Arnold, London (2003)
- [105] P. J. Diggle, N. Lange, F. M. Benes, "Analysis of variance for replicated spatial point patterns in clinical neuroanatomy", *J. Am. Statist. Assn.* 86, 618–625. (1991)
- [106] P.J. Diggle, J. Mateu, H. E. Clough, A comparison between parametric and non-parametric approaches to the analysis of replicated spatial point patterns. *Adv. Appl. Prob.* 32, 331–343 (2000)
- [107] D. Stoyan, H. Stoyan, *Fractals, Random Shapes and Point Fields - Methods of Geometrical Statistics*, Wiley, Chichester (1994)
- [108] K. Schladitz, A. Sarkka, I. Pavenstadt, O. Haferkamp, T. Mattfeldt, "Statistical analysis of intramembranous particles using freeze fracture specimens", *Journal of Microscopy*, Vol 211. pp 137-153 (2003)
- [109] Tewari, A. M. Gokhale, "Nearest neighbor distances in uniaxial fiber composites", *Computational Materials Science*, 31 (2004) 13-23
- [110] J. Ohser, F. Mucklich, "Statistical Analysis of Microstructures in Materials Science", John Wiley & Sons, Ltd (2000)
- [111] J. P. Anson, J. E. Gruzlefski, "The Quantitative Discrimination between Shrinkage and Gas Microporosity in Cast Aluminum Alloys Using Spatial Data Analysis" *Materials Characterization* 43, 319-335 (1999)

- [112] P. A. Karnezis, G. Durrant, B. Cantor, "Characterization of Reinforcement Distribution in Cast Al-Alloy/SiC_p Composites" *Materials Characterization* 40, 97-109 (1998)
- [113] M. Li, S. Ghosh, O. Richmond, H. Weiland, T. N. Rouns, "Three dimensional characterization and modeling of particle reinforced metal matrix composites part I: Quantitative description of microstructural morphology", *Materials Science and Engineering A265* pp. 153-173 (1999)
- [114] M. Li, S. Ghosh, O. Richmond, H. Weiland, T. N. Rouns, "Three dimensional characterization and modeling of particle reinforced metal matrix composites part II: Damage characterization", *Materials Science and Engineering A266* pp. 221-240 (1999)
- [115] S. Ghosh, Z. Nowak, K. Lee, "Quantitative characterization and modeling of composite microstructures by Voronoi cells", *Acta Materialia*, Vol. 45, No. 6 (1997) 2215-2234
- [116] A. M. Murphy, S. J. Howard, T. W. Clyne, "Characterization of severity of particle clustering and its effect on fracture of particulate MMCs", *Journal of Materials Science* 31 (20), 5399-5407 (1996)
- [117] D. J. Green, "An introduction to the mechanical properties of ceramics", Cambridge University Press (1998)
- [118] I. J. McCollm, "Ceramic Hardness", Plenum Press, New York (1990)
- [119] A. Szymanski, J. M. Szymanski, "Hardness Estimation of Minerals, Rocks and Ceramic Materials", Elsevier Science Publications (1989)
- [120] H. Conrad, "Effect of grain size on the lower yield and flow stress of iron and steel", *Acta Metall.* 11 (1963) 75
- [121] A.W. Thompson, M.I. Baskes, W.F. Flanagan, "The dependence of polycrystal work hardening on grain size", *Acta Metall.* 21 (1973) 1017
- [122] H.L. Wang, M.H. Hon, "Temperature dependence of ceramics hardness", *Ceramics International* 25 (1999) 267-271
- [123] A. A. Wereszczak and R. H. Kraft, "Instrumented hertzian indentation of armor ceramics", *Ceramic Engineering and Science Proceedings* 23, Number 3 (53-64) 2002
- [124] J. Sternberg, "Material Properties Determining the Resistance of Ceramics to High Velocity Penetration", *J. Appl. Phys.*, Vol 65(9), 1 May 1989
- [125] <http://library.lanl.gov/cgi-bin/getfile?17-04.pdf>
- [126] R.W. Rice, *Porosity of Ceramics*, Marcel Dekker, 1998, pp. 375-421.
- [127] P.E. Wang, T.K. Chaki, "Sintering behavior and mechanical properties of hydroxyapatite and dicalcium phosphate", *J. Mater. Sci. Mater. Med.* 4 (1993) 150-158.
- [128] R.W. Rice, "Evaluation and extension of physical property-porosity models based on minimum solid area", *J. Mater. Sci.* 31 (1996) 102-118.
- [129] A.K. Mukhopadhyay, K.K. Phani, "An analysis of microstructural parameters in the minimum contact area model for ultrasonic velocity-porosity relations", *J. Eur. Ceram. Soc.* 20 (2000) 29-38
- [130] D.M. Liu, C.T. Fu, "Effect of residual porosity and pore structure on thermo-mechanical strength of SiC-Al₂O₃-Y₂O₃", *Ceram. Int.*, 22 (1996) 229-232
- [131] C. Reynaud, F. Thevenot, "Porosity dependence of mechanical properties of porous sintered SiC - Verification of the minimum solid area model", *J. Mater. Sci. Lett.* 19 (2000) 871-874.

- [132] Quinn JB, Quinn GD, "Indentation brittleness of ceramics: A fresh approach", *Journal of Materials Science* 1997;32:4431-4346
- [133] T.P. Hoepfner, E.D. Case, The porosity dependence of the dielectric constant for sintered hydroxyapatite, *J. Biomed. Mater. Res.* 60 (2002) 643–650
- [134] R. W. Rice, "Use of normalized porosity in models for the porosity dependence of mechanical properties", *Journal of Materials Science* 40 (2005) 983-989
- [135] R. W. Rice, "Comparison of physical property-porosity behavior with minimum solid area models", *Journal of Materials Science* 31 (1996) 1509-1528
- [136] D. Viechnicki, W. Blumenthal, M. Slavin, C. Tracy and H. Skeelee, "Armor Ceramics – 1987", *The Third Tacom Armor Coordinating Conference Proceedings*
- [137] E. Medvedovski, "Alumina ceramics for ballistic protection – Part 2", *American Ceramic Society Bulletin*, Vol. 81, No. 4 (2002) pp. 45-50
- [138] M. Flinders, D. Ray, A. Anderson, and R. A. Cutler, "High-Toughness Silicon Carbide as Armor", *J. Am. Ceram. Soc.*, 88 [8] 2217–2226 (2005)
- [139] N. Orlovskaya, M. Lugovy, V. Subbotin, O. Radchenko, J. Adams, M. Chheda, J. Shih, J. Sankar, S. Yarmolenko, "Robust design and manufacturing of ceramic laminates with controlled thermal residual stresses for enhanced toughness", *Journal of Materials Science* 40 (2005) 5483 – 5490
- [140] M.L. Wilkens, Mechanics of penetration and perforation, *Int J Eng Sci* 16 (1978), pp. 793–807.
- [141] Z. Rozenberg and Y. Yeshurun, "The relation between ballistic efficiency and compressive strength of ceramic tiles", *International Journal of Impact Engineering*, 7 3 (1988), pp. 357–362
- [142] J. Sternberg, "Material Properties Determining the Resistance of Ceramics to High Velocity Penetration", *J. Appl. Phys.*, Vol 65(9), 1 May 1989
- [143] P. Lundberg, R. Renstrom, B. Lundberg, "Impact of metallic projectiles on ceramic targets: transition between interface defeat and penetration", *International Journal of Impact Engineering* 24 (2000) 259-275
- [144] Davidge RW. Mechanical behavior of ceramics, Cambridge, Cambridge University Press; 1979
- [145] Munz D, Fett T. Ceramics: mechanical properties, failure behaviour, materials selection. Berlin: Springer; 1999.
- [146] C. K. Lin, C. C. Berndt, "Statistical analysis of microhardness variations in thermal spray coatings", *Journal of Materials Science* 30 (1995) 111-117
- [147] J. Li, C. Ding, "Determining microhardness and elastic modulus of plasma-sprayed Cr_3C_2 -NiCr coatings using Knoop indentation testing", *Surface and Coatings Technology* 135 (2001) 229-237
- [148] W. Grant Ireson, Clyde F. Coombs, Jr., Richard Y. Moss, "Handbook of Reliability Engineering and Management", McGraw-Hill, Inc. (1995)
- [149] G. E. Dieter, "Engineering Design – A Materials and Processing Approach", McGraw-Hill, Inc., (1991)
- [150] Q. Zheng, X. Zheng, F. Wang, "On the expressions of fatigue life with given survivability", *Engineering Fracture Mechanics*, Vol. 53, No. 1, 49-55 (1996)
- [151] Y. Xu, L. Cheng, L. Zhang, H. Yin, X. Yin, "Mechanical properties of 3D fiber reinforced C/SiC composites", *Materials Science and Engineering A300* (2001) 196-202

- [152] X. Zhu, D. Jiang, S. Tan, "Preparation of silicon carbide reticulated porous ceramics", *Materials Science and Engineering A323* (2002) 232-238
- [153] L. Guerra Rosa, J. Lamon, I. Figuerido, F. A Costa Oliveira, "A method to distinguish extrinsic and intrinsic fracture origin populations in monolithic ceramics", *Journal of the European Ceramic Society*, xxx (2006) xxx-xxxx
- [154] W. J. Tseng, M. Taniguchi, T. Yamada, "Transformation strengthening of as-fired zirconia ceramics", *Ceramics International* 25 (1999) 545-550
- [155] W. Weibull, "A statistical distribution function of wide applicability", *J. Appl. Mech.* 18 pp. 293-297 (1951)
- [156] C. K. Lin, C. C. Berndt, "Statistical analysis of microhardness variations in thermal spray coatings", *Journal of Materials Science* 30 (1995) 111-117
- [157] J. W. Newkirk, S. Thakur, "Mechanical properties distributions of PM parts", *Powder Metallurgy* (2002) Vol. 45 No.4
- [158] T. Valente, "Statistical evaluation of Vickers indentation test results for thermally sprayed materials", *Surface and Coatings Technology* 90 (1997) 14-20
- [159] K. C. Kapur and L. R. Lamberson, "Reliability in Engineering Design" (Wiley, New York, 1977)
- [160] B. Bergman, "On the estimation of the Weibull modulus", *Journal of Materials Science Letters* 3 (1984) 689-692
- [161] G. D. Quinn, "Weibull Strength Scaling for Standardized Rectangular Flexure Specimens", *Journal of the American Ceramic Society*, Vol. 86, No. 3, 508-10, 2003
- [162] G. D. Quinn, R. Morrel, "Design Data for Engineering Ceramics: A Review of the Flexure Test", *Journal of the American Ceramic Society*, Vol. 74, No. 9, pp. 2037-66, 1991
- [163] T. Ohji, Y. Yamauchi, W. Kanematsu, S. Ito, "Tensile Rupture Strength and Fracture Defects of Sintered Silicon Carbide", *Journal of the American Ceramic Society*, Vol. 72, No. 4, pp. 688-90, 1989
- [164] R. Danzer, P Supancic, J. Pascual, T. Lube, "Fracture statistics of ceramics – Weibull statistics and deviations from Weibull statistics", *Engineering Fracture Mechanics* xxx (2006) xxx-xxx
- [165] J. B. Wachtman, "Mechanical Properties of Ceramics", John Wiley & Sons, New York (1996)
- [166] B. Lawn, "Indentation of ceramics with spheres: a century after Hertz. *J Am Ceram Soc* 81 1977–1994 (1998)
- [167] R. Danzer, "A general strength distribution function for brittle materials", *Journal of the European Ceramic Society*, Volume 10, Issue 6, 1992, pp. 461-472
- [168] N. Orlovskaya, H. Peterlik, W. Steinkeller, K. Kromp, "Prediction of strength of recrystallized silicon carbide from pore size measurement - Part I The bimodality of the distribution", *Journal of Materials Science* 35 (2000) 699– 705
- [169] H. Peterlik, N. Orlovskaya, W. Steinkeller, K. Kromp, "Prediction of strength of recrystallized silicon carbide from pore size measurement - Part II The reliability of the prediction", *Journal of Materials Science* 35 (2000) 707– 711
- [170] R.S. Lima, A. Kucuk, C.C. Berndt, "Bimodal distribution of mechanical properties on plasma sprayed nanostructured partially stabilized zirconia", *Materials Science and Engineering A237* (2002) 224-232

- [171] J. M. Schneider, M. Bigerelle, A. Iost, "Statistical analysis of the Vickers hardness", *Materials Science and Engineering A262* (1999) 256–263
- [172] C. C. Berndt and C. K. Lin, "Measurement of adhesion for thermally sprayed materials", *J. Adhesion Sci. Technol.* Vol. 7, No. 12, pp. 1235-1264 (1993)
- [173] M. Factor, I. Roman, "Vickers microindentation of WC-12%Co thermal spray coating - Part 1: statistical analysis of microhardness data", *Surface and Coatings Technology* 132 (2000) 181-193
- [174] C. Selcuk, R. Benthams, N. Morley, J.V. Wood, "Microhardness as a measure of homogeneity of porous tungsten", *Materials Letters* 58 (2004) 1873-1876
- [175] M.T. Lin, D.Y. Jiang, L. Li, Z.L. Lu, T.R. Lai, J.L. Shi, "The effect of creep deformation of a β sialon on Vickers hardness, fracture toughness and Weibull modulus", *Materials Science and Engineering A351* (2003) 9-14
- [176] R. E. Brennan, "Ultrasonic Nondestructive Evaluation of Armor Ceramics", Ph.D. Thesis, Rutgers University, 2007
- [177] M.C. Bhardwaj, "Evolution, Practical Concepts and Examples of Ultrasonic NDC", *Ceramic Monographs – Handbook of Ceramics*, 41, pages 1-7, 1992
- [178] M. Berman, L. M. Bischof, E. J. Breen, G. M. Peden, "Image Analysis", *Materials Forum* 18, 1-19 (1994)
- [179] D. L. Misell, "Image analysis, enhancement and interpretation", Amsterdam; New York: North-Holland Pub. Co., 1978
- [180] Todd R. Reed, "Digital image sequence processing, compression, and analysis", Boca Raton: CRC Press, 2005
- [181] C. J. Shih, V. F. Nesterenko, M. A. Meyers, "High strain rate deformation and comminution of silicon carbide", *Journal of Applied Physics*, (1998) Vol. 83, Number 9, 4660-4671
- [182] D. Ray, R. M. Flinders, A. Anderson, R. A. Cutler, J. Campbell, J. W. Adams, "Effect of microstructure and mechanical properties on the ballistic performance of sic-based ceramics", *Ceram. Eng. Sci. Proc.*, 2007, vol. 27, No. 7, pp. 85-96
- [183] W. J. Moberlychan, J. J. Cao, L. C. De Jonghe, "The roles of amorphous grain boundaries and β - α transformation in toughening SiC", *Acta. Mater.* Vol. 46 No.5 (1998) 1625-1635
- [184] T. Wilantewicz, W. R. Cannon, D. E. Niesz, J. McCauley, "Property Measurements as Estimators of Ballistic Performance", 31st International Cocoa Beach Conference on Advanced Ceramics and Composites, Daytona Beach, FL, January 2007

9. CURRICULUM VITA

Memduh Volkan Demirbaş

1. Education

- Ph.D., Ceramic and Materials Science and Engineering, May 2008
Rutgers University, Piscataway, NJ
- M.S., Ceramic and Materials Engineering, 2004
Rutgers University, Piscataway, NJ
- B.S., Metallurgical and Materials Engineering, 2001
Middle East Technical University (METU), Ankara, Turkey

2. Experience

- Research Assistant, Rutgers University, Piscataway, NJ, 2001-2008

3. Publications

- M. Ozenbas, M.V. Demirbas, M. B. Emre, N. Ozguven, "Preparation and Properties of $\text{Ba}_{1-x}\text{Sr}_x\text{TiO}_3$ Films Deposited by Sol-gel Technique", 5th Ceramic Congress Proceedings Book, Istanbul, Turkey, October 3-5, 2001, Vol. 21, p. 439-444
- M. V. Demirbas and R. A. Haber, "Defining Microstructural Tolerance Limits of Defects for SiC Armor", Ceramic Armor and Armor Systems II, Ceramic Transactions, 178, p. 109-122, 2005
- C. Ziccardi, M.V Demirbas, R. A. Haber, D. E. Niesz and J. McCauley, "Means of Using Advance Processing to Eliminate Anomalous Defects on SiC Armor", Advances in Ceramic Armor, Cer. Eng. Sci. Proc., Vol.7, No.7, p. 271-277, 2005
- M.V. Demirbas, R. A. Haber, "Relationship of Microstructure and Hardness for Al_2O_3 Armor Material", Advances in Ceramic Armor II, CESP, p. 167-179, 2006
- M. V. Demirbas, R. A. Haber, R. E. Brennan, "Spatial Distribution of Defects in SiC and Its Correlation with Localized Property Measurements", 31st International Conference on Advanced Ceramics and Composites Proceedings (in press)